Investigating Chromospheric Magnetic Activity on Young Stars and The Wide Field CAMera for UKIRT

A THESIS SUBMITTED TO THE UNIVERSITY OF EDINBURGH
FOR THE DEGREE OF DOCTOR OF PHILOSOPHY
IN THE FACULTY OF SCIENCE AND ENGINEERING

February 2007

By

Morag Ann Hastie

Department of Physics and Astronomy

Principal Supervisor: **Dr. M. M. Casali**

Contents

Abstract 12

Declaration 14

Preface 15

1 Introduction to Magnetic Surfaces of Young Stars 22

1.1 The Beginnings of Stars 22

1.1.1 The Hertzsprung-Russell Diagram 25

1.1.2 T Tauri Stars 26

1.2 Observational Tools and Techniques 30

1.2.1 Light-curve Modelling 30

1.2.2 Doppler Imaging 30

1.2.3 Zeeman Broadening 31

1.2.4 Chromospheric Indicators 32

1.3 Magnetic Activity on T Tauri Stars 32

1.4 This Study 34

2 Observations of T Tauri Stars in Nearby Clusters 36

2.1 The Clusters 36

2.2 The T Tauri Sample 38

2.3 The Spectroscopic Observations 44

2.3.1 UKST & the 6dF Instrument 44

2.4 Reduction of the Spectra 46

2.4.1 The Flat Field and Tram Line Maps 46

2.4.2 Subtracting Scattered Light . . . 47
2.4.3 Extracting the Spectra . . . 47
2.4.4 Cosmic Ray Rejection . . . 48
2.4.5 The Arc and Wavelength Calibration . . . 49
2.4.6 Fibre Throughput Calibration & The Offset Sky . . . 49
2.4.7 The Object Frames . . . 51
2.5 Resultant Spectra . . . 52
2.6 The Photometric Observations . . . 55
2.6.1 The Automated Patrol Telescope . . . 55
2.6.2 Reducing The Photometric Data . . . 56
2.7 Determining Stellar Parameters . . . 56
2.7.1 Surface Gravity dervied from T_{eff} and L_* . . . 58
2.7.2 Determining IR Colour Index & Bolometric Correction . . . 59
2.7.3 Accounting For Extinction . . . 61
2.7.4 Plotting the HR Diagram . . . 61
2.7.5 Determining Spectral Type . . . 68
2.8 Subtraction of Photospheric Contribution . . . 68
2.9 Quantifing the CaII Emission . . . 73
2.9.1 Mount Wilson S Index . . . 73
2.10 Testing the Selection of the Synthetic Spectra . . . 78
2.11 Correlation between CaII & light variations . . . 79
2.11.1 Weak-line T Tauri Sample . . . 82
2.11.2 Classical T Tauri Sample . . . 93
2.11.3 Binary Targets . . . 96
2.11.4 Field Star Sample . . . 98
2.11.5 Summary . . . 104

3 Modelling the Stellar Surface Magnetic Activity **107**
3.1 The Surfaces of T Tauri Stars . . . 107
3.1.1 A Case Study - V410 Tauri . . . 109
3.2 The Sun as a Reference . . . 113
3.2.1 The V Band Continuum . . . 114

3.2.2 The Continuum at 3950.5Å . . . 115
3.2.3 CaII Emission from Active Regions . . . 117
3.3 Construction of the Models . . . 120
3.3.1 The HEALPix Software . . . 120
3.3.2 The Model Mechanisms . . . 121
3.3.3 Limb Darkening . . . 129
3.4 The Models . . . 130
3.4.1 Graphical Demonstration of the Models . . . 130
3.4.2 Surface Features . . . 134
3.5 Comparison: Theoretical and Observational Data . . . 137
3.5.1 Fractional Coverage of the Stellar Surface . . . 142

4 WFCAM & The Cryostat Thermal Model **146**
4.1 Instrument Overview . . . 146
4.1.1 Science Drivers . . . 147
4.1.2 Optical System . . . 152
4.1.3 The Focal Plane . . . 155
4.2 Fundamentals of Heat Transfer . . . 158
4.2.1 Conduction . . . 158
4.2.2 Convection . . . 160
4.2.3 Radiation . . . 161
4.3 The Cryogenic Design . . . 163
4.3.1 Overview . . . 163
4.3.2 The Radiation Shield . . . 164
4.3.3 The Cold Structure . . . 166
4.4 The Thermal Path Model . . . 168
4.4.1 Comparison of Model with Real Data . . . 174
4.5 Modelling the Detector Cooling Rate . . . 175

5 The WFCAM Science Detectors **182**
5.1 Principles of Infrared Detectors . . . 183
5.1.1 Photon Detection . . . 183

5.1.2 Recording the Photons . . . 185
5.1.3 Structure of Hybrid Arrays . . . 186
5.1.4 The Read Out Procedure . . . 190
5.1.5 The Hawaii-II Device . . . 192
5.2 Theory of Noise . . . 192
5.3 Different Operational Modes . . . 194
5.3.1 Simple Readout . . . 195
5.3.2 Correlated Double Sampling . . . 195
5.3.3 Multiple Non-Destructive Read Mode . . . 197
5.3.4 Fowler Sampling . . . 198
5.4 Detector Properties & Characterisation Tests . . . 199
5.4.1 Crosstalk . . . 200
5.4.2 Flat Field & Reset Anomaly . . . 204
5.4.3 Linearity . . . 210
5.4.4 Noise . . . 210
5.4.5 Persistence . . . 211
5.4.6 Quantum Efficiency . . . 216
5.4.7 Well Capacity & Gain . . . 217
5.4.8 Interpixel Capacitance . . . 218

A Spectra 223

List of Tables

2.1 Stellar parameters of Bouvier and Appenzeller (1992) sample 41
2.2 Stellar parameters of Preibisch et al. (1998) sample 42
2.3 Stellar parameters of Martin et al. (1998) sample 44
2.4 Details of UK Schmidt Observing Run 45
2.5 APT V Band Magnitudes for T Tauri Sample 57
2.6 2MASS J,H,K Magnitude for T Tauri Sample 60
2.7 Derived Stellar Parameters for T Tauri Sample 65
2.8 Comparison with Bouvier and Appenzeller (1992) Derived Parameters . 66
2.9 Adjusted 'Missing' Spectral Types 70
2.10 CaII S Index Observing Windows. 74

3.1 V410 Tau - Spot Properties 110
3.2 V410 Tau - Spot Properties from Joncour, Bertout and Menard (1994) . . 111
3.3 V410 Tau - Changing Features from Rice and Strassmeier (1996) 113
3.4 F_{3950} for spectral type G, K, M. 125

4.1 Seven Year UKIDSS Plan 151
4.2 WFCAM - Filter Properties 156
4.3 Thermal Model - Dimensions 171
4.4 Thermal Model - Masses 172
4.5 Thermal Model - Material Properties 172
4.6 Thermal Model - Example Equations 173

5.1 Properties of semiconductor materials used in photon detectors 184
5.2 Summary of QE 218

5.3 Summary of Full Well Capacity & Gain 219

List of Figures

1.1 The Hertzsprung-Russell 26

2.1 Images of the ρ Ophiuchus and Upper Scoripius 38
2.2 Location of observed T Tauri stars in ρ Oph & Upper Sco 39
2.3 6dF – Background Scatter Fit 48
2.4 6dF – Reduced Arc Frame 50
2.5 6dF – Throughput map. 51
2.6 6dF – Fully Reduced Frame. 52
2.7 6dF – Sky Frame 53
2.8 Spectra – Target Object GSC6798–35 54
2.9 Spectra – Target Object ROXs44 54
2.10 Spectra – Target Object GSC6214–2288 55
2.11 HR Diagram for T Tauri Sample 62
2.12 (J–H) – (H–K) Colour-Colour Diagram for T Tauri Sample 64
2.13 HR Diagram from Bouvier and Appenzeller (1992) 67
2.14 Spectra of 'Missing' Spectral Type T Tauri 69
2.15 GSC6793–994 with Corresponding Synthetic Spectra 72
2.16 GSC6793–35 with Corresponding Synthetic Spectra 72
2.17 GSC6798–35 Spectra with S Index Windows Overlaid. 75
2.18 Timeline CaII Spectra for GSC6794–537: I 76
2.19 Timeline CaII Spectra for GSC6794–537: II 77
2.20 Resultant Plots for: GSC6798–35 83
2.21 Resultant Plots for RXJ1623.8–2341, RXJ1620.7–2348 85
2.22 Resultant Plots for: GSC6793–569, GSC6793–868 86

2.23 Resultant Plots for: GSC6793−797, GSC6793−994 87
2.24 Resultant Plots for: GSC6793−806, GSC6214−2384 88
2.25 Resultant Plots for: GSC6794−537, RXJ1625.2−2455 89
2.26 Resultant Plots for: GSC6794−337, RXJ1621.4−2312 90
2.27 Resultant Plots for: ROXs45f, ROXs5 91
2.28 Resultant Plots for: ROXs39, ROXs3 92
2.29 Resultant Plots for: ROXs6 93
2.30 Resultant Plots for: ROXs30c, ROXs33 94
2.31 Resultant Plots for: ROXs44, ROXs47a 95
2.32 Resultant Plots for: ROXs42c 96
2.33 Resultant Plots for: ROXs29, ROXs21 97
2.34 Resultant Plots for: GSC6215−271, GSC6215−538 99
2.35 Resultant Plots for: GSC6214−14, GSC6214−1115 100
2.36 Resultant Plots for: GSC6213−933, GSC6798−91 101
2.37 Resultant Plots for: GSC6214−2288, GSC6213−1186 102
2.38 Resultant Plots for: GSC6793−562, ROXs9a 103
2.39 Histogram Showing Spread of S Indices 105
2.40 Summary Plots 106

3.1 V410 Tau - Light Curve from Joncour, Bertout and Menard (1994) 111
3.2 The Sun in Four Wavelengths 119
3.3 The HEALPix Sphere 122
3.4 Stellar Model Coordinate System 123
3.5 Stellar Model in Three Wavelengths 126
3.6 Stellar Model - Moving Spots. 127
3.7 Projection Factor 128
3.8 Derivation of Limb Darkening 130
3.9 Limb Darkening on the Sun 131
3.10 Stellar Model - The Simplest Case 132
3.11 Stellar Model - Multiple Active Regions 2 133
3.12 Resultant Plots from Stellar Models 1 134
3.13 Resultant Plots from Stellar Models 2 135

3.14 Resultant Plots from Stellar Models 3 136
3.15 Stellar Model - Increasing Spot Size 137
3.16 Stellar Model - Increasing Complexity 138
3.17 Comparison Results: Weak line T Tauri Sample 139
3.18 Comparison Results: Classical T Tauri Sample 140
3.19 Results: WTTS & CTTS sample 145

4.1 WFCAM on the Telescope 148
4.2 WFCAM - Cross-sectional Drawing 149
4.3 Final Sky Coverage of UKIDSS 151
4.4 WFCAM - Full Optical Path 153
4.5 WFCAM - Cryostat Optical Path 154
4.6 WFCAM - The Tertiary Mirror 154
4.7 WFCAM - The Filters & Filter Paddle Assembly 155
4.8 WFCAM - Focal Plane Layout 156
4.9 WFCAM - Detector Box 157
4.10 Diagram Demonstrating Fourier's Law 159
4.11 WFCAM - The 'Russian Doll' Cryostat 165
4.12 WFCAM - Cryostat Detail 166
4.13 WFCAM - Top Ring Assembly 168
4.14 WFCAM Thermal Model Path 170
4.15 Thermal Model - Results 176
4.16 Detector Failure 177
4.17 Modelling the Detector - PCB Plots 179
4.18 Modelling the Detector - Ceramic Behaviour 181

5.1 Photograph: A Hawaii-II HgCdTe Detector & The WFCAM Focal Plane 183
5.2 Schematic cross-section of an IR detector 187
5.3 Schematic of Hawaii-II Internal Architecture 189
5.4 Diagram of the Electronic Arrangement of the Hawaii-II 191
5.5 Diagram depicting a global CDS readout procedure 196
5.6 Diagram depicting a row-by-row CDS readout procedure 197

5.7 Diagram depicting the MNDR detector readout 198
5.8 Diagram of Quadrant Orientation 200
5.9 Histogram Plots of Crosstalk Results 202
5.10 Crosstalk Ghost Artefacts 203
5.11 CASU Crosstalk Images 204
5.12 Flat Field Stability 208
5.13 Reset Anomaly Stability 209
5.14 Linearity Response of Device #60 211
5.15 Hawaii-II Read Noise 212
5.16 Latency Images on Device #76 214
5.17 Latency Images on Device #63 215
5.18 Latency Images on Device #60 215
5.19 CASU On-Sky Image of Persistence 217
5.20 Full Tile Image of Orion 221
5.21 Zoomed into Orion 222

A.1 224
A.2 225
A.3 226
A.4 227
A.5 228
A.6 229

Abstract

Hertzprung-Russell diagrams are one of the most important tools for understanding pre-main sequence evolution when combined with theoretical evolutionary tracks. They are not only used to deduce the properties of the stars they are charting but to estimate the ages of clusters that house them and to investigate the age spreads for episodes of star formation. It is therefore vital that the determination of these diagrams and tracks are built on solid theoretical and observational foundations. However, work in recent years points to a potential problem. It has long been known that pre-main sequence stars exhibit regions of magnetic activity on their stellar surfaces similar to active regions observed on the Sun. What is not yet well known is the extent to which these active regions cover the stellar surfaces.

Most spectral classification relies on moderate resolution optical spectra which tend to be dominated by the non-active photosphere which is hotter than the active regions. Resultant effective temperatures are overestimated if a large portion of the pre-main sequence stellar surface is covered in active regions, which in turn can lead to substantial error in mass and age calculations. This thesis presents a novel approach to measuring the distribution of magnetic regions on T Tauri stars which aims to overcome limitations of other observing techniques such as Doppler imaging or Zeeman measurements. The central line emission from the strong visible CaII H & K lines are a proxy indicator of surface magnetic fields and are known through observations of the Sun to be enhanced above active plage regions. Simultaneous optical spectroscopic and photometric observations of a significant sample of fast rotating T Tauri stars in the nearby clusters ρ Ophiuchus & Upper Scorpius have allowed us to ascertain a direct correlation between variations in the CaII doublet emissions and light intensities. Computer simulations which model the surface conditions as understood on T Tauri

stars and generate correlations which mimic those in the observational data offer a manipulable tool for estimating how much of the stellar surface is covered.

The Wide Field CAMera for the UKIRT Telescope on Mauna Kea is currently the most capable infrared imaging survey wide field camera in the world. The instrument focal plane consists of four Hawaii-II 2048 x 2048 IR detectors, to facilitate the best operating conditions and practises for the camera these detectors must be carefully characterised such that inherent qualities can either be corrected or accounted for. The second part of this thesis details the detector characterisation work carried out prior to the instrument delivery to the telescope. Obtaining a correct and stable operating temperature regardless of ambient temperature in the dome enclosure is key to the camera functioning optimally to carry out highly successful surveys. Presented here is a full model of the camera's thermal behaviour for the main instrument and the infrared detectors.

Declaration

Except where stated, the work contained in this thesis is that of the author alone.

No portion of the work referred to in this thesis has been submitted in support of an application for another degree or qualification of this or any other university or other institution of learning.

Morag Ann Hastie
Institute for Astronomy
University of Edinburgh
Royal Observatory
Blackford Hill
Edinburgh
EH9 3HJ
U.K.

Preface

Acknowledgements

It is my pleasure to thank my supervisor, Mark Casali, for prompting my return to stellar astronomy after years of trying to make sense of the CMB. In addition to offering his support and guidance over the years of my PhD he moved to Germany half way through this time and allowed me to follow! The months I spent in Munich were not only vital for the progression of the PhD but helped cement my desire to continue working in astronomy and to work aboard. My sincere thanks to secondary supervisors John Cook and John Peacock who both expertly steered me through the administrative maze and helped me enormasly to get through the important last few months of the thesis.

My thanks and gratitude goes to the WFCAM instrument team who collectively made working on the camera a huge learning experience and a great pleasure. Particular thanks to Derek Ives and Ken Laidlaw who taught me all about the infrared detectors and Keith Burch who put up with insistent questions about the mechanical structure of the instrument from me. I wish to thank Paul Hirst and Andy Adamson of the Joint Astronomy Centre, Hawaii who helped make my time in Hilo for WFCAM commissioning not only productive but lots of fun. I have spent the last six years at the ATC where numerous colleagues and friends there have made this time fundamental in shaping me as an astronomer and allowing to find my niche in the astronomical instrumentation community - and supplied countless evenings of fun 'down the pub'.

Thanks to Michael Ashley and Marton Hidas of the University of New South Wales, Sydney who observed and reduced the photometry data of the ρ Oph cluster. I would also like to thank my thesis examiners Phil Best and Phil Lucas who went

beyond the call of duty to read and mark my thesis in record time so I could make my flight to Tucson to take up my new position, it was very much appreciated.

I wish to give a special thanks to Suzie Ramsay who over the last 15 years has been many things to me including, supervisor, mentor, colleague, temperary landlord but most importantly a very good friend. I can safely say without knowing Suzie I would never have even started my PhD far less finish it. Thank you for everything.

To all my friends the world over both in the astronomy community and in 'the real world' - thank you for making my Life rich in many ways, for keeping me sane when required and for not allowing me to get entirely wrapped up in my thesis. Above all thanks goes to my family who has supported my academic pursuits in all ways for many, many years. Thank you for the financial and emotional support, for allowing me to move home when I needed to, for the many hours of proof reading the thesis and especially for never doubting that I could do it.

The Author

Morag Ann Hastie completed her BSc Honours degree in Astrophysics at the University of St Andrews, UK in 1999. After some time out of academia she went on to gain her MPhil in Radio Astronomy (by dissertation) from the University of Manchester in 2001. In September 2001 she was employed by the UK Astronomy Technology Centre, Royal Observatory Edinburgh as a Scientific Officer. Until March 2003 she was part of the Gemini Multi-Object Spectrograph South Instrument team. Her involvement in the instrument spanned from the 'Integration and Testing' phase up until instrument commissioning at the Gemini South Telescope on Cerro Pachon, Chile. She worked with the commissioning team at the Gemini South offices in La Serena, Chile for the four month commissioning period. She then went on to start her PhD at the Institute for Astronomy, University of Edinburgh in March 2003. During her PhD she worked with the UKATC WFCAM Instrument Team during 'Integration and Testing' of the instrument in Edinburgh and was part of the WFCAM commissioning team at the Joint Astronomy Centre and the UK Infrared Telescope, Hawaii for the three month commissioning period. On returning from WFCAM commissioning she was awarded

an eight month studentship at the European Southern Observatory headquarters in Garching, Germany. Morag has recently been awarded the 'Firestone Postdoctoral Fellowship' at the MMT Observatory, Tucson, AZ which she will take up on completion of her PhD.

List of Abbreviations and Notations

2MASS Two Micron All Sky Survey

6dF 6 Degree Field instrument

ADU Analogue to Digital Units

APT Automated Patrol Telescope

(B - V) Colour Index e.g. B magnitude - V magnitude

Ca II Ionised Calcium

Ca II H & K Spectral Lines of Ionised Calcium

CAFOS Calar Alto Paint Object Spectrograph

CAHA Calar Alto Observatory

CASU Cambridge Astronomical Survey Unit

CCC Closed Cycle Cooler

CCD Charge Coupled Devices

CDS Correlated Double Sampling

CGS4 Cooled Grating Spectrometer 4

CMB Cosmic Microwave Background

CMOS Complementary Metal Oxide Semiconductor

CP Co-Planarity

CTTS Classical T Tauri Stars

δ Declination

CVD Chemical Vapour Deposition

DRO Direct Read Out

ESO European Southern Observatory

EW Equivalent Width

FET Field Effect Transistor

FITS Flexible Image transport System file format

FOV Field Of View

GB Gigabyte

GSC Hubble Guide Star Catalogue

HEALPix Hierarchical Equal Area isoLatitude Pixelization

HgCdTe Mercury Cadmium Telluride

H-R diagram Hertzsprung-Russell Diagram

IDL Interactive Data Language

InGaAs Indium Gallium Arsenide

INT Issac Newton Telescope

IPM Interplanetary medium

IR Infrared

IRAF Image Reduction and Analysis Facility

ISM Interstellar Medium

IUE International Ultraviolet Explorer Satellite

LED Light Emitting Diode

Li Lithium

LPE Liquid Phase Epitaxy

MBE Molecular Beam Epitaxy

Mg II Ionised Magnesium

MNDR Multiple Non-Destructive Reads

MOSFET Metal Oxide Semiconductor Field Effect Transistor

MWO Mount Wilson Observatory

NASA National Aeronautics and Space Administration

NDR Non-Destructive Read

NIR Near Infrared

PACE Pattern-Constrained Epitaxy

PATT Panel for the Allocation of Telescope Time

PCB Printed Circuit Board

PMS Pre-Main Sequence stars

psf point-spread-function

PTTS Post T Tauri Stars

QE Quantum Efficiency

RA Right Ascension

RASS ROSAT All Sky Survey

RMS Root Mean Square

ρ Oph ρ Ophiuchus

ROSAT Roéntgen Satellite

ROX ρ Ophiuchus X-ray sources

SDSU San Diego State University

SED Spectral Energy Distribution

SFE Star Formation Efficiency

Si Silicon

SIMBAD Astronomical Database

SNR Signal-to-Noise Ratio

SSS Solar-Stellar Spectrograph project

T_{eff} Effective Temperature

TiO Titanium Oxide

TB Terabyte

UFTI UKIRT Fast Track Imager

UKATC United Kingdom Astronomy Technology Center

UKIDSS UKIRT Infrared Deep Sky Survey

UKIRT United Kingdom InfraRed Telescope

UKST United Kingdom Schmidt Telescope

UNSW The University of New South Wales

UV Ultraviolet

WFCAM Wide Field CAMera

WMAP Wilkinson Microwave Anisotropy Probe

WTTS Weak line T Tauri Stars

ZAMS Zero-Age Main Sequence

ZIF Zero Insertion Force socket

Chapter 1

Introduction to Magnetic Surfaces of Young Stars

The topics of stellar evolution, atmospheres and the generation of observed magnetic fields are vast. The key question we have chosen to tackle with the spectroscopic and photometric variability study presented in the first half of this thesis is: 'what fraction of the young stellar surface is covered by chromospheric emission'.

It has long been known that stars demonstrate the same 'spotted' surfaces as seen on our Sun. Comprehensive studies of the Sun have determined that these spots are due to magnetic fields breaching the upper levels of the solar atmosphere and creating hot 'patches' on the surface which appear dark against the visible photosphere. What is not extensively known nor easy to observe is if 'stellar spots' have the same dimensions and characteristics as those seen on the Sun.

This introductory chapter offers a concise overview of pre-main sequence stars and the evidence for magnetic fields on their surfaces. Summarised are the observational tools used to investigate active regions and previous studies in this field.

1.1 The Beginnings of Stars

Simply described, stars are born from the gravitational collapse of interstellar clouds of dust and gas. Any given interstellar cloud will start contracting if it is sufficiently

large and heavy. The contraction of the cloud causes the dust and gas particles to accelerate towards the centre of gravity of the cloud. This increase in speed of the particles directly raises the temperature of the cloud as the gravitational potential energy is converted to thermal energy and radiative energy. Eventually the internal temperature rises sufficiently that the cloud matter degenerates. The atomic nuclei repel each other as do the electrons, creating an internal pressure gradient which balances the compression of the cloud due to gravity. This generates a state of hydrostatic equilibrium. The initial collapse process is slow and uneven as the central regions collapse more rapidly than the outer regions. A stable core is formed which accretes material from the in-falling envelope. The cloud material begins to 'shine' as energy is released during the contraction phase, however these early stellar objects only become 'visible' to observers by accreting the circumstellar material or dissipating it in some other manner.

During the phase of collapse prior to the establishment of hydrostatic equilibrium the stellar object is called a 'protostar'. After this time the protostar can evolve in two directions. If the protostar is massive enough contraction will continue until the internal temperature is sufficiently high to trigger nuclear fusion and the object becomes a fully radiating star. If the protostar does not have enough mass it will transform into a brown dwarf through a series of evolutionary stages. The sole evolutionary stage this study is interested in is the period between hydrostatic equilibrium and the start of nuclear fusion. During this phase the object is called a 'pre-main sequence star'. The evolutionary paths stars take through the protostellar and pre-main sequence stages depends on the initial mass of the contracting cloud, though all forming stars have common aspects. This concerns solar mass pre-main sequence stars, to demonstrate the processes and properties of young stars we consider the formation of a solar mass star. The evolutionary time from the start of the cloud collapsing through the protostellar phase to the formation of a pre-main sequence star is of the order of 10^6 years. The pre-main sequence star has a lower surface temperature than the eventual radiating star it will become but the radius is much larger and thus the surface area is larger and the star's luminosity is higher. In a newly formed pre-main sequence star convection rather than radiation transports the energy outwards from the centre giving

a stellar luminosity of $\sim 30L_{\odot}$ for around 10^5 years as the material accretes inwards. This accretion continues through the star's contraction and the core temperature rises. Eventually the opacity decreases sufficiently for radiative processes to transport the energy more efficiently than convection. A radiative zone is generated around the core and slowly increases in depth outwards as the inner layers also heat up. Once the core is hot enough to trigger thermonuclear reactions, a few 10^6K, the star's energy source switches from gravitational contraction to nuclear fusion which keeps the star in hydrostatic equilibrium. The star is now called a zero-age main sequence star and enters the longest stage of its evolution, the main sequence, where it converts hydrogen to helium in its core. By this stage the interior transport is entirely by radiation with only the outer layers being convective, as observed in our Sun. The evolution time from the initial collapse to becoming a zero-age main sequence star is a relatively short 2 x 10^7 years, compared to the 1 x 10^{10} years it will reside on the main sequence.

Proto- and pre-main sequence stars have been separated into classes depending on age and distinct properties. The youngest protostars are 'Class 0' objects, young stellar objects which are still accreting most of their mass from the circumstellar envelope. These sources have very strong submillimeter continuum emission but no detectable emission at wavelengths shorter than $\sim 10\mu$m. Class 0 objects have a spectral energy distribution which resembles that of a single temperature blackbody of temperature ≤ 30K. There is also evidence for the presence of a molecular outflow (Andre et al. 1993). After the initial high accretion period during the Class 0 phase the accretion rate steadies and slows due to the finite reservoir of mass. Objects in the later accretion stages are termed 'Class I' objects. These sources are visible in the infrared and have a spectral distribution broader than a single temperature blackbody. After the Class I phase the circumstellar envelopes of the young stellar objects will be mostly cleared away and the protostars become optically visible (Chandler et al. 2001). The protostar then becomes a classical T Tauri star ('Class II' object) which has an optically thick disk. Overtime the Class II object will evolve into a 'Class III' object (a weak-line T Tauri star) with an optically thin disk (Lada and Wilking 1984). Essentially, the 'T Tauri' stars are the link between the deeply embedded protostars which are only visible as infrared objects and main sequence stars of mass less than $3M_{\odot}$. These objects are

extensively discussed in §1.1.2. It is believed that the Sun passed through the T Tauri stage $\sim$ 4.5 x 10^9 years ago and so T Tauri stars are often observed with the aim of understanding the evolution of our own Sun.

1.1.1 The Hertzsprung-Russell Diagram

The Hertzsprung-Russell Diagram, pioneered in 1910 independently by Elnar Hertzsprung and Henry Norris Russell, plots luminosity (or magnitude) as a function of temperature (or colour or spectral type) for stars. Most observed stars fall into four well defined groups: white dwarfs; main sequence stars; giants and supergiants. The majority of stars fall in the the main sequence group, with the white dwarfs having the second largest member numbers. Each of these groups fall into distinct regions of the HR diagram, demonstrated by Fig.1.1, which is an example of a luminosity versus effective temperature HR diagram. The temperature increases to the left of the x-axis with the spectral type classes marked along the y-axis. The most striking group is the main-sequence which diagonally cuts through the diagram, with the giants and supergiants above the main sequence and the white dwarfs below. Marked on Fig.1.1 are the location of some key stars, including our Sun which sits on the 'bottom' half of the main-sequence. The location of stars on the HR diagram is not fixed during their lifetimes, the stellar properties change as they progress through various evolutionary phases, they migrate through the HR diagram. Though our Sun currently sits on the main sequence it is predicted that it will evolve and travel down the red giant branch before ending its life as a white dwarf. How a star evolves depends on many factors including initial mass and chemical composition of the interstellar cloud that it forms from. The first major phase of stellar evolution is this diagonal main-sequence track, stars of differing mass reside at different points of the track. Massive stars, many times more massive than the Sun, are found at the top left of the group where as low mass stars, down to fractions of a solar mass, are at the bottom right (see mass indicators on Fig.1.1). Main sequence stars obey a high dependancy luminosity-mass relation; $L_* \propto M_*^4$. This relation means massive stars use up their supply of nuclear fuel far quicker than low mass stars and thus move through their life cycles more rapidly. The supergiant and giant groups tend to be over-represented on HR diagrams as they

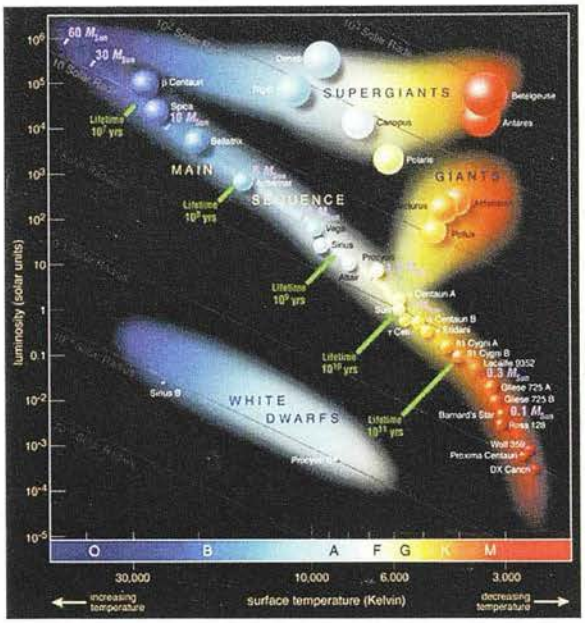

Figure 1.1: A pictorial example of the Hertzsprung-Russell Diagram.

are very luminous, making them easier to observe than low luminosity stars. However, the 'red giant' evolution phase is relatively very short lived making them not readily observable. White dwarfs are the end point for many stars but are so small ($R_* \sim 0.01 R_\odot$) and non-luminous that they are very difficult to observe.

A fifth very important group of stars, and the group of interest to us, is the 'pre-main sequence' (PMS) group. As discussed, before a star evolves onto the main sequence it is not releasing energy from its internal nuclear reactions, it only releases energy as it continues to contract and heat up. The PMS stars we are concerned with, T Tauri stars, are found just above the main sequence at the bottom right half of the HR diagram.

1.1.2 T Tauri Stars

T Tauri stars are among the youngest directly optically observable stages of low mass stellar evolution. A project led by Alfred H. Joy in the 1940's at the Mount Wilson Observatory of variable stars resulted in the creation of this new classification of stars,

the T Tauri stars. Joy (1945) observed eleven irregular variable stars whose physical characteristics were very similar yet sufficiently different from previously known classes of variables to warrant the generation of the new class. The known variable star 'T Tauri', the third variable discovered in the constellation of Taurus in 1852 by John Russell Hind, was one of the brightest stars of the eleven and represented the whole group in terms of spectral emission and absorption features so was taken to be the prototype of the new classification. The criteria Joy (1945) found to distinguish the variable stars included in the T Tauri class from ones excluded were: rapid irregular light variations of ~ 3 magnitudes; spectral type ranging F5 – G5 with emission lines similar to those in the solar chromosphere particularly very strong emission of the ionised calcium H and K lines; low luminosity and an association with dark or bright nebulae. They also noted that the variations in light of the T Tauri stars are so irregular and unpredictable that they cannot be classified on their lightcurves alone. However, it was especially the low luminosity and high intensity of their bright H and K lines which Joy (1945) noted made these stars differ from other known variables. Since the generation of the T Tauri classification hundreds of T Tauri stars have been identified mainly through spectroscopic surveys. The T Tauri phase is typified by stars with masses $\sim 0.2 - 3M_{\odot}$ and ages 0.1 – 10 Myrs (Cohen 1981).

The clouds of dust and gas which condense to form pre-main sequence stars are mainly composed of hydrogen, helium and other trace elements including small quantities of lithium. The lithium is destroyed as the star evolves to the main sequence, hence observational evidence of lithium (6707Å) in absorption in the stellar spectra is an indicator of stellar youth. T Tauri stars are found to reside in the dark clouds they were created from within the last 1×10^7 years. They have not had the time to move from their birthplaces out of the clouds (Herbig 1987).

Observational candidates for T Tauri stars are often identified due to the photometric variations which are evident at all wavelengths from X-ray through to infrared. Time scales for observed variations can range from a few minutes to at least a century (Appenzeller and Mundt 1989). Variations are also detected in spectral and polarimetry observations. Emission lines are seen to change shape and intensity over time and

polarimetric studies indicate variations in the degree and position angle of the polarisation (Appenzeller and Mundt 1989; Johns and Basri 1995). As mentioned, the variations tend to be highly irregular which is thought to be due to a combination of dynamically active chromospheres and obscuration by non-uniform dust clouds. T Tauri stars also show evidence of quasi-periodic variations which are attributed to spots on the stellar surface similar to those seen on the Sun. Observational differences between T Tauri stars and main sequence stars include an excess continuum emission mainly in the UV and IR.

T Tauri stars are separated into two subgroups; Classical T Tauri Stars (CTTS) and Weak line T Tauri Stars (WTTS). The two subgroups are distinguished by the measured strength of the H_α (6564Å) emission line. The H_α line strength is quantified by the equivalent width (EW) and the WTTS are defined to have EW H_α <10Å. Classical T Tauri display an ultraviolet excess and strong emission lines which WTTS do not. The excess in CTTS is thought to be due to circumstellar disks which interact with the central star. Determined masses and sizes for the accretion disks are $\simeq 0.001 M_\odot < M_{disk} < 1 M_\odot$ and $\simeq 10^2 - 10^3$AU (Beckwith et al. 1990). The disk is accretive and the IR excess seen with CTTS is caused by the re-radiation of light from the central star by the disk as well as by radiation released as matter falls from the disk to the central star. Even for a moderate rate of accretion, comparable to the rate of loss due to a stellar wind, the potential energy of the accreting matter is sufficient to explain the energy behaviour seen in CTTS over a wide range of the spectrum (Petrov 2003). The WTTS do not have accretion disks, only magnetic activity on their surfaces. Though there is evidence that cold passive, optically thin disks which reradiate the light from the star cause some IR excesses (Padgett et al. 2006). The presence or absence of accretion disks around T Tauri stars is thought to be connected with the initial star formation conditions and how the circumstellar envelope has been dissipated.

Winds and outflows are a common phenomenon in CTTS and they arrear to be powered by accretion onto the star. The observational evidence for winds and outflows include: forbidden lines (OI and SII) show a high velocity emission component of $\sim$ 100 to 200km^{-1} (Hartigan et al. 1995); imagining and long slit spectroscopy of the circumstellar regions show jets emerging from the stars with velocities in the

range of $200 - 450\mathrm{kms}^{-1}$; profiles of H_α emission lines imply outflowing velocities of $\sim 200\mathrm{kms}^{-1}$; CO observations have detected molecular outflows (Fukui et al. 1993) and radio continuum observations show the presence of outflows of ionised gas (Appenzeller and Mundt 1989).

T Tauri stars rotate relatively rapidly with rotational periods of 2 to 12 days and are observed to have dynamic magnetic fields. The first studies of active T Tauri found an axial rotation velocity of up to $100\mathrm{kms}^{-1}$ (Herbig 1962), which is consistent with theories that stars recently formed should rotate at very high velocities. However later high resolution spectroscopic studies found much slower velocities of $v\mathrm{sini} = 6$ to $70\mathrm{kms}^{-1}$, with an average velocity of $\sim 15\mathrm{kms}^{-1}$ (Bouvier et al. 1986). It was also found that CTTS rotate more slowly than WTTS. Observations in Taurus by Bouvier et al. (1995) found weak line T Tauri stars tend to have rotational periods of $\sim 2 - 5$ days as opposed to the classical T Tauri having periods of $6 - 9$ days. It is probable the presence of accretion disks and stellar winds act to slow down the CTTS rotational velocity.

The optical spectra of T Tauri stars demonstrate the photospheric continuum and absorption spectra with the non-photospheric continuum and emission spectrum superimposed. The underlying photospheric absorption spectra class them as dwarf stars with spectral type later than late F (F - M). The distinguishing detail of the photospheric spectra is enhanced absorption of LiI (6707Å) which is often as strong as its neighbouring CaI line (further discussed in Basri et al. 1991; Magazzu et al. 1992). The emission spectra of T Tauri is similar to that of our Sun's chromosphere (Joy 1945). This implies the emission spectra is generated under physical conditions similar to those seen in the Sun's chromosphere. In the optical spectra the strongest emission lines are those of H_α and the CaII H and K lines. In the near UV the strongest lines are the MgII h and k lines, and in the near IR the strongest lines are the CaII triplet at 8498, 8542 & 8662Å. The IR CaII triplet have the same upper level as the optical CaII doublet. The distant IR spectrum details the T Tauri's surroundings more than the star itself.

A comprehensive review of T Tauri stars, research on them and many reference sources can be found in Petrov (2003).

1.2 Observational Tools and Techniques

Since the discovery of stellar photometric variations due to cool spots many different observation techniques have been tried to deduce starspot properties.

1.2.1 Light-curve Modelling

Two light curving models have been used. Firstly direct light-curve modelling which is based on trial-and-error modelling of pre-assumed geometry of circular spots which may cause the variations. The disadvantage of these models is that they have many free parameters and the shape of spots and their distributions have to be assumed. A second, alternative approach which does not require as many assumptions is light-curve inversion into an image of the stellar surface. An inversion technique is usually applied to photometric light curves in the two temperature approximation. The model assumes that the intensity of each pixel on the surface contains contributions from both the hot photosphere and the cool spots, weighted by a filling factor which is the fraction of the surface covered with spots. However, since a light curve represents a one-dimensional time series the resulting constructed stellar image contains information on the spot distribution in one direction only, longitude. The size of spots and their locations in latitude remains uncertain (Berdyugina 2005 and references therein).

1.2.2 Doppler Imaging

During the last 20 years the Doppler imaging technique has been utilised for studying active regions on active stars. The technique uses high-resolution spectral line profiles of rapidly rotating stars to map the stellar surface. The first inversion technique with minimisation was developed in 1977 by a group led by A. V. Goncharskii. The technique aims to restore starspot distribution information which is contained in time varying line profiles of rotating stars. If the star rotates rapidly enough to cause rotational broadening of a line profile to be significantly larger than the local line profile at a single point on the stellar surface then a cool spot on the surface will give a 'bump' in the profile. As the star rotates the 'bump' will move across the profile with a velocity amplitude depending on the spot latitude.

The Doppler technique however leads to a multitude of different stable solutions. Searching for the unique and stable solution is the named 'ill-posed inverse problem', there are many different approaches and methods developed for solving it. Doppler imaging also relies on an assumption of the nature of starspots. Assumed stellar atmosphere models; atomic and molecular line lists; and stellar parameters all have a significant effect on the results. Errors in calculations of local line profiles have a strong effect on the inversion process and can easily cause artificial features in the maps such as polar caps and belts of cool or hot spots (Unruh and Collier Cameron 1997). Incorrect determination of the stellar rotational velocity or a wrong estimation of effective temperature can also generate artificial features. Recovered spot latitudes strongly depend on the inclination angle of the rotational axis to the line of sight. This technique can be limiting in the equatorial region where spots are recovered with reduced area and contrast. At low inclinations sub-equatorial spots cannot be resolved (Berdyugina 2005; Rice 2002 and references therein).

1.2.3 Zeeman Broadening

A direct method for measuring magnetic field strength on stellar surfaces is to analyse the Zeeman splitting of the spectral lines. In extreme cases, where the magnetic field is several kilogauss strong the spectral lines will split into the Zeeman pattern; splitting of the spectral line into two, three or more closely spaced components. However, in cool stars where the magnetic field is weaker and especially if the Zeeman components are not resolved, this effect merely becomes another broadening function on the spectral line.

In principle, polarisation can be used to enhance the detection of weak Zeeman broadening because each of the components of the Zeeman pattern are polarised. However, typically in F, G and K stars the net polarisation is too small to measure. Attempting to use Zeeman measurements to investigate pre-main sequence stars actually involves measuring the spectral line broadening which is complicated by masking from the Doppler effect.

1.2.4 Chromospheric Indicators

Proxy indicators are one of the most useful tools for probing the lower chromosphere and include: lines of CaII; h & k lines of MgII at 2802Å and 2795Å; H_α; the early Lyman lines; the Lyman continuum; the far ultraviolet continuum and the microwave continuum at wavelengths greater than 0.3mm. However, the most accessible, and thus best studied, are the CaII H & K lines in the visible and the CaII infrared triplet.

The traditional spectroscopic indicators of stellar chromospheric activity have been the emission cores of the singly ionised calcium H & K lines. These lines are located at 3933Å and 3968Å respectively. The attention they have received is in part due to the enhancement of their equivalent widths through the suppression of the local continuum by the powerful absorption lines and in part due to the blue-violet region being convenient for early spectrographs. The lines are very opaque with line centre optical depths of order 10^7 in the photosphere and 10^4 at the temperature minimum. The entire line core is formed in the chromosphere and the photosphere cannot be seen. Since the temperature in the chromosphere increases outward the central line cores appear in emission. A spectrum with strong H & K emission shows the target object has high levels of chromospheric activity. If the star in question has no chromospheric activity these CaII lines are in absorption. Stars with weak activity show central emission reversal in the absorption profiles of the lines.

Many research projects over the years have utilised the accessible CaII H & K lines to study, among other things, the surface of unresolvable stars. The longest running, fully dedicated project is that of the Mt Wilson Observatory's H−K project. This project was started in the mid 1960's by O. C. Wilson and continues today. The research presented in this thesis took its lead for quantifying the CaII H & K emission from the work of O. C. Wilson which is comprehensively discussed in §2.9.

1.3 Magnetic Activity on T Tauri Stars

There is a lot of indirect data indicating the existence of magnetic fields on T Tauri stars. The X-ray luminosity of typical T Tauri stars is three orders of magnitudes greater than that of the solar corona (Feigelson and Montmerle 1985) and correlates

well with the rotational velocity. As the heating of the corona is thought to be caused by the dissipation of magnetic energy the high X-ray luminosity suggests the magnetic field is generated by a dynamo mechanism. X-ray flares have been observed on time scales ranging from a few minutes to an hour.

The strongest evidence for strong magnetic fields on the surface of T Tauri stars are 'stellar spots' which are implied through observed rotational modulation of the brightness and colour of the stars. From the ratio of the amplitudes of the variation measured in the brightness and the stellar colour it is possible to estimate the temperature of the spot. It was found that in most cases the temperature of the spots were comparable to Sunspots, 200 – 1200K lower than the photosphere's temperature. The temperature difference between spots and the photosphere appears to be dependant on spectral type, from 2000K in G0 stars down to 200K in M4 stars (Berdyugina 2005). Though cold spots are detected on both classes of T Tauri only CTTS demonstrate evidence of hot spots. Hot spot temperatures are measured to be $\sim$7000 – 10000K, considerably higher than the temperature of the photosphere (Herbst et al. 1994). Hot spots are also found to be shorter lived and smaller than cold spots. It is assumed that hot spots develop on the surface as a result of accretion from the circumstellar disk since they are only found on classical T Tauri.

A small number of T Tauri stars are good candidates for Doppler imaging and these observations suggest T Tauri stars have large cold spots at high latitudes which are thought to be associated to the high rotational velocity of these young stars. Cold spots are generated by internal magnetic flux tubes breaking out onto the stellar surface. The latitude they reach on the surface depends on the internal structure of the star, particularly the depth of the convective zone, as well as the magnetic field strength and the rotational velocity (Schuessler et al. 1996). Numerous Doppler imaging projects have found upwards of 20% of stellar surfaces covered in spots in a variety of active stars. Other projects using different techniques have found upwards of 50% (O'Neal et al. 2004; Casali 2003; Berdyugina and Solanki 2002).

1.4 This Study

HR diagrams have been one of the most important tools for understanding pre-main sequence evolution when combined with evolutionary tracks. They are used to deduce the masses of T Tauri stars and to estimate the ages of the clusters which house them as well as to study the range of ages for star formation periods (Hillenbrand 1997). It is crucial therefore that these diagrams and tracks rest on solid theoretical and observational foundations.

Work in recent years indicate large scale active magnetic regions on young stellar surfaces which are cooler than the non-active photosphere and can significantly distort the apparent spectral type of a star if a sufficiently large coverage is present. This could present a problem because most spectral classification rely on moderate resolution optical spectra which tend to be dominated by the hotter normal photosphere. Resultant calculated effective temperatures can therefore be over estimated. Taking a normal K2 photospheric temperature of 4900K then assuming a starspot temperature of 3400K and a 20% fractional coverage of the stellar surface gives a 200K error in the estimation of effective temperature. 40% coverage gives a 430K error and 80% a 1039K error. Errors in the effective temperature of this scale could let to errors of up to a factor of 2−3 in mass and 10 in age (Casali 2003; Horrobin and Casali 1998).

Unfortunately most observing techniques, such as light-curve modelling and Doppler imaging methods are only sensitive to high spatial frequency surface structure and do not detect a large diffuse 'carpet' of magnetic regions. Zeeman measurements, while providing a direct measure of the mean field strength over the surface, are difficult to make and interpret for a statistically significant sample of stars. This research attempts a novel approach to measuring the distribution of magnetic activity on T Tauri stars. The amplitude of the CaII H and K emission variation measured over a rotation period should be a measure of the relative size of isolated magnetic regions compared to the general quiet chromospheric emission. Evenly distributed activity over the whole surface would give little variation while strong modulation indicates small active regions. Combining simultaneous photometric and chromospheric observations of a sample of T Tauri stars we can look for any correlation between the variation amplitudes to deduce possible geometry of the active fields. We wish to demonstrate that

this procedure can offer a robust and observationally efficient method for analysing the CaII emission over the stellar surface for a statistically significant sample size

Chapter 2

Observations of T Tauri Stars in Nearby Clusters

2.1 The Clusters

ρ Ophiuchus and the surrounding vicinity is a nearby region of star formation which has been extensively studied (Bernard et al. 1993) and is well suited to the type of study presented here. At a distance of 170 pc, the Ophiuchus dark cloud is one of the nearest sites of star formation in the local Milky Way, whereas the neighbouring Scorpius Centaurus dark cloud is the closest OB association to the Sun. The Scorpius Centaurus association has three subgroups; Upper Scoripius, Upper Centaurus Lupus and Lower Centaurus Crux (Blaauw 1964) and Ophiuchus sits immediately to the East of the Upper Scorpius subgroup.

The Ophiuchus cloud is a vast molecular complex which extends over more than 25 square degrees. Large-scale mapping of the molecular gas distribution shows that the cloud has two major clumps of gas with associated streamers (Bouvier and Appenzeller 1992 and references within). At the centre of the Ophiuchus cloud complex is the ρ Oph cloud core which houses many pre-main sequence stars, X-ray sources and embedded infrared sources. The ρ Oph cloud core shows numerous signs of very recent star formation (Casanova et al. 1995). Multi-wavelength surveys revealed star formation with an unusually high star formation efficiency (SFE $\geq$ 22% as quoted in

Wilking et al. 1989) compared with other star forming dark clouds such as Taurus Auriga. Distance to the ρ Oph cluster is quoted in published literature with a variety of values, including; 120 pc (Knude and Hog 1998), 128^{+12}_{-10} pc (Sartori et al. 2003; Bertout et al. 1999), 130 pc (Shu 1977; Kulesa et al. 2005), 150 pc (Liseau et al. 1999), 150 - 170 pc (Lisse et al. 2001), 160 pc (Chen et al. 1995) and 170 pc (Bouvier and Appenzeller 1992). This demonstrates that the distance to a cluster of stars can be both difficult to determine and subjective. Clusters are made up of numerous stars which lie at a variety of distances from the observer. It is likely that ρ Oph covers tens of parsecs in 'line of sight' depth so the determined distance is dependent on sample used for any given measurement. Though each value in the literature is equally valid we have adopted the Bouvier and Appenzeller (1992) distance of 170 pc for this study. Reasons behind this are explained in §2.7.

Even though Upper Sco's location is close to ρ Oph there is no evidence for ongoing star formation in this cluster and it is essentially free of dense interstellar matter. This is probably due to the strong stellar winds from the plentiful B stars dispersing the original molecular cloud. This causes young stars in Upper Sco to generally have low extinction (Preibisch et al. 1998), $A_V \leq 1$ mag. Upper Sco is the youngest subgroup of the three with an age of ~ 5 Myrs (Preibisch et al. 1998). Analysis of the trigonometric parallax distribution carried out by de Bruijne et al. (1997) gave a mean distance of 145 ± 2 pc for Upper Sco. It is believed that ~ 1.5 Myrs ago a massive star in Upper Sco exploded as a supernova generating a powerful shock wave which passed through Ophuichus triggering the observed star formation which started ~ 1 Myrs ago and continues on today. Fig.2.1 shows images of the two clusters, ρ Ophiuchus on the left hand side and Upper Scoripius on the right. The ρ Ophiuchus image is a $\sim 6^\circ$ R, G, B false colour image taken with small 4" amateur telescope, ©Robert Gendler, Jim Misti and Steve Mazlin 2006. The Scorpius image shows the constellation of Scorpius overlaid on a optical image of the area, the Upper Scorpius association is located to the upper right of the image and includes the 'head' of Scorpius (www.mpifr-bonn.mpg.de/staff/tpreibis).

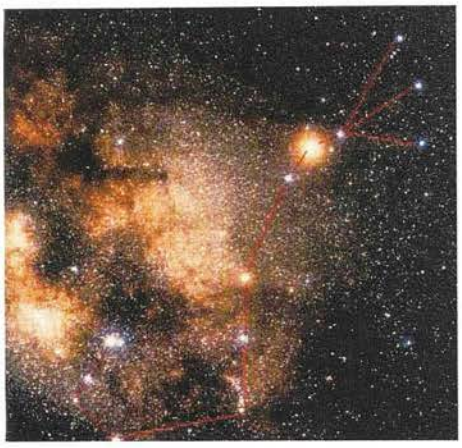

Figure 2.1: Images of the two studied clusters, ρ Ophiuchus on the left hand side and Upper Scoripius on the right. The ρ Ophiuchus image is a R, G, B false colour image ©Robert Gendler, Jim Misti and Steve Mazlin 2006 (source: www.robgendlerastropics.com). The Upper Scoripius image shows the constellation of Scorpius overlaid in red line,on a optical image of the area, the Upper Scorpius association is located to the upper right of the image and includes the 'head' of Scorpius (source: www.mpifr-bonn.mpg.de/staff/tpreibis)

2.2 The T Tauri Sample

Young T Tauri stars are fast rotators so offer a good opportunity to measure the level of magnetic coverage with various parts of the stellar surface in our line of sight over practical time scales. Their typical rotation periods are between 3 and 12 days and this rapid rotation is the probable cause of most PMS stars being strong X-ray emitters (Montmerle 1996). Their X-ray luminosities are $2-3$ orders of magnitude brighter than main sequence stars of similar spectral type so X-ray observations have proved very efficient in discovering and identifying PMS stars among older field stars (Preibisch et al. 1998). The observed X-ray emission is interpreted as being closely connected with enhanced solar-like magnetic activity in the stellar chromosphere. Observations taken with the Einstein satellite (1978-1981) and more recently the ROentgen SATellite (ROSAT) (1990-1999) have shown both classical T Tauri and their weak line compatriots can be detected by X-ray (Casanova et al. 1995).

Our sample of T Tauri stars was gathered from three studies of X-ray selected sources; Bouvier and Appenzeller (1992), Martin et al. (1998) and Preibisch et al. (1998). The two criteria for inclusion in our study were known B magnitudes in the range of 11 - 17 so that medium resolution spectra could be obtained with good signal-to-noise

and spatial location to allow our complete sample to be observed with one 6dF plate configuration without difficulties in placing the fibre feeds. To offer a range of results we have picked a selection of CTTS, WTTS, field stars and binary T Tauri systems. The location of each target star can be seen on Fig.2.2; crosses represent the Preibisch et al. (1998) originated targets, diamonds represent Bouvier and Appenzeller (1992) and the triangle symbols are the Martin et al. (1998) stars.

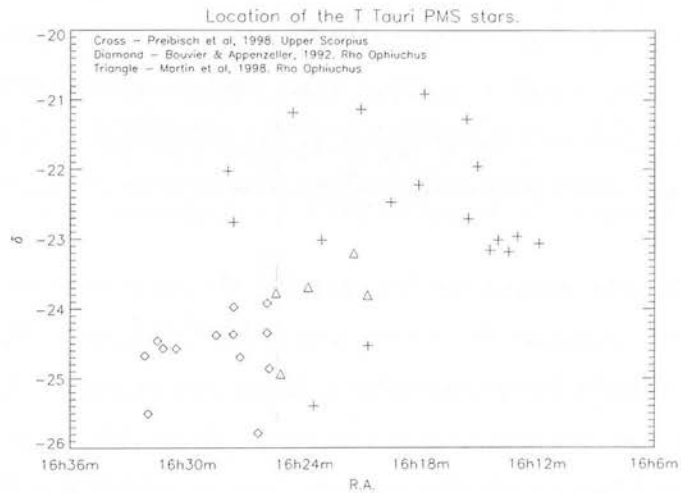

Figure 2.2: Location of the selected T Tauri observation sample in ρ Oph & Upper Sco. Different symbols represent the different source papers, key given above. Accurate R.A. & δ positions are epoch 2000.

Sample from Bouvier and Appenzeller (1992)

The study presented by Bouvier and Appenzeller (1992) is directly connected with the X-ray survey of the ρ Ophiuchus cloud conducted by Montmerle et al. (1983). Using the Einstein Observatory they were able to confidently detect 47 X-ray sources (labelled ROX - ρ Ophiuchus X-ray sources) and 20 source candidates near the detection limit. Thirty of the ROX sources had possible counterparts at other wavelengths which led Montmerle et al. (1983) to suggest that most of the ROX sources are pre-main sequence cloud members. They derived X-ray luminosities between 10^{30} and a few $10^{31}\mathrm{ergs}^{-1}$, which is typical of X-ray luminosities measured for T Tauri stars in other stellar formation regions. Bouvier and Appenzeller (1992) studied 47 optically visible

stars lying in the error circles of 29 ROX sources. In order to avoid confusion between notation for the X-ray sources and their optical counterpart candidates the latter were allocated the name 'ROXs # n' where # n is the X-ray source number. They were able to identify 30 pre-main sequence cloud members as likely optical counterparts of 24 ROX sources, while the other 17 stars are probably background giants. Spectral types were determined by Bouvier and Appenzeller (1992) by using the appearance and relative depths of TiO bands in the 5500−7700Å spectral region. The depth of the TiO band is extremely sensitive to effective temperature for late K and M stars, allowing the spectral type to be derived with an accuracy of ± 1 subclass. Spectral classification of early- and mid-K stars uses the strength of the CaI (4226Å) line compared to the neighbouring G-band of CH (4290−4314Å) - again classification is accurate to 1 subclass.

From a previous study by Bouvier and Bertout (1989) the surfaces of two of the ROXs sample (21 & 29) are known to be covered with large, cool starspots and have rotational periods of 3.5 and 6.3 days respectively. Target stars ROXs10b, ROXs21, ROXs29 & ROXs42c are known to have two components; IR speckle observations found ROXs10b to have a low mass IR companion at a distance of 2.3" (Chelli et al. 1988), Simon et al. (1987) found ROXs21 to be a sub-arcsecond binary from K band lunar occultation observations (Gras-Velázquez and Ray 2005), ROXs 29 is a sub-arcsecond binary (McCabe et al. 2006) and ROXs42c is a double-lined spectroscopic binary with a period of 35.96 days (Mathieu et al. 1989).

Out of the 47 optically visible stars studied by Bouvier and Appenzeller (1992) we selected 15 for our investigations. Details of these stars as given by Bouvier and Appenzeller (1992) of derived spectral type, measured equivalent width of the CaII K line, and photometric properties of the optical counterparts of the Bouvier and Appenzeller (1992) X-ray selected sample are given in Table 2.1. The stellar luminosities given in column 11 of Table 2.1 were derived from the dereddened V magnitude applying the bolometric corrections for dwarfs (Johnson 1966) and assuming a distance of 170 pc to ρ Ophiuchus. Classification between field stars (F), Weak-line (WTTS) and classical (CTTS) T Tauri stars is given in column 12.

Object ID	SpT	R.A. (1950)	δ (1950)	P (d)	K (Å)	V	B−V	V−R	A_V	log $L/L_\odot$	Class
ROXs3	K3/M0	16 22 47.6	−24 44 43		0.3	13.2	1.5	1.0	0.6	−0.2	WTTS
ROXs5	K7	16 22 54.8	−23 48 23			14.5		1.1	2.3	−0.2	WTTS
ROXs6	K6	16 22 54.7	−24 14 01		40.3	12.8	1.5	1.1	2.2	0.4	CTTS
ROXs9a	M0	16 23 20.7	−25 40 33					1.3	3.3		F
ROXs10b	K0	16 23 21.9	−24 14 13			14.6	2.2	1.5	6.6	1.2	CTTS
ROXs21	K4/M2.5	16 24 17.5	−24 34 58	3.4	2.9	13.4	1.5	1.0	0.6	−0.2	CTTS*
ROXs29	K4/K6	16 24 38.6	−24 15 23	6.4	5.6	11.5	1.2	0.8	0.2	0.1	CTTS*
ROXs30c	K4	16 24 37.9	−23 51 37			15.0		1.2	3.6	0.0	CTTS
ROXs33	G0	16 25 31.0	−24 16 06			14.0	2.0	1.4	6.5	1.3	CTTS
ROXs39	K5	16 27 33.6	−24 27 50			13.0		1.1	2.4	0.3	WTTS
ROXs40	K6	16 27 49.9	−24 05 06					1.0	1.6		F
ROX42c	K6	16 28 13.6	−24 27 36			12.5	1.7	1.0	1.9	0.4	WTTS*
ROXs44	K3	16 28 31.5	−24 21 13		16.8	12.6	1.35	0.9	2.1	0.3	CTTS
ROX45f	K7−M0	16 28 58.4	−25 24 03			13.8	1.5	0.9	0.3	−0.7	WTTS
ROXs47a	K2/K7−M0	16 29 09.6	−24 33 59		0.3	13.6	1.7	1.2	2.3	0.2	CTTS

Table 2.1: Stellar parameters of sample selected from Bouvier and Appenzeller (1992). Coordinates are quoted in epoch 1950 as in paper, of course these were updated for our observations. The rotation period (P_{rot}) is given in days for two sources, spectral type, equivalent width of CaII K line, V magnitude, stellar colours, visual extinction, stellar luminosity and classification ('F' = Field, 'WTTS' = Weak-line Tauri, 'CTTS' = Classical T Tauri) are also listed. *Binary target.

Sample from Preibisch et al. (1998)

The first systematic search for pre-main sequence stars in the Upper Sco association was undertaken by Walter et al. (1994) who observed optical counterparts to X-ray sources in 7 Einstein fields, and detected 28 PMS stars. This study assumed a common distance of 160 pc for all the PMS in Upper Sco however, more recent Hipparcos data imply a smaller distance of 145 pc, with a likely spread in the exact distances to individual stars (de Bruijne et al. 1997). Preibisch et al. (1998) investigated both X-ray selected candidates and stars which were not detected as X-ray sources but which were regarded as possible members of the Upper Sco association due to their proper motions being similar to those of known early-type members. This was completed in an effort to investigate the possibility of the existence of a population of 'X-ray quiet' PMS stars in Upper Sco (as found in the Orion nebula region by Wolk 1996). The X-ray selected candidates were taken from ROSAT X-ray satellite All Sky Survey (RASS) which scanned the sky in the 0.1 − 2.4 keV soft X-ray band. In the Preibisch et al. (1998) field in Upper Sco, 606 X-ray sources were detected within the RASS data, though of course not all X-ray sources are pre-main sequence stars. They can also be, among others; active field stars, RS CVn binaries, galaxies and quasars. Using a selection method developed by Sterzik et al. (1995) and an observational constraint on selection

which limited the B magnitude range to $\simeq$ 11 to $\simeq$ 14.5, Preibisch et al. (1998) reduced the sample for study to 130 objects. The X-ray quiet candidates were selected with the criterion that they have magnitudes similar to the RASS candidates and proper motions similar to that of known early-type association members. Table 2.2 gives the stellar parameters as quoted by Preibisch et al. (1998) for the 18 target stars we selected for inclusion in our study, column 9 indicates if the object was initially selected as an X-ray source or proper motion candidate. Other parameters given are; Spectral type, equivalent width of the 6708Å lithium line which was used by Preibisch et al. (1998) to classify the candidates, equivalent width of the H_α line and B magnitude. In column 8 the notation 'F' or 'WTTS' indicates whether the given target star is a field star with a weak Li line or an active WTTS.

Object ID	SpT	R.A. (2000)	δ (2000)	Li EW (Å)	H_α EW (Å)	B	Class	Selection
GSC6213−933		16 15 06.3	−21 57 42	0.05	3.30	11.9	F	Proper Motion
GSC6214−2384	K0	16 19 33.8	−22 28 28	0.55	−0.76	12.0	WTTS	X-ray
GSC6798−35	G1	16 23 32.3	−25 23 48	0.42	0.44	12.1	WTTS	X-ray
GSC6793−994	G4	16 14 02.1	−23 01 01	0.44	0.00	12.2	WTTS	X-ray
GSC6214−14		16 17 50.7	−20 54 57	0.05	3.82	12.2	F	Proper Motion
GSC6214−1115		16 21 07.1	−21 42 54	0.05	2.62	12.2	F	Proper Motion
GSC6794−337	K1	16 27 39.5	−22 45 22	0.55	−0.60	12.3	WTTS	X-ray
GSC6793−562		16 14 27.0	−23 09 40	0.10	3.17	12.4	F	X-ray
GSC6793−569	K1	16 13 29.3	−23 11 06	0.41	−0.63	12.5	WTTS	X-ray
GSC6793−797	K4	16 13 02.7	−22 57 43	0.46	−0.39	12.6	WTTS	X-ray
GSC6215−271		16 24 38.1	−22 11 21	0.08	3.71	12.6	F	Proper Motion
GSC6213−1186		16 15 39.8	−21 16 51	0.09	2.20	12.7	F	Proper Motion
GSC6794−537	K2	16 23 07.8	−23 00 59	0.61	1.49	12.7	WTTS	X-ray
GSC6793−806	M1	16 15 34.5	−22 42 41	0.45	−20.48	13.2	WTTS	X-ray
GSC6215−538		16 27 57.4	−22 01 25	0.03	1.39	13.2	F	Proper Motion
GSC6214−2288	G4	16 18 07.9	−22 13 25	0.18	1.62	13.4	F	Proper Motion
GSC6798−91	G0	16 20 44.7	−24 31 37	0.12	3.04	13.4	F	X-ray
GSC6793−868	M1	16 11 56.3	−23 04 04	0.67	−2.37	14.2	WTTS	X-ray

Table 2.2: Stellar parameters and information regarding the sample selected from Preibisch et al. (1998). Column 9 indicates if target star was selected by Preibisch et al. (1998) through proper motion studies or X-ray observations whereas column 8 states the 'class' nominated to each star, F = non-PMS with very weak Li line, probably an active field star and WTTS = Weak Line T Tauri strs. Spectral type, coordinates (Ep = 2000), Li & H_α equivalent widths and B magnitude also given. The Preibisch et al. (1998) specific IDs have been updated to Hubble Guide Star Catalogue IDs for ease of comparison with other sources.

Sample of Martin et al. (1998)

With the aim of studying the evolutionary status of T Tauri stars in the ρ Oph cloud, Martin et al. (1998) obtained intermediate resolution optical spectroscopy of a subset

of the X-ray sources discovered by Casanova et al. (1995). They used a spectroscopic quantitative criteria developed by Martin (1997) to classify the pre-main sequence stars into different categories, CTTS, WTTS or Post T Tauri star (PTTS). All the optical counterpart candidates Martin et al. (1998) selected for spectroscopic follow-up had to meet two criteria; they had to be optically bright, $V \leq 15$, as determined in the Hubble Guide Star Catalogue and they had to be 30 arcsecs or closer to the original ROSAT X-ray source. Stars which were discovered by this study are given the prefix 'RXJ' by Martin et al. (1998) which stands for ROSAT X-ray Source Julian, then followed by the right ascension and declination for Equinox J2000.

Spectral type, H_α and Li I equivalent widths were determined for their sample. A first visual estimate of the spectral type was done by plotting the calibrated spectrum with spectra coming from a grid of spectroscopic standards observed with similar spectral resolution. M-type stars are classified from the strength of the molecular bandheads of the CaI H and TiO lines - following the procedure of Martin and Kun (1996). G and K spectral type stars were normalized by fitting a low-order polynomial to the continuum then classifying them according to the strength of the forest of metallic lines between 6400−6470Å - mainly Ca I and Fe I lines. The uncertainty in the spectral type classification is quoted to be $\pm$ half a subclass. The H_α equivalent width was measured by Martin et al. (1998) by direct integration of the observed line profile. A number of stars have H_α in absorption which is indicated as a negative presented value (see Table 2.3, column 6). It is common to use the H_α equivalent width to distinguish between CTTS and WTTS - as discussed in Chapter 1. Martin et al. (1998) consider CTTS whose stars with H_α equivalent widths larger than 5Å for spectral type K7 and earlier, 10Å for M0-M2 stars, and 20Å for spectral type of later than M2 - as proposed by Martin (1997). The equivalent width of the LiI 6708Å resonance doublet was measured by Martin et al. (1998) by direct integration of the line profile. Prior to integrating they fitted a Gaussian to the line to determine the pseudocontinuum level. It has been shown that a plot of Li I equivalent width versus spectral type or effective temperature can be used to determine between weak- and post- T Tauri stars (Martin 1997). The main stellar mechanism which supports the distinction between WTTS and PTTS is that of pre-main sequence lithium depletion. CTTS Li I equivalent widths

are reduced by non-photospheric veiling arising in the accretion disc boundary layers. Spectral type, Li & H_α equivalent widths and T Tauri class are stated in Table 2.3 for the 7 target stars in the Martin et al. (1998) we selected for our study.

Object ID	SpT	R.A. (2000)	δ (2000)	LiI EW (Å)	H_α EW (Å)	Class
RXJ1620.7−2348	K4	16 20 45	−23 48 18	0.39 ± 0.03	−0.8	WTTS
RXJ1621.4−2312	K7	16 21 28	−23 12 05	0.59 ± 0.04	−1.6	WTTS
RXJ1622.7−2325ab	M1, M3	16 22 47	−23 25 33	$0.65 \pm 0.05, 0.60 \pm 0.05$	−1.7, −4.1	WTTS, WTTS
RXJ1623.8−2341ab	K5	16 23 50	−23 41 44	0.57 ± 0.08	−0.4	WTTS
RXJ1624.8−2359	K3	16 24 48	−23 59 18	0.39 ± 0.05	−0.06	WTTS
RXJ1625.2−2455ab	M0	16 25 15	−24 55 48	0.76 ± 0.04	−2.9	WTTS
RXJ1625.4−2346	K1	16 25 29	−23 46 18	0.37 ± 0.06	0.86	WTTS

Table 2.3: Stellar parameters and classification for T Tauri starts selected from Martin et al. (1998). Spectral type, coordinates (epoch 2000), LiI & H_α equivalent widths listed. Column 7 indicates all target stars are classified as weak line T Tauri stars by Martin et al. (1998)

2.3 The Spectroscopic Observations

2.3.1 UKST & the 6dF Instrument

The 6dF (Six degree Field) instrument on the 1.2m United Kingdom Schmidt Telescope (UKST) located at the Siding Spring Observatory was utilised to make a series of spectroscopic measurements periodically over six weeks. The 6dF instrument is a bench mounted spectrograph which is fed by 150 optical fibres from a field plate at the UKST's focal plane. The instrument has three dedicated gratings and our programme used the 1201B grating. The grating was set at an angle to include the 3968Å and 3933Å CaII H & K lines as well as some continuum to the blue. The reciprocal dispersion of the 1201B grating is 62Å per mm and the instrumental resolution is 2.1Å. The gratings 820Å bandpass was centred on 4006Å and the 1024 x 1024 instrument CCD has 0.8Å (13μm) pixels. Exposures were taken with 1 x 1 binning on the CCD, giving a spectral coverage of ~3600 to ~4400Å.

The field plate has 150 target fibres of 6.7" (100μm) diameter when fully operational and has four 7-fibre guide bundles for field acquisition. Although the aperture is only 1.2m in diameter, limiting the faintest magnitudes which can be observed, 6dF has an extraordinary six degrees of accessible field diameter, allowing a larger section

of the clouds to be covered in a single exposure. The target fibres are positioned on the steel plate (curved to match the Schmidt focal plane) with a robotic r-theta positioning system with a curved radial-arm. The robot places the magnetic buttons at the collecting end of the optical fibres to a positioning accuracy of ~ 0.7" (10μm). The buttons carry cylindrical 90° prisms which are attached to the ten metre optical fibres which directly feed the spectrograph housed in a light-tight housing in the dome (see Parker and Watson 2000 and the 6dF User Manual).

The allocated time of 38 hours was split into 2 hour nightly blocks made up of half hour exposures over 19 nights. The 19 allocated nights were spread over a six week period, allowing monitoring of at least two rotational cycles for all the target stars. A summary of observations completed and associated conditions can be found in Table 2.3.1. Dome calibration frames were taken with the telescope in the parked position

Date	Integration Time (s)	Conditions and comments
March 13^{th}	1 x 392 1 x 800 2 x 1800	seeing $1-2$", cloud affected cloud affected through some cloud
March 14^{th}	–	conditions too bad to observe
March 15^{th}	3 x 1800 1 x 1000	seeing $2-3$" cloud affected
March 16^{th} – 20^{th}	Not allocated	
March 21^{st}	5 x 1800	seeing very poor at $4-5$"
March 22^{nd}	–	conditions too bad to observe
March 23^{rd}	–	conditions too bad to observe
March 24^{th}	4 x 1800	seeing 3"
March 25^{th}	4 x 1800	seeing 3", some cloud during the night
March 26^{th}	–	conditions too bad to observe
March 27^{th}	–	conditions too bad to observe
March 28^{th}	4 x 1800	seeing $1-2$", lost autoguiding, maintained manually
March 29^{th}	4 x 1800	seeing $1-2$", patchy cloud
March 30^{th}	4 x 1800	seeing $2-4$"
April 1^{st} – 21^{st}	Not allocated	
April 22^{nd}	3 x 1800	
April 23^{rd}	4 x 1800	seeing $1-2$"
April 24^{th}	4 x 1800	seeing $2-3$"
April 25^{th}	5 x 1800	seeing varying $1-3$", some cloud
April 26^{th}	–	conditions too bad to observe
April 27^{th}	–	conditions too bad to observe

Table 2.4: Spectra were observed in a total of 12 nights out of the 19 nights allocated. Table indicates the individual integration times successfully observed and weather/seeing conditions on each of the nights.

facing a reflecting surface. 6dF is a bench mounted spectrograph and flexure is not an issue hence calibration frames do not need to be taken with the telescope pointing at the target field. The calibration exposures were taken once a night either before or after the target fields. Fibre flat fields were created with the object field plate configuration and the telescope pointing at a diffuse Quartz lamp. Arc calibration frames were obtained by taking a 40 second frame illuminated by Mercury, Cadmium and Helium arc lamps. Experience by the UKST staff shows that it is not necessary to take bias or dark calibration frames as they contain little structure. The UKST pointing coordinates were taken from digitised Schmidt photographic plates to get the required accuracy.

2.4 Reduction of the Spectra

The data reduction package for handling 6dF spectra, '6dFdr', processes the raw fits files into dispersion corrected, sky-subtracted one-dimensional spectra. The following sections cover each step of the reduction in detail, including the treatment of the calibration frames. Where appropriate, plots taken straight from the 6dFdr package demonstrate real results at intermediate steps. Where single fibre plots are used to illustrate tasks all results are those from fibre 68 which was positioned on target object GSC6214−14.

2.4.1 The Flat Field and Tram Line Maps

Five 50 second dome flats of Quartz filament lamps were combined using FIGARO task MEDSKY, a median combining routine and used with '6dFdr' for calibrations. The fibre flat field is bias corrected by subtracting the median of the bias strip from the whole frame. The bias strip on the 6dF detectors is an overscan region 25 pixels in width on the red side of the detector. A bias strip is included in each exposure so no additional dedicated bias frames are required.

The flat field image is used to define the 'tram-line map' for extracting the spectra. Due to the nature of the UK Schmidt telescope and its optical design, the spectra lie curved on the CCD hence need to be traced correctly for effective extraction. The

tram-line map tracks the position of the fibre spectra on the CCD and is generated using an optical model of the spectrograph and information about the fibre position on the slit, it defines the correct spatial position of the profiles and is fully automated. Once a tram line map is generated it is used for all subsequent files with the same spectrograph setting within the session. A tram-line map can be generated from any frame but a fibre flat field is ideal due to the high signal-to-noise ratio.

Once the tram-line map has been defined the reduction packages takes all the spectra to be reduced, combines them and generates an average spectral response. It then considers each fibre in turn to see how it differs from the average. Each fibre is divided by the fibre-flat and then multiplied by an average flat field to remove pixel-to-pixel variations as well as fringing effects in the fibres and the detector.

2.4.2 Subtracting Scattered Light

The reduction software facilitates the subtraction of any background scattered light before the spectra are extracted. The background is determined by fitting a function to the signal received through the 'dead fibres' (broken fibres) in the frame. During the processing of the flat frame a list of dead fibres is generated from the file header. Each dead fibre is checked in turn for any residual signal level which can not be due to the sky or any astronomical targets since the fibre is not positioned in the telescope focal plane. Any signal found through these fibres is thus considered to be scattered light internal to the spectrograph. The scattered light model for the 6dF spectrograph has been empirically determined by the instrument builders and the functional form found to be a quadratic with a fall off at each end, forced to be upwards convex. A minimum of three dead fibres are required to fit the scattered light quadratic function to the observed data, an example of which can be seen in Fig.2.3

2.4.3 Extracting the Spectra

There are two fibre extraction methods accommodated for in the 6dFdr reduction software. The simple default method, namely 'TRAM', slices up the image by summing the pixels around the tram-line over a width slightly less than the spacing between the tram lines. The more precise method, 'FIT', does an optimal extraction based on fitting

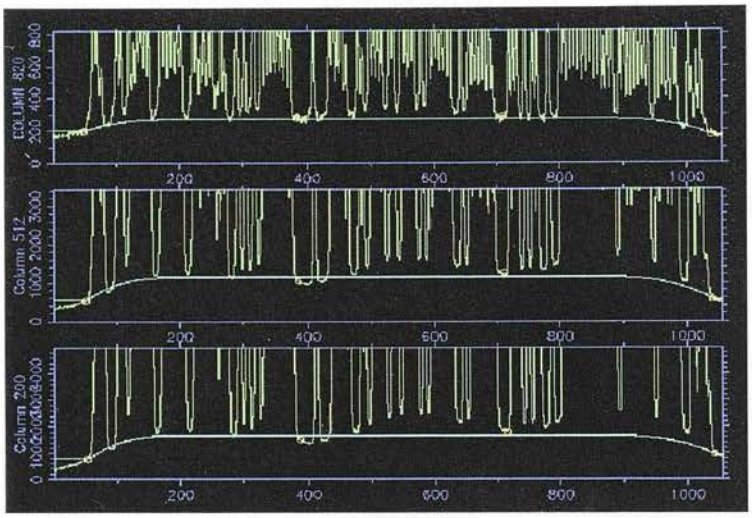

Figure 2.3: Screen shot from 6dFdr package showing the determined fit for compensating for background scattered light. Each box shows one of three cuts through the array, the spectra is in green and the light blue line shows the generated fit.

Gaussian profiles. This profile-fitting routine fits 150 overlapping Gaussian curves to the 150 fibre profiles in a single column of the fibre flat field. It is assumed that the sigma of the Gaussians vary smoothly across the detector and can therefore be described by a polynomial. The height of the Gaussian gives the corresponding point in the spectrum. As this process simultaneously fits each fibre and its neighbouring fibres any contamination of the spectrum from the adjacent fibres is minimised. The more involved 'FIT' method gives better SNR than the simpler 'TRAM' method but is more time consuming. Since we are dealing with relatively few targets we used the 'FIT' method for spectra extraction.

2.4.4 Cosmic Ray Rejection

During the extraction stage cosmic rays are rejected on the basis of spatial profile across the fibre. The spatial profile for a single wavelength channel is compared with the median profile over a block of pixels on either side of the given pixel. If it differs by more than a user set threshold the pixel is rejected and flagged as bad. However, even though in principle a procedure based only on the spatial profile should be insensitive to the spectral structure of the data the best way to remove cosmic rays is during the

combination of object frames.

2.4.5 The Arc and Wavelength Calibration

The reduction package performs an approximate wavelength calibration using information from the spectrograph optical model and the central wavelength in the file header, then refines this using the data from an arc lamp exposure. The wavelength calibrator for our observations is a 40 second exposure of three arc lamps simultaneously: Mercury, Cadmium and Helium. Once the arc frame has been bias subtracted and extracted, the lines are identified and matched against an arc line list. The 'matching' involves a cubic fit between predicted and measured wavelengths of all lines deemed 'good'. A 'good' line can be considered as one that is not too wide (which usually indicates saturation), not too weak and is not a blend (i.e. there are no nearby lines in the list). The wavelengths are refined and the arc spectrum is rebinned onto a linear wavelength scale. This procedure is repeated for each fibre spectrum, which produces a set of polynomial coefficients relating the initial approximate wavelength calibration to the true wavelength scale for each fibre. The object fibres are then shifted accordingly.

It is vital to get the arc reduction correct and it is very easy to get wrong by using an inappropriate arc line list. A plot of the reduced arc offers a quality check on the wavelength calibration, all the lines should lie straight across the frames, as shown in Fig.2.4. For the purpose of our analysis we only needed the wavelength calibration to be accurate to one pixel, 0.8Å.

2.4.6 Fibre Throughput Calibration & The Offset Sky

It is also necessary to correct for fibre-to-fibre differences in throughput and to normalise all the fibres to the same level. Though there are three possible methods for throughput calibration, we have selected to use the 'offset sky' method. However, instead of taking a genuine 'offset-sky' exposure we generated a frame by copying the flat field frame and changed the appropriate header entry. This procedure gives exactly the same result as taking an offset-sky twilight frame but was more practical when, as in our case, more than one project is getting observed each night. The

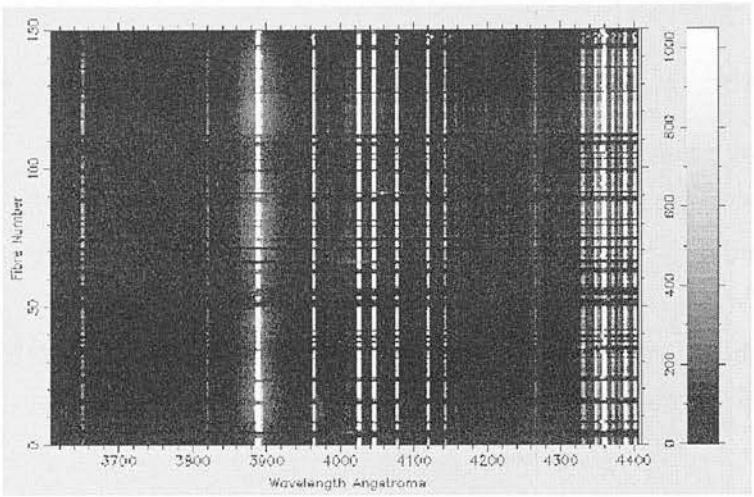

Figure 2.4: Screen shot from 6dFdr package showing a single reduced arc frame - the spectral lines run straight across the detector indicating the wavelength scale for each fibre has been determined correctly. Visually checking the frame is a vital quality control of the reduction process.

offset-sky frame is processed with the same steps as a target field frame but stops at the point of wavelength calibration of extracted spectra. The relative throughput for each fibre is the 'mean signal in the fibre divided by the median over all the fibres'. An example of a 'throughput map' for the single fibre is shown in Fig.2.5. The derived throughputs are applied to the data by dividing each spectrum by its corresponding fibre throughput. It can be seen from Fig.2.5 that the fibre's throughput drops off at wavelengths below 4000Å. There are no dedicated steps in the 6dFdr package to correct for wavelength dependent sensitivity.

The flat-field is normalised to remove averaged wavelength dependence with the intention to correct for pixel-to-pixel flat-field effects. The throughput calibration is a fibre dependent constant value. This means the resultant spectrum is actually:

$$F_n(\lambda) * < T_n(\lambda) > \tag{2.1}$$

where $F_n(\lambda)$ is the spectrum flux entering fibre n at wavelength λ and $< T_n(\lambda) >$ is the average fibre throughput multiplied by the quantum efficiency of the n^{th} fibre at wavelength λ. Any desired flux calibration has to be done post 6dFdr reduction.

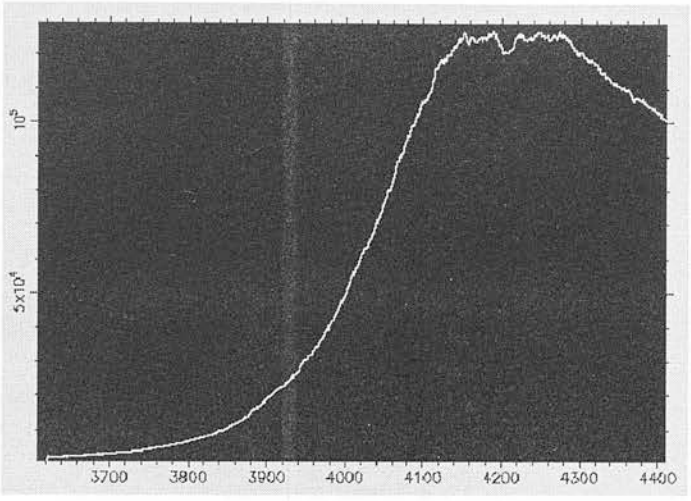

Figure 2.5: Screen shot from 6dFdr package showing the throughput of a single fibre, wavelength v.s. non-normalised flux - highlights how the throughput drops off below 4000Å.

However, as discussed later in the chapter it is not important for our studies to flux calibrate the target spectra.

2.4.7 The Object Frames

The list below gives a brief description of the sequence of tasks carried out on each object frame to obtain a fully reduced frame containing 150 dispersion corrected, sky subtracted, wavelength calibrated, one-dimensional spectra for each of the fibres, stacked together. Fig.2.6 demonstrates a single fully reduced frame. Individual extracted spectra can be seen in §2.5.

Debiassing Mean of the bias strip is subtracted and the bias strip trimmed from the frame.

Scattered Light The deduced scattered light function is fitted to compensate for background contamination.

Fibre Extraction The tram-line map generated from the flat field is utilised to extract the spectra. The resulting file contains the data in the form of a 150 by 1024 array giving the data for each of the fibres.

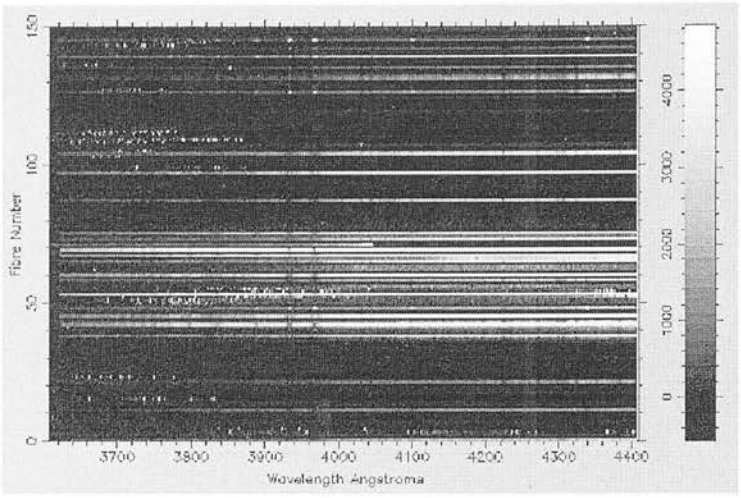

Figure 2.6: Screen shot from 6dFdr package giving an example of the final fully reduced frame for a single exposure. The fibre numbers are shown on the y-axis and the wavelength in Å on the x-axis. The CaII H & K lines can be seen running through the target fibres around 3950Å.

Flat Fielding Divided by the reduced flat field.

Wavelength Calibration Wavelength shift and dispersion determined from an arc lamp frame is used to rebin the data onto a linear wavelength scale.

Throughput Calibration Reduced offset sky frame divided through the object frames for throughput calibration of each fibre.

Sky Subtraction Our target fibre configuration included 22 fibres assigned to sky positions. A MEDIAN operation is used to generate a combined sky spectrum making it insensitive to any sky fibres accidentally contaminated by sources or by cosmic rays. The combined sky spectrum is then subtracted from all the fibre spectrums (see Fig.2.7 for an example of a combined sky frame).

2.5 Resultant Spectra

In this section we present a small taster of resultant one dimensional extracted reduced spectra from the 6dFdr package. Plotted in the following three figures are the spectra for target stars GSC6798−35, GSC6214−2288 and ROXs44 - the top plot in each figure

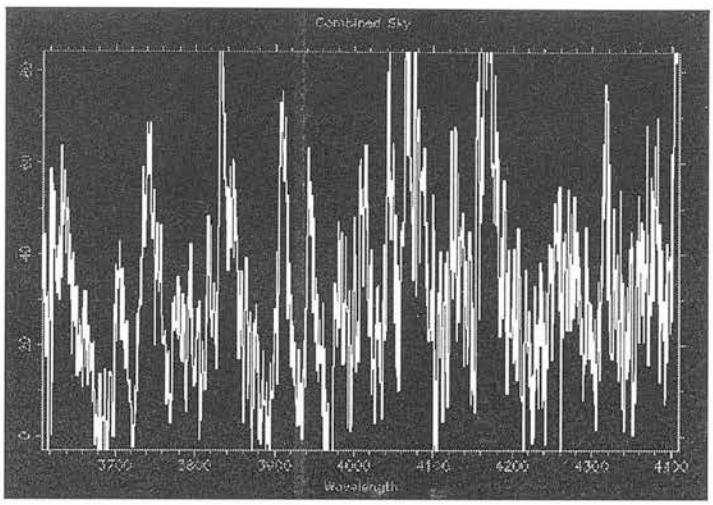

Figure 2.7: Screen shot from 6dFdr package showing the resultant combined sky from all 22 sky fibres in our plate configuration.

it the spectrum as produced by 6dFdr and the bottom plot is zoomed in to only show the area around the CaII doublet. Fig.2.8 shows GSC6798−35, an example of a spectrum where the CaII absorption lines have an emission core at the bottom of the line - indicative of a small amount of chromospheric activity. Fig.2.9 shows the spectrum for target star ROXs44 where the chromospheric activity is sufficiently strong that the CaII H & K lines are fully in emission. Lastly Fig.2.10 shows the field star GSC6214−2288 with the doublet fully in absorption. The spectra seen in Figs. 2.8 - 2.10 were produced by combining the 4, 1800 second exposures, for each of the target stars on the night of April 23rd, 2003. Two factors of the instrument can be seen on the complete spectrum, the overscan region to the very right side of the spectrum and the spectra trails off towards the blue end due to the transmission properties of the fibres which feed the spectrograph. To scale for the reduction in counts at blue wavelengths we could have flux calibrated our spectra, however as we only wish to qualify chromospheric activity using a ratio value (see §2.9) it is valid to leave the spectra as is. Spectra for the complete set of programme stars can be found in Appendix A.

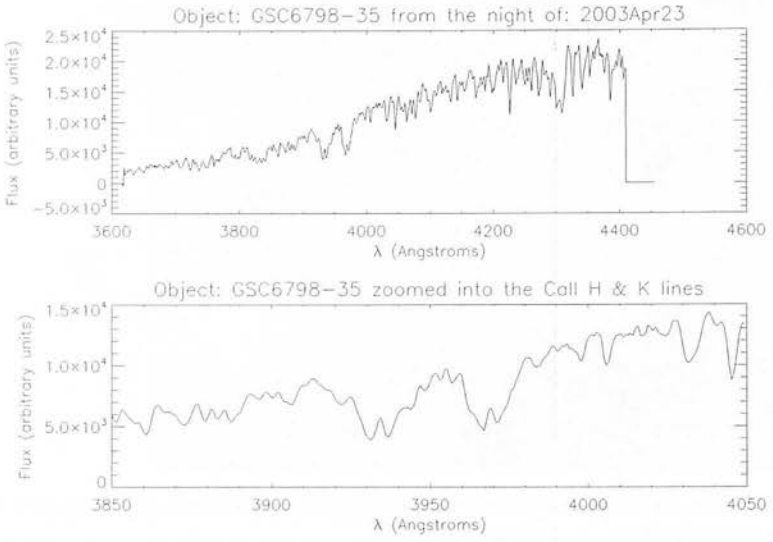

Figure 2.8: Fully reduced spectra for target object GSC6798−35, full spectra at the top and zoomed in spectra around the CaII H & K lines on the bottom. Here the CaII absorption lines have an emission core at the bottom of the line - indicative of a small amount of chromospheric activity.

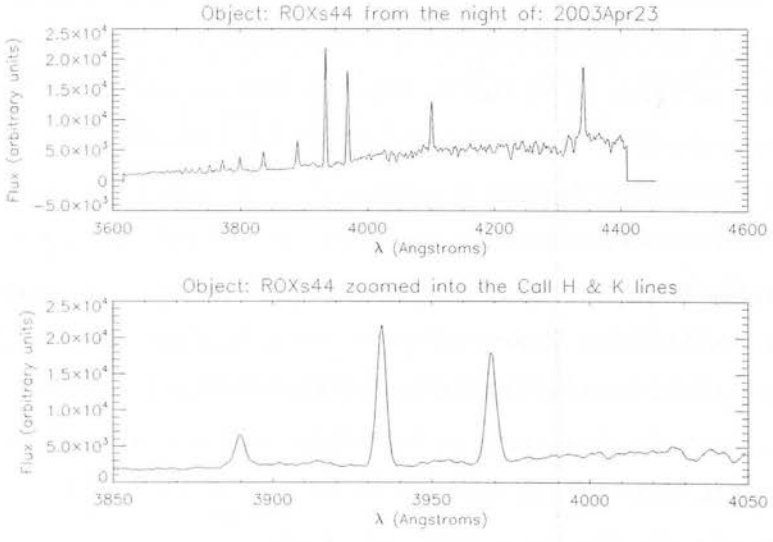

Figure 2.9: Fully reduced spectra for target object ROXs44, full spectra at the top and zoomed in spectra around the CaII H & K lines on the bottom. Here the chromospheric activity is sufficiently strong that the CaII doublet is entirely in emission.

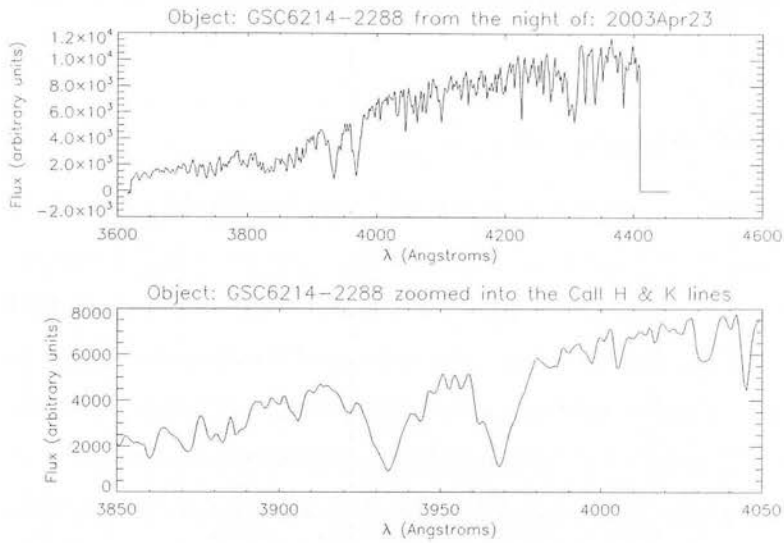

Figure 2.10: Fully reduced spectra for target object GSC6214−2288, full spectra at the top and zoomed in spectra around the CaII H & K lines on the bottom. Here the star is sufficiently chromospherically quiet that the CaII lines are fully in absorption with no evidence of emission cores.

2.6 The Photometric Observations

2.6.1 The Automated Patrol Telescope

In addition to the 6dF spectroscopic observations, near simultaneous photometric measurements of the ρ Ophiuchus target field were made through collaboration with Dr. Michael Ashley of the University of New South Wales (UNSW). The UNSW's own Automatic Patrol Telescope (APT) was used to take V band images during the UKST allocated time. The APT is a wide-field CCD imaging telescope located at the Siding Spring Observatory, it is entirely computer-controlled and can be operated either remotely or automatically. The automatic mode is run within limits set by the reliability of the weather monitoring systems at the dome.

The optical design of the telescope resembles that of a Schmidt telescope but uses a 3-element correcting lens to obtain a wide, corrected field-of-view (FOV). The APT's 0.5m aperture with f/1 spherical primary mirror yields a 5 degree flat field, of which a 2 x 3 degree area is recorded by the 800 x 1200 pixel CCD. The telescope is equipped

with B, V, R & I broadband filters which can only be changed manually (Carter et al. 1995; Hidas et al. 2005)

2.6.2 Reducing The Photometric Data

The photometric observations were fully reduced by our collaborators M. Ashley & M. Hidas at the UNSW. They have developed a very effective pipeline which automates the entire reduction process from raw images to calibrated magnitudes. Each APT frame is reduced in the same manner as the 'tried and tested' Isaac Newton Telescope (INT) Wide Field Survey pipeline software developed by Irwin and Lewis (2001). We were supplied with fully reduced V band magnitudes determined by optimal aperature photometry for each target star on each night, these are listed in Table 2.5, the actual light curves can be found in §2.11 beside the plots for CaII variation. The error quoted is RMS of the measurements taken for each target on each night. Further information and details regarding the reduction pocess can be found in Hidas et al. (2005).

2.7 Determining Stellar Parameters

To disentangle the photospheric contribution from the chromospheric contribution in the CaII spectral lines, the spectra of a chromospherically quiet star must be subtracted from our observed spectra (see §2.8). The most consistent way to do this is to subtract a synthetic spectra, and in order to know which synthetic spectra is appropriate it is required to determine a number of stellar parameters for the programme stars, chiefly effective temperature and surface gravity. Recent studies have found the average metallically for PMS in star forming regions is slightly below that of solar, $\langle [Fe/H] \rangle$ = 0.0 to -0.2 but further studies indicate the presence of photospheric spots affects the final determination of stellar metallicity, in addition to other stellar parameters, which may have future implications on the study of young, magnetically active stars (James et al. 2006; Morel et al. 2004). For this study it is adequate to adopt the metallicity of the T Tauri sample as solar, [Fe/H] = 0.00 $\pm$ 0.03 (Santos et al. 2004). The following sections detail the required steps, giving derivation of equations and

Date	March 13	March 14	March 21	March 25	March 26	March 28	March 29	March 30	April 22	April 23	April 24
GSC6798−35	11.441 ± 0.005	11.467 ± 0.005	11.459 ± 0.024	11.445 ± 0.006	11.474 ± 0.015	11.474 ± 0.005	11.416 ± 0.007	11.461 ± 0.006	11.439 ± 0.007	11.463 ± 0.006	11.448 ± 0.005
GSC6798−91	12.443 ± 0.011	12.477 ± 0.013	12.421 ± 0.048	12.442 ± 0.017	12.456 ± 0.025	12.436 ± 0.007	12.440 ± 0.014	12.436 ± 0.011	12.447 ± 0.014	12.437 ± 0.005	12.435 ± 0.006
RXJ1623.8−2341	14.263 ± 0.038	14.363 ± 0.071	14.398 ± 0.225	14.355 ± 0.053	14.669 ± 0.121	14.246 ± 0.041	14.578 ± 0.085	14.326 ± 0.020	14.352 ± 0.063	14.606 ± 0.071	14.329 ± 0.038
RXJ1620.7−2348	12.659 ± 0.014	12.791 ± 0.014	12.835 ± 0.069	12.695 ± 0.014	12.659 ± 0.016	12.736 ± 0.014	12.639 ± 0.006	12.709 ± 0.010	12.657 ± 0.017	12.744 ± 0.022	12.703 ± 0.011
RXJ1621.4−2312	14.004 ± 0.019	14.177 ± 0.077	13.332 ± 0.096	13.832 ± 0.038	13.937 ± 0.035	13.895 ± 0.018	13.959 ± 0.030	13.782 ± 0.018	13.717 ± 0.062	13.802 ± 0.024	13.896 ± 0.017
GSC6793−569	11.672 ± 0.006	11.782 ± 0.011	11.627 ± 0.021	11.641 ± 0.006	11.789 ± 0.006	11.643 ± 0.008	11.731 ± 0.012	11.762 ± 0.007	11.658 ± 0.008	11.735 ± 0.008	11.747 ± 0.009
GSC6793−868	13.061 ± 0.018	13.045 ± 0.019	10.676 ± 0.010	13.084 ± 0.018	13.143 ± 0.031	13.016 ± 0.015	13.006 ± 0.011	13.043 ± 0.009	13.074 ± 0.019	13.049 ± 0.008	12.993 ± 0.008
GSC6793−562	11.890 ± 0.006	11.858 ± 0.007	11.907 ± 0.023	11.889 ± 0.004	11.926 ± 0.012	11.887 ± 0.006	11.880 ± 0.008	11.888 ± 0.010	11.899 ± 0.009	11.896 ± 0.005	11.897 ± 0.007
GSC6793−797	11.824 ± 0.010	11.751 ± 0.010	11.450 ± 0.024	11.733 ± 0.005	11.871 ± 0.008	11.826 ± 0.009	11.718 ± 0.008	11.808 ± 0.004	11.814 ± 0.023	11.778 ± 0.008	11.795 ± 0.007
GSC6793−994	11.478 ± 0.004	11.631 ± 0.007	11.484 ± 0.023	11.457 ± 0.007	11.703 ± 0.008	11.461 ± 0.006	11.632 ± 0.009	11.468 ± 0.005	11.639 ± 0.013	11.492 ± 0.005	11.454 ± 0.008
GSC6793−806	12.682 ± 0.056	12.796 ± 0.015	-	12.745 ± 0.018	-	12.498 ± 0.001	12.516 ± 0.014	12.494 ± 0.011	12.624 ± 0.016	12.468 ± 0.059	12.628 ± 0.009
GSC6213−933	11.562 ± 0.016	11.570 ± 0.009	11.544 ± 0.028	11.538 ± 0.011	-	11.539 ± 0.003	11.524 ± 0.014	11.532 ± 0.006	11.528 ± 0.007	11.485 ± 0.018	11.527 ± 0.007
GSC6214−2288	13.144 ± 0.106	13.102 ± 0.009	13.255 ± 0.138	13.079 ± 0.019	-	13.085 ± 0.003	13.067 ± 0.021	13.073 ± 0.005	13.081 ± 0.025	13.068 ± 0.004	13.064 ± 0.008
GSC6213−1186	11.897 ± 0.055	11.839 ± 0.005	11.703 ± 0.022	11.823 ± 0.006	-	11.818 ± 0.009	11.815 ± 0.011	11.819 ± 0.001	11.821 ± 0.004	11.825 ± 0.003	11.819 ± 0.007
GSC6214−2384	11.385 ± 0.018	11.439 ± 0.002	11.418 ± 0.028	11.394 ± 0.006	-	11.374 ± 0.009	11.392 ± 0.008	11.428 ± 0.001	11.357 ± 0.008	11.408 ± 0.003	11.443 ± 0.002
GSC6214−14	12.022 ± 0.015	12.013 ± 0.001	12.012 ± 0.029	12.013 ± 0.006	-	12.002 ± 0.014	12.019 ± 0.011	12.007 ± 0.006	12.024 ± 0.005	12.058 ± 0.027	12.016 ± 0.006
GSC6214−1115	11.473 ± 0.028	11.499 ± 0.002	11.520 ± 0.016	11.521 ± 0.003	-	11.507 ± 0.002	11.521 ± 0.008	11.509 ± 0.001	11.519 ± 0.003	11.530 ± 0.010	11.513 ± 0.009
GSC6794−537	11.916 ± 0.016	11.979 ± 0.011	12.262 ± 0.043	11.887 ± 0.009	11.933 ± 0.021	12.030 ± 0.001	11.978 ± 0.010	11.917 ± 0.007	11.964 ± 0.012	11.922 ± 0.013	11.961 ± 0.011
GSC6215−271	12.383 ± 0.022	12.535 ± 0.017	12.549 ± 0.043	12.565 ± 0.013	-	12.565 ± 0.006	12.563 ± 0.014	12.558 ± 0.009	12.562 ± 0.012	12.571 ± 0.016	12.561 ± 0.012
GSC6215−538	12.715 ± 0.076	12.646 ± 0.025	14.804 ± 0.569	12.675 ± 0.018	-	12.693 ± 0.011	11.731 ± 0.010	12.680 ± 0.002	12.701 ± 0.018	12.652 ± 0.038	12.708 ± 0.014
GSC6794−337	11.520 ± 0.024	11.633 ± 0.011	10.558 ± 0.010	11.932 ± 0.028	-	11.745 ± 0.012	11.676 ± 0.024	11.657 ± 0.008	11.942 ± 0.025	11.715 ± 0.009	11.675 ± 0.009
ROXs5	13.606 ± 0.016	13.648 ± 0.022	13.565 ± 0.129	13.669 ± 0.024	13.681 ± 0.015	13.652 ± 0.032	13.637 ± 0.017	13.675 ± 0.016	13.712 ± 0.209	13.704 ± 0.035	13.688 ± 0.021
ROXs30c	14.156 ± 0.034	14.202 ± 0.030	14.228 ± 0.311	14.166 ± 0.052	14.191 ± 0.033	14.098 ± 0.037	14.079 ± 0.015	14.113 ± 0.039	14.223 ± 0.035	14.144 ± 0.029	14.125 ± 0.029
ROXs44	12.776 ± 0.019	12.759 ± 0.013	12.788 ± 0.032	12.822 ± 0.015	12.781 ± 0.018	12.786 ± 0.009	12.751 ± 0.011	12.699 ± 0.005	12.686 ± 0.012	12.696 ± 0.019	12.758 ± 0.012
ROXs47a	13.562 ± 0.031	13.506 ± 0.015	13.818 ± 0.207	13.449 ± 0.020	13.728 ± 0.036	13.424 ± 0.015	13.652 ± 0.032	13.441 ± 0.017	13.529 ± 0.032	13.743 ± 0.016	13.489 ± 0.027
ROXs42c	11.951 ± 0.009	11.962 ± 0.007	11.869 ± 0.017	11.952 ± 0.006	11.977 ± 0.009	12.032 ± 0.008	11.963 ± 0.007	12.021 ± 0.004	11.931 ± 0.008	11.981 ± 0.005	12.055 ± 0.011
ROXs39	12.759 ± 0.035	12.681 ± 0.015	12.711 ± 0.039	12.882 ± 0.018	12.843 ± 0.021	12.725 ± 0.021	12.656 ± 0.008	12.714 ± 0.013	12.720 ± 0.016	12.722 ± 0.017	12.811 ± 0.016
ROXs33	13.928 ± 0.021	13.959 ± 0.027	14.170 ± 0.209	13.951 ± 0.046	14.055 ± 0.039	13.935 ± 0.018	13.933 ± 0.025	14.001 ± 0.022	14.267 ± 0.056	14.044 ± 0.026	14.038 ± 0.043
ROXs45f	12.382 ± 0.010	12.358 ± 0.007	12.507 ± 0.025	12.309 ± 0.015	12.359 ± 0.018	12.357 ± 0.009	12.365 ± 0.008	12.381 ± 0.019	12.293 ± 0.014	12.358 ± 0.009	12.355 ± 0.010
ROXs29	11.458 ± 0.009	11.543 ± 0.009	11.644 ± 0.021	11.399 ± 0.006	11.470 ± 0.009	11.688 ± 0.003	11.616 ± 0.004	11.576 ± 0.007	11.563 ± 0.006	11.655 ± 0.017	11.583 ± 0.013
ROXs21	13.346 ± 0.016	13.242 ± 0.021	13.406 ± 0.092	13.376 ± 0.032	13.291 ± 0.019	13.341 ± 0.016	13.363 ± 0.027	13.344 ± 0.009	13.422 ± 0.038	13.216 ± 0.013	13.373 ± 0.015
ROXs6	12.556 ± 0.005	12.688 ± 0.018	12.757 ± 0.049	12.689 ± 0.023	12.745 ± 0.017	12.756 ± 0.012	12.697 ± 0.022	12.687 ± 0.017	12.755 ± 0.019	12.782 ± 0.015	12.785 ± 0.016
ROXs9a	13.948 ± 0.019	13.936 ± 0.027	14.600 ± 0.241	13.926 ± 0.054	13.919 ± 0.039	13.919 ± 0.017	13.926 ± 0.029	13.937 ± 0.018	13.905 ± 0.038	13.919 ± 0.032	13.935 ± 0.034
RXJ1625.2−2455	14.512 ± 0.050	14.381 ± 0.037	14.723 ± 0.312	14.417 ± 0.039	14.472 ± 0.102	14.360 ± 0.017	14.409 ± 0.051	14.481 ± 0.029	14.520 ± 0.066	14.388 ± 0.052	14.317 ± 0.037
ROXs3	13.042 ± 0.009	13.057 ± 0.018	13.166 ± 0.068	13.094 ± 0.023	13.094 ± 0.019	13.107 ± 0.013	13.095 ± 0.009	13.074 ± 0.015	13.046 ± 0.029	13.008 ± 0.011	13.000 ± 0.007

Table 2.5: V band magnitudes as observed by Drs. M. Ashley & M. Hidas using the UNSW APT. Photometric observations were taken in conjunction with the spectroscopic images. V magnitudes quoted are the mean values for a number of exposures taken of each target on each night, plus or minus RMS error.– entry indicates null data due to observational errors.

sources for conversions used.

2.7.1 Surface Gravity dervied from $T_{\rm eff}$ and L_*

Effective temperature can be obtained from the stellar spectral type via published conversion tables and the surface gravity is calculated from basic principles of stellar atmospheres as follows.

The luminosity of a star can be derived from the effective temperature and stellar radius using:

$$L_* = 4\pi R_*^2 \sigma T_{\rm eff_*}^4 \tag{2.2}$$

where σ is the Stefan-Boltzmann constant. Surface gravity is related to stellar mass and radii by:

$$g_* = \frac{GM_*}{R_*^2} \tag{2.3}$$

By rearranging equation 2.2 to obtain stellar radii in terms of luminosity and effective temperature, substituting this into equation 2.3 then taking the logarithms one derives $\log g_*$:

$$\log g_* = \log G + \log M_* - \log L_* + 4 \log T_{\rm eff_*} + \log(4\pi\sigma) \tag{2.4}$$

Subtracting the comparable equation for the sun allows us to get the stellar surface gravity in terms stellar mass and luminosity in solar units and effective temperture as given by:

$$\log g_* = 4.44 + \log \frac{M_*}{M_\odot} - \log \frac{L_*}{L_\odot} + 4 \log T_{\rm eff_*} - 4 \log T_{\rm eff_\odot} \tag{2.5}$$

where the constant value '4.44' is the log surface gravity for the Sun and the Solar effective temperature is taken to be 5770K (Coelho et al. 2005). The luminosity can be calculated as follows by using the measured magnitudes and colours of the programme stars and the distance to the clouds. The stellar luminosity is related to bolometric magnitude, that is the magnitude of the star measured across all wavelengths such that it takes into account the total amount of energy radiated:

$$\log \frac{L_*}{L_\odot} = 0.4(M_{\rm bol_\odot} - M_{\rm bol_*}) \tag{2.6}$$

where $M_{bol_\odot} = 4.64$ (Baraffe et al. 1998) and the stellar bolometric magnitude is obtained from the observed (apparent) magnitude in the J band via the distance modulus using equations 2.7 & 2.8:

$$m_J - M_J = 5\log D - 5 \tag{2.7}$$

$$M_{bol} = M_J + BC_J \tag{2.8}$$

to give:

$$M_{bol_*} = m_{J_*} - 5 * (\log D - 1) + BC_{J_*} \tag{2.9}$$

where D is the distance to the cluster in pc, BC_J is the bolometric correction in the J band.

2.7.2 Determining IR Colour Index & Bolometric Correction

It would seem most natural to use a optical magnitude to calculate the bolometric magnitude given that the study is in the optical regime and we have taken our own V band magnitudes measurements. However we also need to use the stellar colours to determine the level of extinction due to the inter-cloud and inter-stellar dust. Though it would be possible to obtain the magnitudes in another band, such as B from literature, to combine with our V magnitude measurements it is not ideal as the measurements have not been taken at the same time and thus uncertainties are introduced into the colour due to systematic photometric errors and stellar variability. Furthermore it is more robust to use an infrared magnitude for the calculation of luminosity as it is much less affected by extinction. J, in particular, is often used for this purpose as there is little contamination from infrared excess radiation due to the presence of any circumstellar disk. Therefore the reddening by dust was checked using the (J−H) colour. The J, H & K magnitudes were taken from the Two Micron All Sky Survey (2MASS) database and are listed in table 2.6. A number of conversions are needed to calculate the stellar luminosity from spectral type and colour; effective temperature as a function of spectral type was taken from de Jager and Nieuwenhuijzen (1987) - the values were interpolated to fill in the missing spectral types; bolometric correction in the J band with respect to effective temperature was taken from Baraffe et al. (1998) via D'Antona et al. (1999) - a polynomial fit was used to decrease the steps in effective

ID	J	H	K
GSC6793−868	9.792 ± 0.034	9.101 ± 0.037	8.815 ± 0.034
GSC6793−797	9.322 ± 0.023	8.651 ± 0.047	8.455 ± 0.027
GSC6793−569	9.317 ± 0.027	8.624 ± 0.042	8.494 ± 0.019
GSC6793−994	9.375 ± 0.026	8.774 ± 0.053	8.608 ± 0.023
GSC6793−562	10.490 ±0.024	10.225 ± 0.024	10.151 ± 0.019
GSC6213−933	10.025 ± 0.024	9.741 ± 0.026	9.656 ± 0.021
GSC6793−806	9.382 ± 0.038	8.334 ± 0.038	7.909 ± 0.023
GSC6213−1186	10.142 ± 0.026	9.761 ± 0.023	9.669 ± 0.025
GSC6214−14	10.725 ± 0.029	10.490 ± 0.026	10.356 ± 0.025
GSC6214−2288	11.439 ± 0.022	11.077 ± 0.024	11.009 ± 0.023
GSC6214−2384	9.230 ± 0.019	8.659 ± 0.036	8.509 ± 0.019
GSC6798−91	9.354 ± 0.026	8.733 ± 0.046	8.526 ± 0.021
RXJ1620.7−2348	9.867 ± 0.023	9.141 ± 0.021	8.927 ± 0.019
GSC6214−1115	9.963 ± 0.026	9.668 ± 0.022	9.559 ± 0.019
RXJ1621.4−2312	9.937 ± 0.026	9.031 ± 0.024	8.739 ± 0.019
RXJ1622.7−2325	9.809 ± 0.030	8.653 ± 0.031	8.234 ± 0.027
GSC6794−537	9.042 ± 0.032	8.343 ± 0.040	8.184 ± 0.024
GSC6798−35	8.600 ± 0.024	7.979 ± 0.046	7.695 ± 0.023
RXJ1623.8−2341	10.012 ± 0.024	9.013 ± 0.024	8.599 ± 0.023
GSC6215−271	10.521 ± 0.022	10.116 ± 0.022	10.010 ± 0.023
RXJ1624.8−2359	9.430 ± 0.027	8.275 ± 0.038	7.857 ± 0.020
RXJ1625.2−2455	9.589 ± 0.021	8.578 ± 0.033	8.269 ± 0.024
RXJ1625.4−2346	8.833 ± 0.027	8.081 ± 0.021	7.822 ± 0.027
ROXs3	9.776 ± 0.024	9.045 ± 0.027	8.784 ± 0.023
ROXs5	9.729 ± 0.026	8.773 ± 0.053	8.383 ± 0.026
ROXs6	9.154 ± 0.020	8.145 ± 0.046	7.518 ± 0.024
ROXs10b	8.971 ± 0.032	7.500 ± 0.027	6.571 ± 0.018
ROXs9a	9.224 ± 0.024	8.056 ± 0.049	7.688 ± 0.026
ROXs21	9.424 ± 0.023	8.631 ± 0.044	8.408 ± 0.036
ROXs30c	9.896 ± 0.024	8.722 ± 0.036	8.206 ± 0.017
GSC6794−337	8.942 ± 0.019	8.306 ± 0.053	8.084 ± 0.026
ROXs29	8.440 ± 0.027	7.667 ± 0.042	7.207 ± 0.023
GSC6215−538	10.474 ± 0.024	9.993 ± 0.023	9.869 ± 0.023
ROXs33	8.731 ± 0.027	7.483 ± 0.044	6.850 ± 0.023
ROXs39	9.094 ± 0.019	8.279 ± 0.051	8.025 ± 0.017
ROXs40	9.094 ± 0.032	8.174 ± 0.065	7.878 ± 0.029
ROXs42c	8.357 ± 0.027	7.512 ± 0.051	7.219 ± 0.024
ROXs44	9.233 ± 0.023	8.246 ± 0.057	7.610 ± 0.024
ROXs45f	10.255 ± 0.024	9.554 ± 0.022	9.395 ± 0.024
ROXs47a	9.245 ± 0.024	8.351 ± 0.031	7.929 ± 0.061

Table 2.6: J, H and K infrared magnitude with error for our T Tauri sample taken from the 2MASS searchable archive (source: vizier.u-strasbg.fr). Quoted errors are the total photometric uncertainty including; corrected band photometric uncertainty, nightly photometric zero point uncertainty and flat fielding residual error.

temperature to give more accurate allocation of BC_J and finally the intrinsic (J−H) colour as a function of spectral type was taken from Bessell and Brett (1988). Fundamental to determining all the required stellar parameters is knowing the programme stars spectral type. A small number of our target stars do not have published spectral types in the literature so a rough estimation of spectral type was undertaken, see §2.7.5.

2.7.3 Accounting For Extinction

A final step before being able to plot the programme stars on an HR diagram and determine their mass is to account for extinction. Following equations given by Cardelli et al. (1989) the extinction,A_J, in the J band can be determined from observed colour, $(J-H)_{obs}$, and intrinsic colour, $(J-H)_{int}$, as per:

$$E(J-H) = (J-H)_{obs} - (J-H)_{int} = 0.326A_J \tag{2.10}$$

or

$$A_J = \frac{(J-H)_{obs} - (J-H)_{int}}{0.326} \tag{2.11}$$

and then applying the extinction to the observed apparent magnitude to give the dereddened magnitude by:

$$J_{true} = J_{obs} - A_J \tag{2.12}$$

Extinction was corrected in a target star if $E(J-H) > 0.3$

2.7.4 Plotting the HR Diagram

Given that the luminosity and effective temperatures are now derived for the target stars it is required to plot an HR diagram. Theoretical evolutionary tracks for stars in the mass range of $0.1 - 2.0M_\odot$ in $0.1M_\odot$ increments, and 2.2, 2.5, 2.7 & $3.0M_\odot$, are overlaid so each star can be allocated a mass. Since the purpose of this exercise is to gain surface gravity values for the stars and not absolutely accurate mass values the measurements were judged 'by eye' from the HR diagram to the 'nearest' $0.025M_\odot$. An error in estimating the stellar mass by $0.025M_\odot$ translates to an error in the surface

gravity calculation of ~ 0.01, which is acceptable for this study. The HR diagram can be seen in Fig.2.11, the dotted lines are the evolutionary tracks of constant mass of Siess et al. (2000) with the dashed lines being the age isochrones taken from the same source, lines of constant age are plotted for 0.2, 1.0, 10.0 & 20.0 Myrs. The Siess et al. (2000) tracks and isochrones were computed for PMS models with solar composition and no over-shooting.

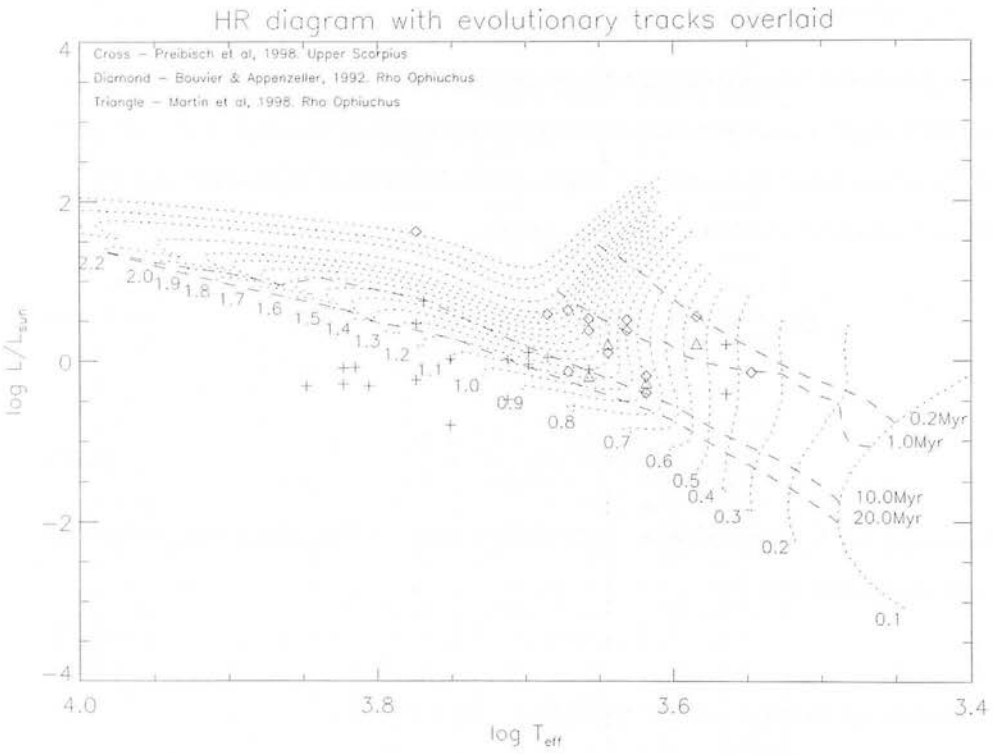

Figure 2.11: Determined HR diagram for the T Tauri sample. Different symbols indicate source each target star was selected from, key on diagram. Overlaid are theoretical evolutionary tracks of constant mass (dotted lines) and isochrones of constant age (dashed lines) taken from Siess et al. (2000). See text for discussion about seven target stars which lie too low on the diagram.

As demonstrated by equation 2.9, distance to the cluster is vital for the calculation of stellar bolometric magnitude, distance to ρ Oph varies in the literature over a range of 120 – 170 pc. The effect of different cluster distance on the determination of stellar surface gravity was calculated to justify selection of one published distance over the

others. Taking a single target star at random for our sample, the stellar parameters were calculated for both 120 & 170 pc. It was found a change in 50 pc leads to a difference in M_{bol} of ~ 0.9 which translates to a difference in logarithm of the luminosity of ~ 0.3. This in turn alters the position on the HR diagram which results in a difference of $0.5M_{\odot}$ in stellar mass. Ultimately this gives a change in stellar surface gravity of ~ 0.3. The key parameter for this study is the surface gravity as this enables us to pick the appropriate synthetic spectra, as fully explained in §2.8, for further analysis and the synthetic spectra we have used only computed spectra in steps of $\log g = 0.5$. Hence, even using the extremes in published distances results in the same rounded $\log g$ value for the selection of synthetic spectra. For this reason we have adopted the Bouvier and Appenzeller (1992) published 170 pc to allow comparison of derived stellar parameters.

It is immediately obvious from looking at the HR diagram that seven of the target stars sit too low, i.e. the stellar luminosity or effective temperatures are not correct. Note that all the 'low' targets belong to the Upper Sco association as deduced by Preibisch et al. (1998) and all bar one do not have published spectral types. §2.7.5 details the process used to estimate the spectral types of these stars but of course spectral type has been used to get effective temperature so an error could have been introduced at this stage. Additionally, luminosity is reliant on distance to the star. If either the target is misclassified as belonging to the given association or if the stars individual distance is distinctly different to the average distance measure for the cluster then an error can be introduced into the luminosity calculation. In order to 'move' these stars into the correct region on the HR diagram would require ~1300K reduction in T_{eff}, which translates to a change of 1 spectral type class, or a increase of ~1 in $\log(L_*/L_{\odot})$, which would need a change in distance of ~150pc. Clearly, an error in spectral type is most likely the source of this error and not unexpected given the crude method of estimation. However, again the main reason for plotting these stars on an HR diagram for this study is determination of surface gravity. Even with a change in effective temperature sufficient to place the targets onto the tracks there is only a change in estimated stellar mass of $\sim 0.5M_{\odot}$, which leads to a change in surface gravity of ~0.3 which does

not change the selection of corresponding synthetic spectra. Though it would be interesting and worthy to discover the source of error in the placement of these targets it is not necessary at this time for the completion of this study. The stellar mass of these targets was estimated by extrapolating the nearest lines of constant mass.

A summary of derived parameters; T_{eff_*}, $\log L_*$, M_*, $\log g_*$, $(J-H)_{obs}$, $(J-H)_{int}$, $(V-R)_{int}$ and A_J is presented in Table 2.7. For interest, Fig.2.12 shows the (J−H) − (H−K) colour-colour diagram for the programme stars with the main sequence and giant branch overlaid, taken from Bessell and Brett (1988) via Meyer et al. (1997).

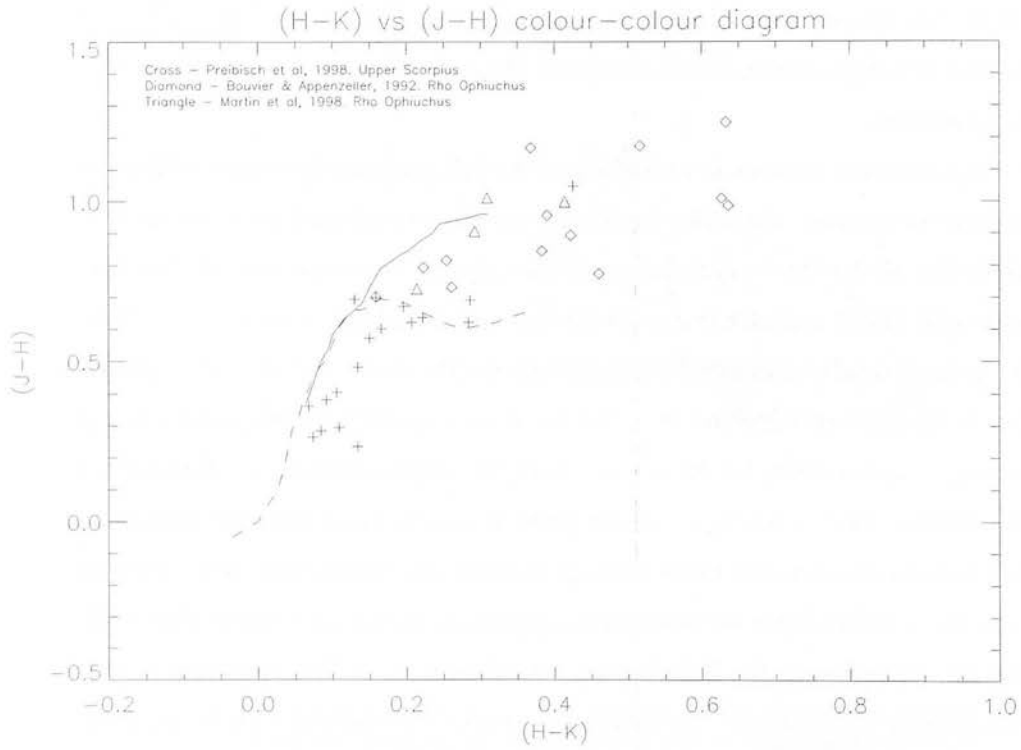

Figure 2.12: (J−H) − (H−K) colour-colour diagram for the programme stars. Different symbols indicate source each target star was selected from, key on diagram. Overlaid are tracks of intrinsic colours of giant (solid line) and dwarfs (dashed line) taken from Bessell and Brett (1988).

For comparison, Table 2.8 shows our derived values for $\log T_{eff_*}$ & $\log L_*$ and rough M_* & age for the Bouvier and Appenzeller (1992) selected stars against the published results in that study taken from their HR diagram, which is reproduced in Fig.2.13.

ID	SpT	T_{eff_*} (K)	$\log L_*(L_\odot)$	$M_*(M_\odot)$	$\log g_*$	$(J-H)_{obs}$	$(J-H)_{int}$	$(V-R)_{int}$	A_J
GSC6798−35	G1	5875	0.752	1.6	3.92	0.62	0.31	0.52	0.96*
GSC6798−91	G0	5943	0.467	1.3	4.14	0.62	0.31	0.50	0.97*
RXJ1623.8−2341	K5	4406	0.213	1.2	3.84	1.00	0.61	0.99	1.19*
RXJ1620.7−2348	K4	4540	−0.188	1.1	4.25	0.73	0.58	0.92	0.45
RXJ1621.4−2312	K7	4150	−0.269	0.9	4.09	0.91	0.66	1.11	0.75
GSC6793−569	K1	4989	−0.044	1.1	4.27	0.69	0.48	0.69	0.65
GSC6793−868	M1	3665	−0.412	0.45	3.72	0.69	0.68	1.39	0.03
GSC6793−562	F7	6398	−0.309	1.25	5.03	0.27	0.29	0.45	0.06
GSC6793−797	K4	4540	−0.108	1.2	4.21	0.67	0.58	0.92	0.28
GSC6793−994	G4	5637	0.026	1.1	4.42	0.60	0.33	0.54	0.83
GSC6793−806	M1	3665	0.204	0.45	3.10	1.05	0.68	1.39	1.12*
GSC6213−933	F5	6653	−0.085	1.35	4.90	0.28	0.23	0.40	0.17
GSC6214−2288	G4	5637	−0.799	1.0	5.20	0.36	0.33	0.54	0.10
GSC6213−1186	G0	5943	−0.236	1.15	4.79	0.38	0.31	0.50	0.23
GSC6214−2384	K0	5152	0.015	1.1	4.27	0.57	0.45	0.64	0.37
GSC6214−14	F2	7047	−0.307	1.4	5.24	0.24	0.17	0.35	0.21
GSC6214−1115	F6	6531	−0.079	1.3	4.85	0.30	0.26	0.42	0.11
GSC6794−537	K2	4842	0.046	1.3	4.20	0.70	0.50	0.74	0.61
GSC6215−271	F5	6653	−0.284	1.3	5.08	0.41	0.23	0.40	0.54
GSC6215−538	K0	5152	−0.483	0.9	4.68	0.48	0.45	0.64	0.10
GSC6794−337	K1	4989	0.106	1.3	4.20	0.64	0.48	0.69	0.48
ROXs5	K7	4150	−0.186	0.9	4.01	0.96	0.66	1.11	0.91
ROXs30c	K4	4540	0.529	1.45	3.66	1.17	0.58	0.92	1.82*
ROXs44	K3	4688	0.635	1.7	3.68	1.00	0.54	0.84	1.37*
ROXs47a	K2	4842	0.586	1.9	3.83	0.90	0.50	0.74	1.21*
ROXs42c	K6	4276	0.380	1.0	3.54	0.85	0.64	1.05	0.63
ROXs39	K5	4406	0.103	1.2	3.95	0.82	0.61	0.99	0.63
ROXs33	G0	5943	1.624	3.0	3.35	1.25	0.31	0.50	2.89*
ROXs45f	K7	4150	−0.396	0.9	4.22	0.70	0.66	1.11	0.13
ROXs29	K4	4540	0.383	1.45	3.80	0.77	0.58	0.92	0.59
ROXs21	M2	3524	−0.144	0.375	3.30	0.79	0.67	1.50	0.39
ROXs6	K6	4276	0.514	1.0	3.41	1.01	0.64	1.05	1.13*
ROXs9a	M0	3837	0.556	0.575	2.94	1.17	0.70	1.28	1.45*
RXJ1625.2−2455	M0	3837	0.217	0.5	3.21	1.01	0.70	1.28	0.97*
ROXs3	K3	4688	−0.131	1.125	4.36	0.73	0.54	0.84	0.59

Table 2.7: Summary of derived parameters for T Tauri sample; spectral type, effective temperature, log luminosity, stellar mass, log surface gravity, extinction in J band and spectral colours (intrinsic & observed (J-H) and intrinsic (V-R)). See body text for details regarding derivation methods. An asterisk marked beside extinction values (A_J) indicate stars strongly effected by reddening due to dust and have had their magnitudes, and thus luminosities, corrected accordingly.

Small discrepancies can be justified by accumulated differences in conversion tables, evolutionary tracks and isochrones used in addition to the crude method of estimation of age and mass (read by eye of the published graphs). Four targets have distinctly different mass and age values. ROXs3 & ROXs47a have noticeable different effective temperatures whereas ROXs44 has two different values for luminosity in the two results. Of course these stars are variable stars so the fundamental parameters used to determine T_{eff} and L_* could have been different at the different observational times. The final target, ROXs5, has similar effective temperature and luminosity in the two studies however comes out with quite different ages, this appears to be due to variations in the isochrones plotted on the HR diagrams and used to estimate age. Even with the discussed mis-matching results the broad location of the Bouvier and Appenzeller (1992) and the T Tauri sample presented here on the HR diagram is similar to that of T Tauri stars of the Taurus-Auriga association, where the T Tauri type stars were first identified.

	Hastie (2006)				Bouvier & Appendzeller (1992)			
ID	$\log T_{eff_*}$	$\log L_*$	$M_*(M_\odot)$	Age (Myrs)	$\log T_{eff_*}$	$\log L_*$	$M_*(M_\odot)$	Age (Myrs)
ROXs3	3.67	−0.13	1.125	10.0	3.59	−0.20	0.525	2.0
ROXs5	3.62	−0.19	0.9	5.0	3.60	−0.21	0.55	2.0
ROXs6	3.63	0.51	1.0	0.8	3.62	0.38	1.125	0.8
ROXs9a	3.58	0.5 6	0.575	0.2	–	–	–	–
ROXs10b	–	–	–	–	3.73	1.20	2.3	0.9
ROXs21	3.55	−0.14	0.375	1.0	3.56	−0.20	0.4	0.8
ROXs29	3.65	0.38	1.45	2.0	3.62	0.15	1.25	2.0
ROXs30c	3.65	0.53	1.45	1.0	3.66	0.00	1.2	8.0
ROXs33	3.77	1.62	3.0	1.0	3.77	1.35	2.3	2.0
ROXs39	3.64	0.10	1.2	3.0	3.645	0.30	1.4	2.0
ROXs42c	3.63	0.38	1.0	1.0	3.62	0.40	1.25	0.8
ROXs44	3.67	0.64	1.7	1.0	3.68	0.30	1.4	4.0
ROXs45f	3.61	−0.40	0.9	10.0	3.60	−0.66	0.6	9.0
ROXs47a	3.68	0.56	1.9	3.0	3.60	0.20	0.75	0.7

Table 2.8: Summary of values published by Bouvier and Appenzeller (1992) for comparison with our results. Effective temperature and luminosity values are quoted in there papers however mass and age values have been read 'by-eye' from their published HR diagram, as with this study. The age and mass of these X-ray emitting members of the ρ Oph cloud are very similar to those of T Tauri stars first discovered in the Taurus-Aurigu association (Bouvier and Appenzeller 1992).

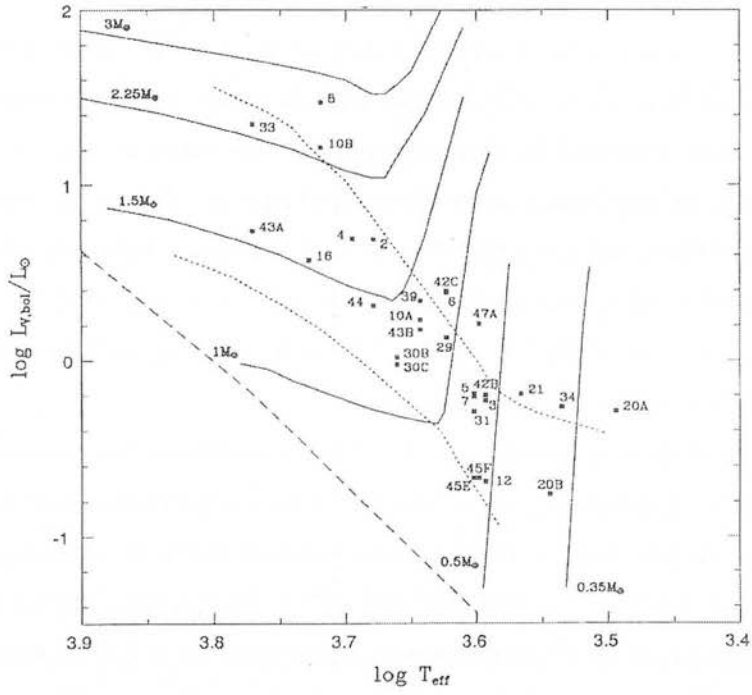

Figure 2.13: Reproduction of HR diagram from Bouvier and Appenzeller (1992) showing the distribution of their identified X-ray emitting cloud members. Stars are labelled with their given ROXs numbers. Solid lines are theoretical PMS evolutionary tracks for stars with a mass between 0.35 and $3M_{\odot}$. The dashed line is the theoretical zero-age main sequence locus and the dotted lines are the theoretical isochrones corresponding to an age of 10^6 yr (upper line) and 10^7 yr (lower line).

2.7.5 Determining Spectral Type

Seven of our programme stars do not have published spectral types so a rough estimation had to be undertaken to enable the calculation of the stellar parameters. As a starting point we took the (J-H) colour index for the each star from their published 2MASS magnitude. From here it was a simple iterative process of plotting the target spectra against the appropriately processed synthetic spectra from the library of Coelho et al. (2005), see §2.8 for details of the synthetic spectra and the reduction process, and judging by-eye which spectral type give the best fit to the object spectra. Table2.9 gives the spectral type as derived from the 2MASS colours (via conversion tables of Bessell and Brett 1988) and the resultant spectral type estimated from the synthetic spectra fitting. As anticipated where the spectral type has changed it is towards a 'hotter' spectral class, indicating that the observed colours are influenced by dust extinction making the star appear cooler. The seven target stars with their 'best fit' synthetic spectra can be seen in Fig.2.14, the solid line is the object spectra and the synthetic spectra have been scaled for plotting purposes.

An accurate method of spectral classification of PMS should consider line ratios or line equivalent widths, for example the ratio of the CaII K line to the Balmer lines or other metallic lines such as TiO, however this was not possible given the spectral range and resolution of our science spectrum (Delgado et al. 1999). Though very simplistic this method is adequate for our needs, as discussed comprehensively in §2.7 an error in spectral type classification, even one full spectral class, does not adversely effect the selection of synthetic spectra for subtraction of the photospheric contribution which is now discussed in §2.8.

2.8 Subtraction of Photospheric Contribution

Determing the contribution from the active chromosphere to the CaII H & K lines involves subtraction of the photospheric component. Methods previously used to estimate the underlying photospheric contribution include; reconstruction of the absorption line profile below the emission peaks by extrapolating the line wings to the

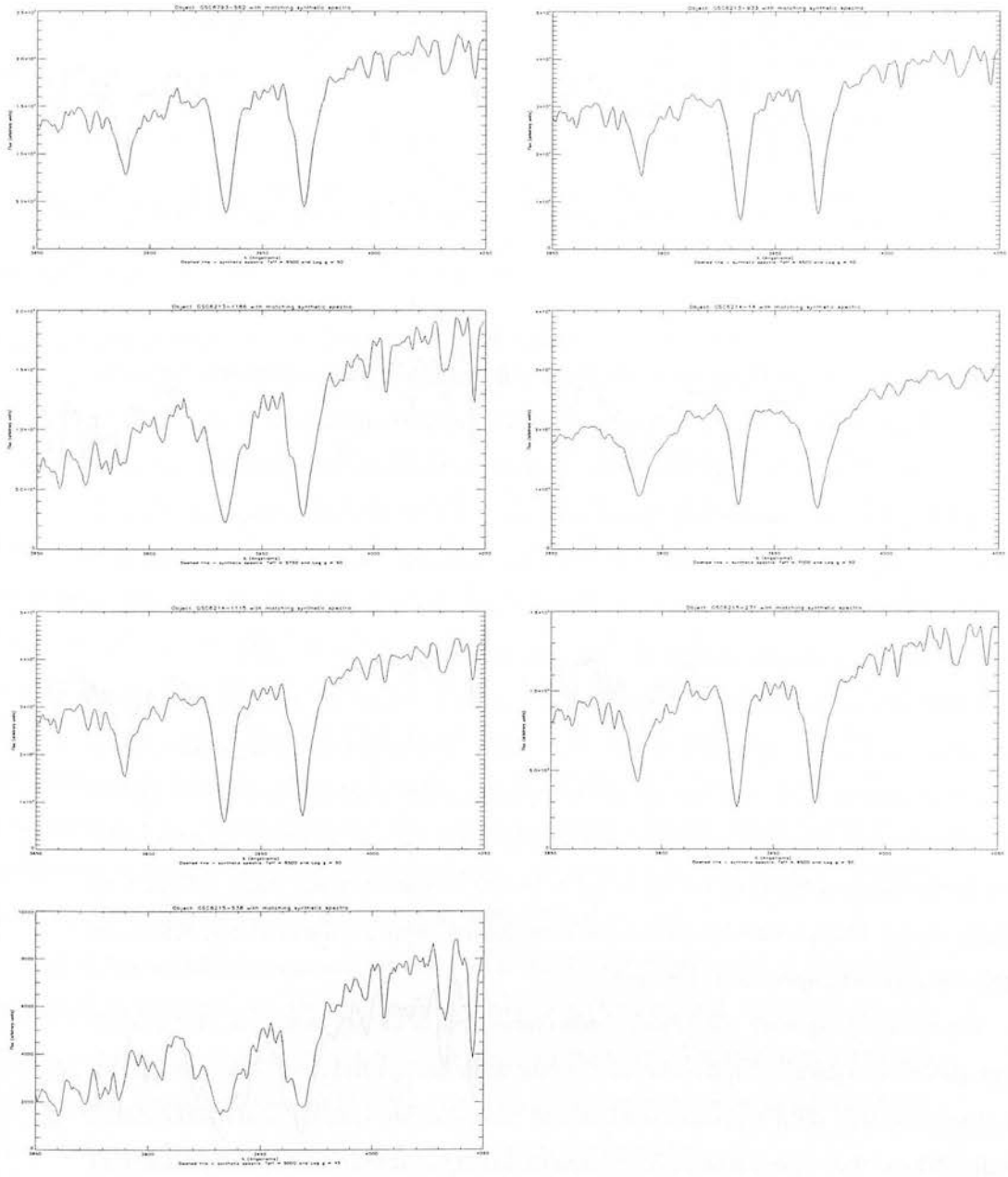

Figure 2.14: CaII H & K lines for each of the seven 'missing' spectral type programme stars. Each have the corresponding 'best fit' synthetic spectra overlaid in a dashed line, determined by-eye judgement through an iterative process.

ID	2MASS (J−H)	Sp T from (J−H)	Resultant Sp T
GSC6793−562	0.265	F7	F7
GSC6213−933	0.284	F7	F5
GSC6213−1186	0.381	G7	G0
GSC6214−14	0.235	F5	F2
GSC6214−1115	0.295	F8	F6
GSC6215−271	0.405	G8	F5
GSC6215−538	0.481	K1	K0

Table 2.9: Short summary of the 'Missing Spectral Type' T Tauri stars in the Upper Sco association. Given are the 2MASS (J-H) colour index and according spectral types, and in column 4 the 'resultant' spectral type determined after a series of iterative comparisons with synthetic spectra.

line centre (Fernandez-Figueroa et al. 1994), subtraction of a photospheric contribution obtained from a pure radiative equilibrium calculation (Linsky et al. 1979), or subtraction of synthesized stellar spectrum constructed from reference stars of similar spectral type and luminosity class to the active target objects (Montes, de Castro, Fernandez-Figueroa and Cornide 1995; Montes, Fernandez-Figueroa, de Castro and Cornide 1995). Libraries of synthetic stellar spectra, both empirical and theoretical libraries have improved dramatically in recent years (Coelho et al. 2005).

Taking the lead from Montes, de Castro, Fernandez-Figueroa and Cornide (1995) we have opted to use synthetic spectra to obtain the photospheric component of our observed spectra. However, we are not completing a full subtraction method, rather we will quantify the CaII 'emission' in the target spectra and synthetic spectra independently then subtract the values to get a 'purely chromospheric' value (see §2.9 for clarification). This process by-passes the need to flux calibrate the stellar spectrum or scale the synthetic spectrum to match.

The synthetic spectra we have chosen come from a library generated by Coelho et al. (2005) who present high resolution synthetic stellar spectra from 300nm to 1.8μm, in steps of 0.02Å, with solar and α-enhanced composition. Coelho et al. (2005) detail in depth how their spectra were computed including information on; computation of atomic lines, selection of model atmospheres, adopted solar abundances, line opacity lists employed and damping constants used. It is not necessary to report the details here however it should be noted that the solar parameters they used were

$T_{eff_\odot} = 5770K$, $\log g_\odot = 4.44$, microturbulent velocity $v_t = 1.0 kms^{-1}$ and the adundances from Grevesse and Sauval (1998). The Coelho et al. (2005) library present both normalised and absolute flux formats for each spectrum and they cover the following stellar parameter space:

- **effective temperature range** $3500 \leq T_{eff} \leq 7000K$ in 250K steps

- **surface gravities** $0.0 \leq \log g \leq 5.0$ in 0.5 steps

- **metallicities** [Fe/H] = -2.5, -2.0, -1.5, -1.0, -0.5, 0.0, 0.2, 0.5

- **chemical compositions** $[\alpha/Fe]$ = 0.0 and 0.4 where α-elements are considered to be O, Ne, Mg, Si, S, Ca & Ti

The synthetic spectra from Coelho et al. (2005) cover a much larger spectral range than we require so the first step was to extract the block of spectra around the CaII doublet from 3850Å to 4050Å. It is important to match the synthetic spectra and target object in terms of detector pixel scale and spectral resolution. The CCD resolution of the 6dF with our instrumental set up is 0.77466Å/pixel whereas the synthetic spectra's 'CCD resolution' is equivalent to the wavelength steps the code was generated with, 0.2Å/pixel. To match the 6dF CCD resolution the synthetic spectra were rebinned, the 200Å extracted spectra were rebinned onto 250 elements to give an effective CCD resolution of 0.8Å/pixel. Secondly, the synthetic spectra must be smoothed to lower resolution to match the 6dF spectral resolution. To achieve this the synthetic spectra were Gaussian smoothed with a Gaussian with FWHM of 1.5Å.

Figs.2.15 and 2.16 show examples of the CaII spectra for programme stars GSC6793-994 and GSC6798-35 with the modified synthetic spectra overlaid. Since we are not concerned with continuum flux values we opted to use the normalised flux extension of the synthetic spectra files and for the purpose of the plots the synthetic spectra have been scaled such to overlay the target spectra on the same scale.

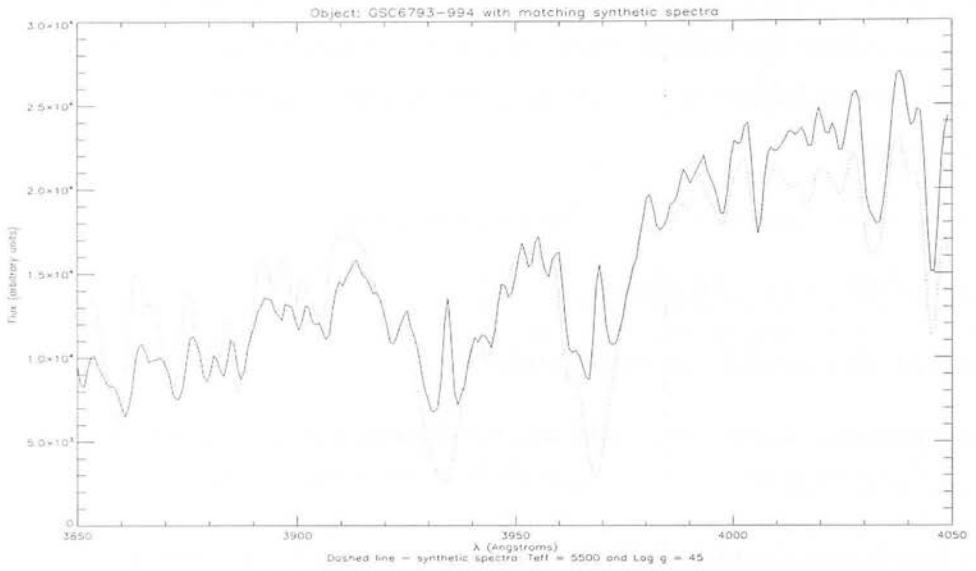

Figure 2.15: GSC6793−994 spectra with corresponding synthetic spectra overlaid (dashed line). Clearly demonstrates the comparison of a star with chromospheric magnetic activity where the CaII H & K line cores are in emission and a star with the same spectral type but a quiet chromosphere.

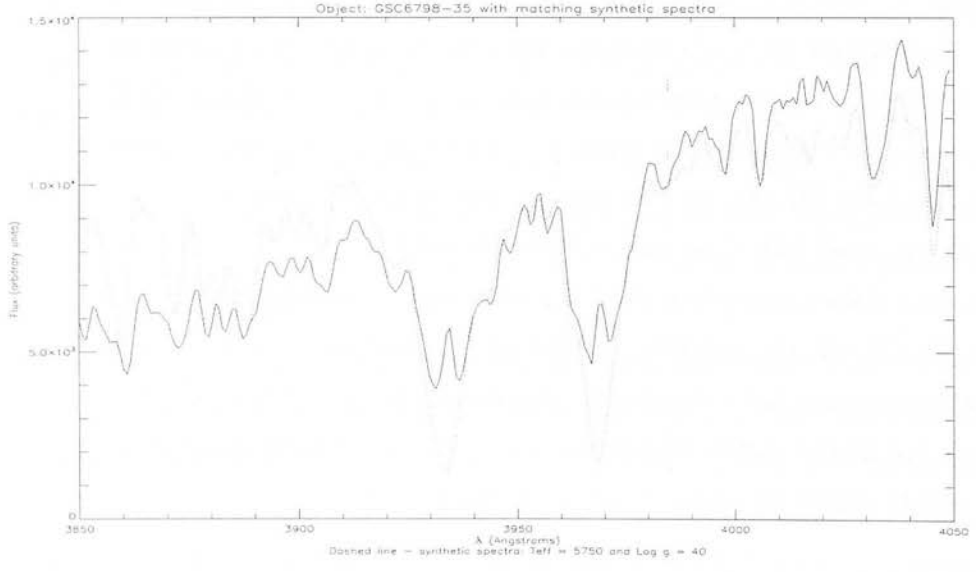

Figure 2.16: GSC6798−35 spectra with corresponding synthetic spectra overlaid (dashed line). The synthetic spectra has been scaled to facilitate plotting on the same axis with the object spectra.

2.9 Quantifing the CaII Emission

2.9.1 Mount Wilson S Index

To be able to make constructive use of the spectral data obtained there needs to be a way of quantifying the amount of excess CaII emission over that of a quiet chromosphere. This issue was first tackled by a survey led by Dr. O. C. Wilson of the Mt. Wilson Observatory (MWO) while measuring the chromosphere H & K fluxes of a number of main-sequence stars using the coudé scanner on the 2.5m telescope as a two-channel photometer (Wilson 1968). The first channel was set to have a 1Å bandwidth and centred on either the CaII H or K line, with a precision of ± 0.02Å, while the second channel measured the combination of two 25Å bands on the continuum, separated by 250Å and located symmetrically either side of the H/K region. In the late 1970s the CaII H & K survey was deemed so vital that a new dedicated four-channel device which included the essential features of Wilson's method was constructed (Vaughan et al. 1978). The new instrument was an off-plane flat-field Ebert spectrometer equipped with an exit multi-slit and a chopper allowing the fluxes of four spectral band passes to be measured sequentially at a chopping frequency of ~ 30Hz with a single detector. The new photometer was mounted at the $f/16$ Cassegrain focus of the Mt Wilson 60-inch telescope. The MWO H−K Project was continued under the direction of Sallie L. Baliunas until 2003. Since 1994 the Solar-Stellar Spectrograph (SSS) project has started observing the Sun and Sun-like stars using the 42 inch telescope at Lowell's Anderson Mesa dark-sky observing site to complement the MWO data set.

In addition to starting the CaII H & K targeted survey Wilson also defined the procedure labelled the 'S-index' to make the quantitative measurement of the received flux in the emission cores (Wilson 1968), taking the lead from a number of different studies we adopted the 'S-index' as defined by Vaughan et al. (1978). The stellar counts are reduced to flux indices; φ_H, φ_K and S such that:

$$\varphi_H \equiv \frac{\mathrm{N_H}}{\mathrm{N_V} + \mathrm{N_R}} \tag{2.13}$$

$$\varphi_K \equiv \frac{N_K}{N_V + N_R} \tag{2.14}$$

$$S \equiv \varphi_H + \varphi_K \tag{2.15}$$

or

$$S \equiv \frac{N_H + N_K}{N_V + N_R} \tag{2.16}$$

where N_H, N_K, N_V and N_R represent the number of counts, background corrected, in the H, K and reference bands on the violet and red sides of the CaII doublet region. Vaughan et al. (1978) had observing windows with central wavelengths and bandwidths as given in Table 2.10. Our windows have the same centre wavelengths as Vaughan et al. (1978) but due to the resolution of our spectra the width of the CaII windows are not the same, the bandwidths we have adopted are also given in Table 2.10. Fig.2.17 shows the spectra for target star GSC6798−35 observed on the night of April 23rd, 2003 with the brackets for the integration of the S line index overlaid. The dashed spectrum is the scaled matching synthetic spectrum. These plots clearly show that the window sizes have been selected to comfortably include to CaII H & K lines in both the target and synthetic spectra. Since we are not looking to compare our derived S indices with any other studies it is not vital for us to have exactly the same observational set-up and reduction procedure, if we did wish to compare results with other published results the indices would need to be transformed appropriately.

	Hastie		Vaughan et al. (1978)	
	Central λ (Å)	Bandwidth (Å)	Central λ (Å)	Bandwidth (Å)
CaII H-band	3968.5	8	3968.5	1
CaII K-band	3933.7	8	3933.7	1
Ref R-band	4001	20	4001	20
Ref V-band	3901	20	3901	20

Table 2.10: Central wavelength and bandwidth (Å) of the 'windows' placed over the CaII H & K lines and reference windows either side of the doublet for calculating the S index. Window values for the study presented here and the original Mt Wilson Observatory H−K project, Vaughan et al. (1978).

Figs.2.18 & 2.19 shows a timeline of the CaII H & K line for GSC6794-537, a K2 weak-line T Tauri star in Upper Sco association which has sufficient magnetic activity to

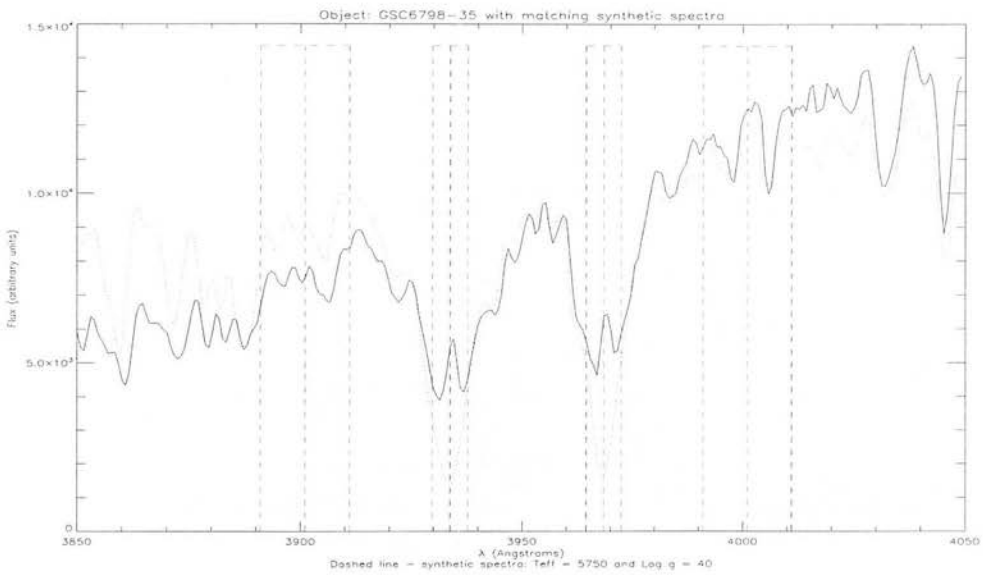

Figure 2.17: The spectra of GSC6798−35 showing the windows, including central wavelength, for calculating the S-index overlaid in dashed lines. The H-band & K-band lie over the CaII H & K lines respectively whereas the reference R-band is the the right of the CaII doublet and the reference V-band to the left.

demonstrate emission cores in the CaII absorption lines. The timeline runs from top left hand plot to bottom right, left to right, starting on Fig.2.18 and continuing onto Fig.2.19. The extent of the variability in the strength of the emission cores with respect to the continuum is not dramatic but does vary over the days. Given that T Tauri stars have typical rotational periods between 3 and 12 days, the 43 day period the 12 observations span could cover anything between 3 and 14 full revolutions of the stars. The resultant photospherically corrected S index for this target indicates the small variation (Δ S index = 0.048), but the level of CaII emission indicates substantial activity. One possible scenario is that a substantial portion of the stellar surface is covered with long living active regions, giving a strong CaII emission which is non-varying with rotation on short time scales. Further discussion on this can be found in Chapter 3.

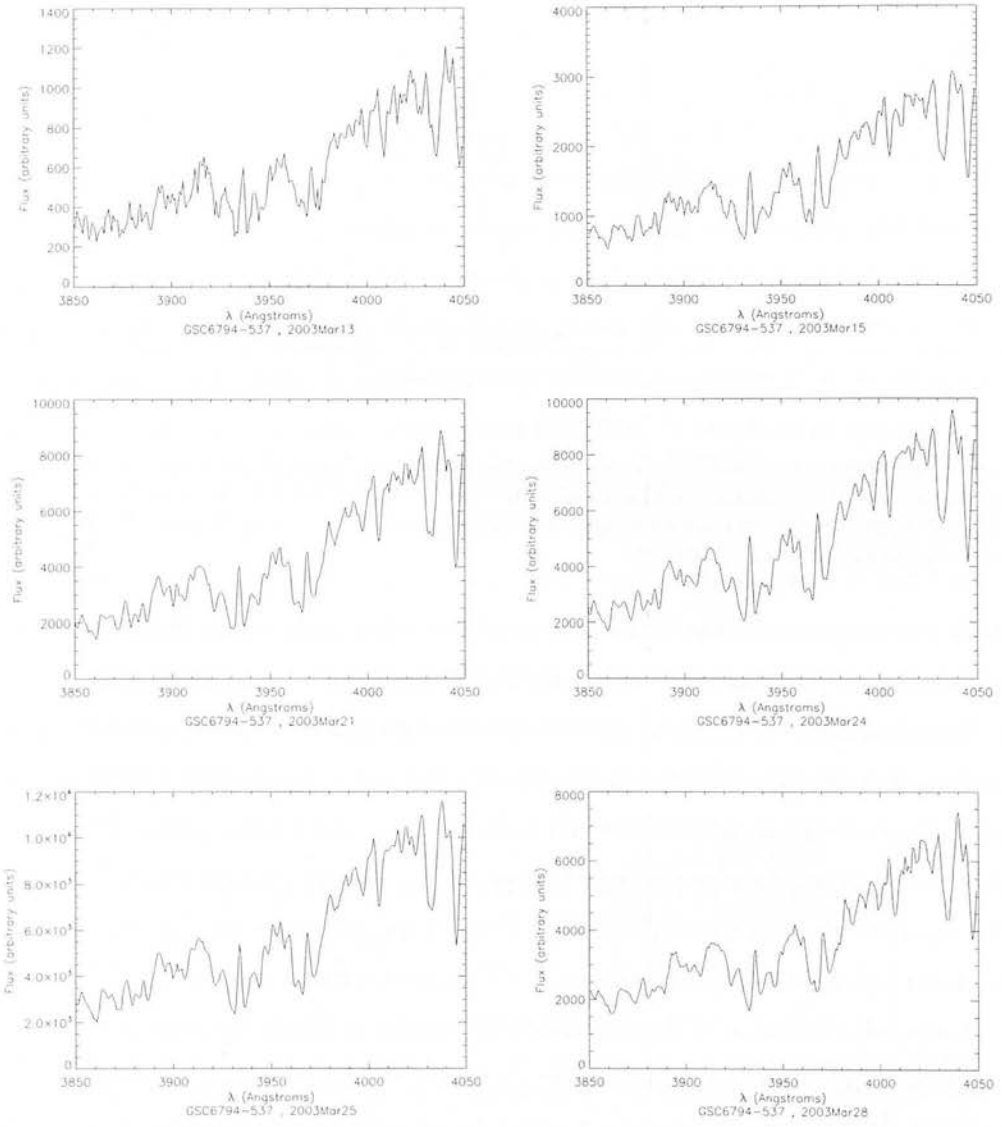

Figure 2.18: Timeline series of spectra of the CaII doublet on target GSC6794−537, starting at March 13th at top left hand plot then running left to right, continuing on Fig.2.19 to end at bottom right with April 25th. Date of each observation is underneath the individual plots.

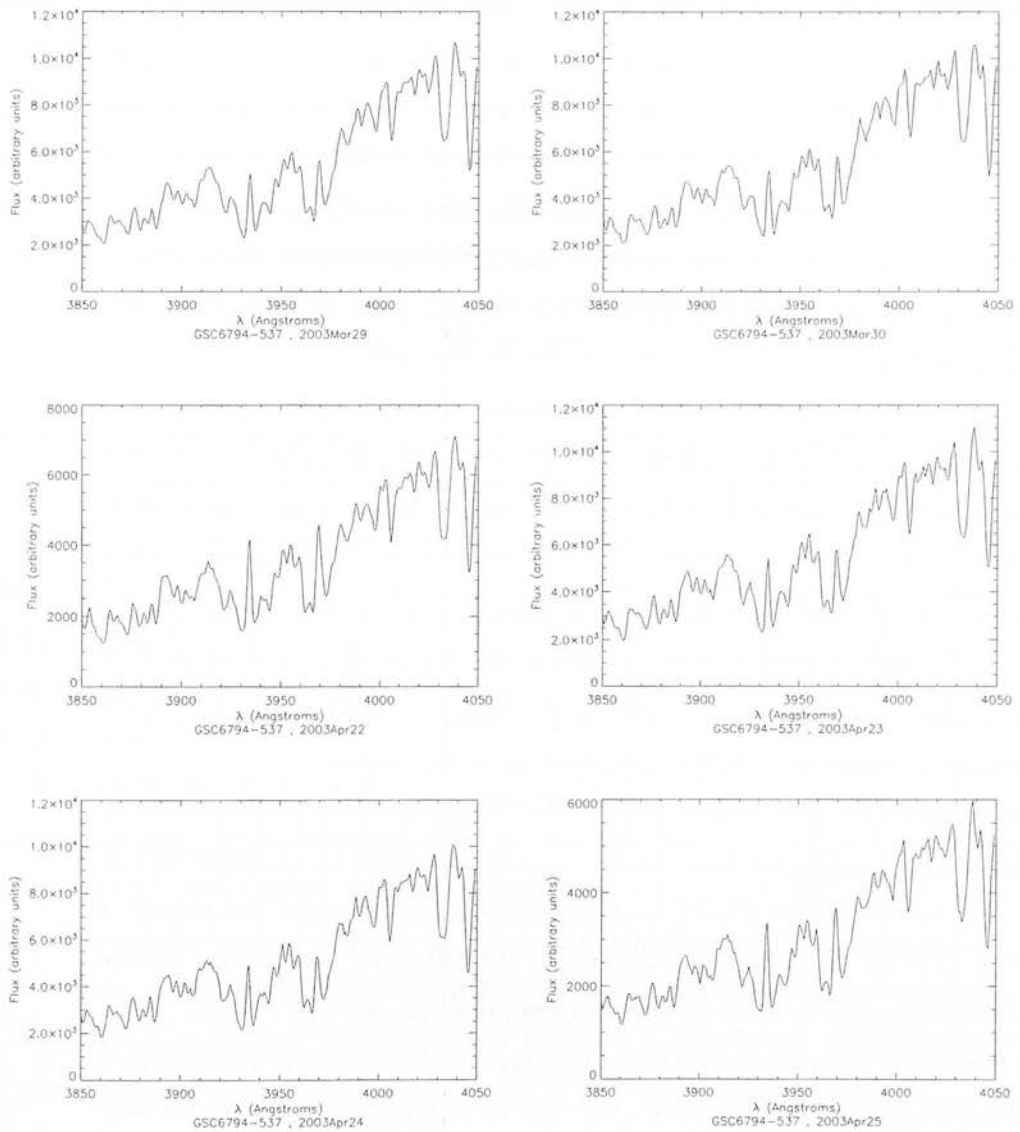

Figure 2.19: As Fig.2.18

2.10 Testing the Selection of the Synthetic Spectra

As fully outlined in §2.7 – 2.9, in order to quantify the CaII H & K emission of the observed stars the photospheric contribution to the spectra is subtracted using synthetic, chromospherically quiet spectra. As discussed, the choice of the synthetic spectrum requires selecting a metallicity, surface gravity and effective temperature for the photospheric spectra from a grid of models. For this study we have assumed solar metallicity values and determined the surface gravities and effective temperatures as described in §2.7. However, to verify this selection method was appropriate we took a single, good quality target and calculated the corrected S index values with metallicities, surface gravities and effective temperatures one grid point on either side of the original parameters.

Target GSC6798−35, a G1 weak-line T Tauri, was re-analysed for the nights of April $23^{\rm rd}$ and April $24^{\rm th}$, both of these nights had good data with high signal to noise. The determined stellar parameters for GSC6798−35 were; effective temperature = 5875K and surface gravity of $\log {\rm g} = 3.92$ which led to the selection of a synthetic spectra with parameters; [Fe/H] = 0.0, effective temperature = 6000K and surface gravity $\log {\rm g} = 4.0$. To probe the effect of altering the synthetic spectra the corrected S index was calculated for all permutations using; metallcity values [Fe/H] = -0.5, 0.0, 0.2; effective temperatures = 6000, 5750, 5500K and $\log {\rm g} = 3.5, 4.0, 4.5$.

It was found on the data from both nights that changing any of the parameters by one grid point changed the resultant S index by at the most 10%, i.e. changing surface gravity from 4.0 to 4.5 with [Fe/H] = 0.0 and $T_{\rm eff} = 6000$K changed the derived S index from 0.115331 to 0.108637, a difference of 0.00669 ($\sim 6\%$). A similar change was found when changing both effective temperature and metallicity by a grid point. Though these changes in resultant S index may seem significant what is vital to note is that the synthetic spectra is selected only once for any given object and the same photospheric contribution subtracted from each observed spectra for that target. This effectively introduces a systematic error which effects each data point the same way. However, this does not effect the ultimate goal and concluding results of this study, namely the correlation between the CaII variations and the photometric variations. A systematic shift of the S index values does not change the slope of any correlations.

2.11 Correlation between CaII & light variations

The key plot for the study presented here is that showing the correlation between the variation in CaII flux and variation in photospheric flux. To generate the most useful resultant linear fit it is important to have both parameters in either linear or logarithmic quantities. Currently the CaII variation is described by a line ratio, a linear quantity, whereas the light variation is given in V band magnitudes, a logarithmic value. The easiest solution is to convert the magnitude values into counts collected on the detector, a linear value to correspond with the spectroscopic quantity. The conversion from stellar magnitude to detector counts is given by:

$$\mathrm{V} = -2.5\log(\mathrm{counts}) + \mathrm{z_p} \tag{2.17}$$

where, z_p, is the magnitude zeropoint. The 'zeropoint' is the apparent magnitude of a star which results in one ADU (Analog-to-Digital Unit) of detected flux at zero airmass. For the Automated Patrol Telescope this is found to be $\simeq 22.5$ in the V band (Hidas 2005). At this stage only the variation in light is important, thus for each target the photospheric counts are divided by the mean counts, i.e. $\mathrm{counts}/\langle\mathrm{counts}\rangle$, to give a distance independent variable. The S index as calculated here is inherently distance independent.

To quantify the level of correlation between the CaII variation and photospheric variation, if any, a linear regression is fitted to the data. Since our data has significant errors on both axes a linear regression algorithm which can deal with error in both variables must be used, a normal least squares algorithm only allows errors in the y axis. The NASA 'astrolib' IDL function FITEXY is well suited for this as it returns a linear least-squares approximation in one-dimension when both the x and y data have errors. It returns the values of A, the intercept, and B, the slope, such that:

$$\mathrm{A_{intercept}} + \mathrm{B_{slope}} * \mathrm{x} \simeq \mathrm{y} \tag{2.18}$$

The error in the measured magnitudes is the RMS of the measurements within each

night as supplied by the APT reduction pipeline:

$$\sigma_{\rm photo} = \pm\sqrt{\frac{\sum_{\rm i=1}^{\rm N_{expP}} {\rm V_i} - \langle {\rm V} \rangle}{\rm N_{expP} - 1}} \tag{2.19}$$

where $\rm N_{expP}$ is the number of photometric observations taken on each target each night. The plotted errors for the calculated S indices are:

$$\sigma_{\rm Sindex} = \pm\sqrt{\frac{\sum_{\rm i=1}^{\rm N_{nights}} \sigma_{\rm i}^2}{\rm N_{nights} - 1}} \div {\rm N_{expS}} \tag{2.20}$$

where

$$\sigma_{\rm i} = \sqrt{\frac{\sum_{\rm j=1}^{\rm N_{expS}} ({\rm S_j} - \langle {\rm S_j} \rangle)^2}{\rm N_{expS} - 1}} \tag{2.21}$$

$\rm N_{expS}$ is the number of spectroscopic observations taken of each target each night and $\rm N_{nights}$ is the number of nights each target was observed. Each measurement of S index for a given target over the observational period is a ratio measurement on the same star normalised to the same exposure time with the same instrumental set up. Smoothing over the total number of nightly observations gives a better estimation of the genuine noise in a single observation. Photometric measurements suffer from a greater number of noise sources than spectroscopic observations and is a direct measurement, hence the quoted $\sigma_{\rm photo}$ is the most appropriate estimation of noise in a single observation.

Our aim is to obtain the best estimate of a straight line fit to the correlation between the global variation due to the rotation of the star however by the very nature of the variation there is an important 'scatter' about any straight line fit. This is a real source of 'error' which contains real processes such as flaring, the sudden release of magnetic energy not related to the normal chromospheric emission as well as statistical variations in the ratio of dark spot area to chromospheric emission. The scatter may also include effects of short lifetime magnetic regions appearing or disappearing or short time scale changes to the patterns of active regions. This is all in addition to the

observational instrumental errors accounted for in the error bars. If this scatter is not taken into account the straight line fitting is weighted to any extreme points which are likely to be short time scale processes, such as flares, which mask the global rotational variations we are interested in. The noise due to the 'scatter', $\sigma_{\rm additional}$, is added to the observational error in the S index in quadrature such as:

$$\mathrm{Y_{sigma}} = \sqrt{\sigma^2_{\rm Sindex} + \sigma^2_{\rm additional}} \tag{2.22}$$

The degree of scatter is unknown and will vary target to target, the simplest way to constrain $\sigma_{\rm additional}$ is by iteration until the returned $\chi^2_{\rm fit}$ by the regression fit equals the number of measurements used for the fitting minus two, $\chi^2_{\rm fit} = \mathrm{N_{points}} - 2$. In order to make sure the best estimate of the smooth global correlation is obtained the data is now 'sigma clipped', such that any points with $\sigma_{\rm fit} > 2.5\langle\sigma_{\rm fit}\rangle$ where:

$$\langle\sigma_{\rm fit}\rangle = \frac{\sum_{\rm i=1}^{\rm N_{points}} |\mathrm{S_i} - \mathrm{S_{fit_i}}|}{\mathrm{N_{points}}} \tag{2.23}$$

Post sigma clipping the whole iterative process is repeated to find the final best straight line fit.

The night of the $12^{\rm th}$ of March had very poor seeing, $4-5''$, which badly effected the magnitude measurements. Also, a small handful of the other photometric measurements of any given target either have much larger error bars or are distinctly outwith the general trend of the variation, which could be attributed to flares or, in the case of classical T Tauri, hots spots due to accretion onto the surface from circumstellar debris discs. These individually selected points and all the measurements from the night of the $12^{\rm th}$ of March have been removed from the data sets before the linear regression line fitting.

Fig.2.20 graphically shows all the steps of the line fitting process using GSC6798−35 (a WTTS) as an example. The top two plots show all the CaII S index (left hand plot) and the V magnitude (right hand plot) against time. The single plot underneath is a demonstration of how the inclusion of $\sigma_{\rm additional}$ changes the fit, each dashed straight line is the linear fit at each iteration step of $\sigma_{\rm additional}$. The two plots on the third line

are the first pass at obtaining the linear fit, the left hand plot shows the pre-sigma clipped data set with two straight line fits over-plotted - the dash-dot-dot line is the fit when $\sigma_{\text{additional}} = 0.0$ which is strongly weighted to the out lying point at (1.008, 0.148) where the dashed line is the 'best fit' where $\chi^2_{\text{fit}} = \text{N}_{\text{points}} - 2$. The corresponding χ^2_{fit} plot is adjacent. The last two plots are the 'post-sigma' fits and corresponding χ^2_{fit} curve. The dashed straight line on the left hand plot is the final best estimate of a linear fit to the correlation and the dash-dot-dot straight line is the 'pre-sigma best fit' for comparison. In this example, the slope of the fit is negative indicating that as the star gets dimmer the CaII emission, i.e. the magnetic fields, gets stronger.

The following sections show the resultant plots with discussion for all the target stars organised by type; weak-line, classical T Tauri, binary or field stars. For each star four plots are give given; CaII S index vs time, V magnitude vs time, pre-sigma clipped data set with 'first fit' and initial 'best fit' overlaid and the final post-sigma clipped data set with the best straight line fine over plotted.

2.11.1 Weak-line T Tauri Sample

Out of the 35 target stars successfully observed spectroscopically and photometrically 17 are classified weak-line T Tauri stars. It has been anticipated form the outset that this method of analysing the chromospheric variation would work most cleanly on weak-line T Tauri candidates. Weak-line T Tauri star, also known as 'naked' T Tauri are largely free from both a circumstellar disk or strong stellar winds. This implies that the variation we see in the observations are not confused by accretion from the disk onto the surface, nor do we have to look through excess dust and debris around the star to see the chromosphere.

The process for finding the correlation between the CaII emission and the light variation was most successful with the WTTS targets, the majority (11 out of 16) of them resulted a negative linear correlation. Our expectation is for a negative slope to the linear fit as this implies that the star gets dimmer as the CaII emission gets stronger, or in other words the star gets dimmer as more active regions rotate into the observers

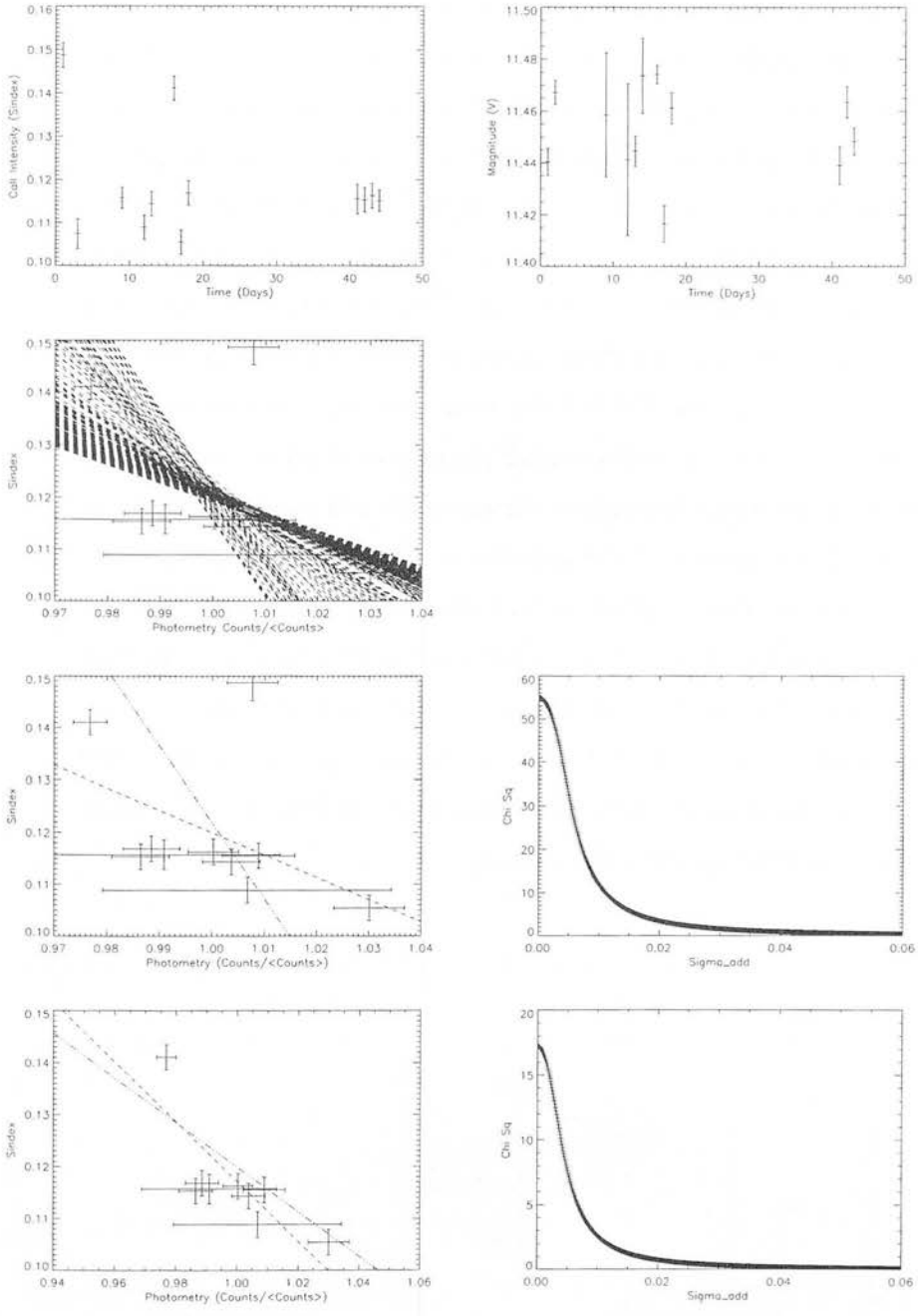

Figure 2.20: Resultant plots for WTTS GSC6798−35. Top left plot: CaII S index vs time. Top right plot: V magnitude vs time. Second left hand plot: Series of linear fits in steps of increasing $\sigma_{\rm additional}$ demonstrating the effect of this inherent scatter. Third left hand plot: Pre-sigma clipped data set with the 'first fit', $\sigma_{\rm additional} = 0.0$ (dash-dot-dot) and the initial 'best fit' (dashed). Second right hand plot: Pre-sigma clipped $\chi^2_{\rm fit}$ curve, 'best fit' is where $\chi^2_{\rm fit} = {\rm N_{points}} - 1$. Bottom two plots are as above for the 'post-sigma' clipped data set. Dashed line is the important final best linear fit to the correlation.

field of view. Of the five target WTTS which give a positive correlation only one target, ROXs3, has a large positive slope. The other four have $0.0 < \delta S/\delta V < 0.2$; this could indicate that we are viewing these stars near pole on and they have substantial active regions around the polar cap. For this situation, as the star rotates the area of the star seen by the observer does not change meaning no variations is emissions due to rotation would be seen. Small variations may be due to active regions changing size during the observing period. The classification of WTTS based on their H_α equivalent width is very good at selecting stars without accretion disks but it is not perfect, and recent studies show small fractions of WTTS may have inner disks which would give some accretion of matter on to the stellar surface (Padgett et al. 2006). Accretion results in hotspots, hotter than the photospheric surface which will affect the correlation between the CaII and V variations. If the accretion is substantial enough a positive correlation may be found. Target ROXs3 suffered from much weaker SNR than the other targets through out the observing run, either due bad transmission of the fibre or bad placement of the fibre on the target, so may not offer a robust result.

Where 'sigma clipping' was activated the majority of the points removed were from 'above the line'. These points could be due to short term flares which result in briefly heightened light intensity and CaII emission.

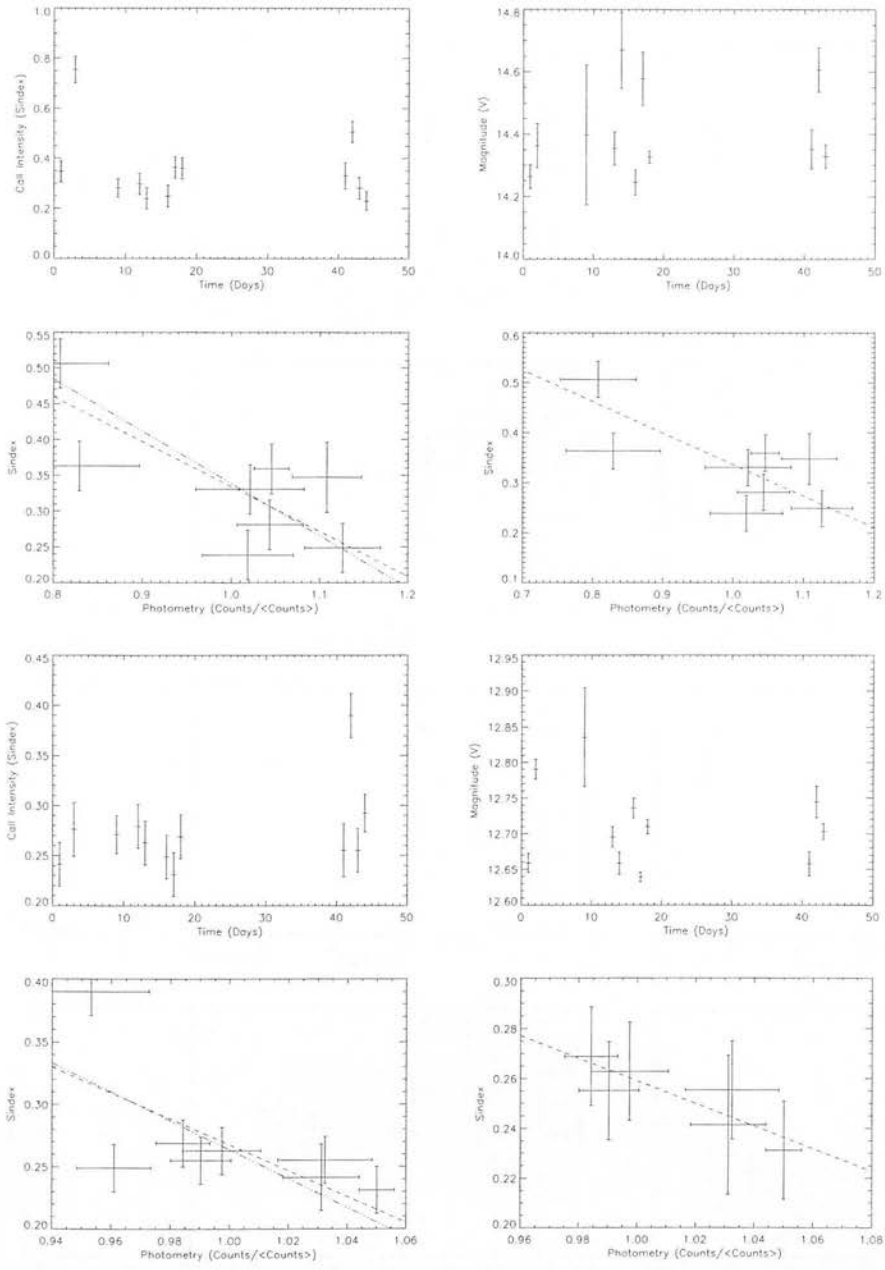

Figure 2.21: Top Four Plots: Resultant plots for WTTS RXJ1623.8−2341; CaII S index vs time, V magnitude vs time, pre-sigma clipped data with 'first fit' (dash-dot-dot) and initial 'best fit' (dashed line), post-sigma clipped data with final best linear correlation overlaid. Bottom Four Plots: As above for WTTS RXJ1620.7−2348.

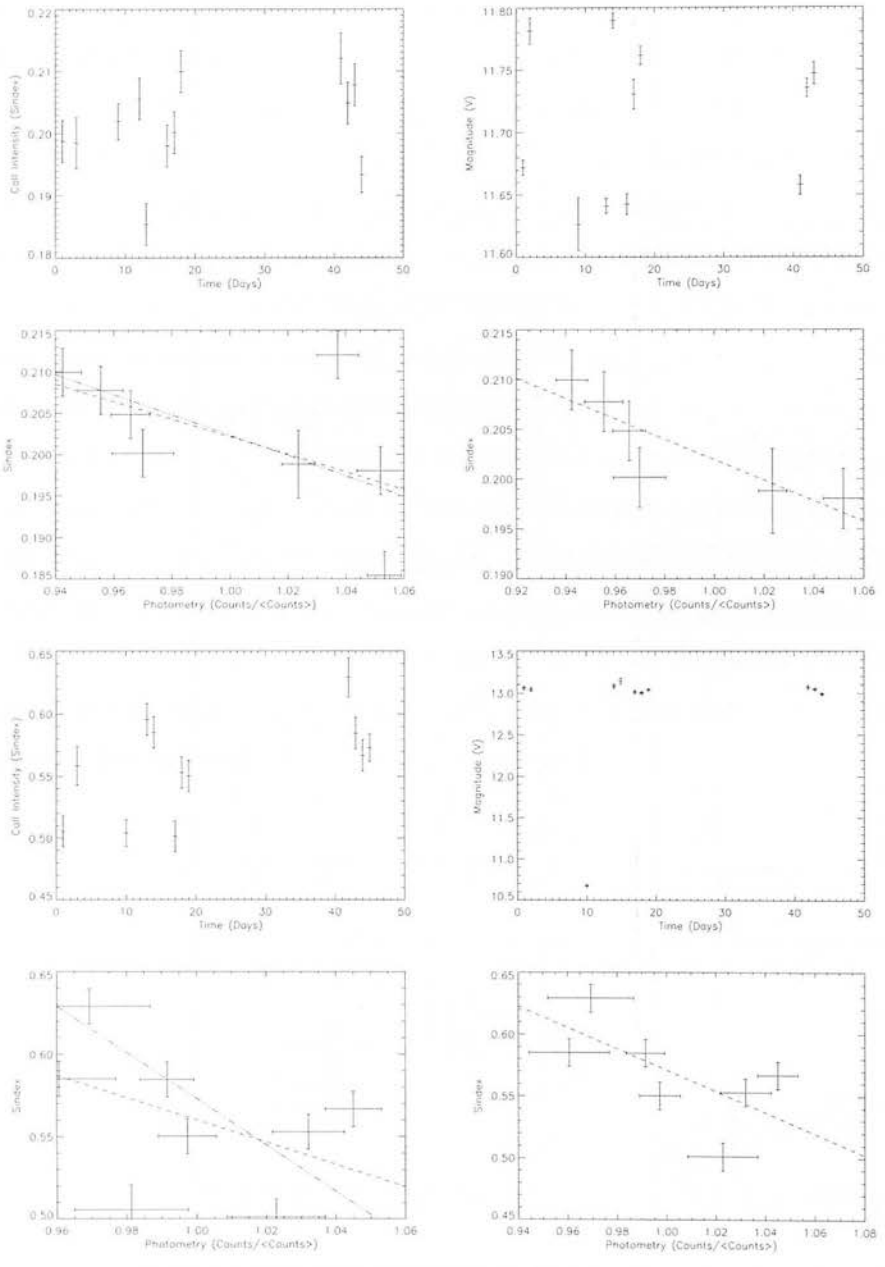

Figure 2.22: Top Four Plots: Resultant plots for WTTS GSC6793−569. Bottom Four Plots: Resultant plots for WTTS GSC6793−868.

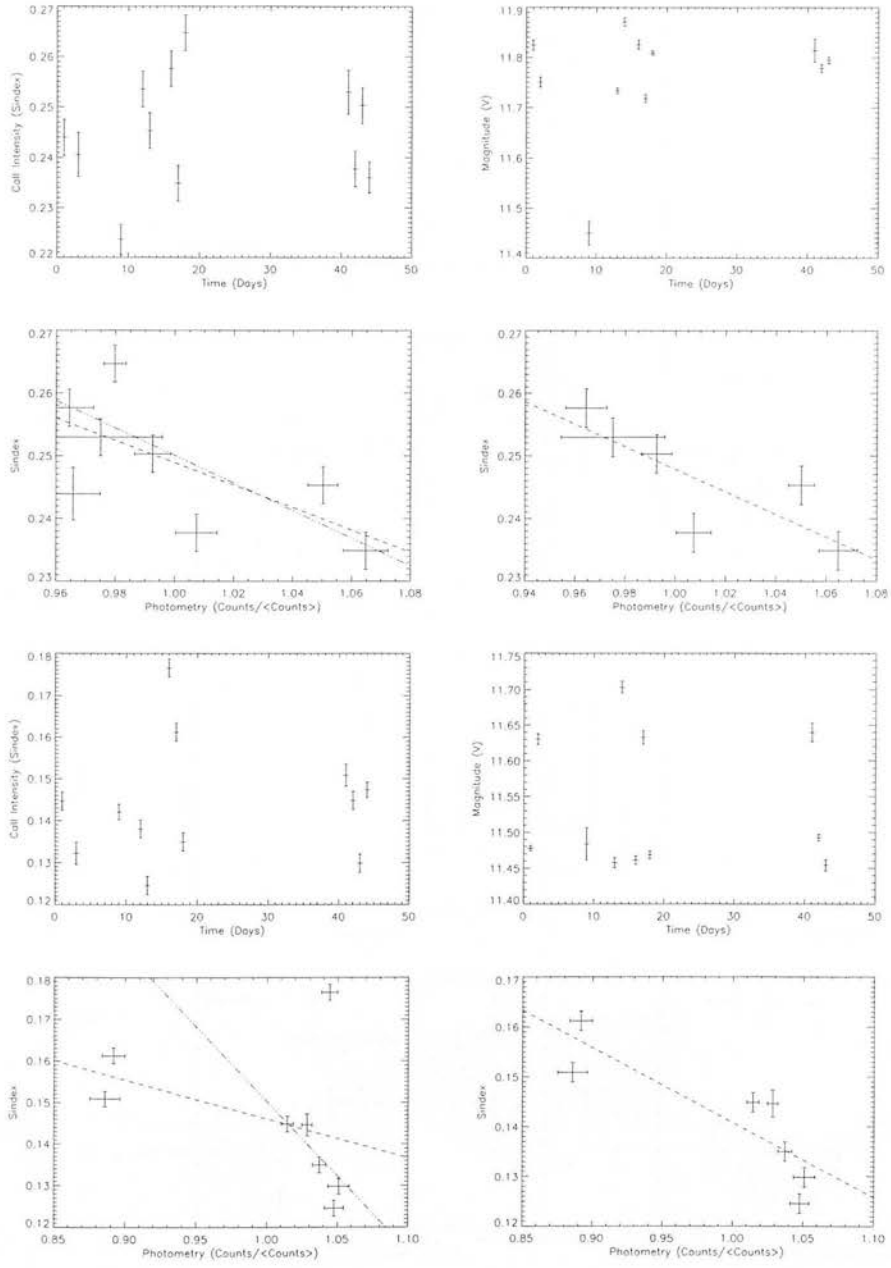

Figure 2.23: Top Four Plots: Resultant plots for WTTS GSC6793−797. Bottom Four Plots: Resultant plots for WTTS GSC6793−994.

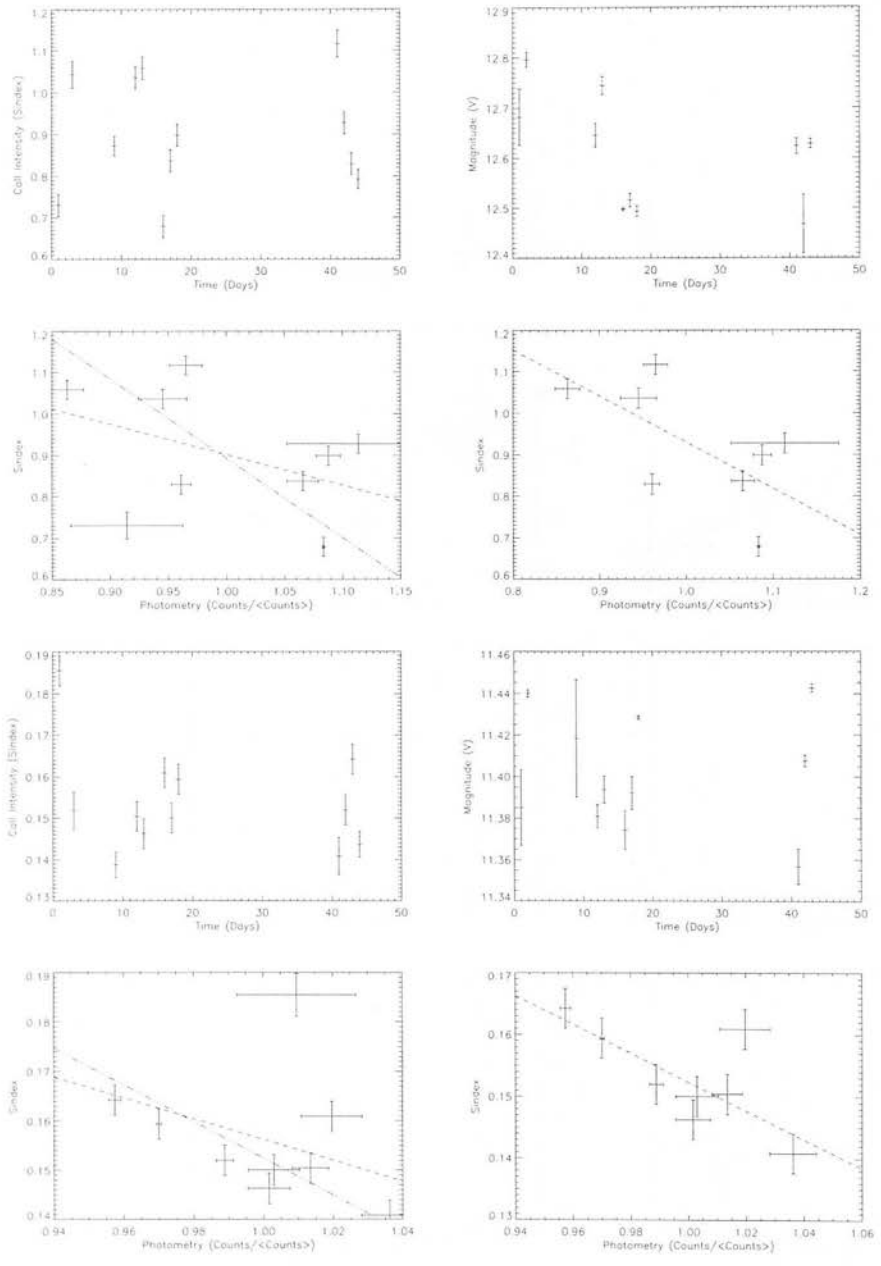

Figure 2.24: Top Four Plots: Resultant plots for WTTS GSC6793−806. Bottom Four Plots: Resultant plots for WTTS GSC6214−2384.

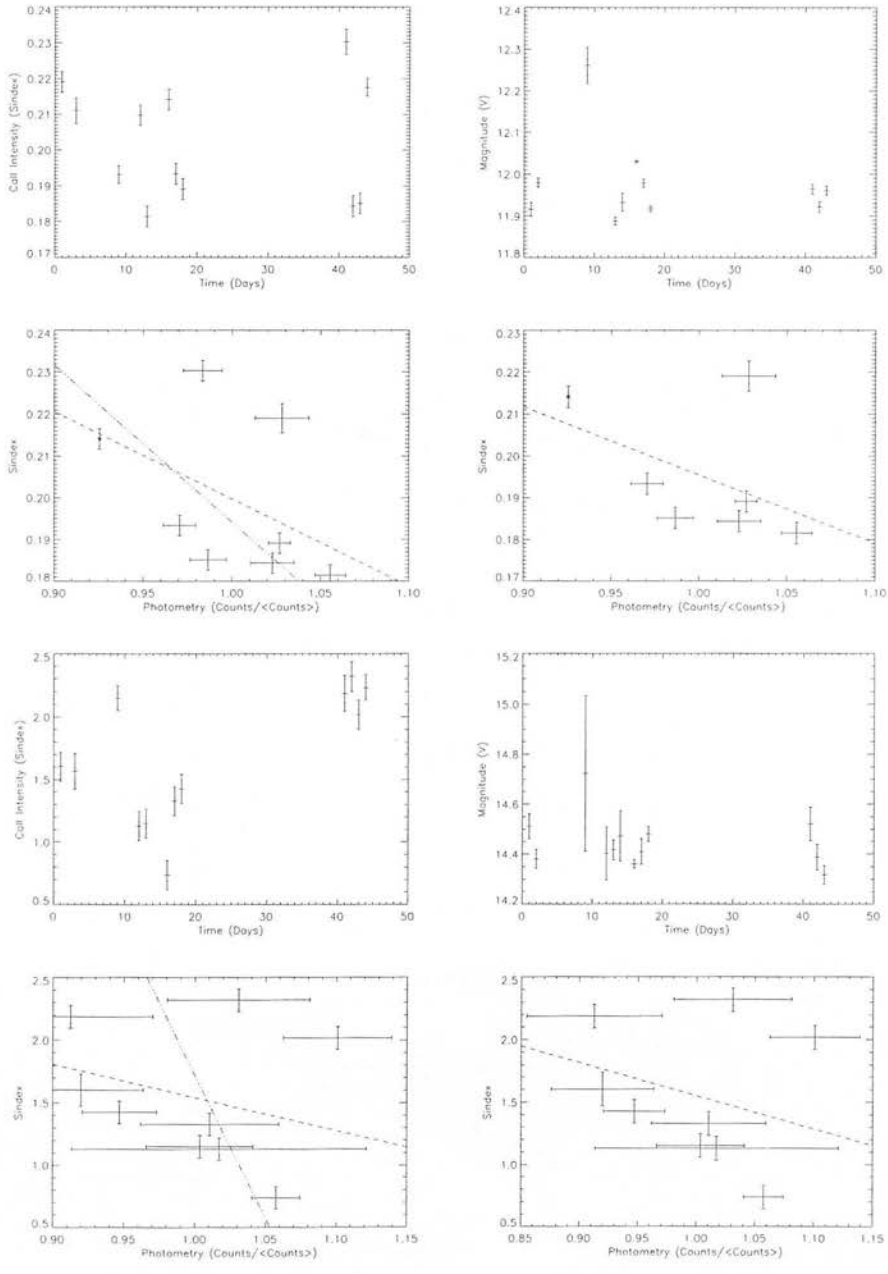

Figure 2.25: Top Four Plots: Resultant plots for WTTS GSC6794−537. Bottom Four Plots: Resultant plots for WTTS RXJ1625.2−2455.

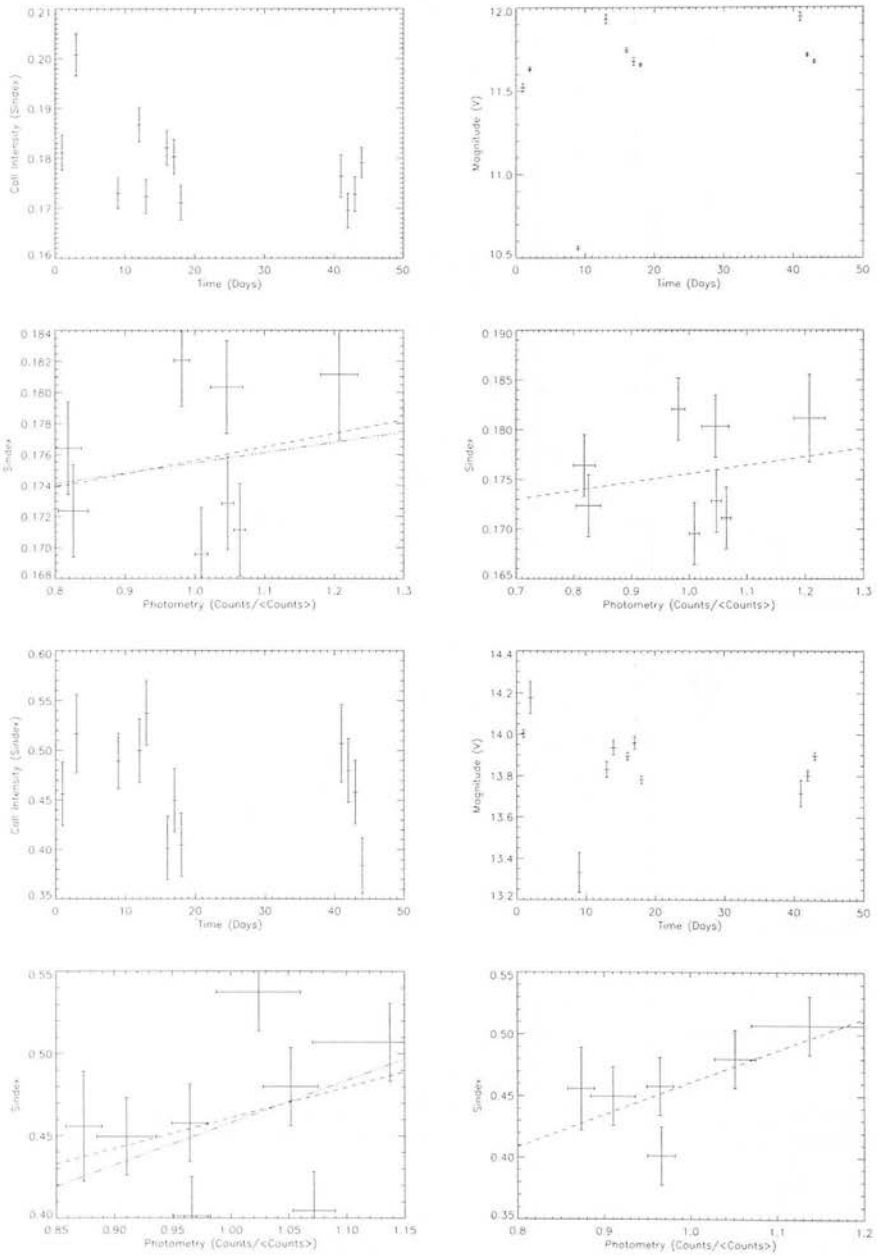

Figure 2.26: Top Four Plots: Resultant plots for WTTS GSC6794−337. Bottom Four Plots: Resultant plots for WTTS RXJ1621.4−2312

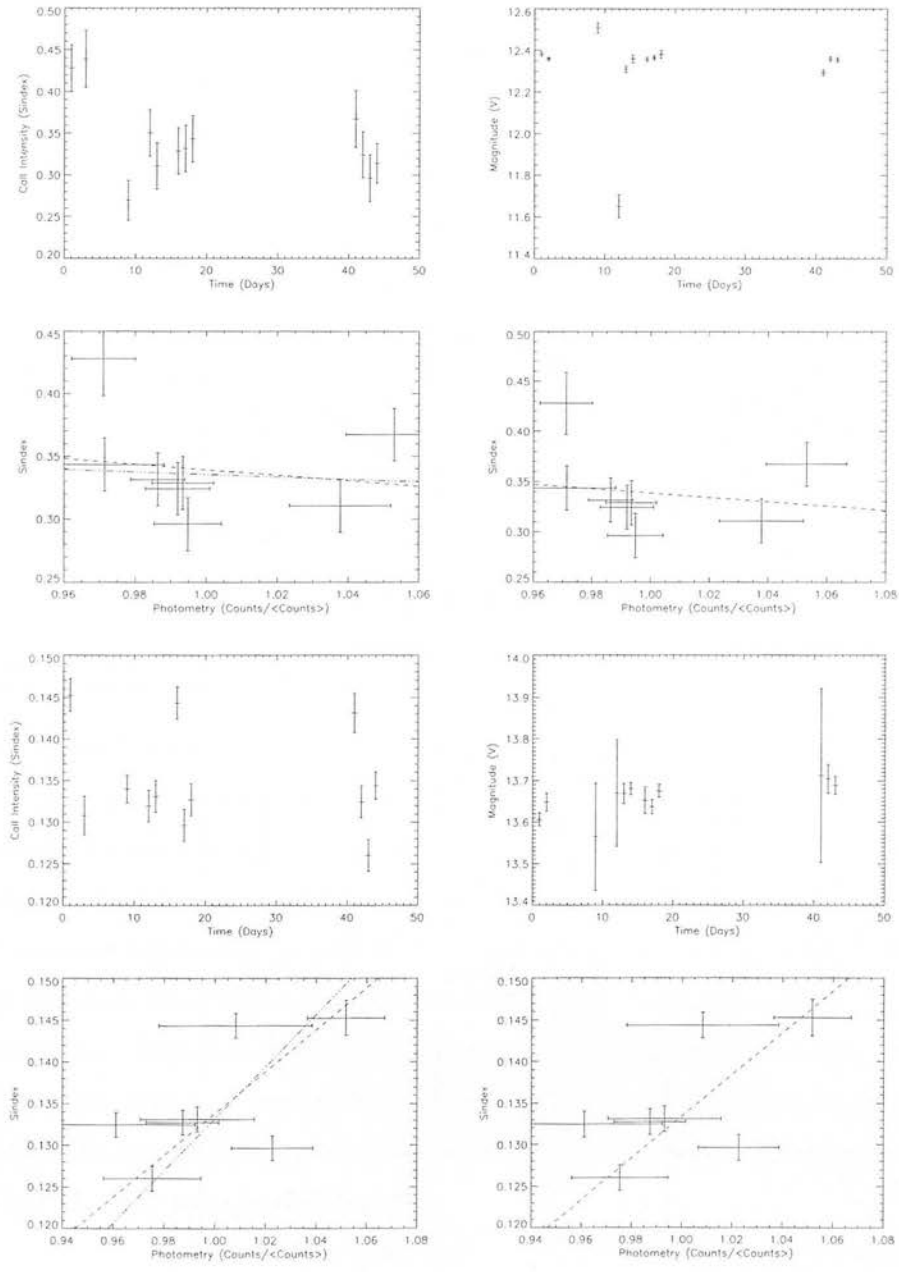

Figure 2.27: Top Four Plots: Resultant plots for WTTS ROXs45f. Bottom Four Plots: Resultant plots for WTTS ROXs5.

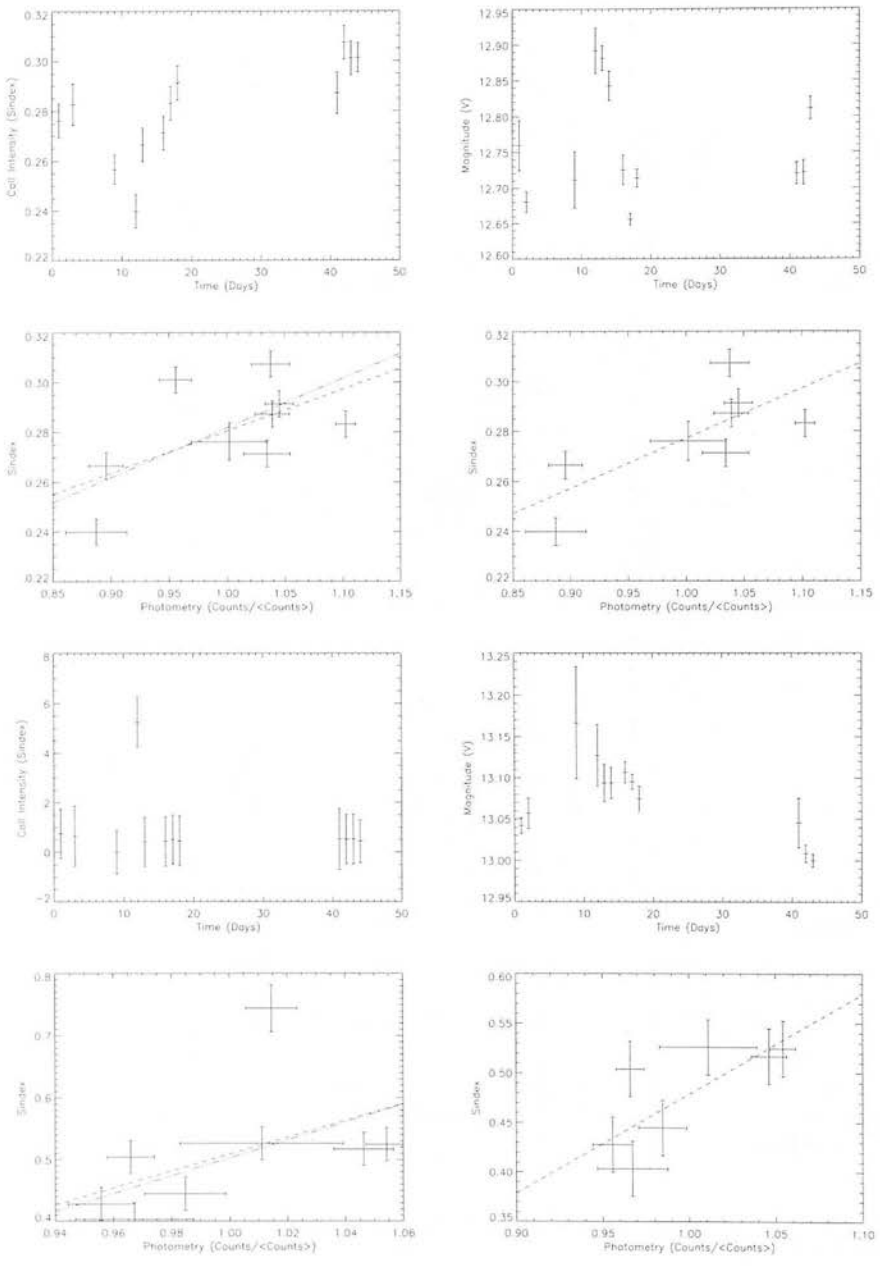

Figure 2.28: Top Four Plots: Resultant plots for WTTS ROXs39. Bottom Four Plots: Resultant plots for WTTS ROXs3.

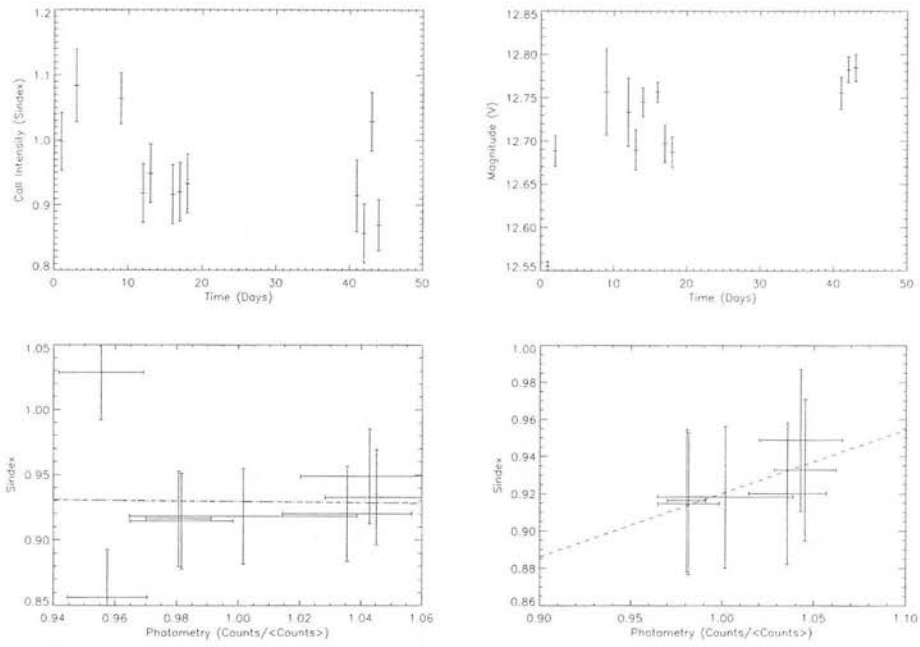

Figure 2.29: Resultant plots for CTTS ROXs6.

2.11.2 Classical T Tauri Sample

Out of the 35 target stars only 5 are classified classical T Tauri stars all located in the ρ Oph association. Only two of the CTTS sample resulted in pleasing negative linear correlations which is not unexpected. By definition the classical T Tauri stars are distinguished from the WTTS by larger H_α equivalent width (> 10Å) and infrared excesses understood to be caused by circumstellar disks which accrete matter onto the stellar surface. Where the accretion makes contact with the surface a hot spot is generated. These hot spots enhance the photospheric emission and thus dilute the correlation. With high enough levels of accretion the correlation becomes positive. All the CTTS measure have higher S indices than the comparable WTTS of same spectral type indicating stronger CaII emission.

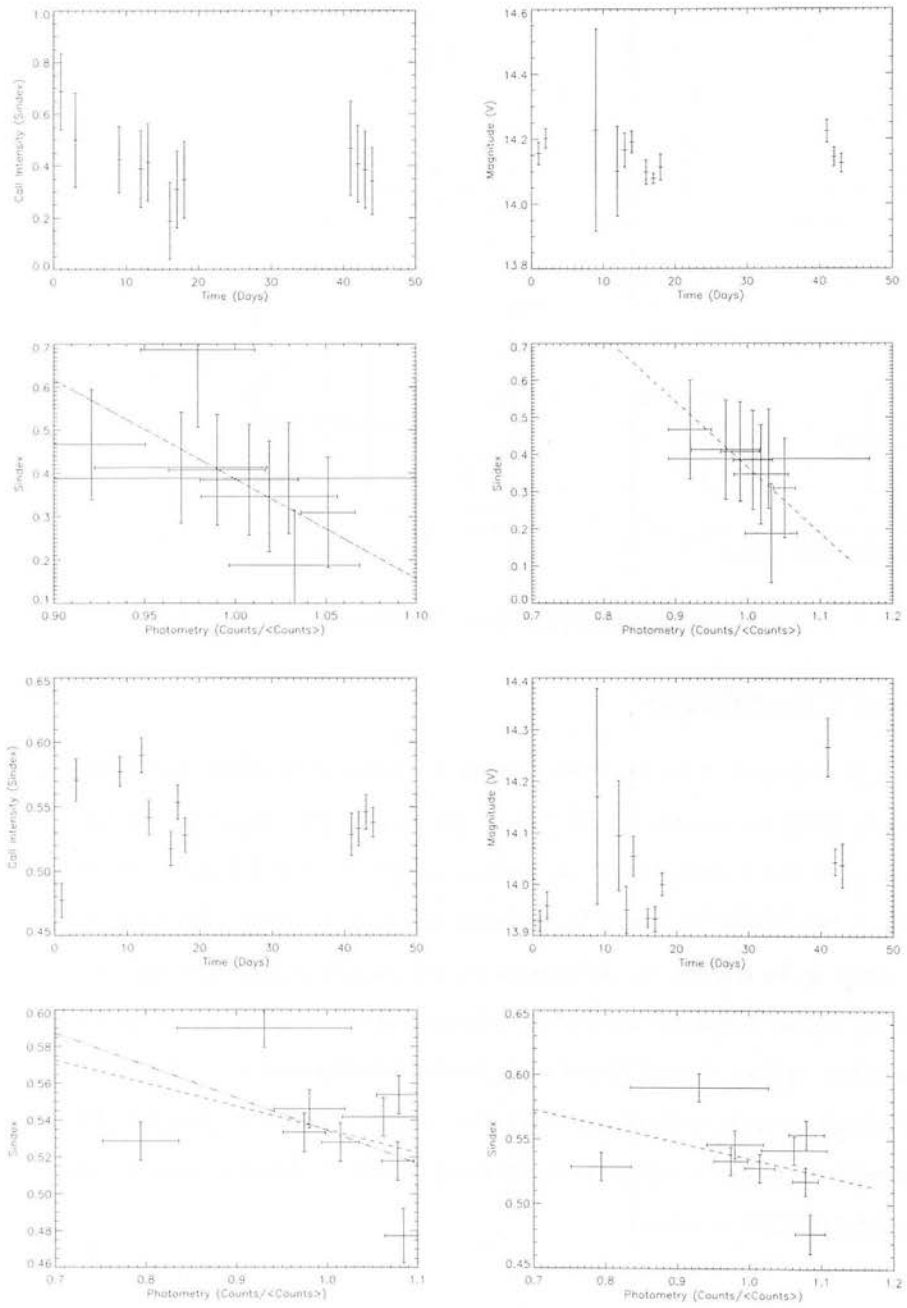

Figure 2.30: Top Four Plots: Resultant plots for CTTS ROXs30c. Bottom Four Plots: Resultant plots for CTTS ROXs33.

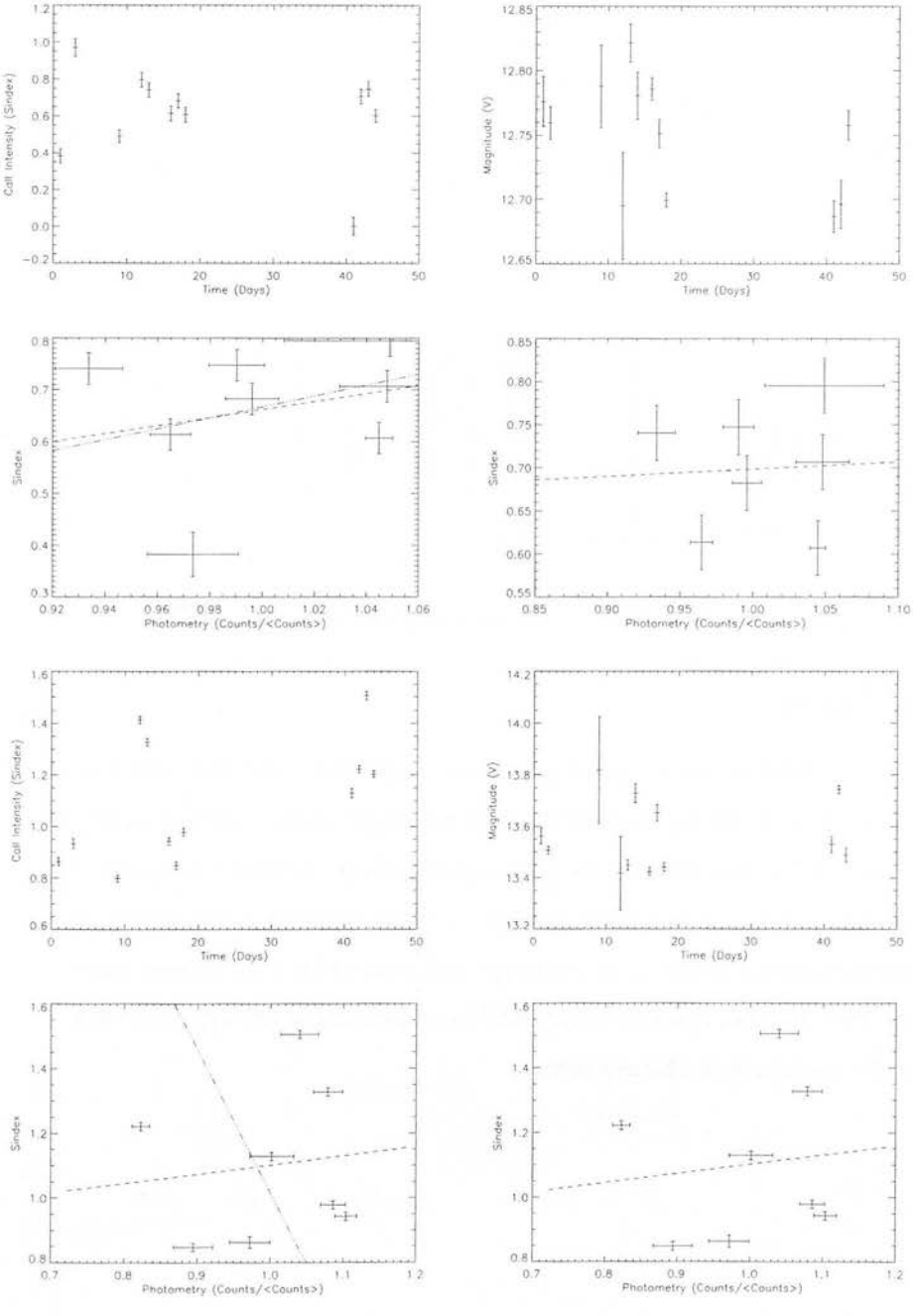

Figure 2.31: Top Four Plots: Resultant plots for CTTS ROXs44. Bottom Four Plots: Resultant plots for CTTS ROX47a.

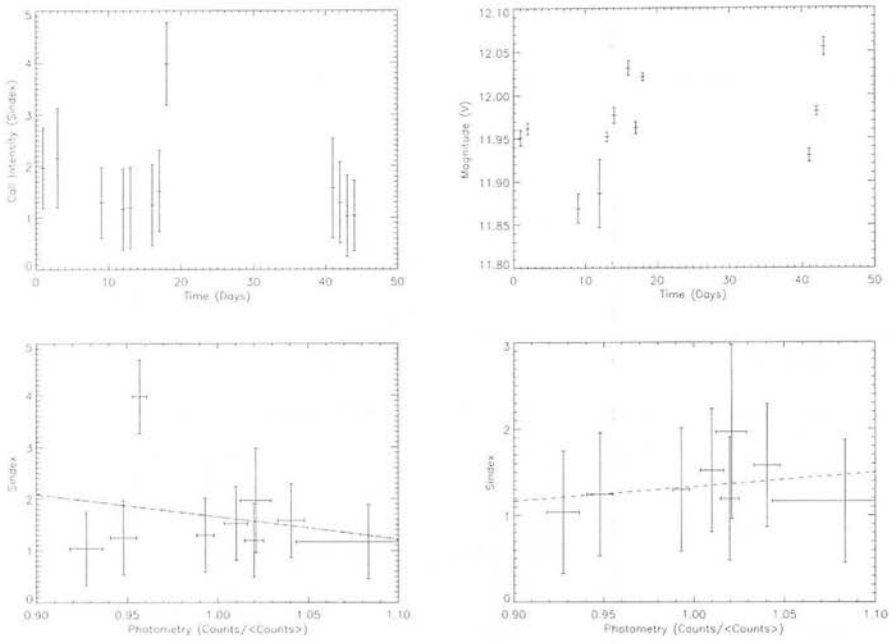

Figure 2.32: Resultant plots for binary target ROXs42c

2.11.3 Binary Targets

Three of our target sample in the ρ Oph cluster are thought to be sub-arcsecond binary systems. Binary systems are very difficult to interrupt because disentangling all the components which contribute to the photospheric CaII variations in nontrivial. It is not possible to know if variations are due to stellar rotation or the two stars co-orbiting. Complex circumstellar disks, accretion and interstellar dust further complicates the outcomes. Further research is required to understand if this type of study can be successfully applied to the binary case.

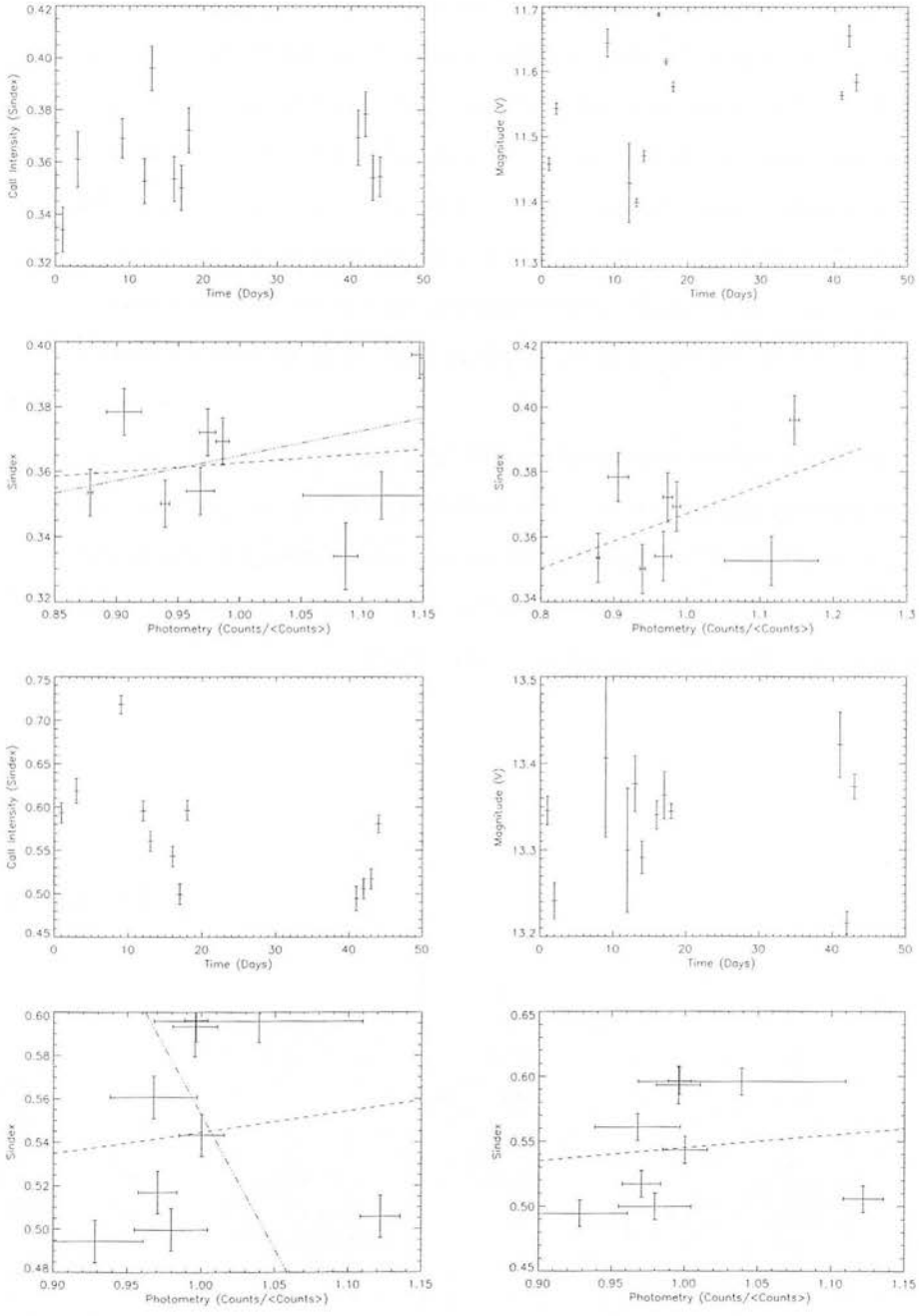

Figure 2.33: Top Four Plots: Resultant plots for binary target ROXs29. Bottom Four Plots: Resultant plots for binary target ROXs21

2.11.4 Field Star Sample

The remaining ten stars are classified field stars, 2 in ρ Oph and 8 in Upper Sco. All are non-active but are determined to field members due to their proper motions. The field stars were observed to verify that any correlation in the measured variability is due to surface active regions. In all bar one case the mean S index values for the field stars are 10% the strength of the common S indices in the pre-main sequence sample. As expected, there is very little variation in the V band magnitudes over the observing period. Since there is no variation in the CaII emission or light curve in most cases the regression linear fitting failed to find a genuine linear correlation and often failed to converge.

ROXs9a is classified a field star by Bouvier and Appenzeller (1992) but our observed spectra shows very strong CaII H & K emission, spectra can be found in the Appendix. The calculated S indices are vary strong and highly varied however, the photospheric brightness did not change to nearly the same extent. This target is an interesting candidate for follow up observations and research.

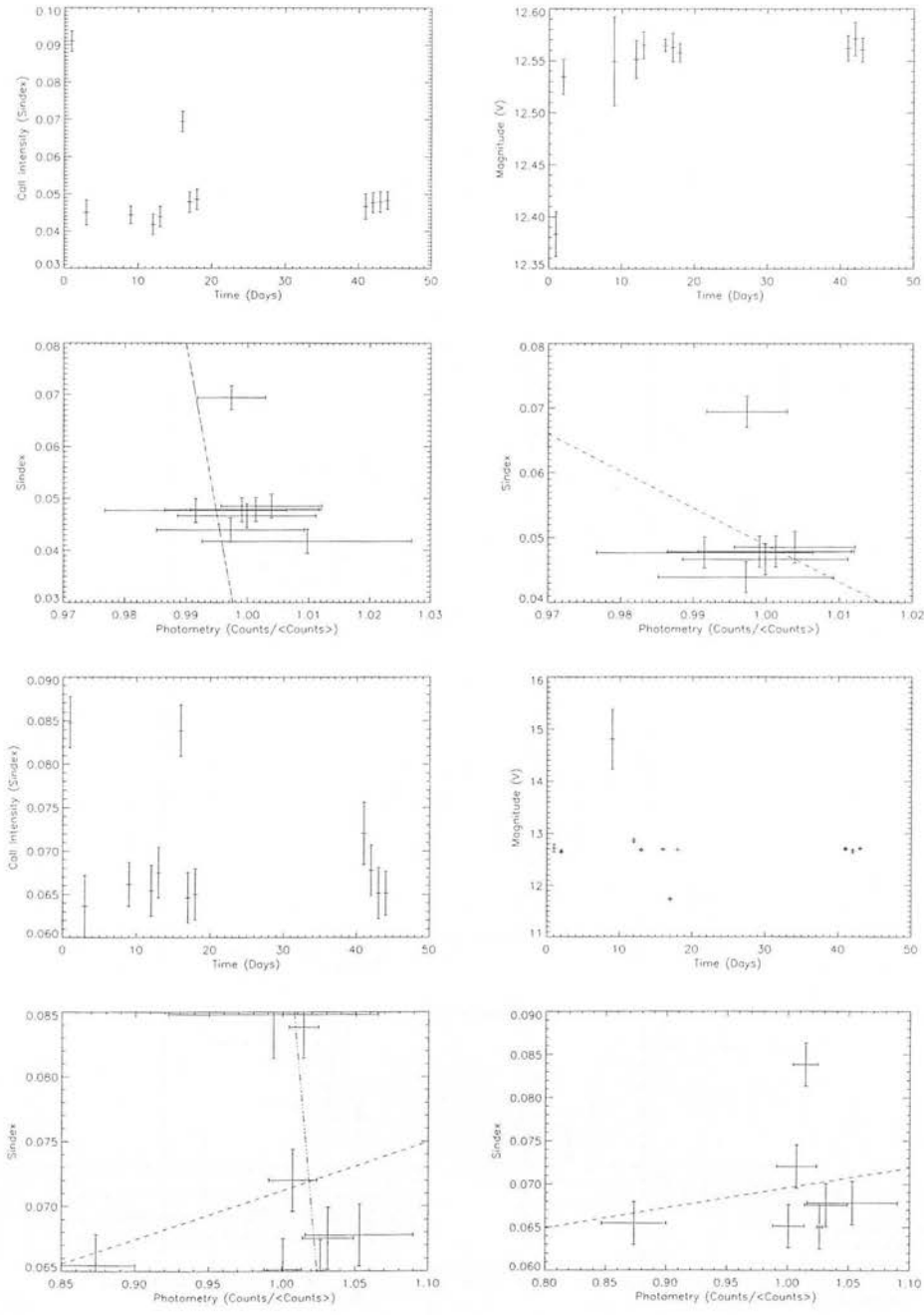

Figure 2.34: Top Four Plots: Resultant plots for field star GSC6215−271. Bottom Four Plots: Resultant plots for field star GSC6215−538.

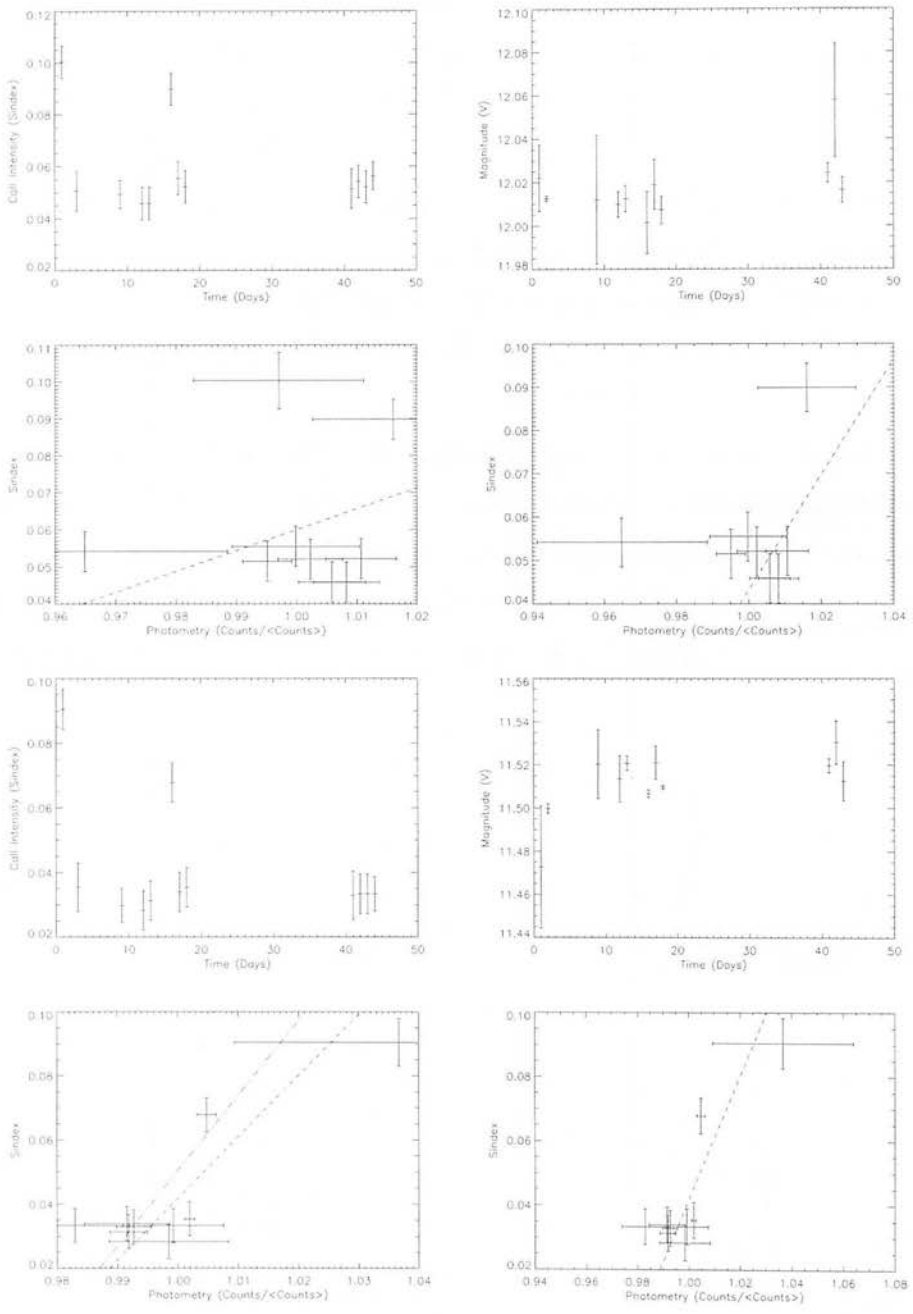

Figure 2.35: Top Four Plots: Resultant plots for field star GSC6214−14. Bottom Four Plots: Resultant plots for field star GSC6214−1115

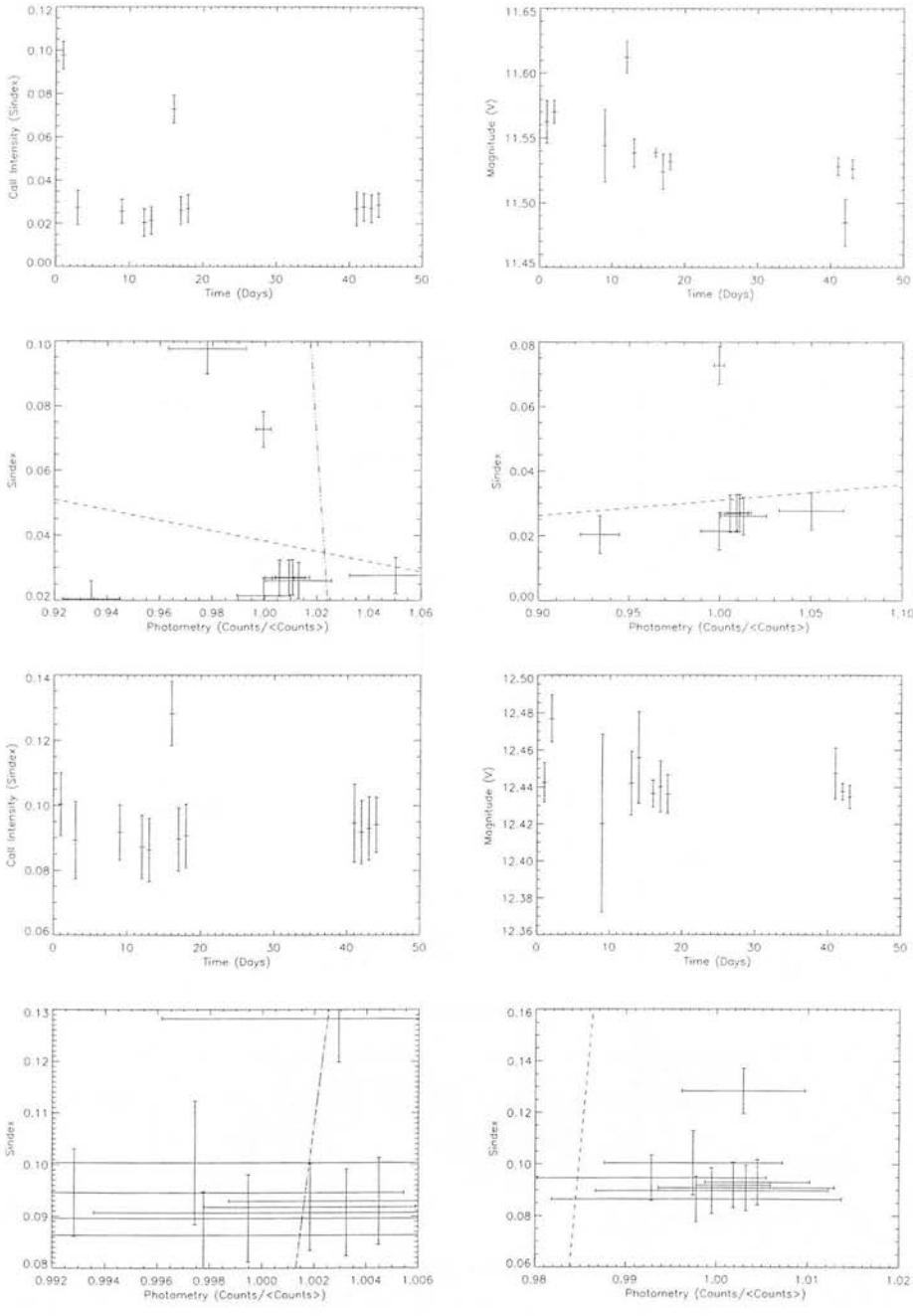

Figure 2.36: Top Four Plots: Resultant plots for field star GSC6213−933. Bottom Four Plots: Resultant plots for field star GSC6798−91.

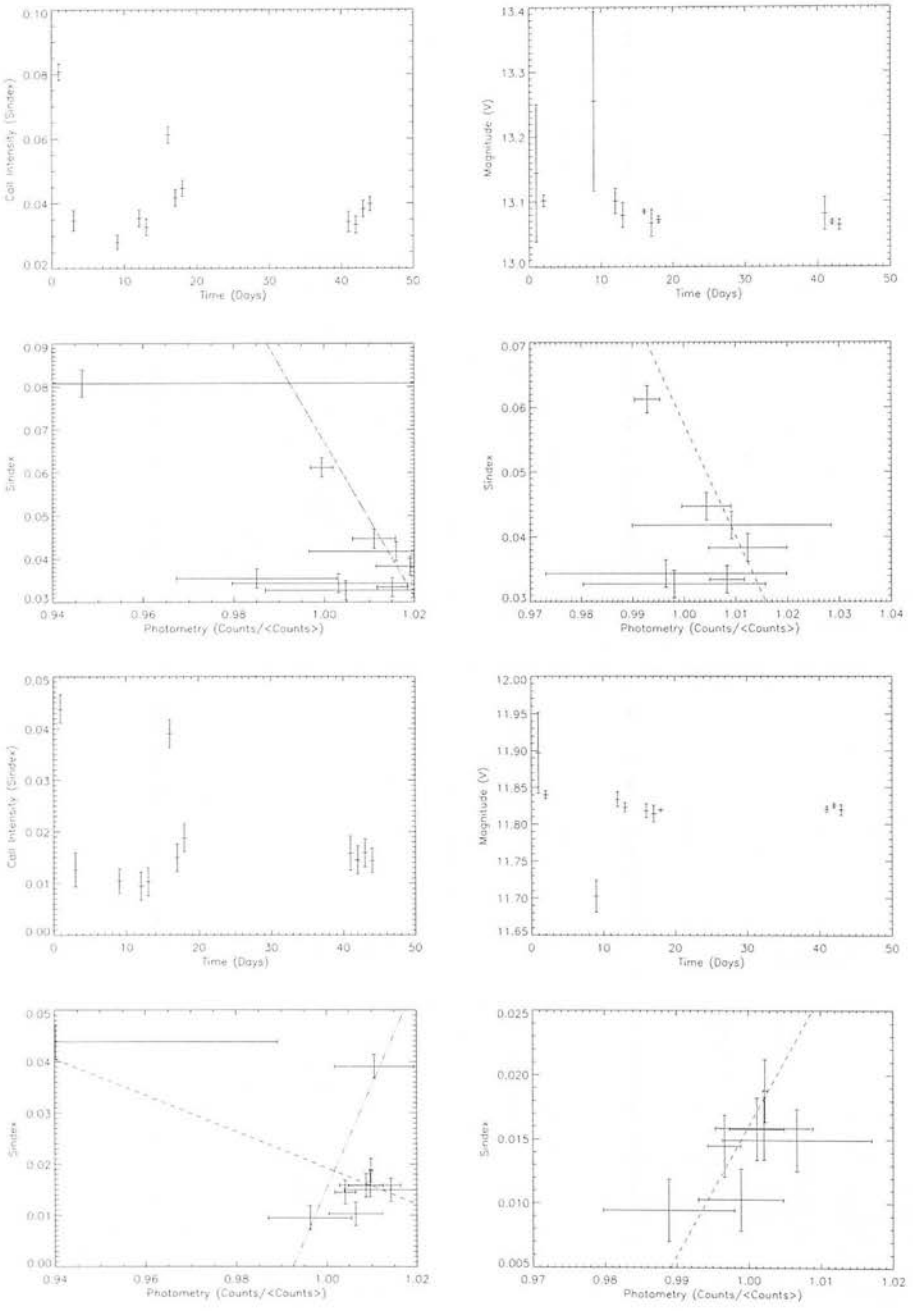

Figure 2.37: Top Four Plots: Resultant plots for field star GSC6214−2288. Bottom Four Plots: Resultant plots for field star GSC6213−1186

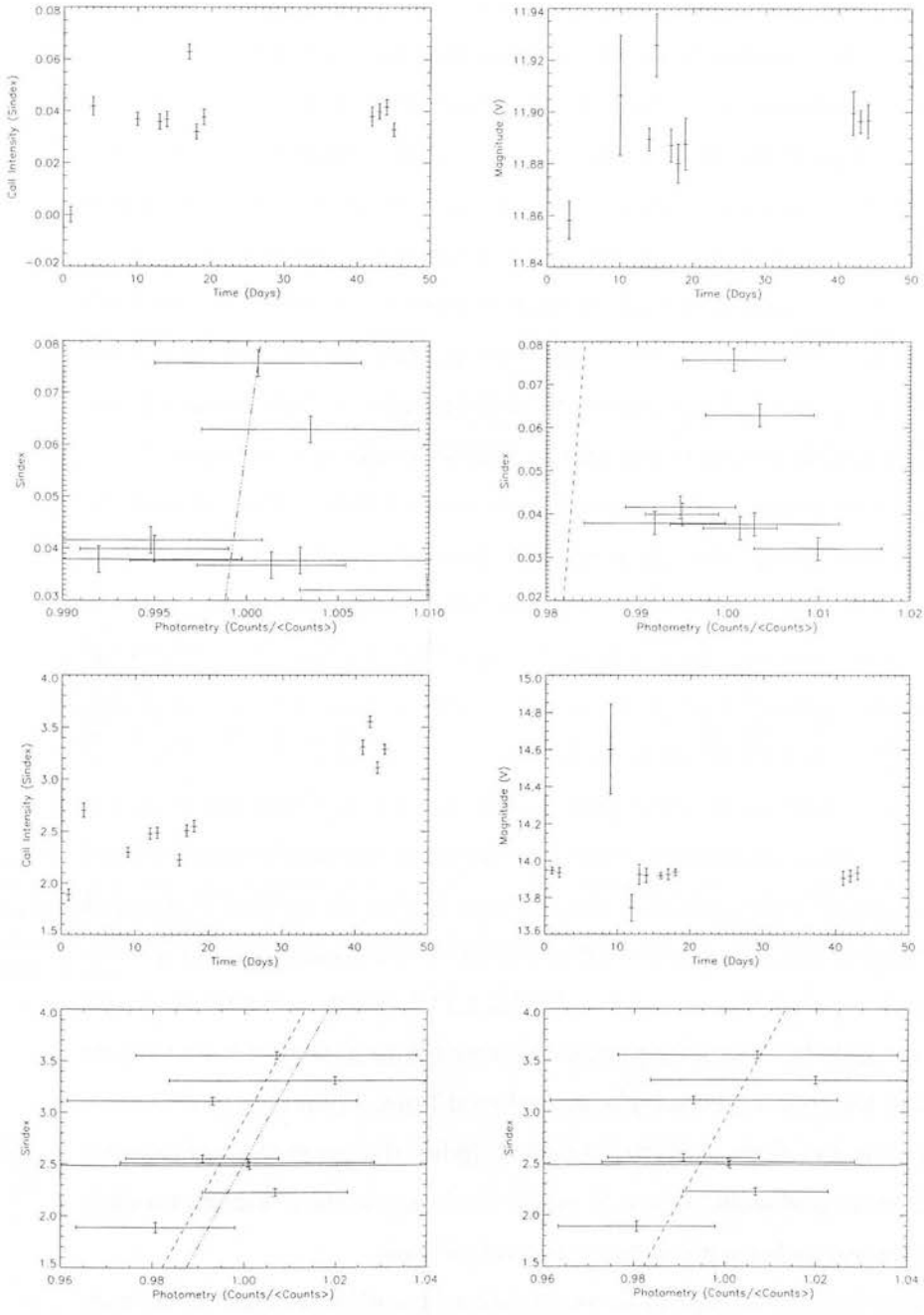

Figure 2.38: Top Four Plots: Resultant plots for field star GSC6793−562. Bottom Four Plots: Resultant plots for field star ROXs9a

2.11.5 Summary

The correlation plots show two patterns of behaviour. There is evidence that the mean S index increases with variation in the photometry. This is expected as larger active regions give more photometric variation and stronger CaII emission. There is also evidence that the slope of the fit gets more negative as the variation in S index increases. As the discrete active regions dominate the CaII emission a good correlation is expected as they rotate in and out of the facing hemisphere. However, as the CaII is dominated by diffuse carpets of CaII emission or a polar cap active region which is always visible the correlation will be begin to be washed out and the correlation slope will move towards 0.0. More discussion about possible surface geometry and the stellar surface models used to investigate scenarios is presented in Chapter 3.

Fig.2.39 shows the number of stars which have mean S index values in each 0.1 bin. The left had plot groups the target stars into pre-main sequence stars and field stars, immediately evident is that all the field stars have $\langle S\mathrm{index}\rangle$ values close to zero and all the pre-main sequences demonstrate stronger CaII emission. The right hand plot groups the stars into CTTS, WTTS and binary targets; generally the classical T Tauri have stronger CaII emission than the WTTS.

Fig.2.40 shows a series of summary plots which give a comprehensive overview of the outcomes of the correlation fitting and are used to compare the observational results with the stellar surface model results to obtain further understand of the total fractional coverage of the young stellar surface by the active regions. The graphs on the left hand side separate the sample into WTTS, CTTS, binary and field stars and the graphs on the right hand side the present the same information divided into three groups related to the sources the sample was selected from. From the top down the three different plots are: slope of fit versus mean S index, deviation of V magnitudes versus mean S index and slope of best fit versus deviation in the S indices for each target. Keys to the symbols are given on the individual plots.

Chapter 3 now leads on to explain the observational correlations found by investigating the nature of the chromospheric emission by modelling the surfaces of T Tauri stars..

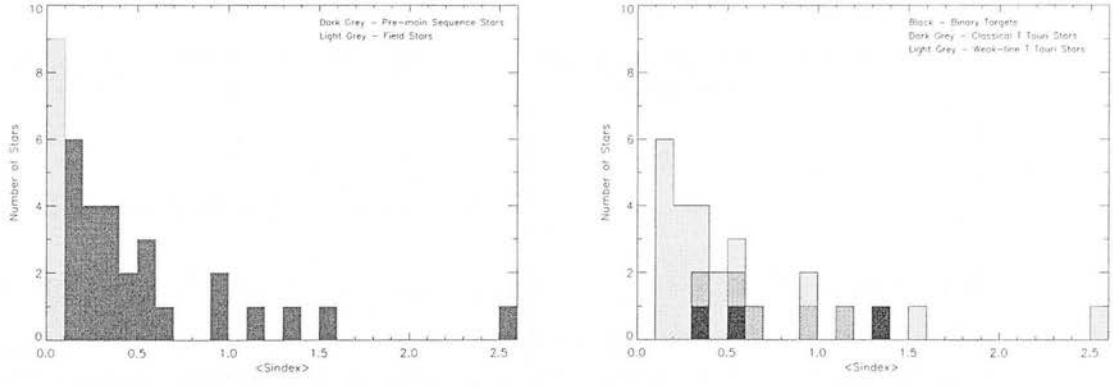

Figure 2.39: Histogram showing the spread of the S indices for the observed target stars. The left hand plots demonstrates that all field stars were found to have substantially weaker CaII H & K emission compared to the active pre-main sequence stars. The right hand plot indicates that generally classical T Tauri stars have stronger CaII emission that their weak line counterparts.

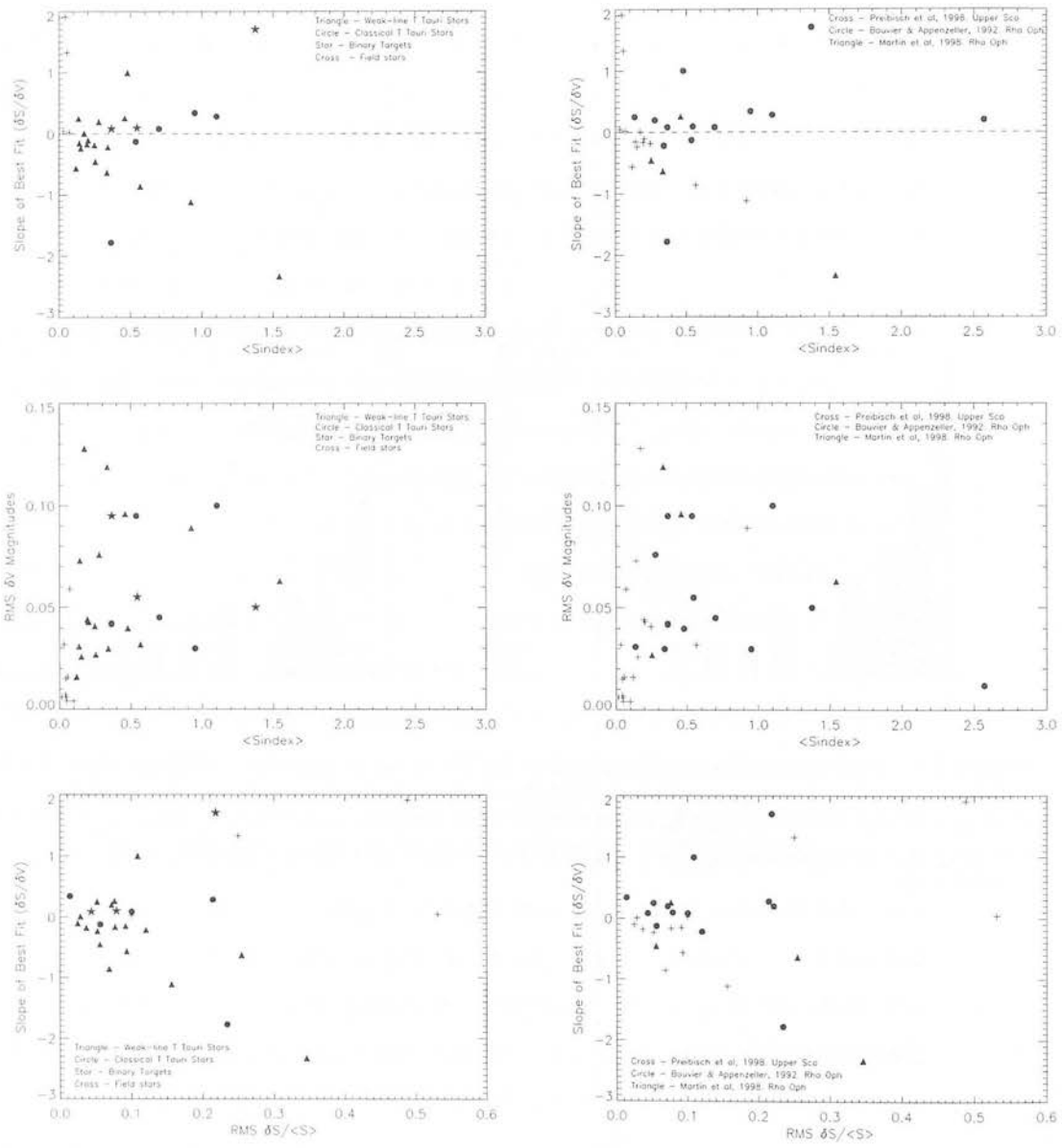

Figure 2.40: A series of plots summarising the outcomes of the correlation fitting for the observed data set. See text for explanation.

Chapter 3

Modelling the Stellar Surface Magnetic Activity

3.1 The Surfaces of T Tauri Stars

Since the 1980s, Doppler imaging techniques have been extensively employed for studying active regions on active stars. Doppler imaging allows the surface patterns of rapidly rotating stars to be reconstructed by looking at high-resolution spectral line profiles (a more comprehensive description of the Doppler image technique is given in Chapter 1). A handful of examples of Doppler studies include; weak-line T Tauri stars - V410 Tau (e.g. Strassmeier et al. 1994; Hatzes 1995; Joncour, Bertout and Menard 1994; Rice and Strassmeier 1996), & HDE283572 (e.g. Joncour, Bertout and Bouvier 1994), classical T Tauri stars - Sz 68 & Par 1724 (e.g. Johns-Krull and Hatzes 1997; Neuhaeuser et al. 1998), PMS single stars - AB Dor (e.g. Kuerster et al. 1994; Collier-Cameron and Unruh 1994; Unruh et al. 1995) and PMS binary systems - V471 Tau (e.g. Ramseyer et al. 1995) & HD155555 (e.g Kürster et al. 1992). The initial resultant images from the Doppler observations comprehensively confirmed the presence of the large dark spots which had been long hypothesised from photometric observations. The key detail these studies highlighted is the location of the spots on the surface of fast rotating stars, differing from the location of those found on the Sun. In the solar case the spots are observed at exclusively low latitudes, within roughly $\pm 30^{\circ}$ of

the equator. On the imaged magnetically active stars the spots are found predominantly at high stellar latitudes with a significant proportion showing dark polar caps (Schuessler et al. 1996; Granzer et al. 2000). The extent that the Doppler imaging departed from the results expected from the solar case led to much discussion in the community about the reliability of the technique. However further work, including that of Bruls et al. (1998) and Unruh and Collier Cameron (1997) confirmed the earlier results.

An explanation for the high latitude location of spots on rapid rotators has been sought by a number of groups through modelling the generation of spots due to magnetic flux tubes rising through the atmospheric layers. A full discussion of the mechanisms behind the generation of starspots is beyond the scope of this study but it is important to have a idea of why the spots might 'migrate' towards the poles as the stellar rotation rate increases. The observed properties of sunspot groups such as their general east-west orientation and Hale's polarity rules suggest the spots result from the emergence of a coherent magnetic structure from a toroidal - azimuthally oriented magnetic flux in the solar interior. This flux system is believed to lie below the convection zone in an overshoot layer (Schüssler 2002). Like the Solar case, magnetic fields on active cool stars are thought to be generated by a dynamo residing at the bottom of the stellar convective envelope. This dynamo produces strands of toroidal field which become directed by non-axisymmetric instabilities once the field strength exceeds a critical amount. The instabilities result in loop structures developing which rise through the convective zone and erupt at the surface to form the active spots (Schuessler et al. 1996; Schussler et al. 1994). The path the loops take through the convection zone is dictated by the buoyancy force acting radially outwards, the Coriolis force which is perpendicular to the axis of stellar rotation, the magnetic tension and the drag forces. The Coriolis force actively deflects the rising magnetic flux tubes towards higher stellar latitudes and increases with decreasing rotation period, hence becomes dominant for rapidly rotation stars (see Schuessler and Solanki (1992) for full discussion). Modelling the effect of the varying force strengths for young and main sequence stars of $1M_{\odot}$, Schuessler et al. (1996) shows that pre-main sequence stars have such deep convection zones and small superadiabaticity that the Coriolis force

dominates even at rotation rates as slow as the present Sun. They suggest that observationally these stars would show a pronounced equatorial gap in the distribution of magnetic spots or a magnetic coverage of the polar cap. Also, the stability properties of PMS stars at mid-latitudes are such that only flux tubes with very strong fields form rising flux loops between roughly $30^\circ - 60^\circ$. These loops effectively rise radially and generate spots at intermediate latitudes on the stellar surface independent of the rotation rate of any given star. The models generated by Granzer et al. (2000) are also able to account for the simultaneous existence of polar and lower-latitude spots for the case of rapidly-rotating T Tauri stars with very small radiative cores. Again they concur that the axisymmetric instability leads to flux emergence at the poles with the low-latitude instabilities enabling low-latitude eruption, resulting in the observed bimodal distribution.

More recent Doppler imaging of both weak-line and classical T Tauri stars have found simultaneous spot occurrence in either extended latitudinal zones or in two discrete latitudinal zones, mostly at or near the pole and at low-to-intermediate latitudes (e.g. with V410 Tau & Sz 68, see Joncour, Bertout and Menard 1994; Johns-Krull and Hatzes 1997 among others.). In the case of weak-line T Tauri HDE283572 low-latitude features are absent but it has a large polar spot (Joncour, Bertout and Bouvier 1994). As for AB Dor a rapidly-rotating zero-age main sequence star, a bimodal spot distribution was found, that is a polar spot in addition to a number of low-latitude spots (Granzer et al. 2000).

3.1.1 A Case Study - V410 Tauri

V410 Tau is a bright weak emission line T Tauri star with an H_α equivalent width of ~ 3Å. It is listed in SIMBAD as having spectral type of K5 though has been classified as a K2 through to K7 in various different studies. It is reasonable to suggest that large spots alter the spectral type such that mean effective temperature varies with the rotational phase suggesting why the published spectral types can be inconsistent. It is one of the most luminous WTTS with a $m_v = 10.6 - 11.2$, (Joncour, Bertout and Menard 1994). It was discovered to have a strongly varying light curve in the early 1970s (Romano 1975) and subsequently photometrically observed on a regular basis. These

studies showed a regular variability over a 1.87 day period which was interpreted as light modulation due to stellar spots rotating in and out of view (Bouvier and Bertout 1989; Vrba et al. 1988). This seen modulation is not sinusoidal which indicates the presence of at least two photospheric spots; a single spot would result is a largely sinusoidal light curve - as demonstrated further in §3.4. Simple model studies carried out by Vrba et al. (1988), Bouvier and Bertout (1989) and Herbst (1989) suggest a spot coverage of $30 - 40\%$ of the stellar disk and a spot temperature 800K to 1400K below the photospheric temperature (Joncour, Bertout and Menard 1994).

However, V410 Tau is prime for studying with Doppler imaging techniques as it is one of the brighter known T Tauri stars, is a fairly fast rotator with $v \sin i = 71 \mathrm{kms}^1$ (Hartmann and Stauffer 1989) and has been observed at virtually all wavelengths. It has little infrared excess, indicating it does not have a significant circumstellar disk, so the photosphere can be reliably Doppler imaged (Rice and Strassmeier 1996). A number of groups targeted V410 Tau in the early 1990s and the remainder of this section details their finds so they can be incorporated into our models. The stellar parameters for V410 Tau adopted by each group is given in Table 3.1.

Parameter	Joncour at al (1994)	Rice at al (1996)	Strassmeier at al (1994)
Spectral Type		K4	
log g	3.6	4.0	
$T_{\mathrm{eff}_{\mathrm{phot}}}$ (K)	4800	4400	4400
$v \sin i$ (kms^{-1})	75	77 ± 2	77
i (°)	70	70	70
log[Ca] abundance		-5.65	
log[Fe] abundance		-4.41	
log[Li] abundance	3.5*	-8.45	

Table 3.1: Stellar parameters adopted by each group who undertook Doppler imaging of pre-main sequence star V410 Tau in the early 1990's. *abundance are on a scale such that $\log N(H) = 12$.

In January 1990 a group led by Isabelle Joncour observed V410 Tau over a wavelength range of 40Å centred approximately on the LiI 6707Å line, at R = 32000. To perform the Doppler imaging analysis they chose the strong resonance line of lithium, λ_c = 6707.84Å, one of the strongest photospheric lines in the T Tauri spectra (Basri et al. 1991). Due to the nature of the Doppler technique and the limited spectral resolution

available (for specific reasons see Joncour, Bertout and Menard 1994), only spots with temperatures at least 800K lower than the temperature of the photosphere will been 'seen' and spots that span less than 12% of the star's diameter in longitude can be resolved. Joncour, Bertout and Menard (1994) found three cold spots: defining visible rotational axis as the stellar 'north pole' they found an extended spot with a smaller adjacent spot at the north pole and a third spot located at intermediate latitude on the opposite, southern, hemisphere. A summary of spot properties is given in Table 3.2 and their resultant V magnitude light curve derived from the Doppler image reproduced in Fig.3.1; the overlaying data points are those of Herbst (1989). The spot parameters quoted are the colatitude, θ, and longitude, ϕ, at phase zero - i.e. the initial observation - and the angular radius, Θ. Also listed is f_{max}, the maximum projected spot area. Joncour, Bertout and Menard (1994) note that possible additional spots

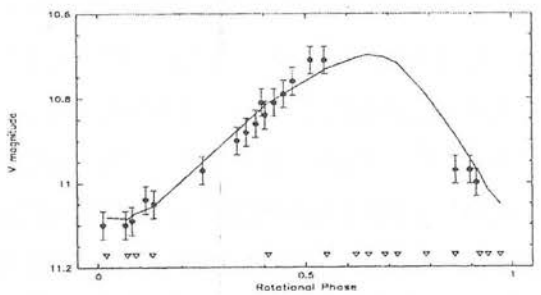

Figure 3.1: Reproduced V magnitude light curve constructed from Doppler observations of V410 Tau by Joncour, Bertout and Menard (1994). They found good agreement between the theoretical light curve derived from the Doppler images and the observational curve measured a year prior to the Doppler observations.

T_{eff} spot	θ (°)	ϕ (°)	Θ (°)	f_{max}
3443	29	−12	45	0.36
3021	40	−105	21	0.09
3765	127	26	26	0.09

Table 3.2: Summary of spot properties of the three cold active regions on the surface of V410 Tau as determined but Joncour, Bertout and Menard (1994). Listed are effective temperature, latitude (θ) and longitude (ϕ), angular radius (Θ) and maximum project spot area (f_{max}) for each of the three detected regions.

could not be detected if they are located at the 'south' pole or visible during a phase of the rotational period missed due to bad weather. However, as can be seen in Fig.3.1 there is good agreement between the theoretical light curve derived from the Doppler images and one observed a year beforehand indicating that at the very least the fractional spot coverage of the stellar surface is consistent.

Two years later a collaboration including J. B. Rice (Bradon University) and K. G. Strassmeier (Universität Wien) started a two year monitoring campaign of V410 Tau with Doppler imaging observations in November 1992 and a year later in December 1993. On both occasions FeI and CaI lines were used for the line profile fitting and Doppler reconstruction however the later observations were of more than twice the resolution. The initial 1992 maps show a large cool asymmetric feature at very high latitudes, not quite a complete polar cap but certainly reaching the visible rotational pole (Strassmeier et al. 1994). A second significant feature is seen at the stellar equator, a double feature with two small spots at 270° and 310° respectively. Three final significant features appear at latitudes & longitudes; (0°, 50°), (0°,100°) and (-30°, 130°). The latter two are separated by a small bright feature at 0° latitude.

The second paper to present the 1993 observations (Rice and Strassmeier 1996) took the prime opportunity to compare the observed features a year apart and make some comments on potential life-spans of the features, what changes occurred in the prominent features and what, if any, evidence of differential rotation. The second set of observations not only had higher resolution but more lines were imaged (simultaneous photometry on two of the three CaII IR triplet and a magnetically sensitive neutral Fe line), and a modified version of the Doppler imaging program was used, all giving a more comprehensive set of results. In general both sets of images show an abundance of cool spots at both high latitudes near the visible pole and in the equatorial region. Rice and Strassmeier (1996) found that the spots at higher latitudes appear to be cooler, larger and elongated as to suggest stretching by shearing forces which can result from substantial differential rotation over a short timescale or small differential rotation active over a prolonged period. They go on to suggest and give evidence for very long lived spots being affected by small differential rotation acting over a long time, perhaps even years. Approximately half the spots appear to persist over the 13

months between the two sets of observations. Table 3.3 reproduces the summary of spot information given by Rice and Strassmeier (1996) showing each features latitude, longitude and apparent changes between 1992 & 1993. Main conclusions include: fea-

Nature	Feature label	Latitude (°)	Longitude (°)	Apparent changes in 1993
Persistent	Spot A	0	75	Comparable size but perhaps weaker
Persistent	Spot B	+65	270 – 0	Displaced to larger longitude& smaller
Persistent	Spot C	−30	0	Possible extension of southerly spots
Changing	Spot D	−30	250	Two spots replaced by one weaker one
Changing	Spot E	0	30	Vanishes between 1992 & 1993
Changing	Spot F	0	220	Vanishes
Changing	Spot G	+70	60 – 170	Vanishes
Changing	Spot H	+90	270 – 90	Weak polar spot appears in 1993

Table 3.3: Summary of active features found on the surface of V410 Tau by Rice and Strassmeier (1996) and how they changed over time. Details each discrete region's location (θ, ϕ) and nature, 'Persistent' for regions which showed little change over 12 months and 'Changing' for ones which either disappeared, appeared or significantly altered over the time period. The noted apparent changes found between observations taken in 1992 then 1993 are giving in column 5.

tures that are common to both maps have moved very little relative to each other, that there would appear to be very little differential rotation on the T Tauri but what little movement there has been indicates a slightly slower rotation rate at higher latitudes, the same as the Sun but a much smaller effect. The conclusion regarding differential rotation is in agreement with conclusions drawn by Hall (1991) from photometric data that short period stars, as in the case of T Tauri stars, seem to be nearly rigid rotators (Rice and Strassmeier 1996). Spots of higher photospheric temperature are seen in both the 1992 and 1993 maps.

3.2 The Sun as a Reference

Ultimately the purpose of the stellar surface model code is to allow us to experiment with the frequency of star spots, their locations and how much of the total stellar surface is covered with heightened magnetic activity to generate plots for comparison with the observed data presented in Chapter 2. Hence, we need to generate outputs from the models which match the observed quantities, namely stellar brightness and chromospheric S index.

The dark, cool spots seen on stellar surfaces are assumed to be the results of the blocking effect on convection caused by magnetic flux-tube emergence, just as seen with solar spots. Thus a natural starting point for detailing the characteristics of stellar spots is to consider the well defined parameters of solar spots. The surface of the Sun is complex and dynamic however. To slim-line the computation of model surfaces, we have nominated four 'regions' to incorporate; the 'pristine' surface, the plage, the penumbra and the umbra.

The umbrae are the clearly seen dark 'cores' of the sunspot which have a surrounding, brighter penumbrae. The ratio of the umbra to penumbra areas is typically 0.32 for large regions (Brandt et al. 1990). Plages are bright features which are coincident to sunspots but are regions of higher temperature and density within the chromosphere. The plage areas are substantially larger than their companion umbral areas, the mean ratio of plage to umbra area is typically 16.7±0.51 (Chapman et al. 1997). The 'pristine' surface is defined to be the remaining surface, the magnetically quiet regions. To allow us to generate the required observed quantities we need to construct an image of the stellar surface at three relevant wavelengths; the V band continuum at λ = 5450Å, the continuum at λ = 3950.5Å and the CaII H & K emission.

3.2.1 The V Band Continuum

Rendering this wavelength image and determining the variation in stellar brightness is relatively straight forward. A 'spot' on the photosphere is made up of two parts, the umbra and the penumbra. On the Sun the temperature and thus intensity depends on the magnetic field strength. Within a typical sunspot the magnetic field depresses the spot temperature from $\sim$ 6000K to $\sim$ 4000K; the resulting drop in surface brightness from the pristine atmosphere to the umbra is $\sim$ 94%. The surrounding penumbra has a typical brightness of $\sim$ 75% that of the pristine photosphere; it is brighter than the umbra due to the magnetic field lines becoming strongly inclined from the vertical at this point (Grossmann-Doerth and Schmidt 1981). Once the spot or spots are defined in this way the total stellar brightness at any given time is simply the integration of the photospheric emission over the visible hemisphere.

3.2.2 The Continuum at 3950.5Å

The continuum flux for a normal stellar surface, one which is absent of magnetic regions must be modeled so that it can be 'subtracted' from the magnetically active areas to mimic the Mt Wilson S index which has been used to quantify the CaII variation in the observational data. The Barnes-Evans relation show that the stellar continuum flux, the power emitted per unit area of the surface, at key points on the spectrum depends only on the stellar colour (Barnes and Evans 1976). As explained in Chapter 2, intrinsic stellar colour is inherent to spectral type.

Pasquini et al. (1988) developed a calibration procedure for converting the observed CaII fluxes into absolute units at the star surface. Linsky et al. (1979) first developed a method for doing this based on absolute photometry collected by Willstrop (1965) and the Barnes-Evans relationship. They derived the surface flux in a 50Å bandpass from 3925−3975Å allowing them to place a given star's relative flux spectra on an absolute surface flux scale. Pasquini et al. (1988) were unable to apply the method of Linsky et al. (1979) as the spectral range of their observations was not wide enough, it did not cover the required 50 plus Å bandpass stipulated by the method of Linsky et al. (1979). Instead they present their observed CaII H & K line profiles on a relative scale using the pseudo-continuum at 3950.5Å as a reference point, 3950.5Å is between the H and K CaII lines. They combined photoelectric measurements of the pseudo-continuum at 3950.5Å with respect to the flux in the V band taken by Catalano (1979) with the Barnes-Evans relation to determine the relationship between the surface flux at 3950.5Å and spectral colour index $(V - R)$.

From 'Astrophysical Quantities', Allen (1973), it is known that the flux at the stellar surface in $\mathrm{ergcm^{-2}s^{-1}\AA^{-1}}$ near 5500Å the V band, is given by:

$$\log \mathrm{F_v} = 4 \log \mathrm{T_{eff}} + 0.4\mathrm{BC} - 8.094 \tag{3.1}$$

where $\mathrm{T_{eff}}$ is the effective temperature, BC is the bolometric correction. Setting Φ be the stellar angular radius in radians and $\mathrm{V_o}$ the extinction corrected apparent visual

magnitude, Pasquini et al. (1988) determined F_v to be:

$$\log F_v = -2\log\Phi - 0.4V_o - 8.44 \tag{3.2}$$

the constant term is due to the absolute flux at the Earth from a star of V = 0.0. Equating the relations and converting the stellar angular radius in radians to a stellar angular diameter in milliarcseconds gives:

$$\log T_{eff} + 0.1BC = 4.2207 - 0.1V_o - 0.5\log\Phi' \tag{3.3}$$

Barnes et al. (1976) defined:

$$F'_v = 4.2207 - 0.1V_o - 0.5\log\Phi' \tag{3.4}$$

where the symbols are as above and the best fit relationships result in:

$$F'_v = 3.977 - 0.429(V-R) : (V-R) \leq 1.26 \tag{3.5}$$

$$F'_v = 3.837 - 0.320(V-R) : (V-R) > 1.26 \tag{3.6}$$

Re-arranging equations 3.1, 3.3 and 3.4 gives:

$$\log T_{eff} + 0.1BC = F'_v \tag{3.7}$$

and

$$\frac{\log F_v + 8.094}{4} = \log T_{eff} + 0.1BC \tag{3.8}$$

and thus $\log F_v$ is shown to relate to stellar colour as given by:

$$\log F_v = 7.814 - 1.716(V-R) : (V-R) \leq 1.26 \tag{3.9}$$

$$\log F_v = 7.254 - 1.280(V-R) : (V-R) > 1.26 \tag{3.10}$$

They then used Catalano (1979) observations of F_v for main sequence stars to determine a linear relationship between the absolute surface flux at 3950.5Å F_{3950}, in

$\mathrm{ergcm^{-2}s^{-1}\AA^{-1}}$ and stellar colour such as:

$$\log \mathrm{F}_{3950} = 8.459 - 2.833(\mathrm{V} - \mathrm{R}) : (\mathrm{V} - \mathrm{R}) < 1.3 \tag{3.11}$$

The observations by Catalano (1979) do not extend to stars later than spectral type M0 which translates to $(\mathrm{V} - \mathrm{R}) \approx 1.3$ hence Pasquini et al. (1988) extrapolated their curves by assuming a trend parallel to that shown by the average surface flux over the 3925–3975Å bandpass. Converting the stellar flux units to the more practical $\mathrm{Wm^{-2}\AA^{-1}}$ such that, $\log \mathrm{F}_\lambda(\mathrm{ergcm^{-2}s^{-1}\AA^{-1}}) = \log \mathrm{F}_\lambda(\mathrm{Wm^{-2}\AA^{-1}}) + 3$, the key resultant equations for continuum flux in terms of stellar colour index are:

$$\log \mathrm{F}_{3950} = 5.459 - 2.883(\mathrm{V} - \mathrm{R}) : (\mathrm{V} - \mathrm{R}) \leq 1.3 \tag{3.12}$$

$$\log \mathrm{F}_{3950} = 2.938 - 0.944(\mathrm{V} - \mathrm{R}) : (\mathrm{V} - \mathrm{R}) \geq 1.3 \tag{3.13}$$

Both equations give a value of $\log \mathrm{F}_{3950} = 1.711$ for $(\mathrm{V} - \mathrm{R}) = 1.3$. Since the $\lambda = 3950.5$Å continuum point lies mid way between the two continuum reference windows averaged in the calculation of the chromospheric S index defined in Chapter 2 we assume that all these points see the same continuum flux which can be seen to be a valid approximation from the spectra. Since we wish to generate a continuum flux emission comparable to the one used in the calculation of the S index, that is two 20Å wide reference bands the total continuum flux emitted from the pristine surface we actually need: $\mathrm{F}_{3950} * 40$ in the units of $\mathrm{Wm^{-2}}$. The continuum brightness decreases over the penumbra and the umbra but not by the same factors as seen in the photosphere. The 3950.5Å continuum flux is in the region of the B band, so by scaling with a blackbody we would expect to see the continuum drop from 100% over the non-active regions and plages to 3% over the umbra and 70% over the penumbra.

3.2.3 CaII Emission from Active Regions

Lastly, we need a reasonable value in the models for the chromospheric CaII H & K emission above the active regions and the plages. The natural value to adopt is that of the flux measured on the Sun. The CaII emission above the Sun spots is complicated but the total emission is dominated but the emission from the large area of the plage,

hence we have chosen to simplify the modelling by only taking into account the CaII emission from the plage regions and not to separate the spot & surrounding area into umbrae and penumbrae. Schrijver et al. (1989) demonstrate that the CaII emission is known to scale with magnetic field strength and provide a direct conversion from magnetic field to absolute CaII emission such that (converted from $\mathrm{ergcm^{-2}s^{-1}}$ given in the paper to $\mathrm{Wm^{-2}}$):

$$\log \Delta \mathrm{F_{CaII}} = 0.6 \log\langle \mathrm{fB} \rangle + 1.8 \tag{3.14}$$

where $\langle \mathrm{fB} \rangle$ is the average magnetic field strength over the given area in Gauss. The solar observations have shown that over the large plage regions the average field strength is 150 Gauss which yields a $\mathrm{F_{CaII}}$ of $\sim 1275 \mathrm{Wm^{-2}}$ (D'Silva and Howard 1993). There is a known CaII 'network' seen on the solar surface which is a carpet of emission over the magnetically quiet atmosphere. This magnetic network coincides with the pattern formed by large-scale convective cells, know as 'supergranulation cells'. Each cell is roughly 30 x 10^6m in diameter and move across the surface of the photosphere carrying the magnetic fields with them. The magnetic fields are swept to the outer edges of the supergranulation cell where they collect and strengthen. Chromospheric heating is produced above these field concentrations which result in the blanket CaII emission outlining the magnetic network (Lang 2006). However, in young active stars the active regions are much larger and therefore the plage emission is expected to dominate. A magnetic field strength of 5 Gauss (Schrijver and Zwaan 2000) allotted to the CaII network gives a flux of 165 $\mathrm{Wm^{-2}}$ compared to 1275 $\mathrm{Wm^{-2}}$ for the plage regions. This implies that if the total plage region is less than 13% of the stellar surface area then the CaII network becomes the dominate emission source over the plage emission.

By setting up two surfaces relating to the 3950.5Å continuum flux and the CaII emission flux we can generate a S index which is directly comparable to the observed index by taking:

$$S = \frac{\Sigma \mathrm{F_{CaII}}}{\Sigma \mathrm{F_{3950}}} \tag{3.15}$$

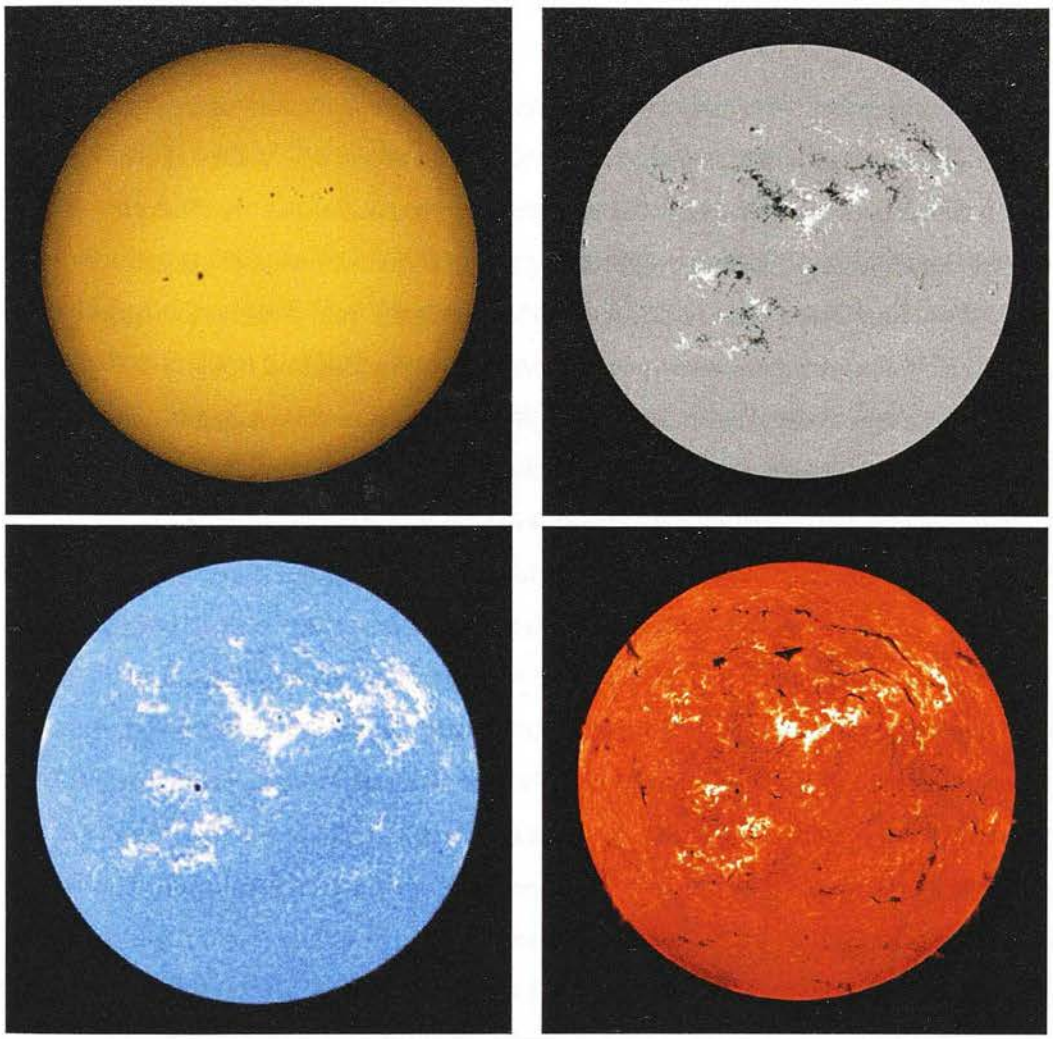

Figure 3.2: The Sun in four wavelengths. Top left hand image is the optical sun, the photospheric continuum shows the cold active sunspot penumbra dark against the non-active quiet photosphere. Top right image is a 'magnetogram' image of the solar chromosphere, grey indicates the quiet surface whereas the black and white areas indicate regions of strong magnetic fields, i.e the plage regions. The white/black colour scheme indicates the polarity of the magnetic fields (north/south respectively). Comparing the top two images clearly demonstrate how the plage regions are not visible at optical wavelengths. The bottom left hand image is the Sun as observed in the CaII K line. This image neatly shows the dominance of the plage emission (white regions) over the penumbral regions and highlights the low level CaII network which takes on the pattern of the supergranulation convection cells (a 'mottled' effect over the quiet chromosphere). The last image, bottom right, shows the Sun in H_α ($\lambda = 6562.8$Å) which highlights more features of the solar chromosphere such as flares and filaments (source: www.bbso.njit.edu).

3.3 Construction of the Models

3.3.1 The HEALPix Software

The basis for our chromospheric activity models is to generate a 'stellar surface', the simplest representation for which is a sphere. To be able to construct various characteristics on the surface the sphere needs to be constructed in such a way that individual 'pixels' can be allocated different values to represent different levels of emission. One invaluable tool for doing exactly this is the 'Hierarchical Equal Area isoLatitude Pixelization' (HEALPix) software. This package was originally devised in early 1997 by Krzysztof M. Górski at the Theoretical Astrophysics Centre in Copenhagen. The prospects of the vast data sets expected from current and future Cosmic Microwave Background (CMB) measuring missions, namely WMAP and Planck, drove the rapid development of HEALPix and the collaborative effort now includes many key cosmologists. Though, clearly the models presented here have nothing to do with the CMB, HEALPix is a clean, effective and versatile way of producing and manipulating a pixelated sphere. As the name suggests the pixelization used produces the subdivision of a spherical surface in which each pixel covers the same surface area as every other pixel, which means the surface is divided without regional dependence. HEALPix allows the user to select the level of partitioning in progressively higher resolution. The resolution of the grid on the sphere is characterised by the parameter 'Nside' which defines the number of divisions along the side of a base-resolution pixel required to obtain the desired grid. The lowest possible (base) resolution comprises of twelve pixels placed in three rings around the poles and the equator, graphically shown in Fig.3.3 by the left hand green sphere, the resolution increases in steps by subdividing each pixel into 4 new ones such that the pixel numbers increase 12, 48, 192, 768 and onwards until 805,306,368 pixels, i.e $N_{pix} = 12 * N_{side}^2$ (due to computational limitations the stellar surface models presented in this chapter use a maximum of 12,288 pixels). The HEALPix pixel centres (represented on Fig.3.3 by the black dots) lie on a discrete number of rings of constant latitude, the number of which is dependent on the selected resolution such that number of rings is equal to $4 * N_{side} - 1$. For example, the simplest grid has 12 pixels and 3 constant-latitude rings, whereas the fourth lowest

resolution (right hand blue sphere in Fig.3.3) has 768 pixels arranged on 31 constant-latitude rings (Górski, Hivon, Banday, Wandelt, Hansen, Reinecke and Bartelmann 2005; Górski, Hivon, Banday, Wandelt and Hansen 2005*b*). All rings which fall between the upper and lower corners of the equatorial base-resolution pixel (i.e the 4 pixels which lie around the equator in the lowest resolution grid) are deemed to be in the 'equatorial zone'. The number of equatorial pixels is given by; $N_{eq} = 4 * N_{side}$. All the other rings are said to be in the 'polar cap regions' and contain differing numbers of pixels depending on their distance from the pole, decreasing towards the pole. Geometrically HEALPix is able to support two number schemes for the pixels, the 'Ring' system where the pixels are counted moving down from the north to the south poles along each iso-latitude ring and the 'Nested' where the pixels are arranged in twelve tree structures corresponding to the base-resolution sized pixels. The choice of numbering scheme depends on the intended application of the HEALPix software, for the models presented in this chapter the Ring scheme is perfectly adequate.

It is not necessary to fully discuss the package's development or abilities for understanding how the software is utilised in this study, it is key to note however that HEALPix contains a suite of routines to read and write FITS formatted data sets and a number of IDL-based facilities for searching the maps and displaying colour coded projections.

3.3.2 The Model Mechanisms

Step one is to generate the sphere with the user selected resolution level. A fixed resolution has not been hard-coded to make the code more versatile, lower resolution spheres are computatively less demanding so can be used as a 'quick look' tool, however higher resolution grids are required to generate more complicated patterns of spots. The IDL HEALPix routine 'pix2ang' is then used to generate the pixel coordinates; the latitude in radians measured southward from the north pole (θ) and the longitude in radians measured eastward (ϕ) (Górski, Hivon, Banday, Wandelt and Hansen 2005*a*). The next step is the populate to surfaces.

To demonstrate, take the simplest case of a star with a single active region. Though on a genuine stellar surface a 'spot' is not perfectly circular, for ease of computation

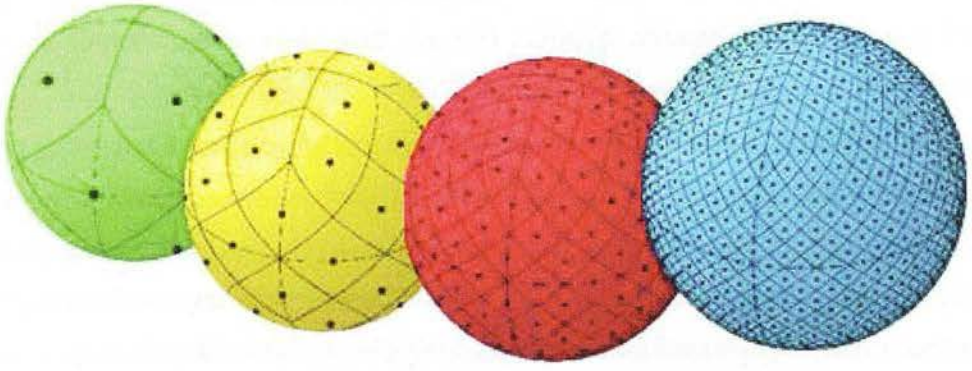

Figure 3.3: This figure graphically represents how the HEALPix package partitions the sphere with progressively higher resolution from left to right. The green sphere (furthest left hand sphere) shows the lowest possible resolution with 12 equal sized pixels, the yellow sphere has 48 pixels, the red sphere 192 pixels and the blue sphere a grid of 768 pixels which translates to $\sim 7.3^{\circ}$ resolution. The maximum resolution possible with the HEALPix package gives a grid of over 805 million pixels. The HEALPix pixel centres (the black dots on the figure) occur on a discrete number of rings of constant latitude, the number of which is dependent on the grid resolution (source: www.healpix.jpl.nasa.gov).

all discrete spots are set to be circular. More complicated active region patterns can be mimicked with multiple overlying spots. The user can either select the 'starting' latitude, $\theta_{\rm spot}$, and longitude, $\phi_{\rm spot}$, for the centre of the spot, or it can be randomly generated. Equally the spot's umbral radius, $r_{\rm umbra}$ can either be user selected or randomly generated within constraints. Both options are useful for different purposes. $\theta_{\rm spot}$, $\phi_{\rm spot}$ and $r_{\rm umbra}$ are fed into the HEALpix idl routine 'query_disc', which finds all the pixels within the disc prescribed by the spot's centre and radius. However, the routine requires the spot centre described in Cartesian co-ordinates rather than polar (θ, ϕ). The conversion between the co-ordinate systems is slightly complicated by the addition of the angle α, which is the angle of inclination between the axis of rotation and the axis of observation. To allow α to be taken into account we need to take the original Cartesian co-ordinates, [x,y,z], perform a single rotation about the y axis and generate a new system [x',y',z'] - doing so by applying a rotation matrix:

$$\begin{bmatrix} x' \\ y' \\ z' \end{bmatrix} = \begin{bmatrix} \cos\alpha & 0 & -\sin\alpha \\ 0 & 1 & 0 \\ \sin\alpha & 0 & \cos\alpha \end{bmatrix} \begin{bmatrix} x \\ y \\ z \end{bmatrix} \tag{3.16}$$

giving equations:

$$x' = x\cos\alpha - z\sin\alpha \tag{3.17}$$

$$y' = y \tag{3.18}$$

$$z' = z\cos\alpha + x\sin\alpha \tag{3.19}$$

Substituting [x, y, z] with the standard transformation equations from polar to Cartesian co-ordinates gives the resulting equations below:

$$x = \sin\theta\cos\phi\cos\alpha - \cos\theta\sin\alpha \tag{3.20}$$

$$y = \sin\theta\sin\phi \tag{3.21}$$

$$z = \cos\theta\cos\alpha + \sin\theta\cos\phi\sin\alpha \tag{3.22}$$

If the angle of inclination, α, is set to zero the above equations resort back to the standard transforms. The sense of the adopted system is shown in Figure 3.4. Axis 'x' is

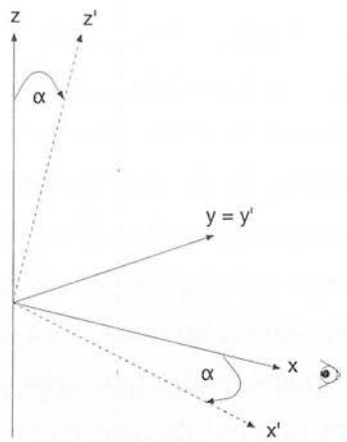

Figure 3.4: Coordinate system adopted for the stellar model code; the x-axis is the axis of observation and the z-axis the axis of stellar rotation. This notation has been used to match that of the HEALPix package. α is the angle of tilt between the axis of stellar rotation and the line of sight for the observer. Translation of the coordinate system from x, y, z to x', y', z' when α is non-zero is derived in the text and results in equations 3.20 to 3.22.

the axis of observation and 'z' the axis of rotation - this notation is adopted to match that of the HEALPix packages, α is set by the user. The 'query_disc' routine does it's

task in a selective manner without scanning all the sky pixels making it less computationally demanding. The output is a list of appropriate pixel numbers to be allocated a different value to distinguish them from the rest of the surface.

The 'query_disc' routine is called three times to generate the required pixels lists corresponding to the plage, the penumbra and the umbra. The area of each region is scaled to the umbral area, such that (see §3.2):

$$\frac{A_{penumbra}}{A_{umbra}} = 3.125; \frac{A_{plage}}{A_{umbra}} = 16.7 \tag{3.23}$$

The area of the umbra can be stated as the area of a spherical cap on the surface of a sphere such that:

$$A_{umbra} = 2\pi(1 - \cos(r_{umbra}))R_*^2 \tag{3.24}$$

where r_{umbra} is the radius 'half angle' in degrees and R_* is the stellar radius. By generating equivalent equations for the other regions the radius half angles for the penumbra and plages as a function of r_{umbra} can be shown to be:

$$r_{penumbra} = \arccos(1 - 3.125(1 - \cos(r_{umbra}))) \tag{3.25}$$

$$r_{plage} = \arccos(1 - 16.7(1 - \cos(r_{umbra}))) \tag{3.26}$$

The model representing the photospheric surface has three pixel values assigned to describe the umbra, the penumbra and the pristine surface. The umbral and penumbral values are scaled to the pristine values as explained in §3.2. As we are only looking for evidence of correlation between the photospheric emission variation and the CaII emission variation the actual value adopted for the 'quiet' pixels is unimportant, it is only the relative values between the spot and the quiet regions that is important. Taking a lead from Grossmann-Doerth and Schmidt (1981) we have chosen to allocate each pristine atmosphere pixel a value of 100, meaning each penumbral pixel receives a value of 75 and each umbral pixel a value of 6 (see §3.2.1 for further details).

The 3950.5Å continuum also has three pixel values assigned to describe the umbra, the penumbra and the 'quiet' surface, with a scaling as detailed in §3.2. However, there is a further complication in that the value of the pristine pixels is subject to stellar

colour. It is not required to calculate F_{3950} for each individual spectral type, the stellar colour changes by sufficiently little which warrants combining each class of spectral type together and using a mean stellar index. Table 3.3.2 gives $\langle(V-R)\rangle$ and the pristine, penumbral & umbral 3950.5Å flux adopted for each spectral type class G, K & M0 – M3. The last surface which represents the CaII H & K emission has a low level

Spectral Type	$\langle(V-R)\rangle$	F_{quiet} (Wm^{-2})	$F_{penumbra}$ (Wm^{-2})	F_{umbra} (Wm^{-2})
G	0.55	298,800	209,160	8964
K	0.94	22,400	15,680	672
M0 - M3	1.44	1,550	1,085	46.5

Table 3.4: Summary of the 3950Å continuum flux as calculated from equations derived by Pasquini et al. (1988) for G, K and early M spectral type stars. F_{3950} depends on the $(V-R)$ colour index which varies with spectral type, see Eqns. 3.12 & 3.13. The flux over the penumbral and umbral active regions is scaled to the flux over the 'quiet' non-active surface such that $F_{penumbra} = 0.7 * F_{quiet}$ and $F_{umbra} = 0.03 * F_{quiet}$, see §3.2.2. What is immediately noticeable is that the flux level changes dramatically with varying spectral type.

everywhere to represent the CaII network except for the plage areas. Pixels out-with the plage regions are given a value of 165 and pixels inside the plage regions a value of 1275 - tying in with §3.2.

Fig.3.5 graphically shows how the stellar surface is constructed at each wavelength for the simplest case of a single circular active region; the upper diagram demonstrates the photospheric surface whereas the lower diagrams, the complimentary chromospheric surface, the left hand side the 3950.5Å continuum flux and the right hand side the CaII flux. Fig.3.5 and all the colour diagrams exploited to depict the model surface properties are orthographic projects generated using the HEALPix IDL routine 'orthoview'. An orthographic projection is a projection on to a tangent plane from infinity which preserves neither area nor angle, each one of the two circles per projection represents a single hemisphere of the projected sphere, i.e. the visible hemisphere and the reverse of the 'star'.

The most effective way of computation to simulate stellar rotation and thus the variation in emission due to rotation is to 'fix' the quiet stellar surface and rotate the spots with respect to the background surface. Hence, in the case of Fig.3.6 with a single spot, the stellar models are 'rotated' and the spot can be seen crossing from one hemisphere to the other as it moves from the 'visible' hemisphere to the 'back of the

star'. In §3.4 'time snapshots' are used to indicate how the various modelled surfaces rotate. As stated, the key output from the models are plots which can be compared

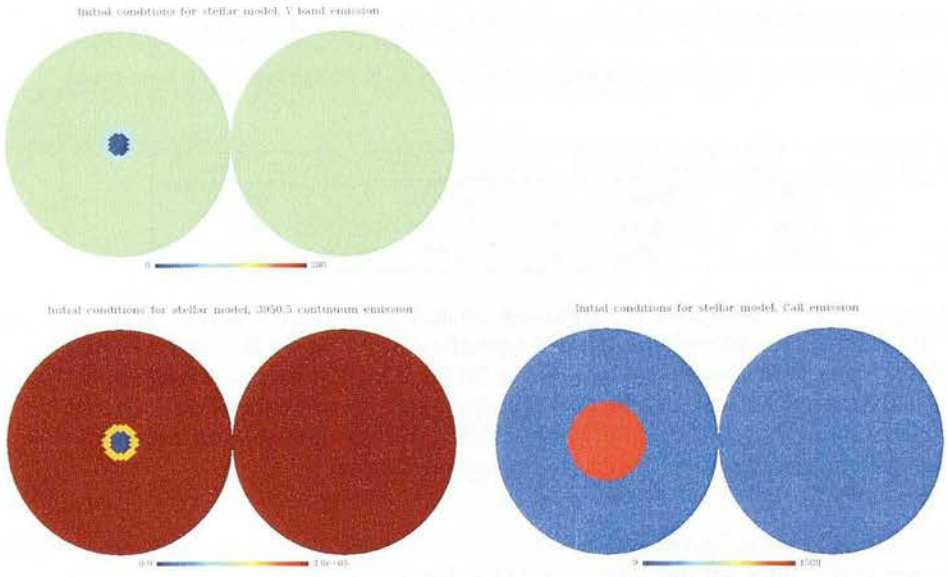

Figure 3.5: Orthographic projection of the initial conditions for the simplest case model in each of the three wavelengths. The top circles show both the visible and 'hidden' hemisphere for the V band flux. The bottom left diagram is the same for the 3950Å continuum flux and the CaII emission is shown in the bottom right hand diagram. The angular radius of the umbra was selected to be $5°$ which results in scaled values for $r_{penumbra} = 8.84°$ and $r_{plage} = 20.54°$. The spot was placed on the stellar equator, $(\theta_0, \phi_0) = (90, 0)$, and with no tilt angle, $\alpha = 0.0$. The fractional coverage of the stellar surface of an active region of this radii is calculated to be $A_{umbra} = 0.19\%$, $A_{penumbra} = 0.59\%$ and $A_{plage} = 3.18\%$.

with those from the observations presented in Chapter 2, variation of chromospheric S index, variation in light intensity and the correlation between them. To generate the light curves and CaII emission plots the total amount of photospheric and chromospheric flux (then converted into a S index as per equation 3.15) over the visible stellar surface must be integrated at appropriate time intervals. The value of every visible pixel must be added together, however a distortion factor must first be applied to account for reduction in emission received at the observer dependent on location of the emitting pixel. More flux from a pixel at the centre of the visible hemisphere directly in observers line-of-sight will reach the observer than flux from a pixel at the edge of the visible surface due to projection effects. Fig.3.7 can be used to explain the

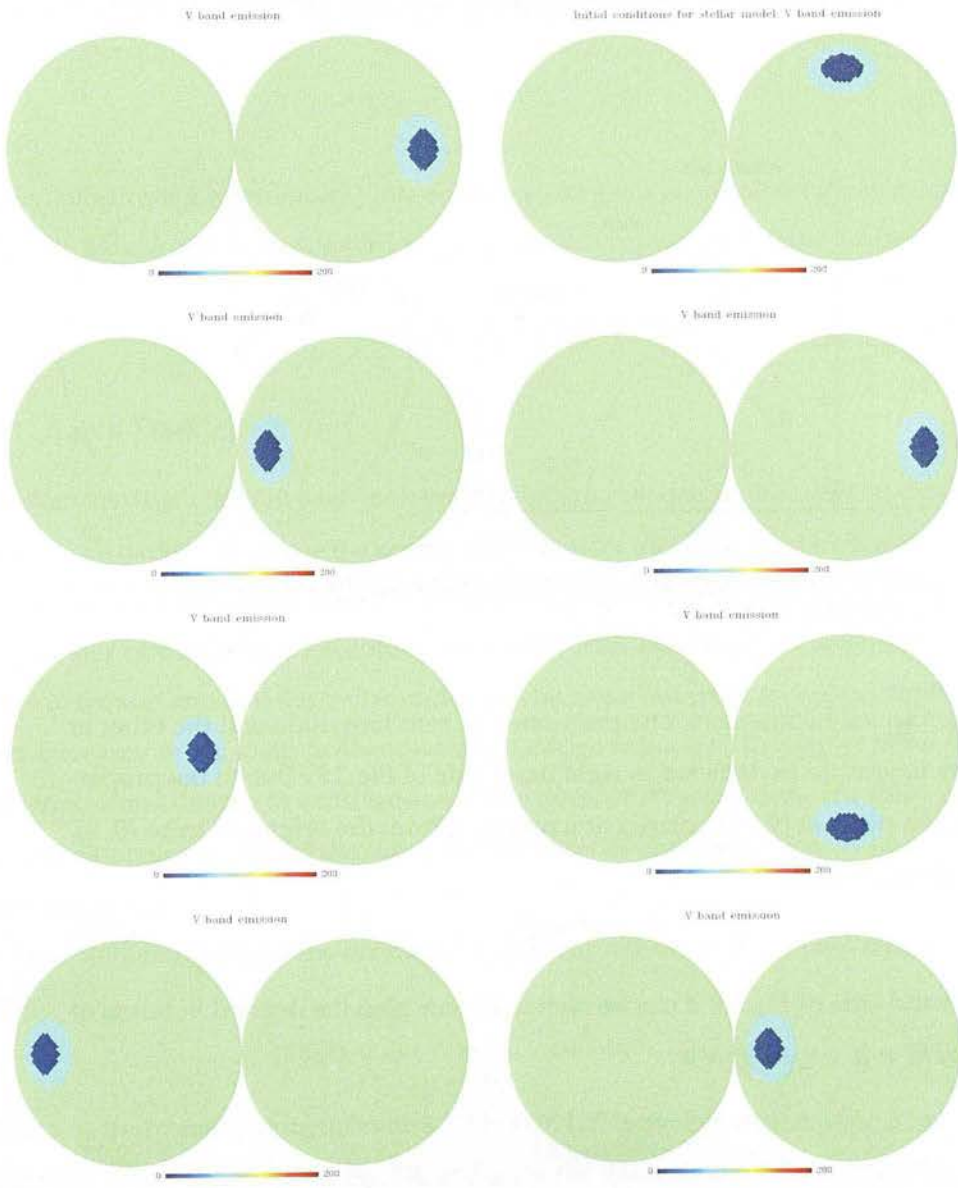

Figure 3.6: This figure graphically demostrates how the spots move with respect to the observer due to stellar rotation. The left hand four plots (starting from the top) show an active regions with $(\theta_0, \phi_0) = (90, 0)$ passing firstly across the visible hemisphere then onto the 'back' of the star, the hemisphere not visible to the observer. The tilt angle, α, is set to be zero in this case. The right hand four plots show how the tilt angle can effect observational outcomes. In this case the active region is set to have $(\theta_0, \phi_0) = (45, 0)$ but the tilt angle is set to $90°$. The observer is effectively looking directly at the northern plot along the axis of stellar rotation. As the star rotates the spot remains on the visible hemisphere at all times. In this extreme case though enhanced CaII emission is observed due to the active region there is no variation of the chromospheric or photospheric light with stellar rotation. If $\alpha = 270°$ then the observer would be looking at the southern pole and the region would not be visible at any time.

derivation of the distortion factor. Take two equal area pixels at a distance, R, from the

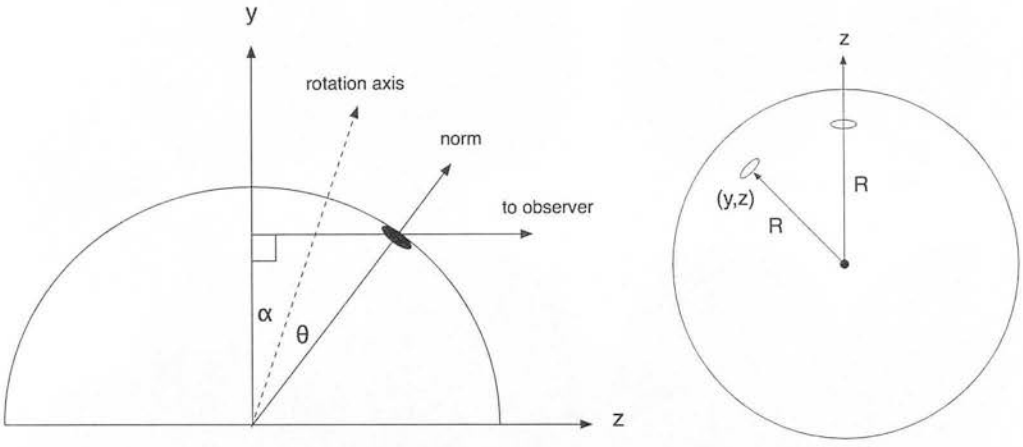

Figure 3.7: Diagrams showing angles and coordinate systems for the derivation of the 'projection factor'. See text for explanations.

centre of the projected hemisphere, one positioned at zero longitude and the other at some arbitrary longitude as depicted in right hand side of Fig.3.7. Due to the properties of a circle if a point at (y, z) is placed at a radius, r, from the origin set to be (0, 0), then r can be described as:

$$\mathrm{r}^2 = \mathrm{y}^2 + \mathrm{z}^2 \tag{3.27}$$

From the left hand side of Fig.3.7 if can be seen that r can also the defined in terms of α and θ, where $\mathrm{X} = \alpha + \theta$, as give by:

$$\mathrm{r} = \cos(\mathrm{X}) \tag{3.28}$$

The 'area projection factor' is effectively the angle between the normal to the pixel in questions and the observer which is given by:

$$\mathrm{df} = \sin \mathrm{X} \tag{3.29}$$

Utilising the trigonomic identity, $\cos^2 \mathrm{X} + \sin^2 \mathrm{X} = 1$ the distortion factor can be written as:

$$\mathrm{df} = \sqrt{1 - \cos^2 \mathrm{X}} \tag{3.30}$$

Substituting equation 3.27 into equation 3.28 gives:

$$\cos^2 \mathrm{X} = \mathrm{y}^2 + \mathrm{z}^2; \mathrm{X} = \alpha + \theta \tag{3.31}$$

Finally, substituting equation 3.31 into equation 3.30 gives the resultant useable equation, 3.32, for calculating the distortion factor for each pixel on the stellar surface:

$$\mathrm{df} = \sqrt{1 - (\mathrm{y}^2 + \mathrm{z}^2)} \tag{3.32}$$

3.3.3 Limb Darkening

One element which has not been incorporated into our models of the stellar surface is that of 'limb darkening'. Limb darkening is the term for the diminishing intensity of a star measured as one moves from the centre to the edge. It is the result of the effective temperature of the stellar atmosphere decreasing with increasing distance from the centre of the star and that the stellar radius at which one can see to an optical depth of unity increases as one looks further towards the edge of the star. In simpler terms the temperature and density of a star reduces as the distance from the centre increases and the intensity reduces. Fig.3.9 demonstrates the effect of limb darkening on an optical image of the sun.

Limb darkening can be approximated by a linear relation of the type (Frasca et al. 2005):

$$\mathrm{I}(\theta) = \mathrm{I}_0 * (1 - \mu_\mathrm{V} + \mu_\mathrm{V} \cos\theta) \tag{3.33}$$

where I_0 is the intensity from the centre of the star, $\mathrm{I}(\theta)$ is the intensity coming from the direction θ to the observer (see Fig.3.8) and μ_V is the linear limb darkening coefficient for the V band ($\mu_\mathrm{V} = 0.77$, Diaz-Cordoves et al. 1995). The effect of limb darkening is very small in real observing conditions. In Fig.3.8 the observer is stationed at position P, a distance r from the centre of the star. As r tends to large distances, the angle θ increases to very small angles even at the very edge of the star. Hence, the drop in intensity at the edge of the star is a fraction of a percent from the intensity at the centre. Our models are dealing with first order effects as we are trying to understand the broad, orders of magnitudes, variation in the CaII emission and limb darkening is

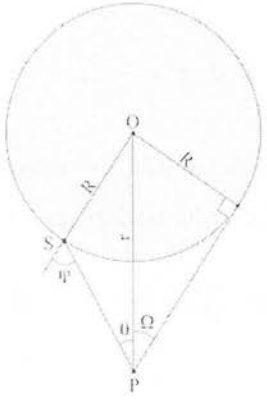

Figure 3.8: Diagram showing angles and corodinate system for Eqn.3.33, the effect of limb darkening on I(θ).

such a small effect in this context that it has been left out of the models.

3.4 The Models

3.4.1 Graphical Demonstration of the Models

Figs.3.10 to 3.11 show the graphical output of each of the three surface models for three different scenarios for the population of the surface with active regions. Fig.3.10 is the simplest case of a single active region, for this example the spot is at low latitudes mimicking an active region covering the southern pole. Fig.?? shows the surface populated with 10 active regions though not all the regions are discrete. The model code selects each region's initial location, (θ_0, ϕ_0) with no restrictions, hence more complicated regions are simulated when two circular regions are overlaid. With multiple spotted surfaces the key difference to note between the three wavelengths is the extent of the surface the plage regions cover in comparison to the total penumbral surface area. Fig.3.11 shows a surface generated by 30 randomly placed active regions, though again not all regions are discrete. An upper limit of fractional coverage of the stellar surface by patterns of active regions generated by 30 spots is 22.8% for the umbral regions, 71.25% for the penumbral regions and complete coverage by the plage regions. However, this is only achieved if there are no overlapping to the circular

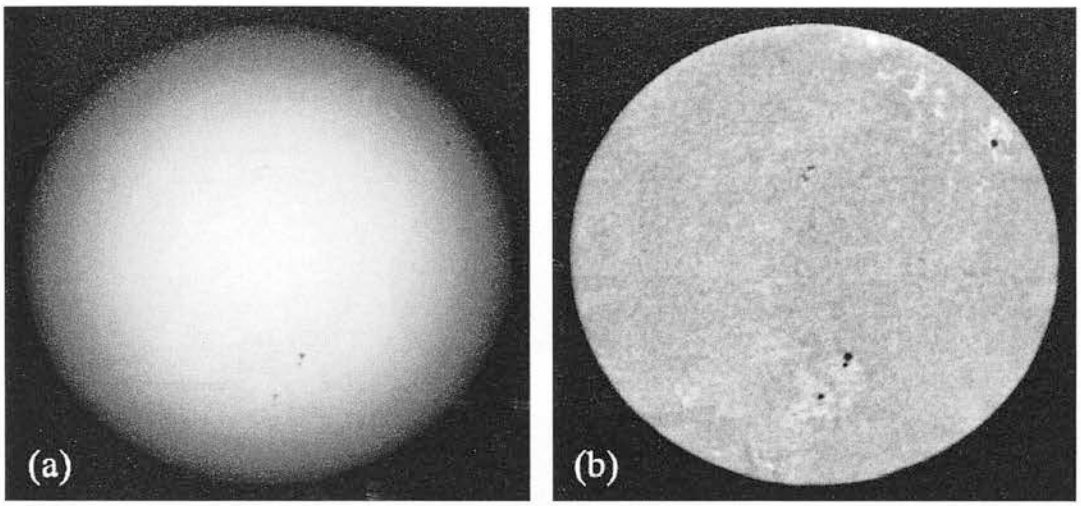

Figure 3.9: Simple demonstration of the effect of limb darkening on an image of the Sun. The left hand image, (a), shows the Sun with no correction for limb darkening, highlighting the diminishing intensity towards the 'edge' of the Sun. The right hand image, (b), is the same image corrected for limb darkening, the intensity is now 'smooth' over the whole solar disc.

spots, Fig.3.11 clearly demonstrates this is an upper limit as many spots overlap.

Figs.3.12 to 3.14 give the resultant three plots from the three cases shown in Figs.3.10 to 3.11: the V magnitude light curve, the CaII S index variation curve and the correlation between the two varying quantities. These plots can be directly compared to the results from our spectroscopic and photometric observations presented in Chapter 2. The simple case of a single active circular region, shown in Fig.3.12, clearly shows how the light emission dims as the CaII emission enhances when a star spot passes across the visible stellar hemisphere. In all three cases there is a negative correlation of normalised photometric flux to CaII S index, as expected. When more complicated and extensive patterns populate the surface the model can result in a 'scatter' about the linear correlation similar to that seen in the observations, see Fig.3.4.1. This indicates the scatter is not only due to processes such as flares and measurement errors but there is a factor purely due to the regions passing in and out of view.

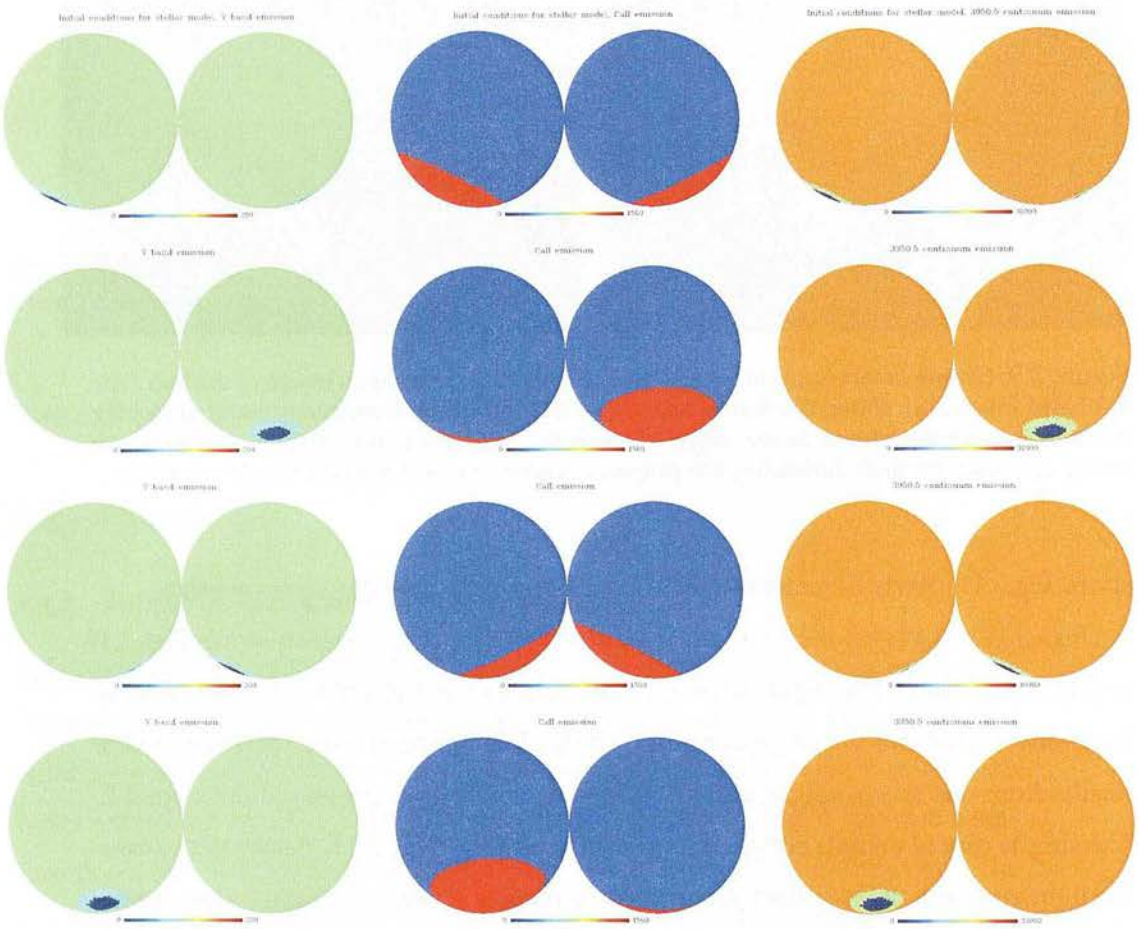

Figure 3.10: The simplest case: single circular spot and $\alpha = 0.0$. Each row shows the three surface models for each wavelength at a given time step, starting with the initial conditions on the top row. Each column shows the star rotating over time for each given wavelength. The left hand column is the photospheric V band continuum, the middle column the CaII emission and the right hand column the 3950Å continuum. Each diagram has an associated colour bar underneath. The resultant plots from this scenario can be found in Fig.3.12.

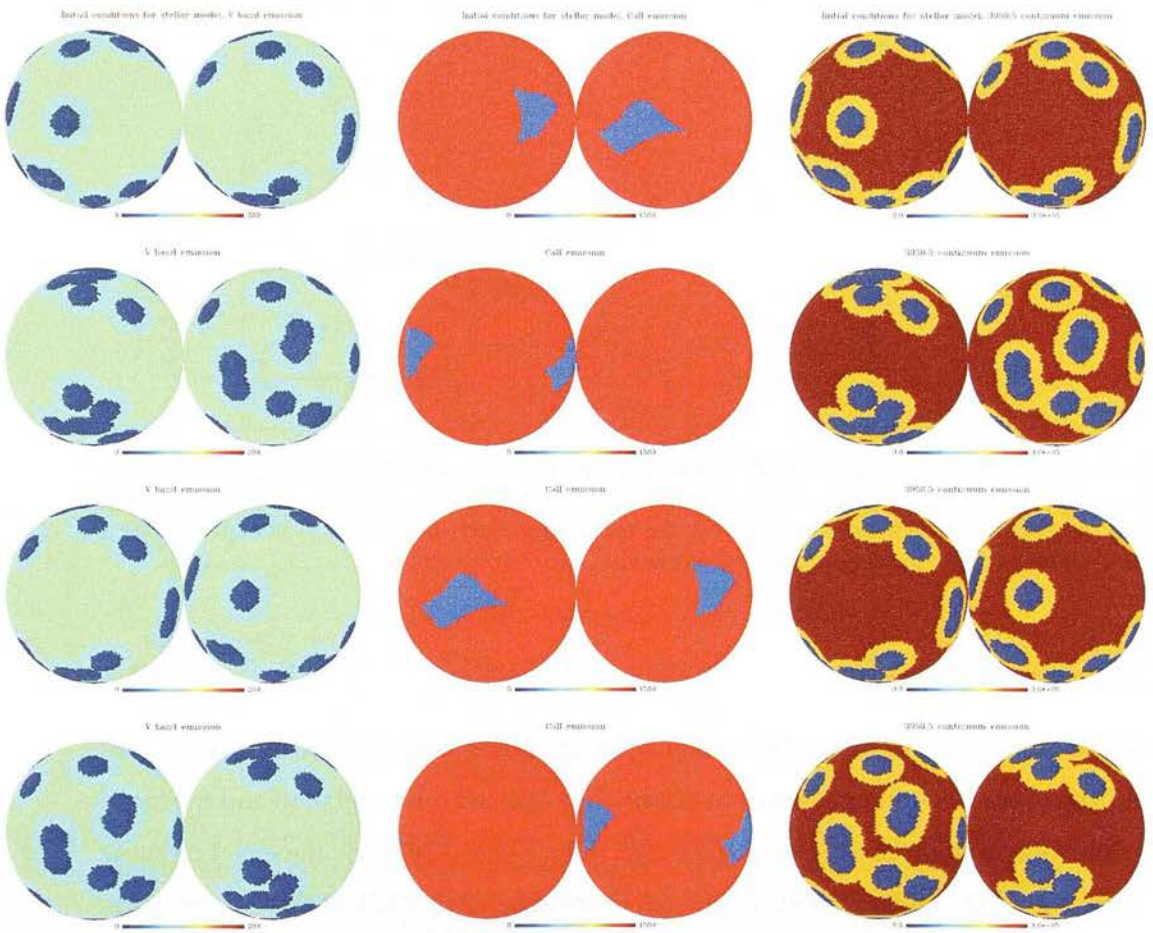

Figure 3.11: As for Fig.3.10 but with multiple active regions. The more complex non-circular regions are simulated when 'spots' overlay each other. Care has been taken when writing the code structure that overlaying spots 'merge' together such that umbral areas are not incorrectly over written by penumbral areas. In this case the upper limit for the fractional area of the stellar surface covered by penumbral regions is 71.25%, however is this only achieved if all the spots are discrete which is not the case. So much of the stellar surface is covered in active regions that there is nearly complete coverage by plage regions and enhanced CaII emission. Resultant plots from this scenario can be found in Fig.3.14.

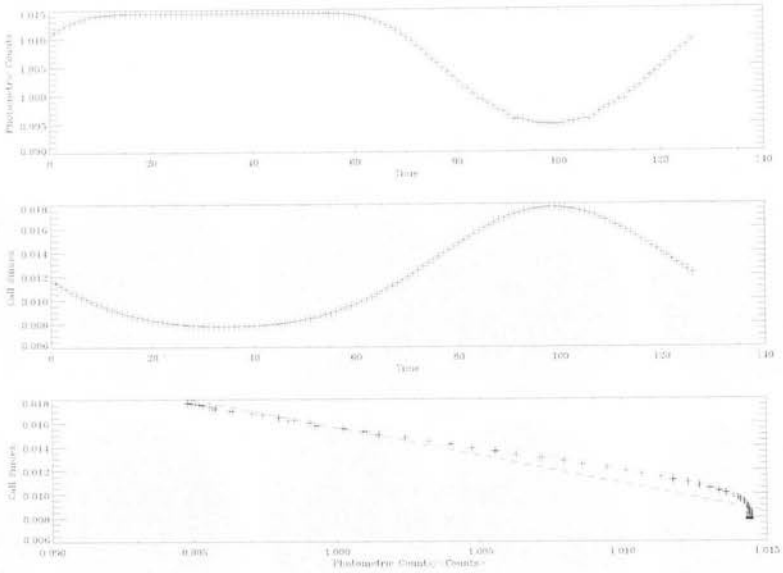

Figure 3.12: Resultant plots for the simplest case. The three graphs are: light curve, CaII S index curve and the correlation between the two variations. In the bottom graph the dashed line represents the best straight line fit to the correlation data. Behaviour is as expected for a single active region passing in and out of view.

3.4.2 Surface Features

Before comparing the models directly with the observational data the model was utilised to see how changing various parameters effected the correlation and the mean value and variation of the S spectral index. Figs.3.15 & 3.16 show the effect on these three quantities when changing the size of a single spot and the number of spots, respectively. In each figure the top graph show the slope $(\delta S/\delta \mathrm{V})$ for the linear correlation with increasing parameter, the middle graph the mean S index with increasing parameter and the bottom graph the spread of the S indices $(\sigma_S/\langle S \rangle)$ with increasing parameter.

Firstly, the model was run with a single circular active region located at θ_0=90 (i.e. on the stellar equator) with an umbral radius of 5° to 25° in 2.5° steps. From $\mathrm{r_{umbra}} = 10^\circ$ upwards the correlation steadily tends towards 0.0, i.e. it becomes less steeply negative, and the mean S index steadily increases. This is expected because with a larger region of activity the CaII emission is entirely dominated by the rapidly

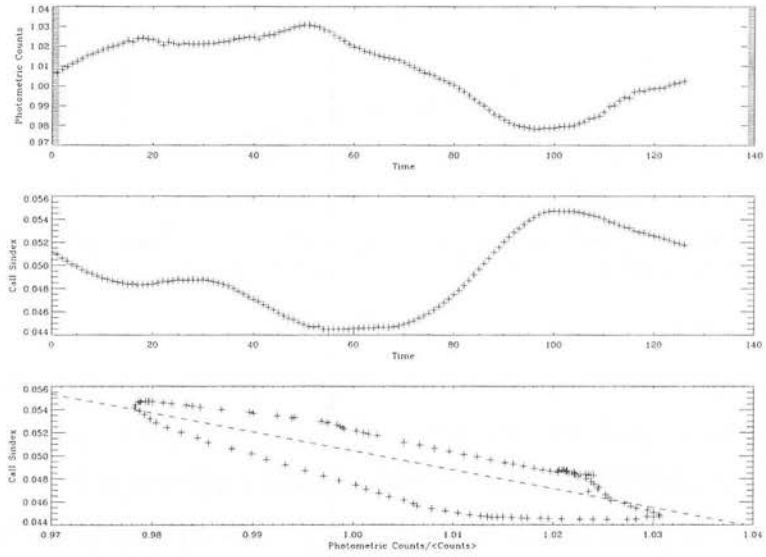

Figure 3.13: As Fig.3.12 for the multiple active region case presented in Fig.??. Most interestingly, though there is a clear correlation between the CaII and V band variations there is a distinct 'scatter' about the linear correlation. Evidence of a scatter about a linear correlation in real observation data was found in studies of the ρ Oph cluster. This scatter could in part be due to the effect of such large plage areas which dominate the CaII emission with respect to the umbral area which dominate the photospheric emission.

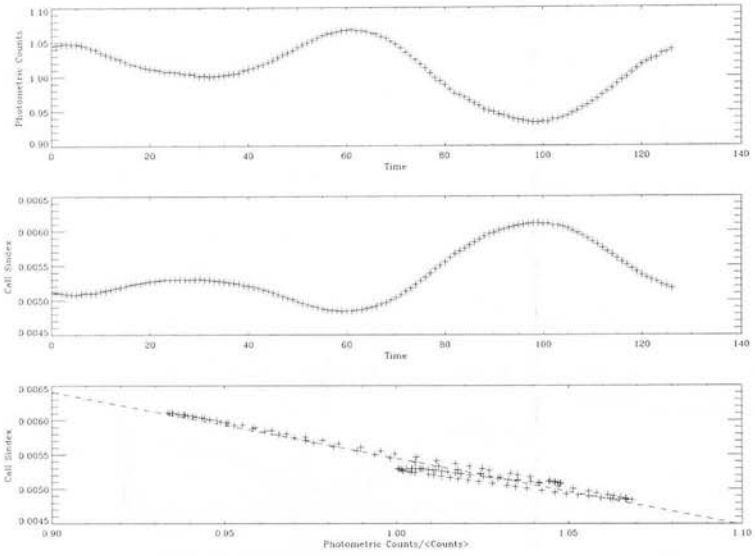

Figure 3.14: As Fig.3.12 for the multiple active region case presented in Fig.3.11. As expected the S index is stronger when more of the surface is covered in active regions.

increasing plage region whereas the photometry is dominated by the relatively small umbral region. Below $r_{umbra} = 10^{\circ}$ the behaviour is slightly different. For $r_{umbra} = 10^{\circ}$ the fractional umbral area is 0.76% of the stellar surface which implies the penumbral area is 2.38% and plage covers 12.69% of the stellar surface. As explained in §3.2.3 when the active region is smaller than 13% of the stellar surface it is the low level CaII network which dominates the CaII emission not the enhanced emission above the plage regions.

Secondly, Fig.3.16 shows the three plots as the pattern of active regions is generated by increasing numbers of spots. For simplicity of coding and understanding each 'spot' is of the same size, $r_{umbra} = 10^{\circ}$, selected as it is the point at which the plage region begins to dominate the CaII emission. Each spot is randomly placed on the surface by the programme which leads to some scatter in the plots but general trends are clear. On each occasion the tilt angle $\alpha = 0.0$. As the number of spots increases both the slope of the linear correlation and the mean S index tend to a 'maximum' value whereas the deviation of the S index tends to a 'minimum'. The greatest rate of change in the plots occurs from the single spot case to 10 spots. In terms of fractional coverage

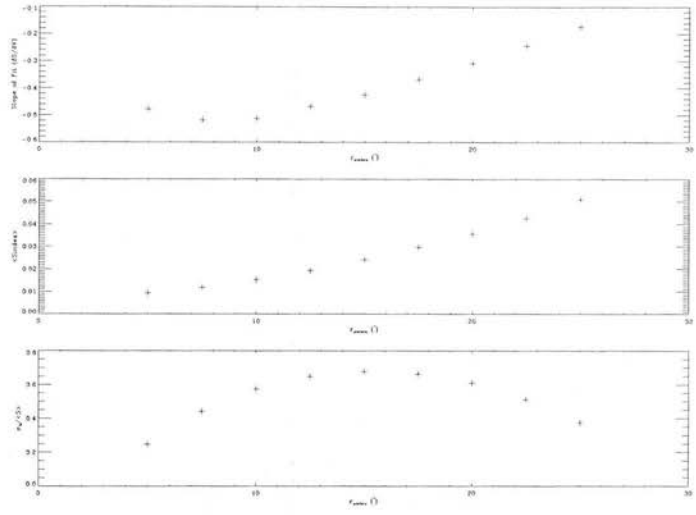

Figure 3.15: Investigating how changing spot size affects the outcomes of the model. The top plot shows change in slope of the linear correlation with increasing spot size, middle graph change in mean S index with increasing spot size and finally change in the spread of the S index values with increasing spot size.

of the stellar surface, 1 spot to 10 spots translates into upper values: A_{umbra}=0.76% to 7.6%, $A_{penumbra}$=2.38% to 23.8% and A_{plage}=12.69% to complete coverage. There is a 'levelling off' point at 25 and greater spots where the upper umbral fractional area is 19% and the upper penumbral area is 60% of the stellar surface, so much of the stellar surface is covered in active regions that the variation with rotation is greatly diminished.

3.5 Comparison: Theoretical and Observational Data

Given the model outputs have been investigated to verify that it behaves as anticipated the next step is comparison with observational data to facilitate a comprehension of what may be occurring on real T Tauri stars. The stellar sample observed in the ρ Oph and Upper Sco clusters have been separated into WTTS, CTTS field and binary targets in §2.10. From now on we are only going to consider the weak and classical T Tauri stars which are known to be single targets. Field stars were only included in the target sample to clarify that any correlation seen in the pre-main sequence stars was

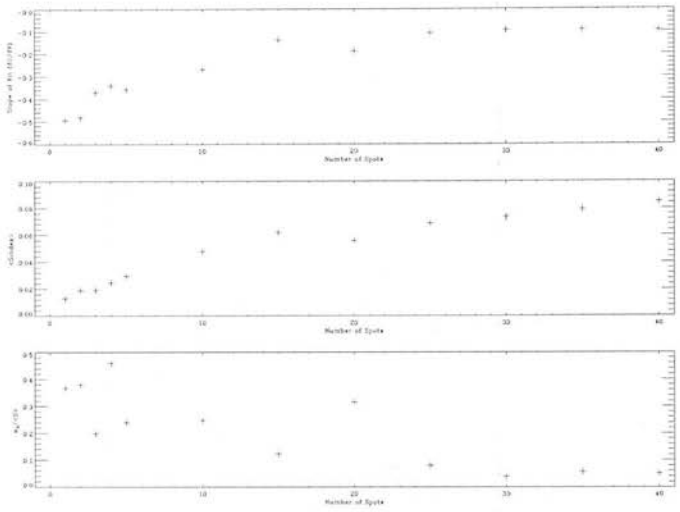

Figure 3.16: As for Fig.3.15 but increasing the total magnetic active coverage by adding more and more 'spots' randomly on to the surface to create more complex and extensive patterns.

due to active regions, and are not of interest for this section. Binary targets are situated in too complicated an environment to be easily understood with these straight forward models. Investigating binary targets may prove a worthy extension of this research in the future.

Observationally, weak line T Tauri stars are the ideal candidates for this investigation as their chromospheres are easily accessible with no substantial circumstellar debris disks and dust clouds which are often seen round classical T Tauri. However, it is still worthwhile to consider the CTTS sample in comparison to the models. Fig.3.17 shows the WTTS sample plotted with various examples of the model output. Each symbol represents spectral class G, K or M with the open symbols showing the 6dF/APT data and the filled symbols the model outputs. The top graph gives mean S index versus slope of the correlation and the bottom graph plots the deviation of the S index values ($\sigma_S/\langle S \rangle$) against slope. Fig.3.18 shows the same for the CTTS sample; note we only observed K type CTTS. The points generated for the models were a selection of different surface features and a selection of tilt angles with respect to the observer to give a good range of possible outputs.

Immediately the first result to note with the WTTS sample is that for G and K type

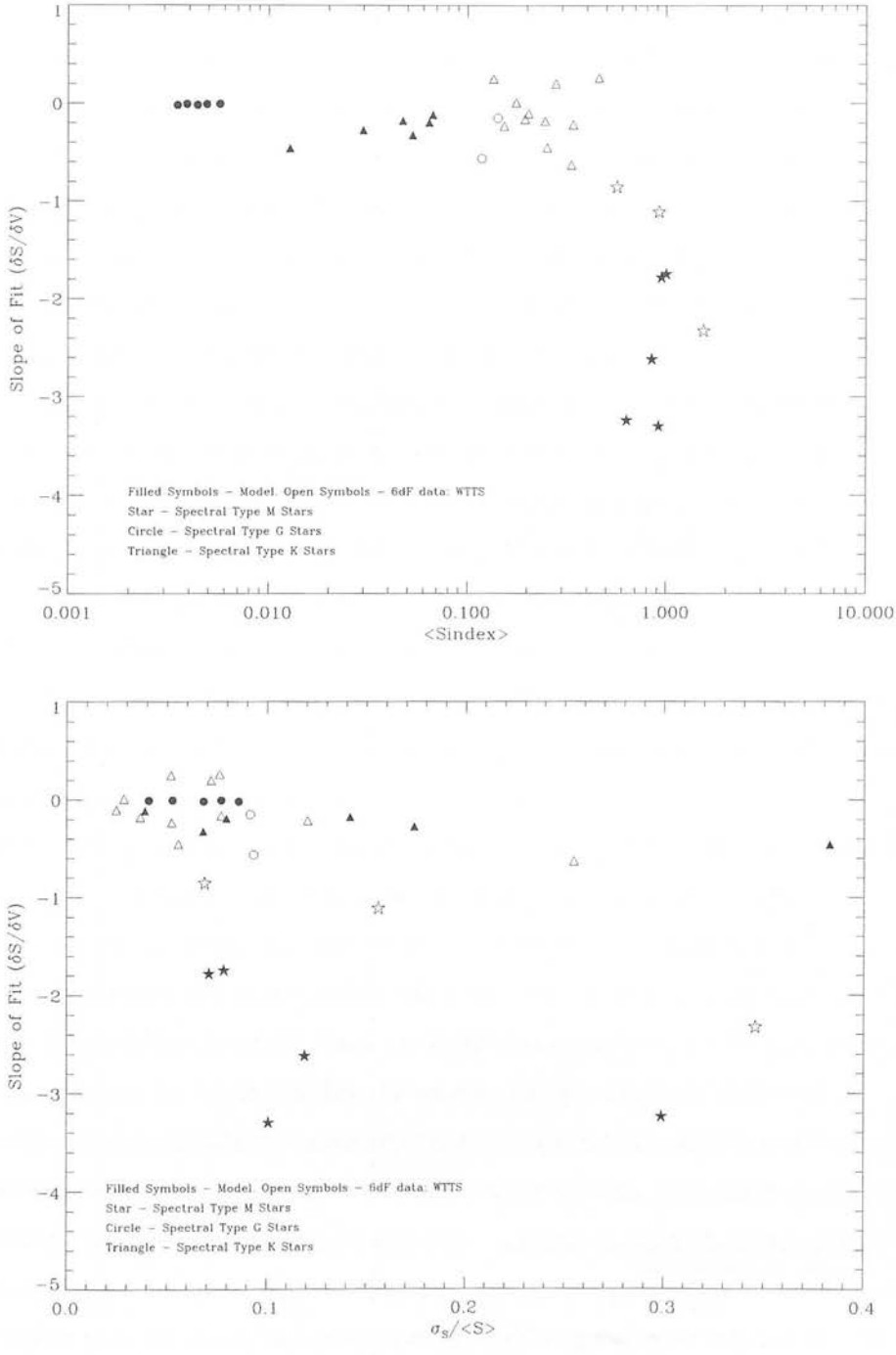

Figure 3.17: Weak line T Tauri sample observed in the ρ Oph and Upper Sco clusters with 6dF (presented in Chapter 2) plotted with resultant outputs from the stellar models. The different symbols represent different spectral types; G, K or M (key on the graphs). The open symbols are the 6dF observational data and the filled symbols those from the models. The model was run with a number of different surface patterns and tilt angles to get a good representation of the range of outputs.

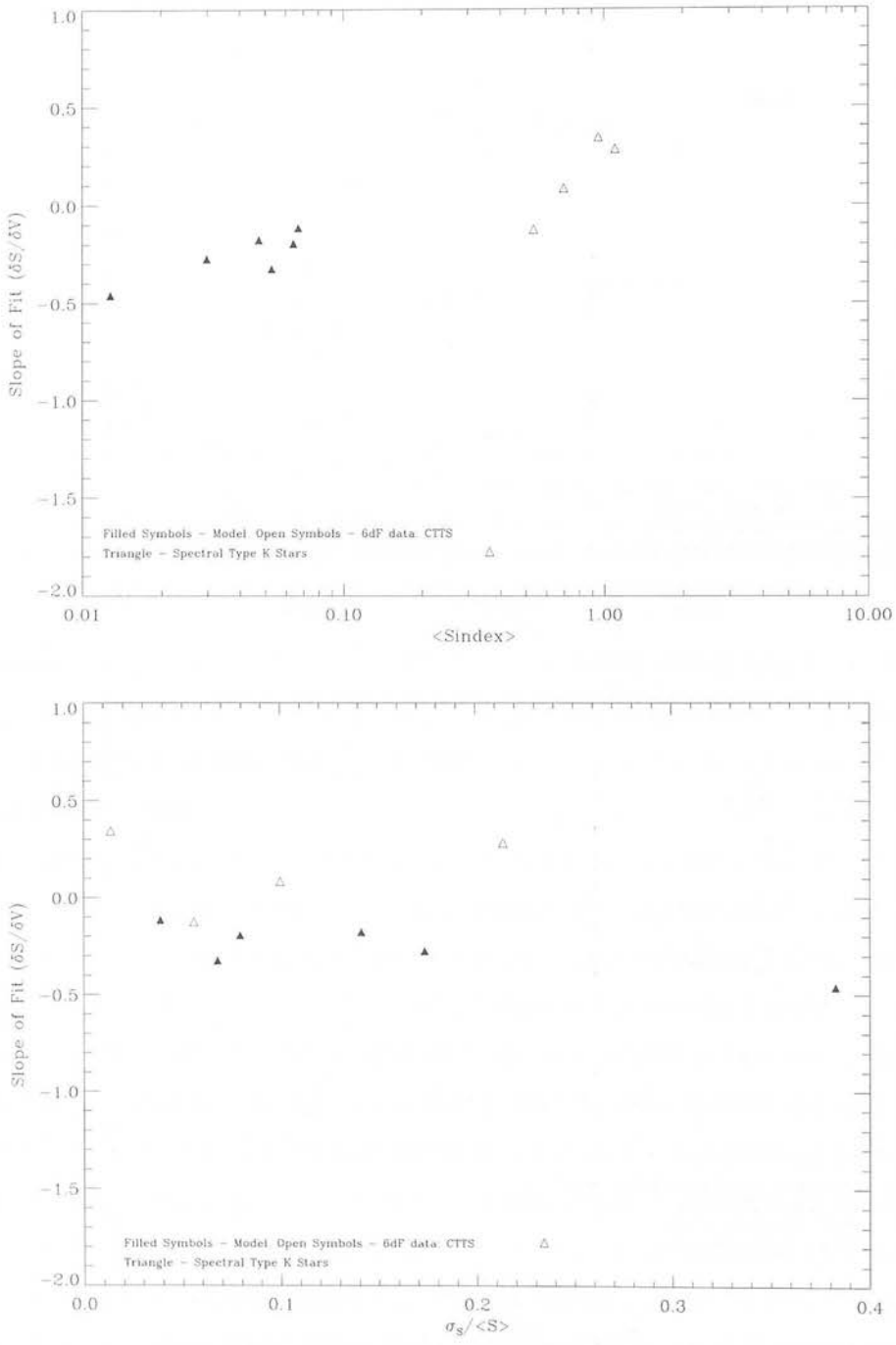

Figure 3.18: As Fig.3.17 for the classical T Tauri sample observed in ρ Oph association. Only spectral class K classical T Tauri stars were observed.

stars the mean S index values are greatly underestimated by the models. The mean S index for G type stars from the model all come out ~ 0.005 whereas the two G type WTTS observed have a $\langle \mathrm{Sindex} \rangle \sim 0.1$. Similarly with the K type stars, the model $\langle \mathrm{Sindex} \rangle$ came out in the range $0.01 - 0.09$ and the observed $\langle \mathrm{Sindex} \rangle$ is in the range $0.2 - 0.5$. The slope of the correlation is also greatly underestimated by the model for G type stars compared to the observational data. For M type stars the model mean S index came out in the same range as out observed stars but the slope of the correlation is slightly overestimated. The models do however estimate the variation in S index for WTTS quite correctly, bottom graph Fig.3.17. The CTTS target sample, Fig.3.18, resulted in very similar findings. The mean S index is underestimated by the stellar model but the variation in S index is well estimated. As expected the slope of the correlation is not well matched for the CTTS sample as the correlation is altered by accretion hot spots from surrounding debris disks. The mean S index for K spectral type stars can be pushed up to reach the lower values of the observed S indices by covering nearly the whole stellar surface in active regions, but this does not give a value for the spread of the S index values consistent with the observations. It is not possible to simulate the observed mean S index for G type stars with the model regardless of how much of the surface is covered in active regions.

These findings suggest that either the determination of the 3950Å continuum flux as derived by Pasquini et al. (1988) for main sequence stars is not appropriate to use for pre-main sequence stars and the flux is actually weaker, or that the magnetic fields which produce the active regions are stronger on T Tauri stars than in the Sun. Stronger magnetic fields would cause stronger CaII emission over the plage regions and thus enhance the mean S index. However, stronger magnetic fields would suggest more of the photospheric convection in the spot would be suppressed leading to less photospheric emission and colder effective temperatures. Doppler imaging studies currently suggest the effective temperature in spots on T Tauri stars is similar to that measured in Sunspots but it understood that these young stars are more active and variable than the Sun which in itself suggests stronger magnetic fields. It is likely to be a combination of these effects which results in an underestimation of the CaII S index.

3.5.1 Fractional Coverage of the Stellar Surface

The key question we set out to get a better understanding of at the start of this research is: "What fraction of the young stellar surface is covered by regions of magnetic activity". Running the stellar model with increasingly larger portions of the surface covered in active regions and comparing against the observational data gives the indication that T Tauri stars have much higher fractional coverage than is observed on the Sun.

Our observational pre-main sequence sample contained 16 spectral classified K stars but only 2 G type & 3 M type stars. To claim general conclusions about fractional coverage for G and M type T Tauri stars with so few observations is not robust so for the remainder of this section we will only contemplate the K type stars.

Firstly, the CaII emission in the models was adjusted to raise the mean S index to match the observational data (see§3.5). It was found that an increase of magnetic fields in the plage regions from 150 Gauss to 1500 Gauss and around the CaII network from 5 Gauss to 50 Gauss moved the modelled mean S indices into the correct range. The model was then run multiple times with increasing active regions and different tilt angles. Fig.3.19 plots the model outcomes along with the K type WTTS and CTSS observational data, the top graph is mean S index versus slope and the bottom graph is S index variation versus slope. In both plots the filled star symbols represent the weak-line T Tauri and the open star symbols the classical T Tauri sample. All other symbols represent the models run with active regions made up of 15, 20, 25, 30, 35 and 40 $r_{umbra} = 10^{\circ}$ spots (key in the figure caption). In each case the programme was run three times with inclination angle $\alpha = 0^{\circ}, 17^{\circ}$ and 62°.

All scenarios plotted have mean S indices within the range of the WTTS sample, however this is not a genuine 'result' as the CaII emission was enhanced unscientifically to obtain this. The model is not able to reproduce the spread of the mean S indices seen in the observational sample. It is clear that only stars with patterns of active regions made up of 25 or more 'spots' have a correlation between the light variation and the variation in the S index comparable to the observed data. Those with patterns of 15 and 20 spots (cross and asterisk symbols respectively) have too steep a

correlation. This suggests that our T Tauri sample have fractional coverage of 50% upwards of penumbral area. With this level of coverage the strong plage CaII emissions covers most of the stellar surface.

The measured slope from the model does not get beyond ~ -0.4 regardless of fractional coverage, ~ 0.2 lower than the majority of the observed sample. The slope measured through the observations can be washed out by accretion and extreme angles of inclination, the model does not simulate hot spots due to accretion and though tilt angle does effect the modelled slope this effect is reduced when more of the star is diffusely covered. This may indicate that the genuine surfaces are covered in fewer but larger active regions which have similar total fractional coverage. The bottom plot demonstrates that the deviation of the S indices is correctly estimated by the model in all cases which further suggests that the discrepancy between the modelled and observed slopes is mainly due to non-accurate modelling of the photospheric variation.

The main conclusion from these models is that the T Tauri surfaces are highly covered in active regions of $> 50\%$. This finding is in agreement with the few studies previously carried out. Though T Tauri stars are frequently observed, studies often target the parameters of individual spots. Casali (2003) found high resolution infrared spectroscopy of T Tauri in the Ophiuchus association implies fraction coverage of greater than 50% by cool magnetic regions, Doppler imaging studies by Joncour, Bertout and Menard (1994) found $\sim 60\%$ of the stellar surface of V410 Tauri to have active regions and Joncour, Bertout and Bouvier (1994) found through Doppler imaging that T Tauri HDE283572 had a single visible spot covering $\sim 15\%$ of the stellar surface and a high angle of inclination.

The modelling also indicates that the magnetic fields over magnetic regions on T Tauri's are much stronger than those measured on the Sun in agreement with Zeeman broadening observations by Valenti and Johns-Krull (2004).

This research can be progressed in the future by extending the observational data set to include many more T Tauri stars over a range of spectral types in nearby, well constrained clusters. The larger the observational sample the more opportunity to make well formed general conclusions that are not skewed by the more unusually

behaving targets. The stellar models have the scope to be developed further in sophistication in describing the T Tauri surface including the inclusion of hot spots due to accretion from circumstellar disks. The models may also prove to be a very useful tool for future investigations into the relative areas or relative luminosities of the umbra, penumbra and plage regions which may not be the same as the solar values which have been adopted here. As more knowledge is gained regarding the magnetic field strength and the nature of the chromospheric continuum flux on young pre-main sequence stars, the models will become stronger tools.

This the first time a large photospheric and chromospheric CaII variation study has been used to estimate the geometry of non-resolvable magnetically active regions on young stars. It offers a viable way of simultaneously studying a large number of targets in practical observing time scales and concurs with other studies that large fractions of the PMS surface is covered in active regions.

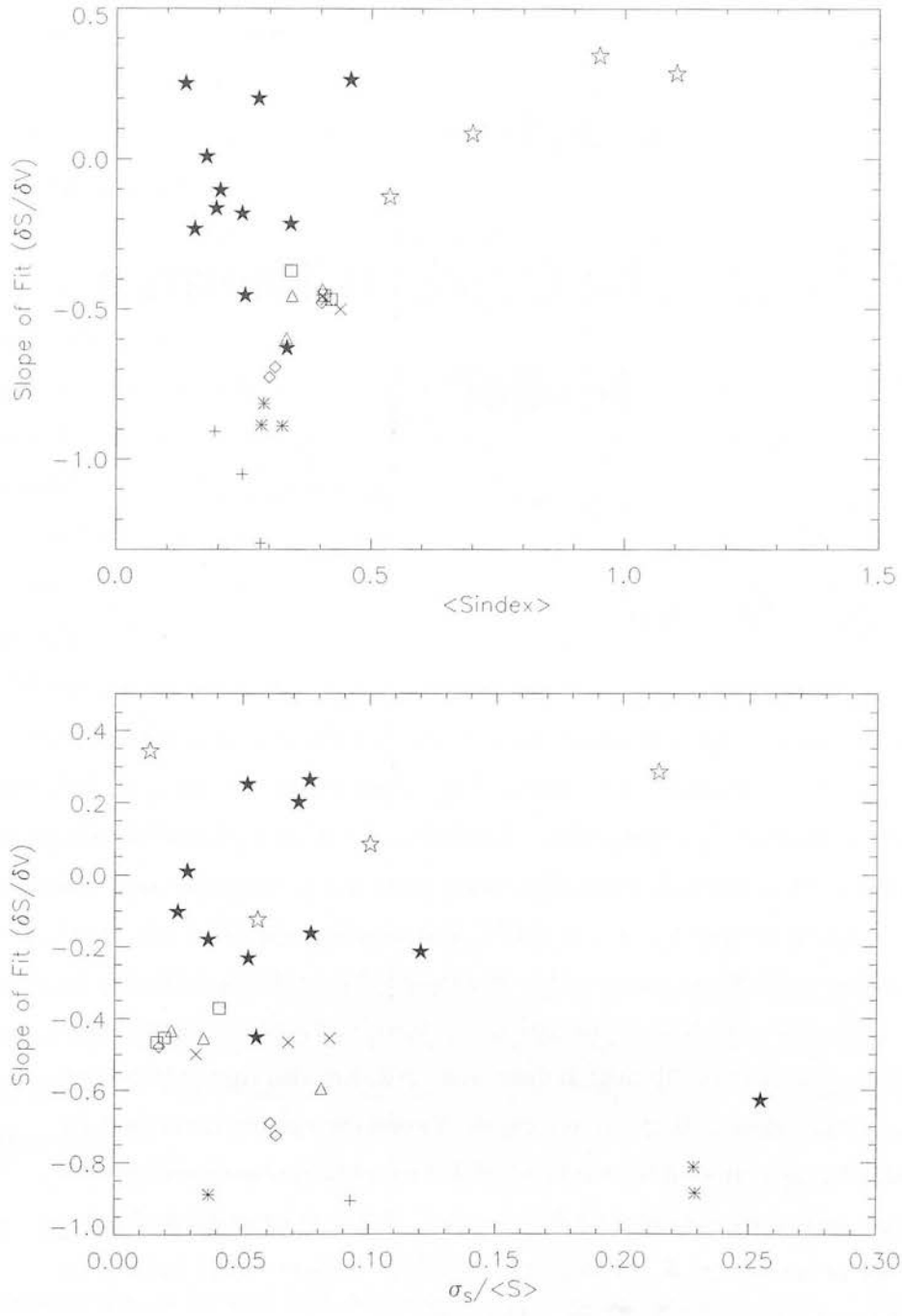

Figure 3.19: The K type WTTS and CTTS sample plotted with the models run with enhanced CaII emission. The filled star symbols are the weak line stars, and the open star symbols are the classical T Tauri. The other symbols show the result from running the models with increasing fractional coverage of the stellar surface with active regions generated using: 15 spots (plus sign), 20 spots (asterisk), 25 spots (diamond), 30 spots (triangle), 35 spots (square).

Chapter 4

WFCAM & The Cryostat Thermal Model

4.1 Instrument Overview

The Wide Field Camera (WFCAM) is an infrared camera installed on the UK 4m infrared telescope (UKIRT) designed and constructed by the UK Astronomy Technology Centre (UKATC) in Edinburgh, Scotland. The project began in earnest in 1999 with first light on the telescope being achieved in October 2004. At the time, WFCAM was the widest field-of-view IR camera ever attempted and posed many technical challenges. It was conceived to convert UKIRT into a survey telescope. For many generations of telescopes those with small apertures have been utilised as 'survey instruments' to cover large portions of the sky to a reasonable depth. Comprehensive surveys are not only scientifically valid in their own right, they also supply target lists for follow up observations with larger telescopes. A good example of this is the 1.2m class Schmidt telescopes around the world which have provided countless targets for 2m & 4m class telescopes over the last few decades. It is now essential to develop the capabilities of current 2m & 4m telescopes to obtain deeper surveys suitable for feeding targets to the 8m and beyond class telescopes.

The speed at which a given telescope can survey a portion of the sky to a desired flux level is proportional to the optical étendue which is a product of the telescope

aperture area and its field-of-view, A_ω = aperture x FOV in m^2deg^2 (Liang et al. 2005; Casali et al. 2006). Large surveys require high étendue such that vast portions of the sky can be observed in practical time-scales. Given that WFCAM could not change the aperture of the UKIRT the FOV had to be maximised, achieved by replacing the secondary mirror and introducing an additional cold tertiary mirror to the system to change the focal length.

Fig.4.1 shows a fish-eye lens photograph of the full instrument completely installed on UKIRT, the camera is the large black 'tower' in the centre of the telescope. Instruments are often mounted on the back of the telescope at the Cassegrain focus, at the primary focus (in place of a secondary mirror) or on the fixed Nasmyth platform. None of these options were possible for WFCAM due to the required focal length and the available space. WFCAM is relatively novel as it sits between the primary and secondary mirrors in place of the central baffle, mounted on a custom made mirror plug. This location was chosen to overcome the optical challenges for converting the focal length of the telescope. The 'instrument' in total consists of: a cryogenic camera with a four IR detector focal plane, a system of cryogenic fore-optics including a tertiary mirror, 8 interchangeable filters, a new tip-tilt 0.474m secondary mirror and a complete on instrument auto-guiding system. Fig.4.2 shows a cut through mechanical drawing of the complete instrument showing from top down: main instrument and auto-guider field lenses, cryostat window, corrector plate, detector box, filter paddle assembly, cold baffles, tertiary mirror, cooling wicks and the mounting structure. Light enters the cryostat from the secondary mirror through the field lens, reflects off the tertiary mirror at the rear of the cryostat, through the filters and onto the focal plane which effectively looks 'downwards'. Each of these components will be discussed in more depth in §4.3.

4.1.1 Science Drivers

The main intention behind WFCAM was to provide unprecedented deep and large-scale infrared imaging. To do this the design team had to 'better' the previous best infrared survey project: the Two Micron All Sky Survey (2MASS). The 2MASS project, which begun routine survey observations in June 1997 was a ground breaking project

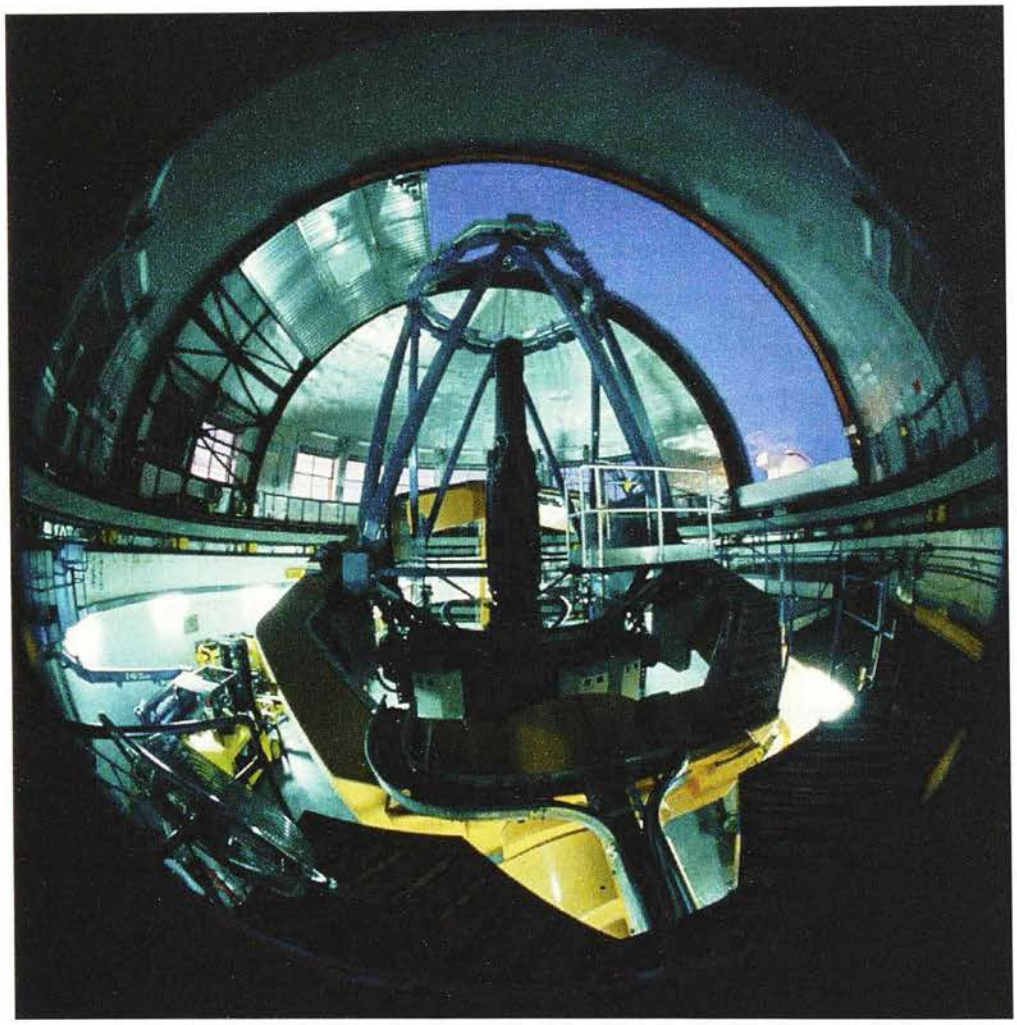

Figure 4.1: A 'fish-eye' lens photograph of the full camera completely installed on the UK Infrared Telescope. The camera is the large black tower which can be seen sitting on the mirror plug at the centre of the primary mirror. The bottom half of the tower which is slightly wider is the vacuum vessel which houses the main components of the camera including the tertiary mirror and detector focal plane array. The narrower field tower sits on top of the cryostat and supports the field lens ~4.8m above the primary mirror.

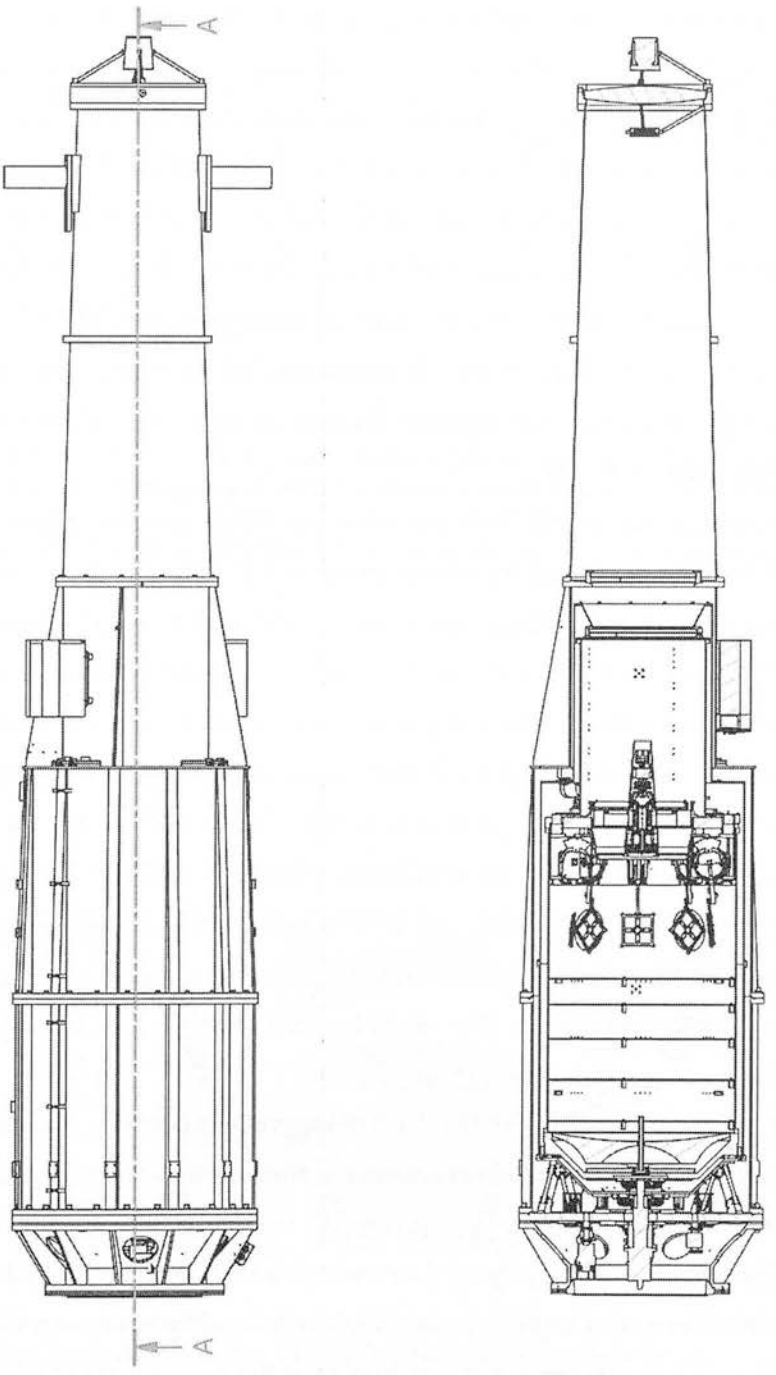

Figure 4.2: Mechanical CAD drawing of the complete WFCAM structure. An external view of the cryostat and filed tower on the left and a cross section on the right.

however due to the small aperture of the 2MASS telescopes (two 1.3m telescopes at Mt. Hopkins & Cerro Tololo) and small detectors (a single 256 x 256 IR detector) it has a limiting magnitude (K = 14.3) which does not match the typical spectroscopic limits on 8m class telescopes, e.g. limiting magnitude range for short wavelength medium resolution spectroscopic using ISAAC on the VLT 17.5 - 19.5, source: www.eso.org/instruments/isaac/overview.html (Skrutskie et al. 2006). WFCAM is designed to be more than 100 times faster at NIR surveying than 2MASS by utilising the available 3.8m primary mirror, a larger possible single-exposure FOV, better image quality and better telescope site. It has approximately 300 times move surveying power than the previous survey instrument at the host telescope, the UKIRT Fast Track Imager (UFTI) (Casali et al. 2006).

The public surveys planned for WFCAM consist of five hierarchical complementary surveys, designed and controlled by a consortium of UK astronomers, named UKIDSS (United Kingdom Infrared Deep Sky Survey). The four principle science drivers for UKIDSS, and thus for WFCAM, are: the coolest and nearest brown dwarfs, high-redshift dusty starbust galaxies, elliptical galaxies and galaxy clusters at redshifts $1 < z < 2$ and the highest redshift quasar $z = 7$ and beyond. Each of the five imaging surveys use some or all of the WFCAM standard broad-band filters (z'YJHK see §4.1.2) but span a range of areas, depths and Galactic latitudes (Warren et al. 2006). The data product of the UKIDSS surveys will be made public simultaneously to all astronomers in ESO member states via the WFCAM Science Archive with a world wide release 18 months later. The First Data Release to ESO members took place on 21^{st} July, 2006 (Warren et al. 2006).

A summary of the basic details of the five UKIDSS surveys is given in Table 4.1 and Fig.4.3 gives the planned final sky coverage, each coloured block represents the surveys (key given in Table 4.1), the dashed lines marks the Galactic plane and the dotted line the ecliptic. Further description of the planned surveys are not required at this time: discussion of the instrumental technical issues will be related to the surveys in up coming sections. For a comprehensive discussion on the surveys and the First Data Release see Warren et al. (2006); Lawerence et al. (2006).

Survey Name	Filters	Area	5 σ K	No. of nights	Primary Science	Key
LAS	YJHK	4000	18.4	262	White, Pop II Brown, T+ and low mass dwarfs, z > 6 quasars	Yellow
GPS	JHK	1800	19.0	186	Star formation, x-ray counterparts, AGB stars, planetary nebulae	Purple
GCS	z'YJHK	1400	18.7	74	Stellar mass function in sub stellar regime down to $\sim 25 M_{Jupiter}$	Green
DXS	JK	35	21.0	118	Galaxy cluster abundance $1 < z < 1.5$ and $z \geq 1$ for cosmological parameters, star formation, AGN	Blue
UDS	JHK	0.77	23.0	296	Epoch of spheroid formation, map of z = 3 Universe	Red

Table 4.1: Survey names: Large Area Survey (LAS), Galactic Plane Survey (GPS), Galactic Clusters Survey (GCS), Deep Extragalactic Survey (DXS), Ultra Deep Survey (UDS). In total the surveys will use 1000 nights of WFCAM observing over a seven year period. This table summarises the filters, areas, depths in K, number of nights and primary science goals for each of the five surveys. Column 7 gives the colour coding for Fig.4.3 (www.ukidss.org).

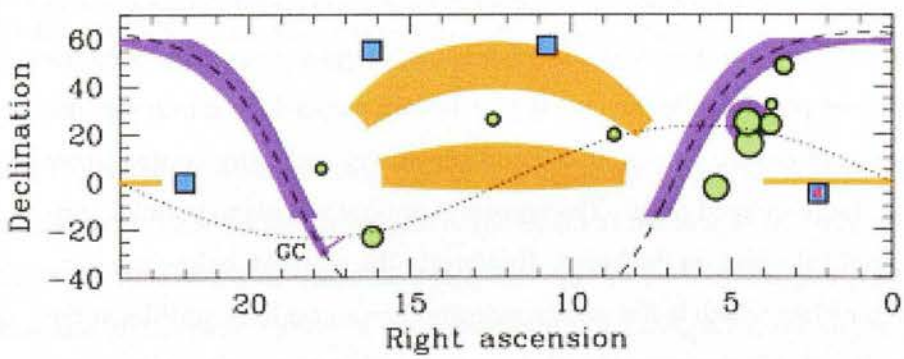

Figure 4.3: Diagram of the planned final UKIDSS sky coverage, the key to the colour coding is given in the last column of Table 4.1. The dashed line marks the Galactic plane and the dotted line the ecliptic. (www.ukidss.org/surveys/surveys.html).

4.1.2 Optical System

The optical design of the main instrument is a forward-Cassegrain quasi-Schmidt camera, including a cold stop where the pupil is re-imaged. The dedicated WFCAM secondary mirror delivers a f/9 focus about 5.7m above the primary mirror while the cold tertiary converts this beam into the f/2.44 input beam required to give the correct pixel scale at the focal plane. The secondary mirror is mounted on a fast 2-axis tip/tilt platform which is mounted on a hexapod stage, allowing the secondary to be precisely moved in six axes. WFCAM actively uses the secondary mirror in conjunction with the autoguider to compensate for tracking wobble, wind-shake and dome seeing. The whole system, telescope and camera, need to be regularly refocussed to accommodate for changes in the telescope truss and shape length which in turn changes the physical distance between the primary and secondary mirrors. During the night the trusses vary due to changing dome temperature causing thermal motions and flexure as the telescope changes pointing. Refocussing involves a series of short exposures in which WFCAM will determine and then move the location of M2 to give the best focus at that time.

Fig.4.4 shows the optical path for the complete system, telescope and camera and Fig.4.5 shows the cryostat optical layout. Note the field lens is external to the cryostat, mounted on top of the field lens tower, 2.25m above the cryostat window at the intermediate focus (Henry and Lee 2002). The field lens is equi-convex and forms the image of the entrance pupil inside the cryostat. The cold stop which minimises the thermal background to ensure maximum K-band sensitivity and helps control stray light is located at the re-imaged pupil. The cryostat window is a plane parallel window and has no optical effect on the beam. Just inside the cryostat, below the window is the corrector plate which is flat on one side and has an aspheric profile on the other which corrects off axis aberrations such as coma in addition to spherical aberrations generated by the mismatch between the primary mirror and the new secondary mirror. The tertiary mirror is a concave ellipsoid mirror and is ~81cm in diameter, making it one of the largest cryogenic astronomical mirrors, slightly smaller than the Spitzer Space Telescope's primary mirror (Casali et al. 2006). The tertiary is mounted on three flexures allowing differential contraction between the Zerodur mirror and

the aluminium cryostat structure when cooled to cryogenic operating temperatures. Fig.4.6 is a photograph of the M3 sitting on the bench in the laboratory, with optical engineer D. Henry from the UKATC for scale. The beam now passes through a filter paddle which holds four separate plane parallel filters, one for each detector array, before meeting a plano-concave fused silica field flattening lens which acts as a window on the detector box directly in-front of the focal plane. The observing wavelength

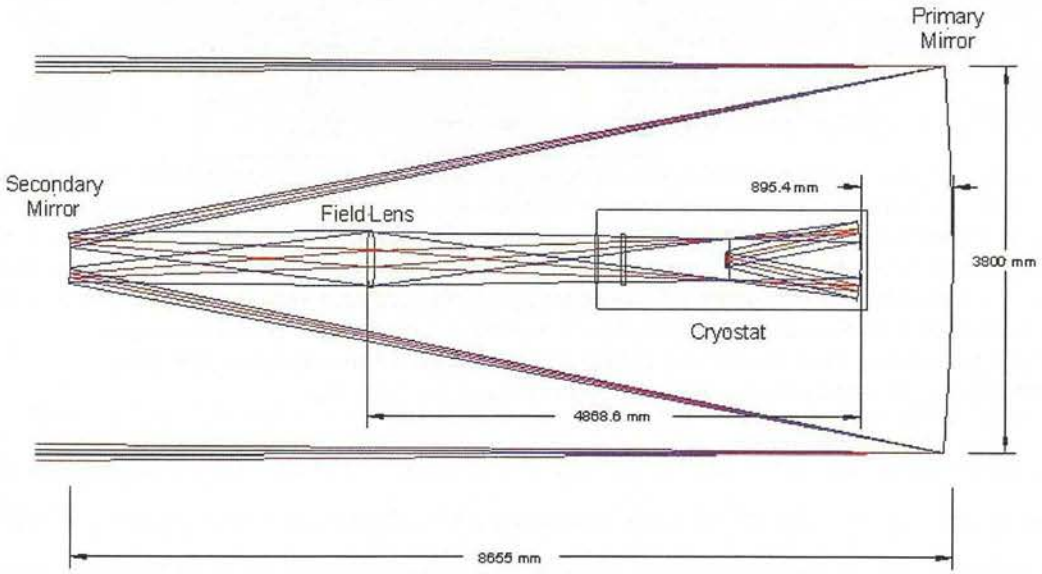

Figure 4.4: The full optical path of the system, telescope and camera. The telescope aperture is to the left of the diagram and key dimensions are marked. The boxed section in the middle is the camera cryostat, for a zoomed diagram of this region see Fig.4.5.

for each exposure is selected using one of the eight interchangeable filter paddles, the non-required paddles are stored out of the beam at the side of the cryostat. Each paddle stores four filters of the same bandpass, one for each of the four science detectors and a fifth separate filter for the autoguiding CCD. Fig.4.7 shows, with the left hand photograph, one of the small filters being installed by hand into the filter frame and the right hand photograph shows the fully assembled paddle assembly on a hoist waiting to be installed in the camera. As previously noted in §4.1.1, the majority of the WFCAM survey scientific goals are fulfilled using the Y, J, H and K filters so the initial filters to be installed in the camera are the broadband filters z', Y, J, H, K and the narrowband filters br Gamma and H_2 giving the camera an operational coverage of

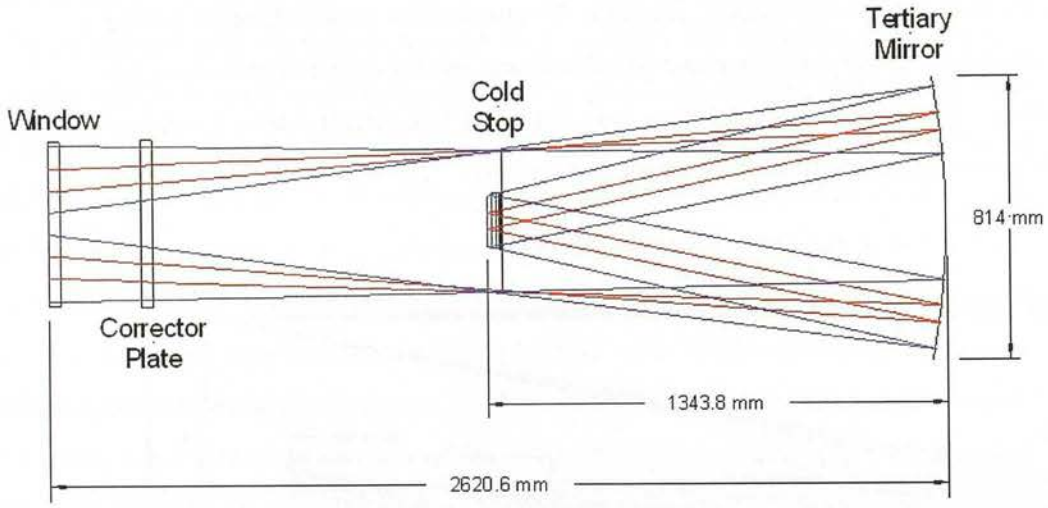

Figure 4.5: A zoomed in view of the optical path through WFCAM's cryostat. The telescope aperture is to the left of the diagram. The focal plane assembly is located at the cold stop where it detects the light coming from the tertiary mirror at the 'bottom' of the cryostat. The filter paddle assembly is positioned between the tertiary mirror and the cold stop.

Figure 4.6: Photograph of the tertiary mirror sitting on the bench in the laboratory in Edinburgh. UK ATC optical engineer Mr. D. Henry in the background gives an impressive of the size of the mirror, one of the largest cryogenic single piece mirrors in world.

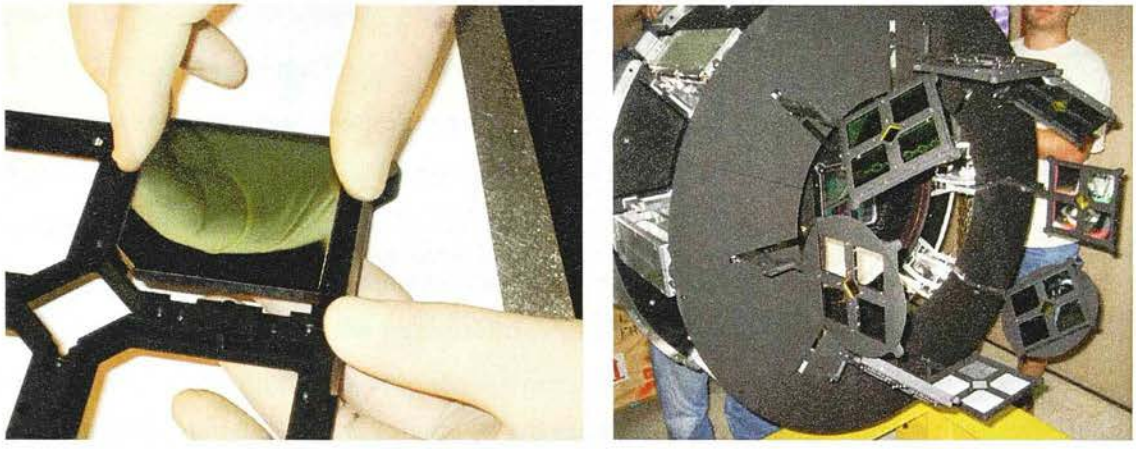

Figure 4.7: The left hand photograph shows one of the filters being installed into a 'paddle'. Each paddle has five filters, one each for the four science devices and a smaller one in the centre for the auto-guiding detector. The complete filter paddle assembly on a hoist in the laboratory in Hilo can be seen on the right. WFCAM instrument scientist Dr. P. Hirst seen behind the assembly at the far right of the photograph gives a sense of size.

$\sim 0.88 - 2.5\mu m$. The basic details of the filters are given in Table 4.2. The eighth 'filter' is an opaque aluminium blank necessary to take dark exposures. As the demanded filter is changed the focal length of the camera is altered. To achieve optimum performance and have no degradation of image quality, the optical system is refocussed after a filter change. The detector focus mechanism moves the whole focal plane assembly unit, including field flattening lens, with respect to the plane of the filters and is controlled by pre-determined look-up tables for the installed filters in the software. The optical design was optimised for best average image quality over the entire FOV from J to K and the final design gives near diffraction limited performance at K.

4.1.3 The Focal Plane

The focal plane consists of four 2048 x 2048 Rockwell Scientific Ltd Hawaii-II detectors spaced by 94% of a detector size. The detectors themselves are discussed in depth in Chapter 5, this section details the assembly housing the detectors in the camera. The Hawaii-II arrays are not buttable, the active array is entirely surrounded by casing, printed circuit board (PCB) and associated wiring which forces the separation between the arrays. Fig.4.8, left hand side, shows a simple diagram illustrating the focal plane

Filter	Central λ (μm)	λ range (μm)	Bandpass (μm)
z'	0.878	0.83 – 0.925	0.095
Y	1.02	0.97 – 1.07	0.1
J	1.25	1.17 – 1.33	0.16
H	1.635	1.49 – 1.78	0.29
K	2.20	2.03 – 2.37	0.34
H_2, S1	2.12	2.111 – 2.132	0.021
br Gamma	2.166	2.155 – 2.177	0.022

Table 4.2: Summary of central wavelength, bandpass and subsequent wavelength range of each of the seven filters installed in WFCAM at the time of commissioning. The 8^{th} paddle contains the aluminium blank required for taking dark exposures.

layout. The pink squares and number $1-4$ are the IR science arrays, the blue offset square in the centre is the autoguider CCD. Marked on the diagram are the important dimensions given in arcseconds, the detectors pixel scale is 0.4"/pixel. Clearly the focal plane footprint on the sky mirrors the focal plane layout hence to obtain a completely filled in 'tile' in the sky requires four telescope pointings, schematically shown with the right hand side of Fig.4.8 - the coloured squares represent the footprint of the science detectors on the sky with the numbers indicating the four pointings Hirst (2006). A single exposure covers 0.21 sq. degs on sky with the four compos-

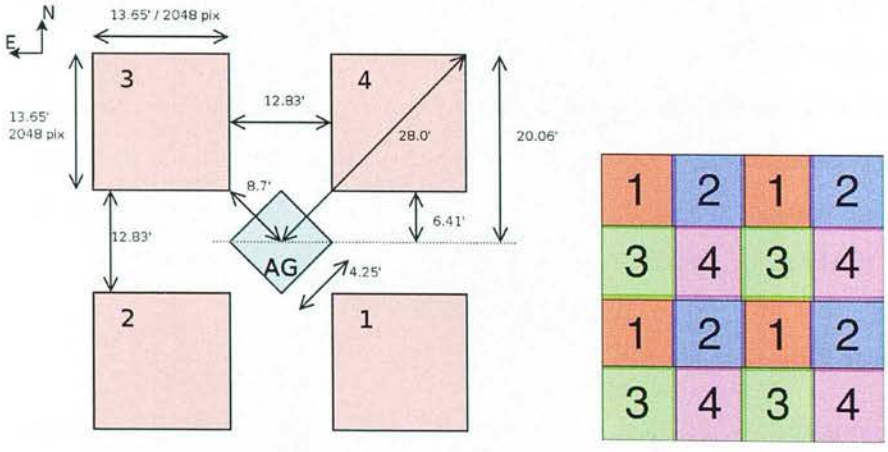

Figure 4.8: Left hand diagram illustrates the focal plane layout. Squares numbered $1-4$ are the science arrays and the diamond labelled 'AG' is the autoguiding CCD. Marked are dimensions and separations given in arcseconds. The right hand schematic diagram simply demonstrates how four telescope pointings build up the WFCAM 'tile' and fill in the 'gaps' in the focal plane foot print.

ite exposures giving a filled tile of 0.78 sq. degs (0.883° along each side). The pixel scale of 0.4"/pixel facilitates the large survey area but does not critically sample the UKIRT/WFCAM psf under usual observing condition. 'Microstepping' involves taking several separate integrations at precise telescope offsets corresponding to precise fractions of a IR detector pixel along each axis. Of course, even with microstepping the images are always smoothed by the pixel scale (Hirst 2006).

As mentioned, in addition to the science IR detectors the focal plane has a 1024 x 1024 CCD in the centre for the autoguiding system. The CCD is rotated by 45° and is on a raised plane with respect to the science detectors, Fig.4.9 shows a photograph of the focal plane enclosed in the detector box. As the position of the CCD is fixed with respect to the IR arrays the guide stars will be preselected. The science arrays

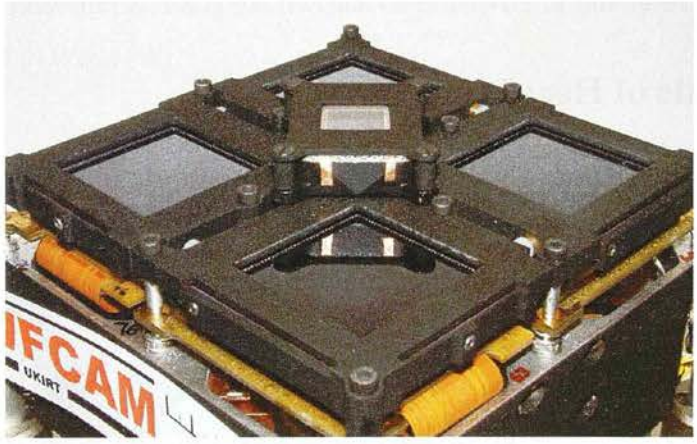

Figure 4.9: Close up photograph of the detector box which houses the five detector focal plane without the field flattening lens cover. The raised and rotated CCD plane can be clearly seen.

are readout using a 128 channel San Diego State University (SDSU) system, one 32 channel controller per detector all running in parallel. The controller units and electronics are stored in electronic cabinets mounted behind the telescope to limit stray heat in the telescope FOV and to keep the profile of the cryostat to a minimum. The readout options possible with the SDSU controllers are discussed at length in Chapter 5. The system handles upwards of 120GB data per night which is real-time pipelined at the summit. The raw and reduced frames are saved on to 3TB tapes before being posted back to the UK for further reduction (object extraction, precision astrometry

and photometry) and archiving. Further information regarding the surveys, off-line reduction and archiving can be found at www.ukidss.org, www.ast.cam.ac.uk/vdfs and surveys.roe.ac.uk/wsa.

It is vital to cool infrared instruments for two key reasons. Firstly, the heat or infrared emission from all the filters, lenses and instrument metallic structure must be eliminated, if it is not cold then the detector will be swamped by this thermal radiation and there would be no hope of observing astronomical infrared radiation. Secondly, infrared detectors are thermal detectors, operating them cold greatly reduces the detectors own thermally generated background, as discussed extensively in Chapter 5 (McLean 1997). The remainder of this chapter deals with development of a model which tracks how each of the sub-assemblies of WFCAM cools down to operating temperature.

4.2 Fundamentals of Heat Transfer

'Heat' is the energy transfered from a body at a higher temperature to a body of lower temperature due to the given temperature difference. The amount of heat transfered depends on the method of transfer; conduction, convection or radiation.

4.2.1 Conduction

The conduction of heat is the transfer by contact of more energetic particles with adjacent less energetic ones. In gases the transfer is caused by collisions between higher-energy molecules in regions of high temperature with the lower-energy molecules in the adjacent cooler regions. In dielectric solids the vibrations of molecules are transmitted through a body as a wave due to the elastic bonding between the particles. In solid and liquid metals conduction is almost entirely by means of the valance electrons.

Fourier's Law of Conduction

Fourier's law is an empirical law based on observation. This law states that the rate of heat flow, dT/dt, through a homogenous solid is directly proportional to the surface area of the section perpendicular to the direction of the heat flow. For example, consider a plane body of cross-sectional area, A, and of thickness, d, see Fig.4.10. The two surfaces have corresponding temperatures, T_1 and T_2, so the resultant rate of conductive heat flow through the body is given by:

$$\dot{Q} = Q * A \tag{4.1}$$

$$\dot{Q}^c_{12} = \frac{A}{d} * \kappa * (T_1 - T_2) \tag{4.2}$$

where Q is the heat flux and κ is the thermal conductivity of the material of the body. $\dot{Q}^c$ is measured in Watts (W).

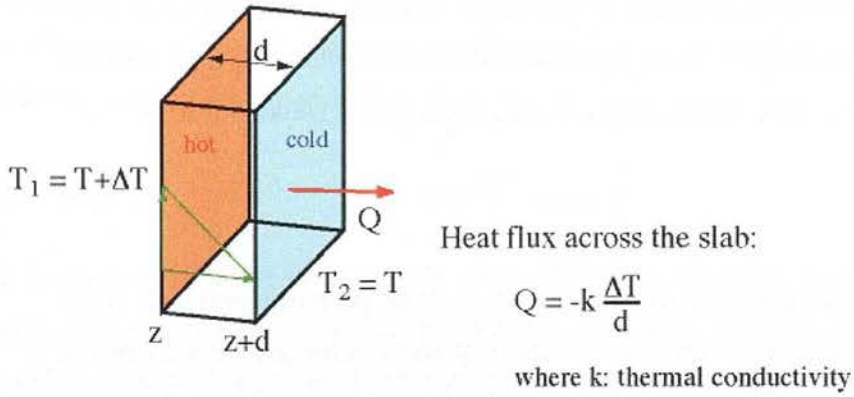

Figure 4.10: Equation for the heat flux, the flow of heat per unit area, per unit time in W/m^2. The minus sign indicates that heat flows in the direction of decreasing temperature.

Thermal Conductivity

The thermal conductivity, κ is a property of materials that expresses the amount of heat that will flow through the given material if a certain temperture gradient exists

over the material. Thermal conductivity is normally expressed in $\mathrm{W/mK}$ and is a property which decribes a semi-static situation, the temperature gradient is assumed to be constant, κ is a function of temperature.

There are wide variations in values of thermal conductivity depending on the type of materials involved. As mentioned above, gases conduct heat by direct collisions between molecules so their thermal conductivity is low compared to most solids. Non-metal solids transfer heat by lattice vibrations so there is no net motion of the material as the energy propagates through. Metals are much more effecient thermal conductors than non-metals because the same mobile electrons which participate in electrical conduction also take part in the transfer of heat. The metals that are the best electrical conductors are also the best thermal conductors. At a material specific temperature the thermal and electrical conductivities of metals are proportional but raising the temperature increases the thermal conductivity and lowers the electrical conductivity. The thermal conductivity increases with the mean particle velocity as the forward transport of energy increases however, the electrical conductivity decreases with increased mean particle velocity because the collisions divert the electrons from forward transport of charge. The Wiedemann-Franz Law quantifies this behaviour to be:

$$\frac{\kappa}{\sigma} = L\mathrm{T} \tag{4.3}$$

where σ is the electical conductivity and the constant of proportionality, L, is the Lorenz number. This relationship between thermal and electrical conductivities of metals and alloys holds well over a wide range of temperatures but becomes less accurate at very low temperatures.

4.2.2 Convection

Convection is the process of heat transfer in a fluid by the movement of the fluid itself. That is, the less energetic particles are replaced by particles energised at the hot body boundary and requires a flow in the given fluid. 'Natural convection' is when the motion of a fluid is solely due to the presence of a hot body giving rise to a temperature and thus a density gradient so that the fluid moves under the influence

of gravity. 'Forced convection' results from the relative motion between a hot body and a fluid being maintained by some external agency, such as a draught.

4.2.3 Radiation

Radiation is an energy transfer due to emission of electromagnetic waves and does not require direct physical contact between the two bodies. Any body at a temperature greater than 0K emits electromagnetic radiation due to the body's atoms vibrating. The emitted power per unit surface is proportional to the body's temperature:

$$\mathrm{E} \propto \sigma \mathrm{T}^4$$

where T is the emitter's temperature and σ is the Stefan-Boltzmann constant and E is in $\mathrm{W/m^2}$.

The maximum radiated power is achieved when the body is a 'blackbody', which is a body that absorbs all the radiation incident upon it and has no reflecting power. The total amount of energy of all wavelengths emitted by a blackbody at a given temperature is given by the Stefan-Boltzmann Law:

$$\mathrm{E} = \sigma \mathrm{T}^4 \tag{4.4}$$

If the given body is not a true blackbody, emissivity comes into play. Emissivity, ϵ, is the ratio of power per unit area radiated from a given surface to the power per unit area radiated from a blackbody at the same temperature. Therefore, ϵ for a blackbody is 1 and for a grey body, $0 \leq \epsilon < 1$ and is incorporated into the Stefan-Boltzmann Law for grey bodies as:

$$\mathrm{E} = \sigma \epsilon \mathrm{T}^4 \tag{4.5}$$

Thus, the radiation emitted by a grey surface is given by:

$$\dot{\mathrm{Q}} = \epsilon \sigma \mathrm{A} \mathrm{T}^4 \tag{4.6}$$

where A is the surface area.

Kirchhoff's Law

Kirchhoff's Law for radiation states: 'for any point on a thermal radiator, a body which emits radiation as a result of internal thermal vibrations of atoms, at thermal equilibrium the emissivity in any direction is equal to the absorptance of incident radiation coming from the same direction', valid for all wavelengths. The equation of Kirchhoffs law is::

$$\epsilon = (1 - \mathrm{R}) = \alpha \tag{4.7}$$

or in words:

$$\text{Emissivity} = (1 - \text{Reflection}) = \text{Absorption}$$

Hence for a single surface:

$$\dot{\mathrm{Q}}_{\text{reflected}} = (1 - \alpha)\dot{\mathrm{Q}}_{\text{incident}} \tag{4.8}$$

In general, the determination of the net rate of heat transfer by radiation between two surfaces is complex since it depends on the properties of the surfaces, their relative orientation to each other and the interaction of the medium between the surfaces with the radiation. However, for the development of this thermal model we need only consider a special case where two surfaces at temperatures, T_1 and T_2, 'see' only each other with a surface area of $\mathrm{A}_{\text{surface}}$ and are separated by a gas, such as air, which does not interact with the radiation. This scenario sufficiently approximates the radiative transfer between pairs of surfaces in WFCAM modeled in this chapter. For this special case the rate of radiation heat transfer between the two surfaces is given by:

$$\dot{\mathrm{Q}_{12}} = \mathrm{A}_{\text{surface}}\sigma\epsilon_1\epsilon_2[\mathrm{T}_1^4 - \mathrm{T}_2^4] \tag{4.9}$$

where $\mathrm{A}_{\text{surface}}$ is the area of the radiating surface which can be 'seen' by the second surface and ϵ_1, ϵ_2 the emissivity of the two surfaces.

Eqns. 4.2 and 4.9, Fourier's Law and Kirchhoff's Law respectively are the two key equations required for developing a model of the thermal behaviour for the WFCAM instrument. These two equations are used to calculated the cooling power, $\dot{\mathrm{Q}_{\text{in}}}$, into each 'node', i.e. the connection point between two heat transfer links. Once $\dot{\mathrm{Q}_{\text{in}}}$ is

known it can be used to determine the change in temperature over the link in each time step as:

$$m * C_p * \Delta T = \dot{Q_{in}} * \delta t \tag{4.10}$$

where m is the mass of the each body, C_p the specific heat capacity of the material, ΔT the change in temperature over the link in a time period of δt. The specific heat capacity of a material is the measure of heat energy required to raise the temperature of 1 kilogram of the material by one degree, in units of $Jkg^{-1}K^1$.

Mechanically, the instrument is cooled using an external closed cycle cooler (CCC) which is attached to cooling 'wicks', lengths of woven copper, running throughout the instrument conductively cool the main instrument structure. The optical elements are conductively isolated from the cryostat structure and are cooled through radiation. The following sections detail each main assembly of the camera then discuss how each assembly was separated into radiative and conductive links. The thermal model itself calculates the heat transfer through each link by breaking the entire cooling time period into very small time steps then uses the laws of heat transfer to determine the temperature changes either side of the links at each sequential time step.

4.3 The Cryogenic Design

4.3.1 Overview

The WFCAM instrument consists of cylindrical vacuum vessel which acts as an outer 'shell' to an internal vessel which is cryogenically cooled and houses the 'guts' of the camera (see Fig.4.11). The two vessels are mechanically linked at the base of the vessels where the instrument is mounted onto the telescope, the internal cryostat is supported by the vacuum vessel by insulating A-frame trusses. A single radiation shield envelops the internal cryostat and is covered in a superinsulating blanket to cut down on radiative heat loads from the surrounding environment. The cryostat and radiation shield are cooled and maintained at operating temperature by a single two stage CCC which is mounted below the base plate 'underneath' the instrument. In addition to the CCC there is access for a can of liquid nitrogen to be attached to the cooling wicks. The cryostat is so large that its cooling rate is time consuming, so the liquid nitrogen

is applied for an initial rapid cooling to help speed up the cooling time.

The first stage of the CCC is attached to the base of the radiation shield through a flexible copper wick. The electrical cabling for the mechanisms internal to the vacuum vessel are also heat sunk to the base of the radiation shield. A 'top ring' structure at the top end of the cryostat supports the filter assembly, the focus drive stage and the focal plane assembly. The focal plane assembly houses the infrared and auto-guiding detectors is cooled by the second stage of the CCC through flexible copper wicks that run the length of the internal cold structure. The detectors themselves are conductively linked to the detector box. The cryostat aperture is at the very top of the cryostat above the top, here the cryostat narrows in width and supports the corrector plate lens on insulated trusses. The tertiary mirror is supported by insulating trusses at the 'base' of the cryostat.

The vacuum vessel is fabricated in aluminium alloy and o-ring seals are used where ever the vessel is broken. Similarly the radiation shield and cryostat vessel are also fabricated out of aluminium alloy with the same thermal contraction characteristics. The insulating fibreglass trusses which bolt the radiation shield and cryostat vessel to the external vacuum vessel, as well as support the structure accommodate, differential contraction. The cryostat is not under closed loop control but is allowed to reach steady state however, the detector assembly which needs to be accurately controlled has its own dedicated resistive heater for closed loop control.

4.3.2 The Radiation Shield

The radiation shield is a multi-layer cylinder of special material fitted round the cryostat with a dish shaped base to accommodate the tertiary mirror bezel (see bottom picture in Fig.4.11). Radiation shields of this nature are thin, parallel, highly reflecting sheets placed between radiating surfaces to reduce the energy transfer between them. Using many sheets of material separated by a vacuum provides a series of alternating radiative and conduction barriers which proves to be a highly effective insulation system. Commonly, thin sheets of highly reflective metallic films such as aluminium or silver spaced by cloth with large gaps between its fibres are used to construct radiation shields (Siegel and Howell 1981). In the case of WFCAM, aluminium was used to

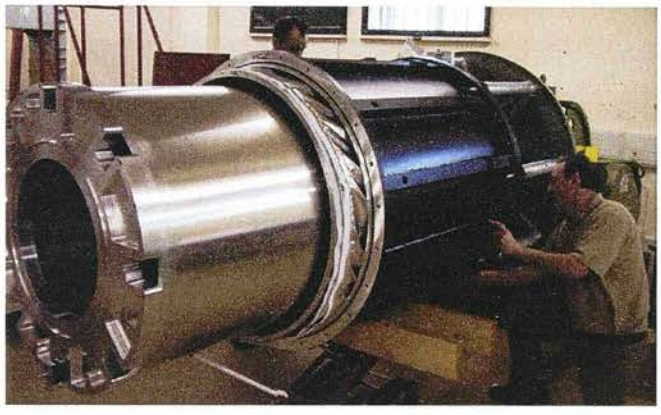

Figure 4.11: Two photographs of the cryostat in partial build mounted on the bode in the laboratory in Edinburgh, showing the 'Russian Doll' nature of the cryostat design. The top photograph shows the bottom half of the internal cryostat (silver structure) mounted inside the vacuum vessel (black) with the part of the radiation shield in between. UK ATC mechanical engineers Mr. J. Elliot and Mr. K. Burch are pictured beside the instrument, showing the size of the camera. The bottom photograph shows the complete internal cryostat vessel covered in the radiation shield.

match the thermal properties of the main cryostat structure. The bottom surface of the shield has fastener detail to which the thermal wick from the first stage of the CCC is attached, as well as connectors for the liquid nitrogen pre-cool can. There are breaks in the radiation shield for the electrical cables which control motors, switches, detector readout and heat regulation of the detector box. The radiation shield is held off the vacuum vessel base with four A-frame brackets consisting of G10 glass fibre blades bonded into stainless steel interface feet. There are also thermal connections from the radiation shield to the tertiary mirror bezel by the means of thick cylindrical shims.

4.3.3 The Cold Structure

A cross-sectional drawing of the cold mass is shown in Fig.4.12 with the Closed Cycle Cooler, main instrument G10 support trusses, tertiary mirror, radiation shield, detector assembly, focus drive, filter mechanism, top ring and corrector plate all labelled.

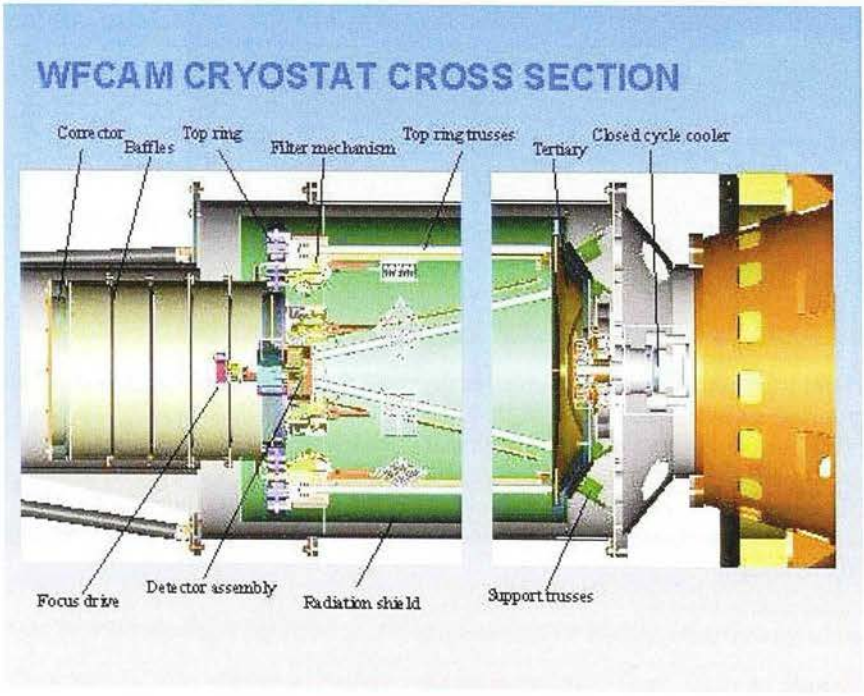

Figure 4.12: Mechanical cross sectional drawing of the WFCAM cryostat. Location of the closed cycle cooler, the radiation shield, the top ring and the corrector plate shown. The cryostat's window is off the diagram to the left hand side.

Tertiary Mirror

The tertiary mirror is a large Zerodur double-arched mirror. Zerodur is a glass ceramic manufactured by Scott which has an extremely low coefficient of thermal expansion but also has exceptionally good homogeneous mechanical and thermal properties. The tertiary mirror is supported by fibreglass trusses which keep it conductively isolated from the main cryostat structure. The mirror is radiatively cooled to a stable temperature by the inside of the cryostat vessel and the corrector plate at the cryostat window. Radiatively cooling the mirror protects it from potential temperature gradients which can develop when conductively cooling using multiple point contacts. Temperature gradients would place the mirror under undesirable stresses. Due to its size the tertiary mirror is one of the slowest elements to cool.

Top Ring

The top ring assembly consists of a circular ring structure which supports three different subassemblies, the filter assembly, the detector focus assembly including the detector box and the heat rejection baffle & corrector plate assembly. The detector focus assembly is hung from the top ring by a 'spider', a four strut structure which can be seen in Fig.4.13. The cooling wicks are passed from the 2nd stage of the CCC along the outside of the cryostat to the top ring then along the struts of the spider and down to the detector box. The spider passes through the focal plane field of view so had to be carefully designed to cause as little obstruction to the beam as possible.

Filter Assembly

The filter paddle assembly is designed to deploy a filter set in front of the detectors by one of the eight paddle arm mechanisms. The mechanisms consist of a counterbalanced deployment arm that is driven by a worm and wheel gearing. A stepper motor is used to drive the worm and micro-switches are used to define a datum position and the range of travel.

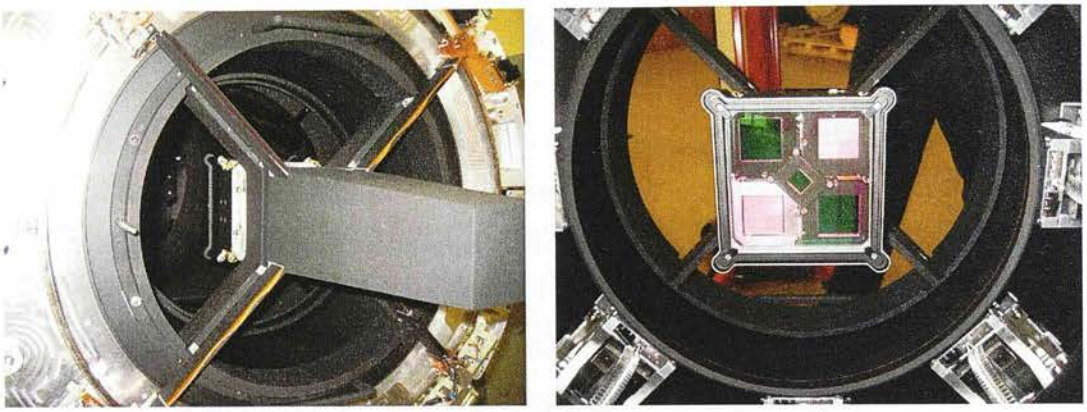

Figure 4.13: Two photographs of the top ring, complete detector box and focus mechanism. The view on the left shows the 'top' of the assembly, the black box houses the focus mechanism which is used to move the detector box with respect to the filter paddles. The image on the right is the view of the detector box and focal plane from the tertiary mirror.

Detector Focus Assembly & Box

The detector box houses all four science arrays, the auto-guiding CCD and the field flattening optics. The box is suspended above the tertiary mirror by the four struts of the spider, see Fig.4.13. The detector box sits directly in the centre of the beam so had to be designed and engineered to be able to fulfil its task in as small a space envelope as possible to limit impact on the beam. The cooling wicks enter the box from the spider then via a series of complex conductive links reach the back of the detectors.

Sitting directly above the detector box is the focus assembly housing. The focus assembly enables the whole detector box to be translated along the z-axis of the instrument. Measured offsets of this stage are used to place the focal plane at the optimal focus position for each of the different filters.

4.4 The Thermal Path Model

The gross thermal specifications for the instrument were decided on at the beginning of the design phase based on requirements for UKIDSS Science goals. The two main specifications were; the array temperature must be controlled to any temperature between 60K & 70K to $\pm$0.2K and the internal cold structure must be cooled to less than

160K with the exception of the corrector plate which acts as a floating radiation shield and should equilibrate at ~250K.

The thermal model was developed to track the cooling of each part of the instrument to give resultant steady state temperature for four key parts of the instrument: the corrector plate, the radiation shield, the top ring and the detector box. It is important to know the steady state temperature of both the corrector plate and the radiation shield as they are interfaces between the ambient temperature and the cryostat. The top ring temperature represents the settled temperature of the main cryostat mass and thus the cooling from the 1^{st} stage wick and the detector box the 2^{nd} stage and importantly the operating temperature of the science detectors.

The division of the instrument into heat transfer lines is detailed in Fig.4.14. The main block diagram shows the bulk of the camera with the small dashed box at the bottom the 'zoomed in' detail of wick 3. As discussed, the instrument is cooled by a two stage CCC. The 1^{st} stage is connected by a short length of wick (WICK1) to the radiation shield and the 2^{nd} stage is connected by the much longer wick (WICK2) up to top ring. After the top ring the cooling path is continued to the detector box along the spider by WICK3 which is more complicated than the other two wicks which are simply made of woven copper; the components of WICK3 are detailed in Fig.4.14. A legend explaining all the notation can be found at the bottom right hand side of the diagram, shaded boxes represent radiative links with the open boxes for the conductive links. Each conductive link has the actual instrument part responsible for the link and its material labelled on the box.

Each of the individual links were determined through conversations with the UK ATC WFCAM project team's mechanical engineers and studying the mechanical CAD drawings. The dimensions used to calculated each part's length, surface area and cross-sectional area was taken from the precision CAD design drawings used for manufacture and the mass from the instrument mass budget determined by the WFCAM mechanical engineers. Details of the dimensions; length, surface area and cross-sectional area, of the main components in the model can be found in Table 4.3 and the masses finally adopted in Table 4.4. The last information needed for the model are the properties of all the materials used in the instrument, namely specific heat capacity and the

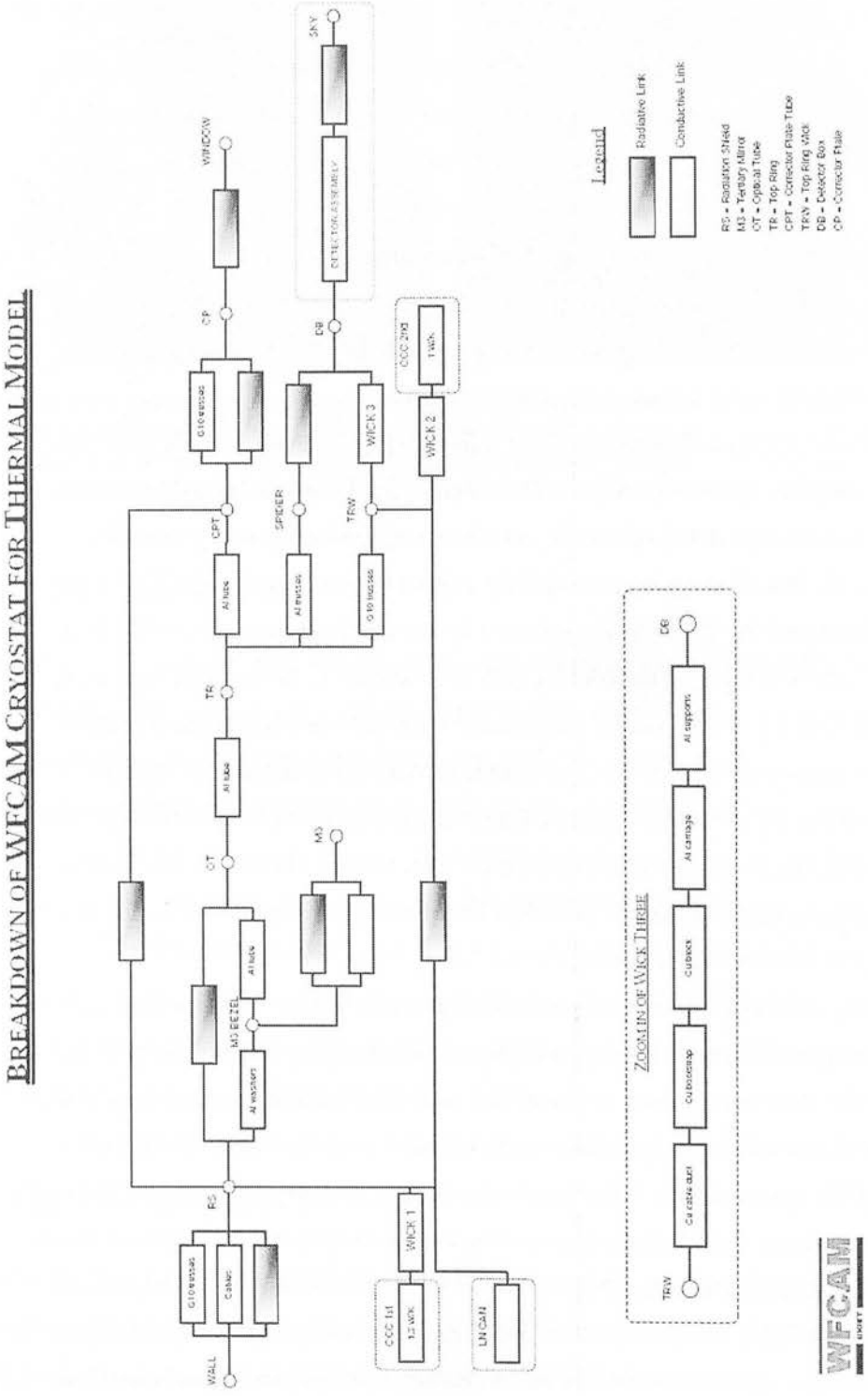

Figure 4.14: Diagram showing the thermal conductive and radiative links for the WFCAM cryostat.

thermal conductivity coefficient. Details of the properties for each of the material can be found in Table 4.4.

Dimension	Notation	Value	Units
Cross-section area of trusses to Rad Shield	$A_{RS-truss}$	$4.32x10^{-3}$	m^2
Length of trusses to Rad Shield	$L_{RS-truss}$	0.150	m
Cross-section area of cables to Rad Shield	A_{RS-cab}	$2.35x10^{-5}$	m^2
Length of cables to Rad Shield	L_{RS-cab}	0.3	m
Surface area of Rad Shield	SA_{RS}	6.73	m^2
Cross-section area of CCC 1st stage wick	A_{WICK_1}	$8.14x10^{-4}$	m^2
Length of CCC 1st stage wick	L_{WICK_1}	0.128	m
Cross-section area of Optical Tube	A_{OT}	0.011	m^2
Length of Optical Tube	L_{OT}	0.703	m
Surface area of Optical Tube	SA_{OT}	3.84	m^2
Surface area of Top Ring	SA_{TR}	0.528	m^2
Cross-section area of trusses top ring to CP	$A_{CP-truss}$	$2.16x10^{-4}$	m^2
Length of trusses top ring to CP	$L_{CP-truss}$	0.028	m
Surface area of CP	SA_{CP}	0.189	m^2
Surface area of CP tube	$SA_{CP-tube}$	1.485	m^2
Length of CP tube	$L_{CP-tube}$	0.8134	m
Cross-section area of CP tube	$A_{CP-tube}$	$7.2x10^{-3}$	m^2
Surface area of cryostat window	SA_{WIN}	0.126	m^2
Cross-section area of CCC 2nd stage wick	A_{WICK_2}	$6x10^{-4}$	m^2
Length of CCC 2nd stage wick	L_{WICK_2}	2.09	m
Surface area of CCC 2nd stage wick	SA_{WICK_2}	0.212	m^2
Cross-section area of the Spider support	$A_{SPIDER-support}$	$2.8x10^{-3}$	m^2
Length of the Spider support	$L_{SPIDER-support}$	0.1335	m

Table 4.3: Dimensions adopted for the instrument components in the thermal model, stated notation is used throughout the thermal model code.

The thermal model is constructed 'piece-by-piece' by setting the initial temperature conditions and calculating all the temperature changes at each node sequentially from the initial conditions for each time step, until all the nodes stop changing temperature and the 'instrument' is in a steady state. For each heat transfer link between instrument part 'a' and part 'b' we need to calculate:

$$\Delta T_a = \frac{\dot{Q}_{in_a}}{M_a C_{P_a}} \delta t \qquad (4.11)$$

$$\Delta T_b = \frac{\dot{Q}_{in_b}}{M_b C_{P_b}} \delta t$$

	Notation	Mass (kg)
Radiation Shield	m_{RS}	135
Tertiary Mirror	m_{M3}	83
Optical Tube	m_{OT}	77.58
CP Tube	m_{CPT}	21.6
Top Ring	m_{TR}	39.5
Spider	m_{SPIDER}	10.2
Corrector Plate	m_{CP}	15.8
Window	m_{WIN}	14
Detector Box	m_{DET}	2.65

Table 4.4: Masses adopted for the instrument components in the thermal model.

Material	κ ($Wm^{-1}K^{-1}$)	C_P ($Jkg^{-1}K^{-1}$)	Where used
FR4 fibre glass	0.293	1300	Detector PCB
PEI plastic	$6.7x10^{-2}$	2000	ZIF socket
Beryllium Copper	112.5	418.41	ZIF socket pins
FeNiCo	91	500	Detector carrier pins
Copper	404	379	All straps & cables
G10 fibre glass	0.435		All isolating trusses
Al 6082	180	1256.1	Radiation shield and main structure
OFHC Copper	460	380	Cooling wicks
Aeraeus infrasil - fused silica		1010	Corrector plate & cryostat window
Ceramic	1.04	800	Detector carrier
Zerodur - glass ceramic	$0.0 \pm 0.1x10^{-6}$	0	M3

Table 4.5: Thermal properties of the materials used to build the instrument components Thermal conductivity and specific heat capacity quoted.

where for conductive links:

$$\dot{Q_{in_a}} = \frac{A_{xs}}{L}\kappa(T_b - T_a) \qquad (4.12)$$
$$\dot{Q_{in_b}} = \frac{A_{xs}}{L}\kappa(T_a - T_b)$$

and radiative links:

$$\dot{Q_{in_a}} = A_{surface}\sigma\epsilon_a\epsilon_b(T_b^4 - T_a^4) \qquad (4.13)$$
$$\dot{Q_{in_b}} = A_{surface}\sigma\epsilon_a\epsilon_b(T_a^4 - T_b^4)$$

Once all temperature changes of each heat link into a given node are calculated the total temperature change for that node at any given time is simply all the individual temperature changes added together. The initial temperature conditions where selected to be: CCC 1st stage = 34K, CCC 2nd stage = 11K, cryostat wall & window = 298K (room temperature in the laboratory). Table. 4.6 demonstrates a few of the dozens of links calculated to get the final instrument temperatures.

	Equations
Cryostat Wall to Rad Shield	$Q^c_{RS-truss} = (A_{RS-truss}/L_{RS-truss}) \cdot \kappa_{G10} \cdot (T_{WALL} - T_{RS})$
	$Q^c_{RS-cab} = (A_{RS-cab}/L_{RS-cab}) \cdot \kappa_{Copper} \cdot (T_{WALL} - T_{RS})$
Optical Tube to M3	$Q^r_{OT-M3} = SA_{M3} \cdot \sigma \cdot \epsilon_{M3} \cdot \epsilon_{OT-inner} \cdot (T^4_{OT} - T^4_{M3})$
Optical Tube to Top Ring	$Q^c_{OT-TR} = (A_{OT}/L_{OT}) \cdot \kappa_{Al} \cdot (T_{OT} - T_{TR})$
Top Ring to Corrector Plate	$Q^c_{TR-CPT} = (A_{CPT}/L_{CPT}) \cdot \kappa_{Al} \cdot (T_{CPT} - T_{TR})$
	$Q^c_{CPT-CP} = (A_{CP-truss}/L_{CP-truss}) \cdot \kappa_{G10} \cdot (T_{CP} - T_{CPT})$
Top Ring to Detector Box	$Q^c_{TR-DET} = (A_{SPIDER-support}/L_{SPIDER-support}) \cdot \kappa_{Al} \cdot (T_{TR} - T_{DET})$
	$Q^c_{TR-TRW} = (A_{TRW-truss}/L_{TRW-truss}) \cdot \kappa_{G10} \cdot (T_{TR} - T_{TRW})$
Cryostat Window to Corrector Plate	$Q^r_{CP-WIN} = SA_{WIN} \cdot \sigma \cdot \epsilon_{WIN} \cdot \epsilon_{CP} \cdot (T^4_{WIN} - T^4_{CP})$

Table 4.6: A few example equations for the transfer of heat between nodes, many of these equations used to build up the model. Explanation of the notation can be seen in Table 4.3.

There are two cases where the simple equations of heat transfer were not fully

appropriate, firstly when modelling the links between the CCC cold heads and the radiation shield or detector box, and secondly for the radiative link between the cryostat wall, the radiation shield and the optical tube. The paths from the CCC cold head along the wicks two or more conductive links are in series, see Fig.4.14 in particular WICK3. For wicks 1 & 2 the first part of the conductive path is the cold heads themselves, their cooling power has to be incorporated to obtain a realistic cooling rate. For two conductive links in series between nodes 'a' and 'b', the equation for calculating the heat becomes:

$$\dot{Q_{in_a}} = \left(\frac{1}{\frac{A_1}{L_1}\kappa_1} + \frac{1}{\frac{A_2}{L_2}\kappa_2} \right)^{-1} (T_b - T_a) \tag{4.14}$$

For the case of wicks 1 & 2, the first conductive link is replaced by the inverse of the cooling power, 1^{st} stage = 1.3W/K and 2^{nd} stage = 1W/K. For wick 3, the whole link consists of five conductive links in series.

The radiative links between the cryostat wall to the radiation shield and from the radiation shield to the optical tube can be considered to be the radiative transfer for an enclosure consisting of two parallel, infinite and opaque plates. This is valid because there are two closely spaced cylinders with a separation between them much smaller than their radii. Using the principles of radiative transfer between two surfaces that can only 'see' each other, it can be shown that:

$$\dot{Q_{in_a}} = \frac{\sigma T_a^4 - \sigma T_b^4}{\epsilon_a^{-1} + \epsilon_b^{-1} - 1} \tag{4.15}$$

and

$$\dot{Q_{in_b}} = -\dot{Q_{ina}} \tag{4.16}$$

Eqn.4.16 is expected from the conservation of energy. Because there are only two surfaces which can only radiatively 'see' each other the heat loss at one surface becomes the net radiative heat gain at the other.

4.4.1 Comparison of Model with Real Data

The WFCAM camera has permanent temperature sensors located around the instrument on the radiation shield, the top ring structure, the detector box and the corrector

plate mount. These sensors are routinely read out and logged by the instrument control electronics during instrument integration and to this day as it operates on the telescope. To analyse if the thermal model worked the curves of the real thermal behaviour were plotted against the model outputs. Fig.4.15 gives the final plots for the temperature of the radiation shield (top graph), top ring structure (middle) and corrector plate (bottom) with the dashed line representing the true instrument behaviour and the solid line the model output. As can be seen the model for the bulk of the instrument never fully matched the genuine behaviour, it never quite got cold enough. However, the modelling of the detector box and the detectors themselves worked well and had a unexpected use, see §4.5 for further details.

The real cryostat undergoes pre-cooling with liquid nitrogen to give an initial rapid cooling rate. The pre-cool is not a steady cooling rate applied to the wicks, as the liquid nitrogen convectively cools the wick it warms up as they head towards an equilibrium which, in turn reduces its cooling power. It is very difficult to model a consistently changing heat flow hence the pre-cool was never successfully incorporated into the model. Further, the transfer links were calculated in a relatively straightforward manner and another level of sophistication of the model could be gained by more complex calculations and by adding more of the small detailed instrument parts into thermal path. The original intention was to use the model to verify if the cooling wicks installed in Edinburgh that maintained the operating temperature in the warm laboratory, would continue to do so in the telescope dome where the ambient temperature can be significantly colder. For the model to be truly useful it needed to track the real thermal behaviour to within a few degrees, which this model was not able to do.

However, project events took an unexpected turn and the successful modelling of the detector box found a new use, as discussed in the following section.

4.5 Modelling the Detector Cooling Rate

During a cool down of one of the science grade IR devices in the test cryostat for initial testing the detector catastrophically 'de-laminated', the active part of the detector broke apart with such force it was found in shards on the bottom of the test cryostat.

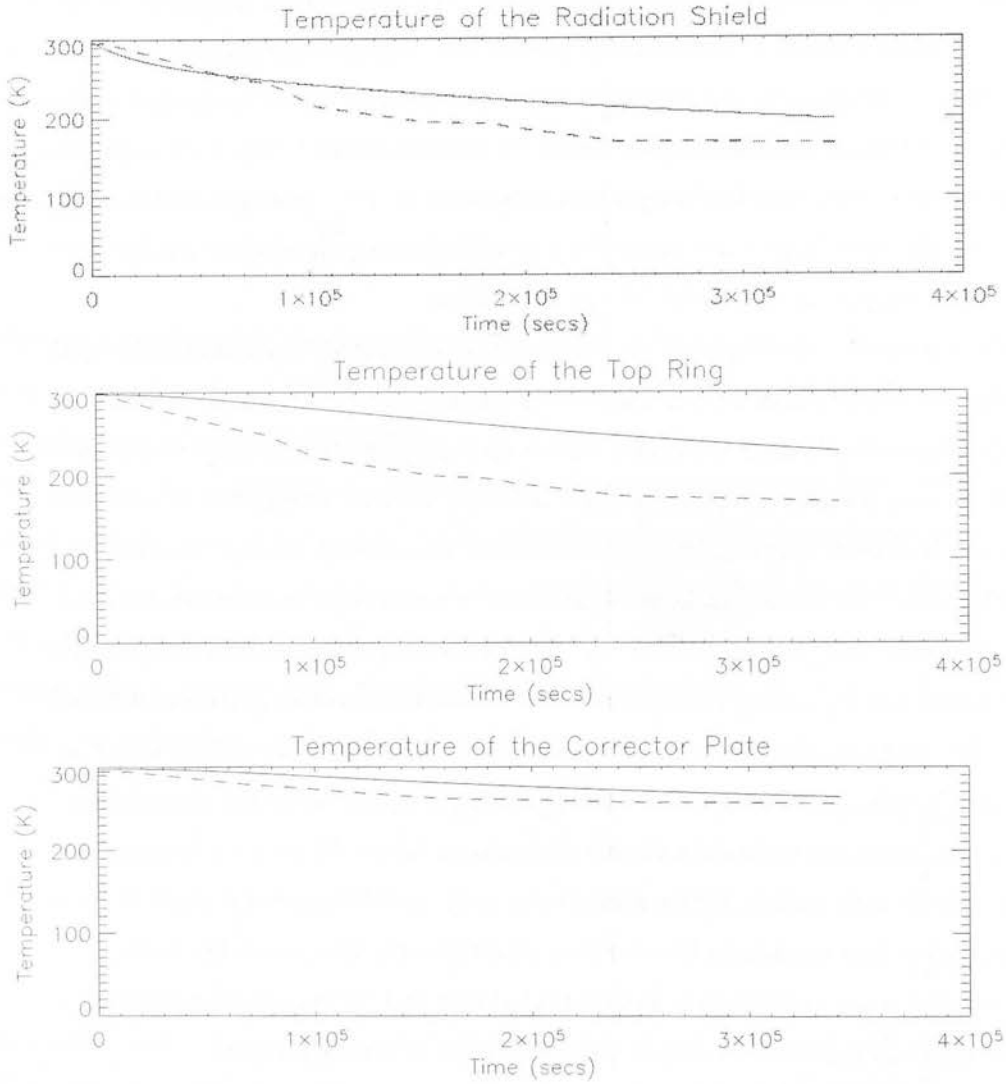

Figure 4.15: Outcomes of the thermal model plotted with the measured temperature logs measured with WFCAM in the laboratory in Edinburgh. The solid line shows the model results and the dashed line the real thermal curve. Overall cooling period plotted is just short of 2 days.

The photograph in Fig.4.16 shows the result of a second detector failure which happened later in the project when all four IR devices were mounted in the detector box. After the first failure the project stopped for a lengthy period of time when numerous tests were carried out to try and isolate why the failures happened. Potential issues which needed to be analysed were: if the mounting of the detectors in the focal plane were placing mechanical forces across the detector due to differential contraction between the support pins and the detector carrier; if there were differential contraction between the detector control printed circuit board (PCB) and the carrier; if the rate of cooling in the test cryostat was too rapid; or if there were temperature gradients generated across the detector due to different cooling rates being applied. The mechanical issues were addressed by the project team engineers but the thermal model presented here allowed us to look at the potential influence of the PCB design on the detector cooling rate and potential sources of temperature gradients across the detector without endangering another device with multiple cool down cycles.

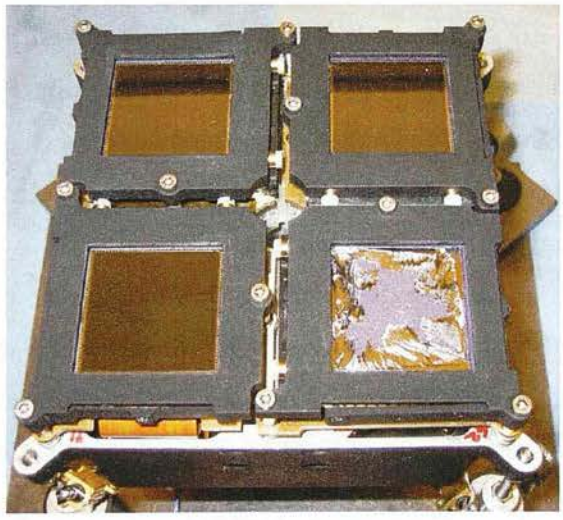

Figure 4.16: End result of the catastrophic failure of one of the Hawaii-II detectors during a cool down in the laboratory in Edinburgh.

The Hawaii-II infrared devices are mounted on a ceramic carrier which is placed into a zero insertion force (ZIF) socket which is then mounted on a PCB. The PCB connects the detector signal output pins to the cable which takes the signals to the detector controllers external to the cryostat and is mounted in the detector box by four

pins. The Hawaii-II devices have a grid of 361 pins, 192 of which carry the signal out of the multiplexor and 169 which only act to cool the array. The cooling pins are evenly placed over the middle of the array with the signal pins round the outside. The cooling pins pass through the ZIF socket and the PCB then into a copper block which conductively transfers the cooling power from WICK3.

The original design of the system had a 'solid' PCB with the copper block at the back and the pins passing through individual holes in the PCB to make contact with the block. After the detector failure there were concerns that the contact between the copper block and the cooling pins was not uniform and a new design with a hole in the PCB underneath the ZIF socket large enough for the copper block to sit flush against the back of the ZIF was devised.

The thermal model for the detector box and IR detectors was developed to incorporate finer detail. A 12 node breakdown of the system allowed tracking of the thermal behaviour from the point of contact with the copper block through the cooling pins, through the PCB, ZIF socket and ceramic materials out to the edges of the detector. The three components; PCB, ZIF and ceramic, are conductively linked through the cooling pins, the cooling pins are conductively linked to the signal pins through the materials of each of the components. To simulate the difference between a solid PCB and one with a hole in it, the conductive link through the PCB material is broken as there is no PCB material in contact with the cooling pins.

Fig.4.17 shows the results of running the model for both the 'solid' and 'holed' PCB scenarios. The top two plots show the behaviour with the solid PCB against real temperature curves measured in the test cryostat and the bottom plot compares the two PCB design options. The very top plot of Fig.4.17 shows modelled detector box temperature versus the measured temperature curve in the WFCAM cryostat (solid line). This shows how, unlike the main instrument structure the model simulated the functional form of the genuine cooling curve accurately. The second graph shows the comparison of the modelled temperature (dashed line) over time of the ceramic carrier versus that measured in the test cryostat (a temporary temperature sensor was placed on the detector ceramic during a thermal cycle of the cryostat). The modelled

temperature very accurately followed the measured curve. The final plot shows comparison of the model run for both the PCB designs, there was effectively no difference found between using a solid PCB or one with a hole in it on the rate of cooling for the detector ceramic carrier. Ultimately the decision was made to switch to the new PCB design with the 'hole' but not due to impacts on the cooling rate.

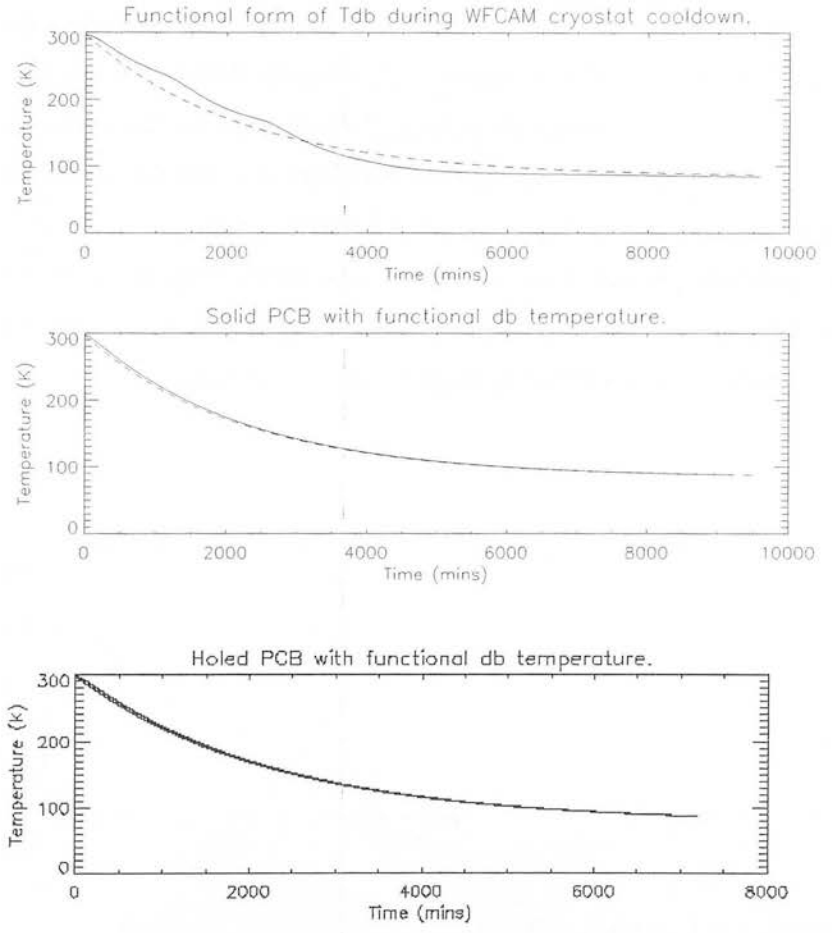

Figure 4.17: Resultant plots of the modelling of the detector detector box and ceramic carrier using both PCB designs. The dashed lines represent the output of the model and the solid line shows the measured data. The model showed virtually no change between a solid PCB and one with a hole to accommodate the copper cooling block.

Lastly, the model was used to analyse the temperature lag between the detector

box and the detector ceramic, the PCB and the ceramic and the inner and outer portions of the ceramic. The results can be seen in the top three plots of Fig.4.18. As expected at the start of the cooling process the component which is closest to the CCC in the thermal path cools quickest giving a notable difference between the two surfaces, however after time the 'lagging' component catches up as the whole system come into equilibrium. The largest temperature difference found by the model was, unsurprisingly, between the detector box and the ceramic carrier, but even here the largest difference of 5.5K is not sufficient to cause a catastrophic detector failure. Further evidence is shown by the bottom graph in Fig.4.18 which gives the rate of change of temperature for the ceramic carrier through out the cooldown. The rate of change at the beginning of the cooling period is a very small 0.0014K per minute.

Through the modelling presented here and numerous other testing in the laboratory we confirmed that we were not exposing the IR devices to any forces through any mechanical or thermal processes sufficiently large to cause the damage.

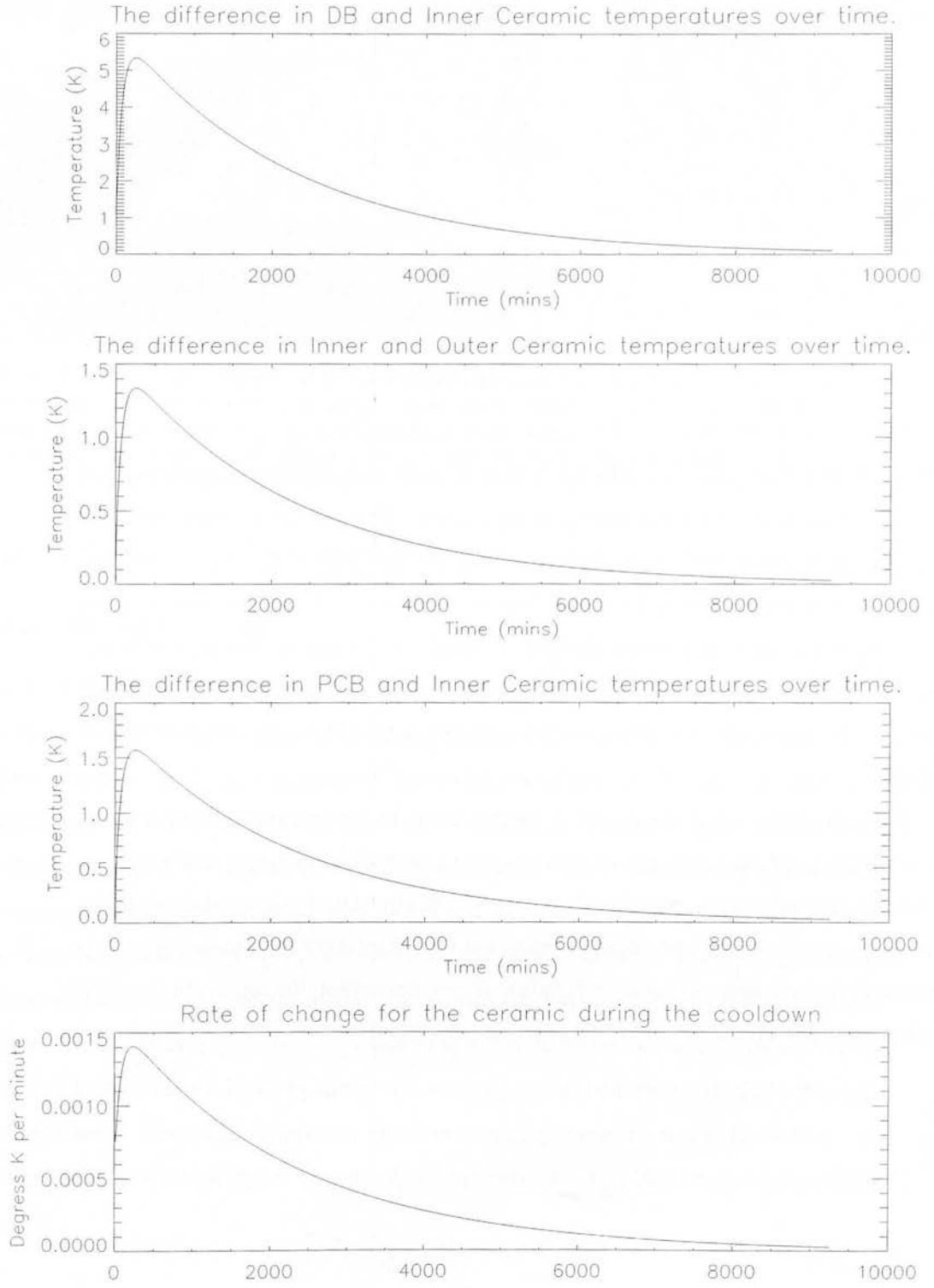

Figure 4.18: Temperature difference and rate of change of temperature for the detector ceramic carrier.

Chapter 5

The WFCAM Science Detectors

The WFCAM focal plane is made up of four infrared detectors for imaging the sky and one optical CCD for the auto-guiding system. The science infrared detectors are 'Hawaii-II' Mercury, Cadium, Telluride (HgCdTe) hybrids constructed with PACE technology bought from the Rockwell Scientific Company LLC (at the time of print the company is operating under Teledyne Scientific & Imaging). The Hawaii-II device is an evolutionary step up from the same manufacturers successful Hawaii-I 1K detector. The Hawaii-II devices have 2048 x 2048 pixels with a physical pixel size of 18μm.

It is important to characterise the properties of the IR detectors to facilitate the best operating conditions and practises for the camera, such that inherent qualities can either be corrected or accounted for. This chapter will start by discussing the principles of construction and operation of the devices then the characterisation tests and performance of the real detectors will be detailed. Where important, the implications of the characterisation on the use of WFCAM will be discussed.

Figure 5.1: The left hand photograph is a single Hawaii-II detector showing the ceramic carrier, the electrical connections and the active substrate. The 5p coin indicates scale. The right hand photograph is the complete WFCAM focal plane with a rule for scale. The focal plane has 4 coplanar science IR detectors and a single optical CCD for the autoguiding system which sits above the IR devices rotated by 45°

5.1 Principles of Infrared Detectors

5.1.1 Photon Detection

Infrared detectors exploit the properties of intrinsic semiconductors to detect incident photons by direct methods. Consider the depiction of an atom according to quantum theory, a single atom has a number of 'energy bands' where an electron can reside depending on its energy levels. The two key bands for understanding semiconductors in this context are the 'valance band' and 'conduction band' which are separated by an energy gap, E_G. The energy gap in a semiconductor ranges typically from a few tenths of an electronvolt up to two electronvolts. The smaller the energy gap the easier an electron can be excited into moving from the valance layer to the conduction layer. When a photon penetrates a piece of semiconductor material it causes a bound electron in the valance layer to 'jump' the energy gap so it can move freely in the conduction band. The incident photon must have energy equal to or greater than E_G in order to remove the electron. The energy of a photon, E_p, is related to its wavelength, λ_p, by:

$$E_p = \frac{hc}{\lambda_p} \tag{5.1}$$

where 'h' is Planck's constant and 'c' the speed of light. The longest wavelength, $\lambda_{\rm cut-off}$, the detector is sensitive to is determined by the bandgap energy by:

$$\lambda_{\rm cut-off} = \frac{\rm hc}{\rm E_{bandgap}} \tag{5.2}$$

To be sensitive to infrared photons the semiconductor material must have a low bandgap energy. Devices for detecting visible wavelengths typically use silicon (Si) with $\lambda_{\rm cut-off} = 1.05\mu{\rm m}$ which is too short for the IR regime. Other useable materials include Indium Gallium Arsenide (InGaAs) - often used for near infrared observations - Platinum Silicide (PtSi), Indium Antimonide (InSb) and Mercury Cadium Telluride (HgCdTe) are the most common materials for infrared detectors. A sample of frequently used materials can be found in Table 5.1, listing their typical $\rm E_G$, $\lambda_{\rm cut-off}$ and operating temperature. The bandgap energy is also effected by the temperature of the semiconductor

Semiconductor material	$\rm E_{bandgap}$ (eV)	$\lambda_{\rm cut-off}$ (μm)	T (K)
Silicon (Si)	1.18	1.05	150 - 300
Indium Gallium Arsenide (InGaAs)	0.7	1.7	77 - 200
Platinum Silicide (PtSi)	0.25	5.0	40 - 60
Indium Antimonide (InSb)	0.23	5.4	20 - 40
Mercury Cadmium Telluride (HgCdTe)	0.25 - 0.5	2.4 - 4.8	60 - 77

Table 5.1: Properties of semiconductor materials often used in photon detectors detailing bandgap energy ($E_{bandgap}$), Cut-off wavelength ($\lambda_{cut-off}$) and operating temperature (Beckett 1995).

material, which means the effective cut-off wavelength is also temperature dependent. Various models have been developed to define the temperature dependence of $\rm E_G$, the full explanation of the origin of the dependence and the development of the models is outwith the scope of this work and is not necessary to discuss beyond noting that the dependency is due to the materials used in the construction of the semiconductor, Varshni (1967), by the equation:

$$\rm E_G = E_{G0} - \frac{\alpha T^2}{(\beta + T)} \tag{5.3}$$

where $\rm E_{G0}$ is the bandgap energy for the given material at $\rm T = 0K$ and the constant α, β are related to the alloy semiconductor materials. The implication of equation 5.3

is that the lower the operating temperature the higher the bandgap energy and thus the lower the cut-off wavelength. Since the bandgap energy is clearly related to the semiconductor material, alloy semiconductors can be 'tuned' by adjusting the balance of the composite materials to give the desired cut-off wavelength. The WFCAM detectors are made of the HgCdTe alloy which has been tuned to give a wavelength sensitivity in the range of $1 - 2.5\ \mu$m at operating temperatures of $60 - 77$K.

5.1.2 Recording the Photons

When the incident photon bumps the electron into the conduction band a net positive charge, termed a 'hole', is left behind which behaves as a positively charged particle. The generated electron-hole pair carries a measurable electric current, a photocurrent (Young 1999). High performance detectors exploit the photovoltaic effect to measure and record the photocurrent and infer the number of incident photons. The photovoltaic effect arises at the junction between two dissimilar, materials when one of the materials is exposed to electromagnetic radiation a voltage difference across the junction is produced. In the case of infrared detectors the two materials in question are two semiconductors of opposite polarity and the interface is a simple pn junction. The diode junction is created by impregnating it with ions from an appropriate material. The junction is operated with an externally applied voltage to cause a reverse bias which produces an electric field over the junction separating the electron-hole pair so that they cannot recombine. Since both the electron and positive hole migrate there is no recombination noise. This migration of the charged particles changes the electric field across the junction effectively making the diode behave as a capacitor. At the end of a given integration period the voltage across the diode is measured. Since the photoelectrons discharge the junction capacitance, as long as the initial capacitance of the junction is known then the number of electrons can be determined and the number of detected photons can be inferred.

Two main technologies used for manufacturing photon detectors are Charge Coupled Devices (CCDs) and Direct Readout (DRO) devices. CCDs are a single structure devices where electrodes on the surface are used to couple the pixels together such

that the charge can be transferred across the surface of the array to a single output amplifier. A photon absorbed by the active silicon layer creates an electron-hole pair. A series of surface electrodes are biased to create an electric field which determines the 'pixels' and collects and stores the electrons in the pixels during the integration period. After the desired exposure time the surface electrons are used to read out the detector in a manner that transfers each pixel's electrons sequentially to neighbouring pixels until they reach a single amplifier in one corner of the device. Readout electronics at the on-chip amplifier logs the pixel values in turn. DRO arrays on the other-hand are are devices constructed from a large number of individual pixels each of which have a individual multiplexor, amplifier and readout electronics and pixels are completely discrete from each other. The most common infrared detectors used for astronomical purposes are DROs.

Silicon is an ideal material for manufacturing semiconductor detectors as it can be doped to be both positive and negative without disturbing the crystal structure. It is photosensitive across the whole visible region to the atmospheric cut-off at 1μm, however it is insensitive beyond 1μm so cannot be used as the active layer for infrared devices. To complicate matters, the technology for manufacturing complex integrated circuits on other infrared sensitive semiconductor materials is not currently advanced enough to facilitate using the same materials as the photo sensitive layer and the layer containing the readout electronics. It is thus common to built infrared detectors from two different materials, utilising silicon for the shared addressing and readout circuitry below a suitable active detector layer. Such detectors are known as 'hybrid arrays'.

5.1.3 Structure of Hybrid Arrays

Hybrid arrays have an infrared sensitive detecting layer bonded to a silicon integrated circuit containing an array of pixels each with their own individual storage site and amplifier. A series of switches in the silicon, called a 'multiplexor', provide an individual signal path from the pixel to the output. Figure 5.2 shows a diagram of a cut through a hybrid array showing the different required layers and the connecting indium bump bonds (Böker et al. 2001), the following sections describe each layer.

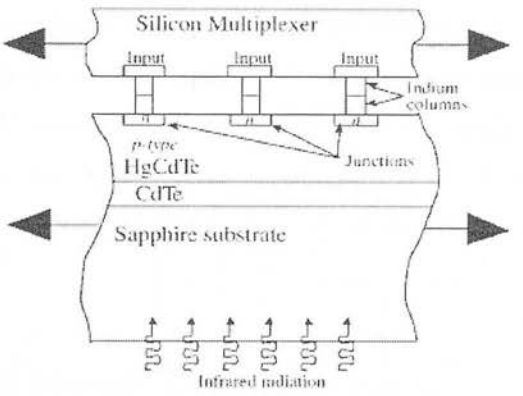

Figure 5.2: Schematic cross-section of an IR PACE detector array, not to scale. The incident light arrives at the non-active sapphire substrate (bottom of diagram), passes through the IR sensitive layers to the semiconductor junctions, along the indium bump bonds to the read-out electronics in the silicon multiplexor (Böker et al. 2001).

Hybrid arrays are especially difficult to manufacture as the various layers are made of different materials which have different thermal properties. The detectors are produced at room temperature but are operated at cryogenic temperatures of anywhere between 20K – 80K. Any difference in thermal contraction between the layers can cause the device to break apart while it is changing to and from operating temperature. This has hindered the size of infrared detectors that can be robustly manufactured. Nevertheless, one advantage of hybridising techniques is that each of the constituent layers can be independently optimised.

The Top Layer

Many hybrid detectors have a sapphire layer on the top that is transparent to radiation in the 1 – 5μm wavelength range to help strengthen the device. The surface of the sapphire is not anti-reflection coated and consequently around 10% of the incident photons are lost from reflections at the front of the device.

The Active Layer

The radiation sensitive layer of the detector absorbs the incident photon and generates an electron as explained in §5.1.2. If this electron is to be detected it must be produced

near the diode junction and the readout circuitry. The arrays are 'backside illuminated' such that the photons must travel through the thickness of the active layer before being absorbed. To increase the chance of a photon being detected the top layer must be thinned. Narrow insulating strips are used to form barriers between the implanted diodes to separate them and define the 'pixels'. These barriers lead to dead space between the pixels where incident photons cannot be detected.

The Interconnecting Bonds

Columns of metallic indium are deposited on each pixel to create the connection between the detector and the readout circuitry. When the two layers of the array, the top infrared sensitive layer and the silicon layer, are pressed together the indium cold-welds to form an electrical connection along which the current can travel. It is quite common for the indium bonds to break during the lifetime of the detector causing isolated dead pixels on the array surface. Often the gap between the two layers is filled with an epoxy to improve the mechanical integrity of the detector, however this is not the case for the Hawaii-II detectors.

The Pixel

When DRO arrays are manufactured each pixel is an independent system which has its own charge storage site and readout circuitry. The semiconductor junction capacitance is pre-charged to a fixed voltage (the same voltage level for all the detector's pixels) prior to the exposure, the arriving electrons discharge the capacitance until there is no more potential left. Since saturation of the pixel occurs when the diode is fully discharged there can be no charge leakage onto neighbouring pixels, which is a phenomenon often seen on CCDs, called 'blooming'. Figure 5.3 shows a schematic diagram of the internal architecture of a Hawaii-II detectors, the unit cell circuit of the pixel is enclosed in a dashed line box at the top of the diagram (Hass 2002).

The Multiplexor

Each pixel's capacitor is connected to the input of an insulated gate field effect transistor (FET). FETs are solid state devices which can be utilised as amplifiers due to how

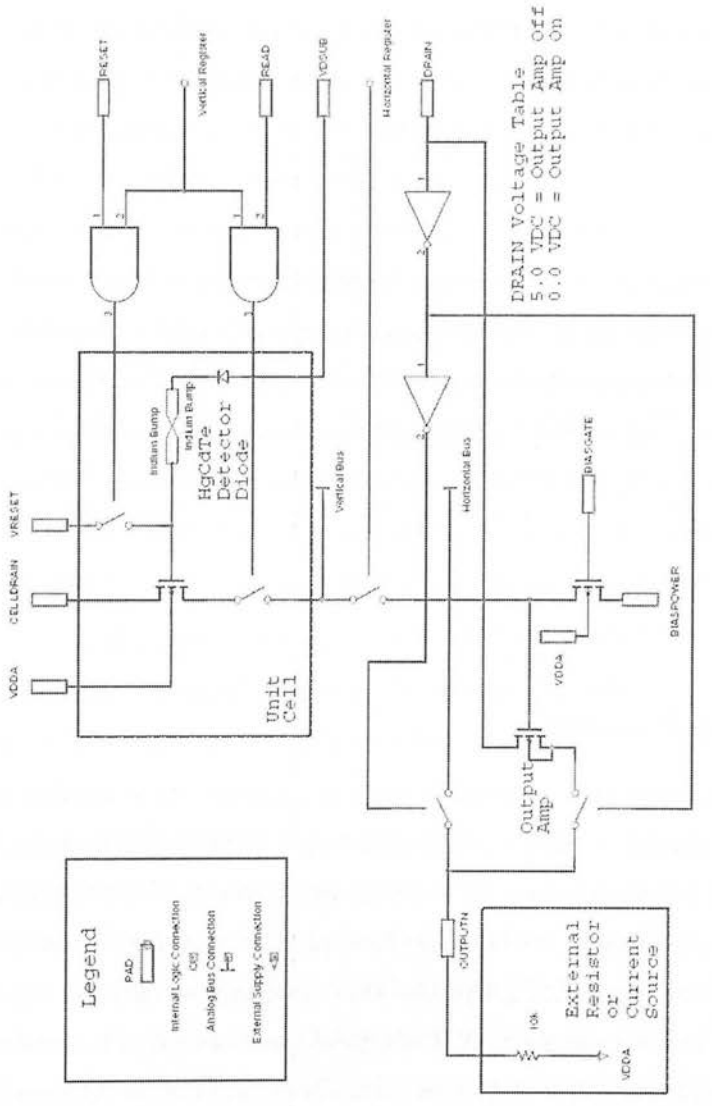

Figure 5.3: Schematic diagram of the internal architecture of the Hawaii-II detector, a pixel is made up of the 'unit cell' which grouped by a box at the top of the diagram (Hass 2002).

they behave when current is passed through them. A comprehensive description including diagrams can be found at Jim Lesurf's web pages on www.st-andrews.ac.uk among other sources.

A blanket of FET switches is the layer directly under the active substrate in the hybrid structure and is called the 'multiplexor'. Performance of the multiplexor is as critical to the success of the array as is the quality and performance of the active layer. The two layers are electronically connected by the indium bump bonds. Multiplexors use on-chip row and column shift registers to generate the x & y address of the each pixel incrementally rather than having individual address lines or address decoders. The shift registers work in a way which makes it possible to skip over any number of pixels without reading their signal, and allows sub-arrays to be read very quickly.

The design of the multiplexor electronics is related to the background we expect for the given detector, correct readout speed is vital to stop the detector saturation. Examples of background levels; low background environments include space-borne cryogenic telescopes, intermediate backgrounds include spectrographs in ground based instrument whereas high backgrounds can be found in ground based broad-band cameras.

5.1.4 The Read Out Procedure

The electronic arrangement of the Hawaii-II chips is such that there are four completely independent quadrants which can be read out by either 1 or 8 outputs, WFCAM will use 8 outputs per quadrant (32 channels per detector) which significantly reduces readout time. Effectively the WFCAM focal plane (4 Hawaii-II devices) consists of 128 detectors each of 128 x 1024 pixels. With a rapid read out of $\sim$ 187 kHz and 32 channels per detector the entire WFCAM focal plane is read out in under 0.7 seconds. This is necessary to keep readout overheads practical for 5 – 10 second exposures which are typical lengths for background-limited WFCAM astronomical observations (Hirst et al. 2006).

Fig.5.4 shows a simple diagram of the electronic arrangement of the Hawaii-II detectors. The quadrants are rotated by 90° with respect to each other because each quadrant's readout amplifiers are located on a different edge of the detectors, i.e. Quadrant

1 has the readout amplifiers on the left hand side of the detector, Quadrant 2 on the top of the detector and so forth. The readout of a DRO array can be quantitatively

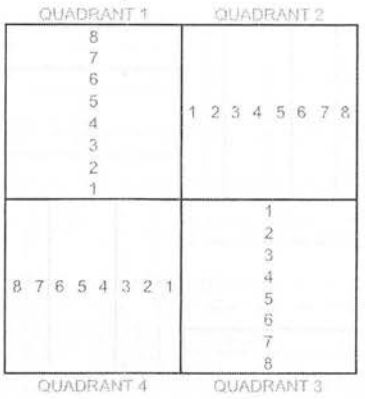

Figure 5.4: A simple diagram showing the electronic arrangement of the Hawaii-II detectors as set up in WFCAM. Each quadrant uses 8 outputs - a total of 32 channels per detector. Each quadrant is rotated by 90° with respect to each other due to the location of each quadrant's readout amplifiers. The entire WFCAM focal plan is readout by 128 channels in under 0.7 seconds.

described as; each pixel's capacitance is pre-set to a fixed level, during integration the level decreases due to incoming IR photons. The reduced capacitance voltage reduces the detector reverse bias voltage in the diode which reduces the pixel's collecting efficiency as the pixel fills.

The capacitance of the diode is dependent on the voltage across it, and such as the relationship between the voltage and the number of photons is not linear. There is always a 'trade-off' to be made when setting the initial capacitance level for the diodes, the larger the 'rest voltage' the more charge the pixel can store but the greater the noise equivalent charge, explained further in §5.4.7 (McLean 1997).

The duration of the exposure time of a infrared camera is not controlled by a shutter as it is with a visible camera. A shutter for an IR camera would have to be cold (internal to the cryostat) to avoid radiating and be rapid acting to facilitate short exposure times to cope with high sky emissions, much shorter than optical exposure times. A shutter of such nature is very difficult to manufacture robustly so an alternative is required. The exposure time of a pixel is set to be the time between the reset (setting

the pixel's initial voltage level) and the final readout of the pixel's detected signal. Actual 'exposure time' depends on the readout mode selected as will be explained further in §5.3.

5.1.5 The Hawaii-II Device

The Hawaii-II PACE devices are vertically-integrated hybrid arrays. The PACE manufacturing technique is a version of epitaxy technologies for growing diodes, 'PACE' is also known as Liquid Phase Epitaxy (LPE) (Cabelli et al. 2000). The epitaxy fabrication process was invented in 1960 and is a growth method for depositing a thin layer, in the region of $5 - 20\mu$m thickness, of a single crystal material onto a single crystal substrate, often through chemical vapour deposition (CVD). At the time of invention epitaxy made a tenfold improvement of the operational speed of transistors (source: http://www.corp.att.com).

The PACE substrates of the Hawaii-II devices are made by first growing Cadmium Telluride (CdTe) onto a prepared sapphire substrate, then the HgCdTe active layer is grown by LPE from a telluride rich melt. The necessary photovoltaic n-on-p junctions are formed by implanting boron ions at room temperature. PACE devices have fast output amplifiers which gives sample times of $\sim 5\mu$s/pixel but they do suffer from degrading quantum efficiency (QE) at short wavelengths.

5.2 Theory of Noise

Every single measurement of electrons taken by a detector has associated uncertainties or 'noise'. The noise comes from a combination of the nature of photon generation and the processes involved in detecting them.

Photon Noise

The actual signal the infrared detectors measure is based upon light and therefore the quantum nature of light plays a significant role in the noise. Detectors attempt to count individual photons so noise from the fundamental statistical nature of photon production is evident.

Consider a given pixel. It cannot be assumed that for two consecutive but independent measurements separated by a time interval, T, the same number of photons will be counted. The laws of quantum physics which governs photon production only allows the average number of photons generated in a time period to be dealt with. The probability distribution of average photons detected during in a period, T, is known to be Poisson and is described by:

$$P(p/\rho, T) = \frac{(\rho T)^p e^{-\rho T}}{p!} \tag{5.4}$$

where 'p' is the number of photons, and 'ρ' is the rate or intensity parameter in photons per second. It is very important to note that even if the detector was perfect and there were no other sources of noise in the detector or associated electronics then the statistical fluctuations associated with photon counting over finite time interval would still lead to a finite signal-to-noise ratio (Young et al. 1998).

Photon noise breaks three of the traditional assumed characteristics of the relationship between signal and its noise; photon noise is dependent on the measured signal, photon noise is not Gaussian and photon noise is not additive. During science observations, if the exposures are long enough to be background limited but the target object is fainter than the shy then the observation is photon noise limited from the sky photons. If the target object is very bright then the dominant source can be the photon noise in the object count.

Thermal Noise

Electrons can be freed from the valence layer in the semiconductor material through internal thermal vibrations as well as incident radiation photons. The electrons generated by thermal vibrations are indistinguishable from 'true' photoelectrons and have an associated thermal noise or 'dark current'. Thermal noise is a function of integration time, the longer the integration time the greater the number of thermal electrons are produced and recorded. By operating the detector at cryogenic temperatures it is possible to significantly reduce the number of 'thermal electrons' which give rise to thermal noise. However, the simple act of collecting photons warms the detector up

so the detector must be actively cooled at all times during operation.

An additional contributory factor to dark current is signal from background infrared radiation (heat) incident on the detector, that is radiation from non-astronomical sources. This is mainly warm optics and structure in the detector field-of-view, out-of-band filter leakage and luminescence from on-chip electrical components. The efforts involved in reducing all these 'non-astronomical' heat sources within the instrument is discussed in depth in Chapter 4. Dark current is compensated for in object frames by subtracting each object frame by a dark frame of the same integration time.

On-chip Noise

Noise in the multiplexor's output MOSFET is a major source of noise in IR detectors and had a $1/f$ characteristic where 'f' is the frequency the FET is operated at. In addition to this $1/f$ noise there is a 'readout noise' which is due to random thermal agitation of electrons in the semiconductor leading to uncertainty in the mean value of the reset voltage. Reset noise can be described in volts or electrons as (McLean 1997):

$$\sigma_{\mathrm{kTC}}(\mathrm{Volts}) = \sqrt{\frac{\mathrm{kT}}{\mathrm{C}}} : \sigma_{\mathrm{kTC}}(\mathrm{electrons}) = \frac{\sqrt{\mathrm{kTC}}}{\mathrm{e}^{-}} \tag{5.5}$$

where 'C' is the diode capacitance, 'T' is the operating temperature of the array, 'k' the Boltzmann's constant and e^{-} is the charge on an electron.

kTC noise is a 'one time' value per pixel that occurs during the reset procedure and is totally independent of integration time. Both $1/f$ and the reset noise can be reduced to manageable levels with proper electronic design and intelligent readout procedures. In practise the kTC readout noise is entirely eliminated by using a CDS readout mode, see §5.3.2.

5.3 Different Operational Modes

An infrared DRO array can be read many times without affecting the charges accumulated on the individual pixels allowing it to be readout in a number of different ways. The main readout modes used in operations are; the simple readout, a global correlated double sample (CDS), row-by-row CDS and versions of multiple non-destructive

read (MNDR). The read noise and performance of the IR detector can be improved by proper selection of the readout mode for the given observation type.

5.3.1 Simple Readout

In the simplest of methods, sometimes called the 'End Read Method', the exposure is determined by resetting each pixel, exposing and then reading the resultant voltage developed on the pixel. This method can be very noisy due to the uncertainty in the level of the reset voltage arising from the kTC noise. This method is the most efficient mode since there is only one read, however it is only useful in high background cases and is rarely used for astronomical observations.

5.3.2 Correlated Double Sampling

Correlated Double Sampling (CDS) is a reset-read-read sequence, Figure 5.5 shows a schematic of the global CDS readout procedure. The array is firstly reset, then read out immediately after. The exposure starts as soon as the first read takes place and after the specified integration time a second readout takes place. The second read is subtracted from the first to give the pixel values for the raw image. Although all the pixels are not read out simultaneously, the interval between the two reads of any given pixel is exactly equal to the integration time, Figure 5.5. Taking the difference of two read values improves the noise measurements by overcoming the uncertainty in the initial voltage level and reduces the effects of long-term, low frequency drifts. The overhead for an CDS exposure is 'reset-time plus read-time', however in practise the reset time for the array is so fast the overhead is effectively only the read time. During a global CDS mode the whole array is reset in sequence before starting the first read. If an integration time is set to be 'T' then the actual exposure time is roughly 'T + t' where 't' is the detector readout time. The efficiency of the readout sequence is given by:

$$\text{Efficiency} \simeq \frac{\mathrm{T}}{\mathrm{T}+\mathrm{t}} \tag{5.6}$$

With infrared detectors it should be possible to set the integration time, T, between a minimum of the reset time and a maximum of 30 minutes depending on sky levels

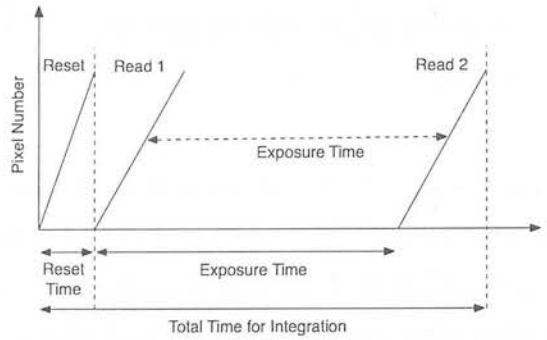

Figure 5.5: Schematic showing the breakdown of reset time, read time and integration time for a global CDS frame: the entire detector is reset, then the entire detector is readout. There is then a pause for the demanded integration before the entire detector is readout for a second time. The raw frame which is stored is equivalent to Readout 2 minus Readout 1.

and observation types. Typically broadband IR observations are around ~ 5 seconds and due to instrument specifications no more that 1 frame every 10 seconds is stored (WFCAM document 'Specification of IR detector readout modes'). Frame storage rate means in the number of coadded exposures, N, must conform to: $N * (T + t) > 10$, implying typically two coadded frames for broadband images. Since there is a readout overhead for each exposure taken the overheads are not reduced by multiple exposures and the total efficiency of a series of global CDS exposures remains $\sim T/(T + t)$

Other versions of the reset-read-read method can treat each pixel as a single entity or do a row-by-row reset-read-read. Figure 5.6 shows the schematic for a row-by-row CDS mode. This mode can reduce the overheads for multiple coadded exposures but can introduce array instabilities. The advantage of the row-by-row version of the CDS readout mode over the global version is that the overhead is only one full frame read time independent of number of reads, and is given by:

$$\text{Efficiency} \simeq \frac{N * T}{(N * T + t)} \tag{5.7}$$

If the number of coadded frames, N, is 1 then there is no efficiency gain over global CDS.

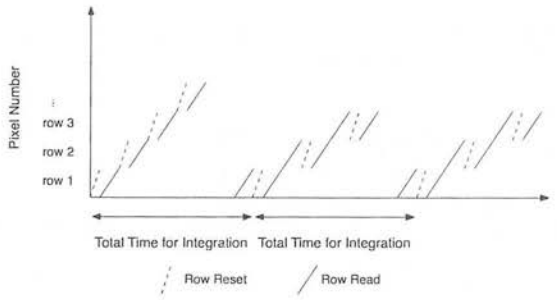

Figure 5.6: Schematic showing the breakdown of three Row-By-Row CDS frames: reset & readout of Row 1 then reset & readout of Row 2 repeating through all rows. Wait for integration time then read - reset - read of Row 1, read - reset - read of Row 2 until all rows have had this treatment. This procedure is repeated for as many exposures as required after which each pair of reads are subtracted then added together and stored as a raw frame.

5.3.3 Multiple Non-Destructive Read Mode

Multiple Non-Destructive Reads (MNDR), or linear fitting method, is similar to CDS except the readouts occur more frequently, at regular time intervals throughout the integration time, Figure 5.7 shows the schematic for the MNDR procedure. Once the exposure has finished, a straight line fit to all the readouts of each pixel in turn is calculated. The gradient of the line fit represents the flux arriving at the pixel, i.e. the incident photon rate. This mode helps to further reduce the read noise in the exposure, which can be improved by $\sqrt{N/12}$ better than CDS as it reduces the $1/f$ noise by taking frequent samples of the signal size. In practise, bias is reduced to such a low level that real time science data can be displayed without the need for dark subtraction.

The minimum rate for MNDR mode is when the readout process starts at the beginning of the exposure and continues, without reset, until the integration time is complete. Each measurement made during a MNDR exposure reduces the error in the slope therefore effectively reduces the read noise. Typical total exposure times are of the order of minutes such that several hundred reads may be combined to form one final frame which is stored as the raw image. For the 'continuous readout' version of the MNDR mode the resultant output voltage is closely proportional to the integration time and the slope of its value against time becomes the measured quantity.

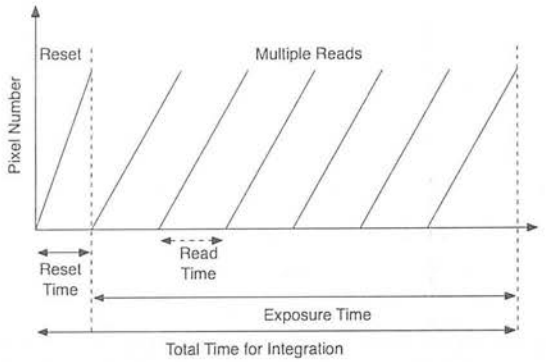

Figure 5.7: A schematic for the MNDR readout procedure: the entire detector is reset then the entire detector is read out regularly every few seconds (the time interval is set in the detector controller) throughout the total integration time. The stored raw frame is the least squares fitted slope of all the read values multiplied by the total integration time. The pixel values registered are the counts not the counts per second.

5.3.4 Fowler Sampling

By reading the whole array 'N' times at the beginning and the end of each exposure, then averaging the read values before subtraction of the first averaged read from the averaged read after the integration period the noise can be reduced by the order of $\sqrt{N}$ (Glass 1999). Descriptively the sequence of the Fowler read mode is such that; the detector is globally reset, the initial pixel values are repeatedly readout N times, the start values are co-added pixel-by-pixel and stored, there is then a pause for the demanded integration time before the end pixel values are again read N times, the end values are again co-added pixel-by-pixel and stored. Importantly when reading out a given pixel it must be re-addressed at each readout, a source of noise is related to this multiple addressing of the pixel.

Studies of the SNR values for multiple sampling read modes have been completed by Fowler and Gatley (1990) and Garnett and Forrest (1993) among others. They found optimal results are obtained, in the read noise limited case, when the pixels are sampled continuously for the first and last thirds of the integration time but not during the middle third. It is also shown by Garnett and Forrest (1993) that in the same scenario the line fitting continuous process (continuous MNDR) is slightly better than the optimised Fowler sampling. Both MNDR & Fowler read modes are useful for longer

integration exposures, for example narrow band filter images or spectroscopy of faint objects, though the increased readout activity could cause pickup problems.

5.4 Detector Properties & Characterisation Tests

There are several properties and characteristics of detectors which need to be well quantified before the devices can be used to their full potential. Information on some of these properties will influence how the detector electronics and software are optimised whereas effects from other properties need to be corrected in post-reduction. The characterisation tests for WFCAM were done in the laboratory at the UK ATC in Edinburgh with further optimisation carried out with the complete instrument installed on the telescope. The following subsections will describe the properties being tested, the test set up and analyses methods before presenting the results and comments on any effect.

A number of tests were carried out either in conjunction with or by the electronic engineers of the WFCAM instrument team. A number of the results which were not directly taken by myself have been included in this section in order to offer a complete picture of the detector's abilities and attributes. Credit is given where appropriate for results attained by colleagues. More details are given regarding the procedures and analysis for the characteristics I was active in measuring than for the others where simple descriptions and results are stated.

During the laboratory characterisation work in Edinburgh the four science grade infrared detectors were housed in a custom built small volume cryostat which housed the whole detector box as if in the real instrument such that the four IR detectors and the auto-guiding CCD are facing the bottom of the cryostat (see §4.1 for a full description of the instrument, detector box and focal plane). A window into the cryostat with a blocking filter allowed radiation onto the detectors. There were a number of infrared light sources available for each test; a focussed near IR diode external to the cryostat mounted on a precision XY stage allowed spot images to be projected anywhere on any of the detectors, an unfocused near IR diode external to the cryostat to give a diffuse light source and a similar unfocused diode internal to the cryostat. The central

wavelength of the NIR diodes used was 850nm.

The detectors are given an identification number by the manufacturers which was used to distinguish the detectors throughout the characterisation tests. The identifications being; #41, #60, #63, #76. The data reduction and analysis for the characterisation tests were done using the 'Image Reduction and Analysis Facility', commonly known as IRAF. Fig.5.8 is a simple schematic to show where each quadrant is displayed by IRAF, all detector images presented in the following chapters are this orientation unless otherwise noted.

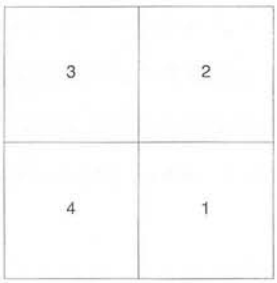

Figure 5.8: Simple diagram showing the orientation of the quadrants as displayed by the standard IRAF tasks. Each image of a WFCAM detector in the following sections are at this orientation unless stated otherwise.

5.4.1 Crosstalk

Crosstalk visible on IR detectors can be an effect due to both electrical and optical properties of the detector. The crosstalk artefacts are essentially time derivatives of saturated incident signals. The crosstalk effect is seen as a 'ghost' image when a strong signal is incident on a 'different element'. Different elements can be between individual pixels, between rows and/or columns of pixels and between readout channels. There can be both charge drift from one pixel to another pixel and electrical crosstalk due to common power supply coupling. This is an inherent property of the detectors and can not be 'removed' entirely. The readout electronics can be adjusted to help minimise the effect or it can be removed off-line in post-reduction. The identification and quantification of crosstalk on the WFCAM arrays is particularly important due to the intended purpose of the camera. Since WFCAM is a very wide FOV imager

it will be used to survey large parts of the sky with many astronomical targets. If the crosstalk effect is too large it could limit how effectively the camera is used for observing crowded star fields.

Test Set Up & Analysis

The science grade detectors (detectors #41, #60 & #63 were available at the time of testing, #76 was a late replacement for a science array which catastrophically failed during initial testing.) were mounted and cold in the small test cryostat. The precision XY stage was used to focus a spot onto one channel of one quadrant of the selected detector. Multiple exposure CDS frames was taken with a variety of exposure times between 1ms and 4s. A dark frame of equal integration time was taken after each spot image. Using standard IRAF commands the dark frames were subtracted from the object frames, allowing the crosstalk ghosts to be seen. The intensity and FWHM values of each ghost image was recorded, then the percentage of the intensity ratio (ghost/spot) determined.

Results

A consistent behaviour is seen regardless of which detector is used, spot position on detector or exposure time. The ghost image does differ depending on which channel the crosstalk is measured with respect to the channel the spot was projected on. On all non-adjacent channels the crosstalk ghosts have a standard positive profile and are all measured to be $< 0.04\%$ of the incident spot intensity regardless of exposure time. However ghost images on the directly neighbouring channels have a very different profile with both positive and negative components.

Figures within 5.9 present histogram plots for the three analysed detectors giving the percentage values of the ghost images. The x-axis represents the detector channels, $1 - 8$ with the percentage ratio of the images on the y-axis. It is clear from the plot which channel the spot was projected on for each data set by the lack of data for the given channel. The different integration time used for each data set is shown by the different coloured columns.

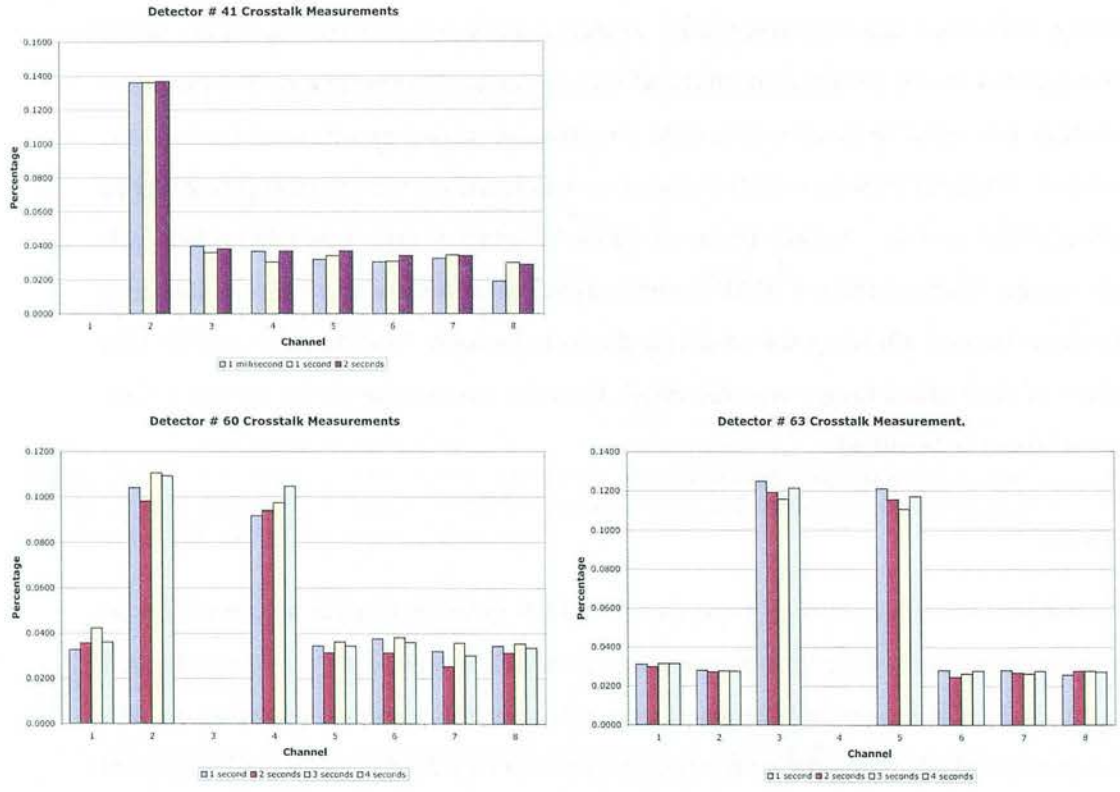

Figure 5.9: Histogram plots showing strengths of the crosstalk 'ghost' images. X-axis represents the 8 channels of the measured quadrant and on the y-axis the strength is given as a percentage of the incident signal strength. Plots clearly show that the channels directly neighbouring the heavily exposed spot have ghost artefacts 3 – 4 times stronger than all other channels regardless of integration time (indicated by colour of the bars, keys are underneath each individual plot.

In all cases the ghost images on the channels directly adjacent to the incident spot are stronger than the other ghosts, the crosstalk ghosts peak at $< 0.14\%$. The adjacent ghost images also have a more complex profile. Both the positive and negative components of the ghost images have roughly the same strength as seen in Figure 5.10, left hand side, which is a line-cut through a single adjacent ghost image. For all the images analysed, regardless of integration time or readout channel the positive/negative components had strengths $\leq \pm 0.15\%$. Figure 5.10, right hand side, shows an image of an incident spot with the two adjacent ghost artefacts. It was found that the ghost profiles were consistently negative on the same side of the ghost regardless of location with respect to the incident spot and channel used. A colour bar is found at the bottom of the figure, black is negative while white is positive. There was no measurable inter-quadrant crosstalk found in the lab. The Cambridge Astronomical Survey Unit

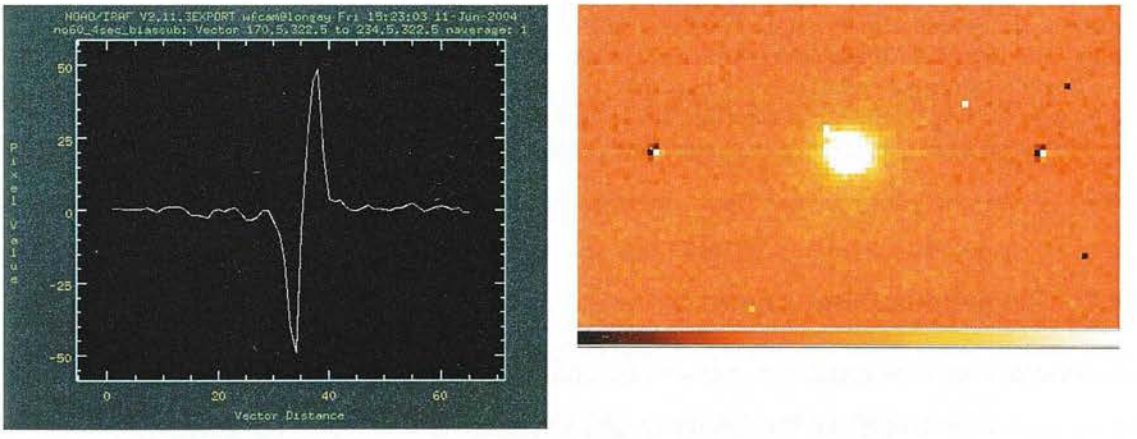

Figure 5.10: Left hand figure shows a cross-section through a crosstalk ghost image adjacent to the incident spot. The profile of the ghost demonstrates the complex nature of the ghost with both a positive and negative component. The right hand figure shows how the profiles of the ghost images were consistently found to be negative on the same side regardless of location with respect to the incident spot. A colour bar is located at the bottom of the figure.

(CASU) continued to investigate the crosstalk issue during instrument on-sky science verification to aid development of their post-reduction pipeline. On sky they found ghost artefacts manifested themselves as either a 'doughnut' shaped image from a heavily saturated star or a 'half-moon' shaped image from weakly saturated stars. Adjacent crosstalk ghosts had strengths $\sim 1\%$ the flux of the offending star with the

secondary ghosts dropping to $\sim 0.02\%$. They also found, as I did in the test cryostat, that there were no inter-quadrant crosstalk. As the artefacts are non-astronomical in appearance they can be removed in automated post-reduction (Irwin 2006).

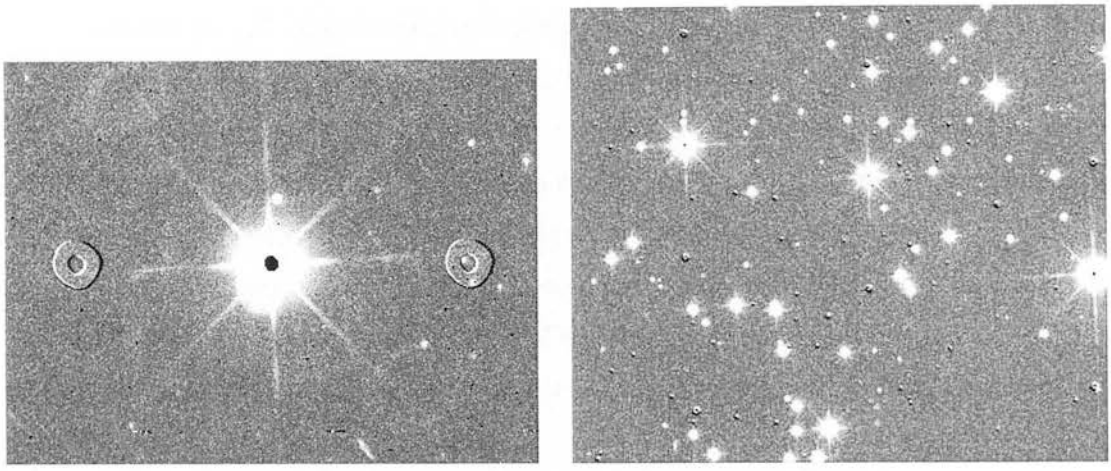

Figure 5.11: Evidence of crosstalk in images taken by CASU during WFCAM science verification. The left hand image shows the 'doughnut' shaped ghost in the adjacent channels to the a heavily saturated star. Crosstalk becomes a larger concern in crowed fields as shown in the image of an open cluster in the right hand figure. Given that the crosstalk artefacts are non-astronomical in character they can be removed in the reduction pipe-line (Irwin 2006).

5.4.2 Flat Field & Reset Anomaly

All detectors have inherent variations in quantum efficiency (QE) over their surfaces on various scales (see §5.4.6 for details on QE). On scales of less than a few tens of pixels there will be pixel-to-pixel variations in QE, extreme examples of these variations can be hot or dark pixels. Detectors will often have noticeably larger-scale variations in QE over tens or hundreds of pixels or over significant fractions of the device. There can also be evidence of a gradient to the QE over the entire device. Gross variations in QE are deemed 'flat field characteristics' of the detector and it is important to verify that these variations do not vary over time-scales from hours to a day.

All IR detectors also suffer from a 'reset anomaly' to some degree or another due to detector construction methods. The main component of the reset anomaly seen on the Hawaii devices is a large intensity ramp at one edge of each quadrant, the edge

where the readout electronics are located. Fig. 5.13 shows the evidence for the reset anomaly on the WFCAM Hawaii-II detectors. A discussion on the origin of this effect is give by Mackay (1999). As we have seen, hybrid devices consist of a sandwich of a detecting layer and the silicon multiplexor layer. The technology utilised to create the multiplexor relies on very high degrees of insulation between the electronic components and the silicon substrate they are embedded in. The substrate needs to be at a fixed potential such that all the multiplexor components are effectively capacitively coupled. Every time the device is reset, electrical potentials are established between the FET electrodes and the substrate and even though the electrodes are insulated, activating them causes displacement currents to flow from the ground potential in the substrate. This indicates that there is a substantial change in the substrate potential depending on the state of the device, it being clocked, active or dormant. However, since the substrate is only capacitively coupled to the FET electrodes what is actually seen is the effect of a change in state of the device from dormant to active. Once the operation of the device is established the substrate potential returns to its dormant level. This short-term effect in the substrate potential translates into a short-term 'glitch' in the output level. Of course, a similar effect occurs when the device changes activity from 'operating' to 'dormant', however at this point the device is not being read out so it does not affect the image (Mackay 1999). As with flat field characteristics it is most important to verify that the reset anomaly is stable over time-scales of hours to a day so it can be confidently removed from the object frames.

Test Set Up & Analysis

It can be problematic to disentangle variations in QE which are intrinsic to the detector and variations due to the instability of the lamp source used to illuminate the device in test situations. The CP cryostat was set-up with the diffuse external LED to give the same level of light intensity on the whole detector surface. A blackout cloth was used to shield the cryostat window to limit the radiation seen by the detector to only that from the diffuse LED. With this basic set-up it can be difficult to get a genuine flat level of intensity over the whole detector, however it is more important to keep the set-up constant between test exposures since we are concerned with changes in

behaviour over time rather than a measure of QE performance over the detector. Flat field exposures of various integration times were taken with a complementary dark frame. The experimental set-up was then left undisturbed for a number of hours so that a comparable set of images could be taken after an extended period. The data sets were taken 2, 17 and 21 hours apart. For each data set three dark frames, identical in length to the flat field frames, were averaged to give a 'mean dark frame' which was used for dark subtraction. Using standard IRAF tasks, paired images either side of the set time interval were divided to obtain a ratio, then a mean count over the resultant frame was determined.

Every effort was made to ensure that the experimental set-up was left unchanged over the time gaps, however there was some movement of dust particles on the blocking filter at the cryostat window with respect to the detector plane. This was due to small thermal movements of the focal plane with respect to the cryostat window over time. This gave some low level structure in the resultant frames which was confirmed to be due to out of focus dust particles by examining the raw flat and dark images. Fig. 5.12 shows the same area of a detector in a 1 second dark frame (top right), the raw 1 second flat field (top right) and the ratio of two flat fields taken two hours apart (bottom left). The location of the dust particle is circled on all three images.

The dust particle is quite clear in the raw flat field (top left image) but there is extremely little evidence in the dark frame (top right image). The very small structure in the dark frame (made more visible by the level cuts used in IRAF) is likely to be due to a very small amount of IR radiation coming through the cryostat window during a dark exposure. Note there was no 'shutter' on the CP cryostat or cold blank filter, a dark frame was achieved by doing the best job possible of blocking all IR radiation getting onto the cryostat window. In the real cryostat there is a cold Aluminium blank filter which will be placed in the beam during dark exposures.

To reduced the effect of the 'moving' dust particles which is not a real characteristic of the detector, the raw flat frames were shifted to align the dust particle images before dividing the frames.

In addition to stable flat field characteristics the reset anomaly must be stable over similar time scales such that it can be removed from object frames. Dark frames of

various exposure lengths were taken at time intervals of 2, 17, 21 and 40 hours. The testing set-up was left unaltered during the time intervals.

Results

Regardless of the time separation between flat fields there was no structure or gradient over the resultant divided frame. Hence, the flat field characteristics of the Hawaii-II devices were confirmed very stable over times scales of minutes to 20+ hours. The mean signal count over the divided frames for all time periods was $\sim 1 \pm 0.1e^-$ on all measured detectors.

The reset-anomaly, the intensity ramp along the quadrant edge with the readout electronics, can be seen in the top left image of Fig.5.13. The bottom left hand plot on Fig.5.13 shows a cut through of the ramp demonstrating how the pixel counts rise from normal noise levels at the edge of the quadrant. Note, we experienced an intermittent fault with the readout from one channel in quadrant 2 during laboratory testing, hence the lack of signal on channel 3, quadrant 2 in this image. Top right image, Fig.5.13 is the divided frame of two 3 second dark exposures taken 40 hours apart. There is no evidence of structure or gradient, the mean signal count over the divided frame was $\sim 1 \pm 0.05e^-$ (see bottom right hand plot, Fig.5.13) regardless of time separation, up to two days.

Observationally this quality of stability means that a single series of flat and dark frames can be taken at the beginning of the night, with appropriate integration times to cover the planned observations. By doing calibrations before the start of the night overheads are limited during the dark time. The flat field variations are removed from object images by dividing the given image by an appropriate (same integration time, same read mode and same number of co-added frames) normalised flat field exposure.

During WFCAM commissioning it was found that the simple CDS readout resulted in a heightened reset anomaly which did not accurately subtracted out. Inserting 2 rapid dummy reads between the initial reset and the first proper read reduced

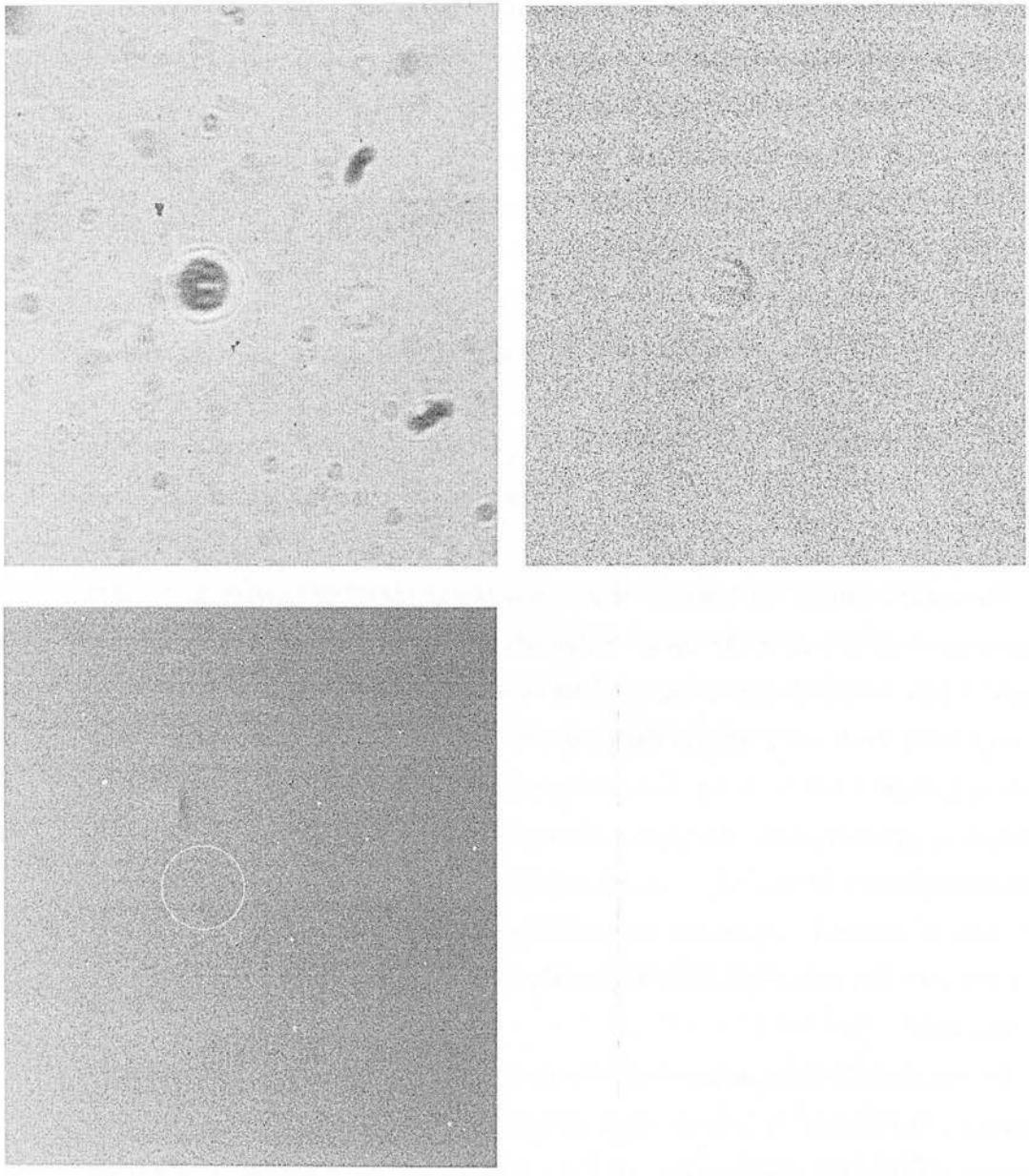

Figure 5.12: Images demonstrating structure on flat field test images due to dust particles. The top left image is a portion of the detector from a raw 1 second flat field, the out of focus 'blobs' are due to dust particles on the blocking filter at the cryostat window. There is a very small amount of structure in the 1 second dark frame (top right figure) due to the largest dust particle, circled in green. This is due to IR radiation leaking through the cryostat window not due to genuine structure in the dark current. The final figure, bottom left, shows the divided frame of two 1 second flat field exposures taken two hours apart. The green circle highlights the location of the large dust particle in the raw flat field, there is no evidence of the dust particles in the divided frame. The lack of structure in the divided frame indicates that there is no variation in the flat field characteristics over the two hour period.

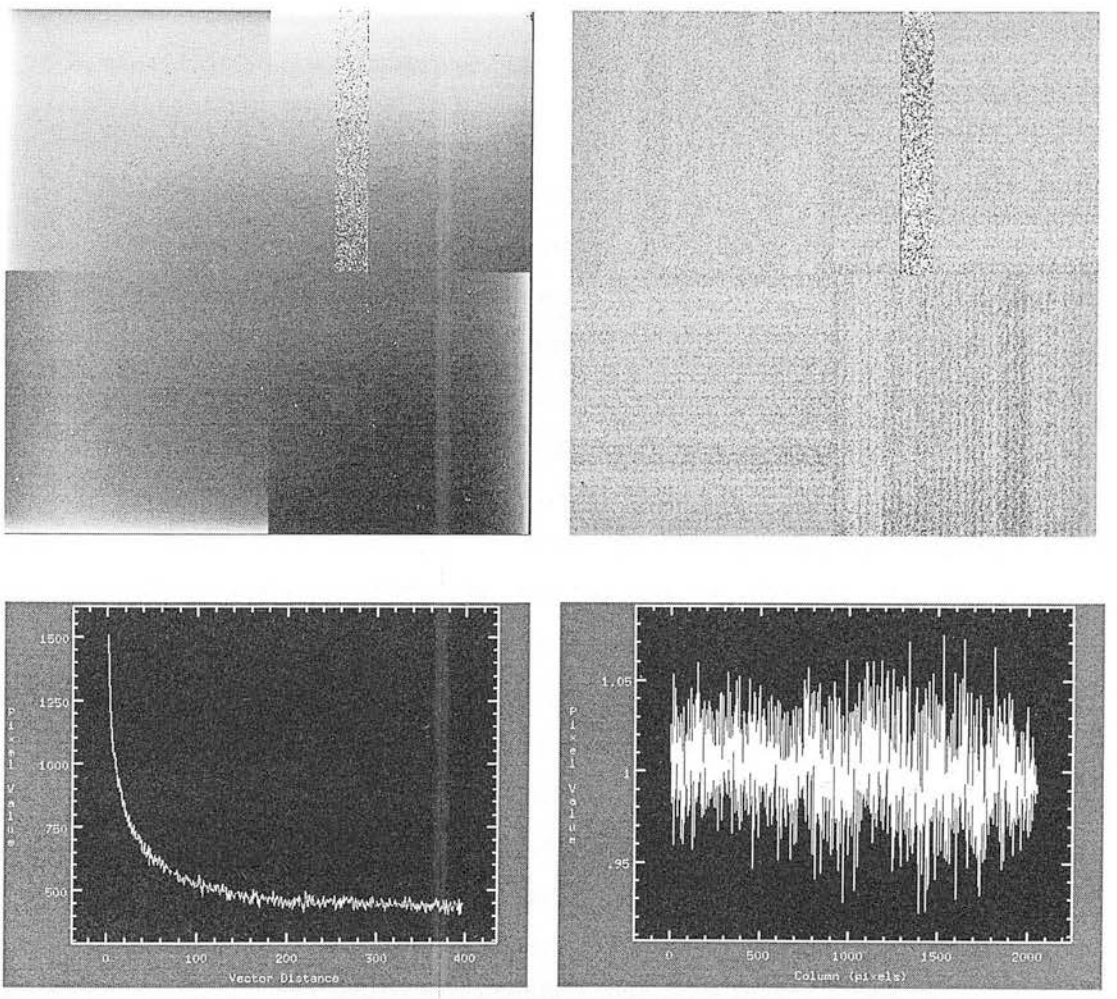

Figure 5.13: Testing the reset anomaly stability. Top left hand image, the intensity ramp of the reset anomaly can be seen on this raw 3 second dark frame. A cross-section of the reset anomaly ramp is given in the bottom left hand plot. Top right hand image is the divided frame of two 3 second dark frames taken 40 hours apart, the testing set up was unchanged during the time interval. No gradient or structure is evident in the divided frame. The mean count over the divided frame can out as $\sim 1 \pm 0.05e-$ (bottom right hand graph). During testing we experienced an intermittent fault in the readout of channel 3, quadrant 2 leading to no signal on this channel. This fault was later tracked down to a broken pin in the controller cable's plug.

the effect by a factor of 10 allowing for good dark subtraction. The inclusion of dummy reads increased the overhead for each CDS exposure from 0.7 seconds to 1.0 second. Any residual effect of the reset anomaly is removed by the CASU pipeline algorithms (Hirst et al. 2006; Irwin 2006).

5.4.3 Linearity

An ideal detector would give a signal which was linear to the amount of light integrated however, infrared detectors are inherently non-linear due to the way they collect electrons. Plotting mean signal versus amount of incident signal produces a linearity curve describing the response of the detector. As this relationship is unvarying over the lifetime of the detector it can be neatly calibrated prior to scientific operation and accounted for in instrument set up. It is important to be aware of the detectors linearity as astronomical observations should not use the detector at levels where it deviates from linearity.

Derek Ives of the UK ATC took and analysed a series of flat images from 150ms - 4000ms to look at the science array's responses. Fig.5.14 shows an example of the response of the WFCAM science detectors, device #60. The left hand plot shows signal (ADU) versus exposure time (ms) with the over plotted dashed line giving the linear fit to the data. Note, the fit is calculated from the first data point (at 300 ADU) not the origin to take into account read noise. The right hand plot shows the deviation from linearity over the signal range, given as a percentage of non-linearity as a function of signal strength. The non-linearity peak-to-valley percentage is $< 3\%$ for all four WFCAM science detectors from 5% to 80% of the full well capacity.

5.4.4 Noise

As discussed in §5.2 'readout noise' is the noise which is visible on the system in the absence of any input signal. For infrared detectors the read noise is typically 10 - 20e^-, no signal which is smaller than the read noise can be detected by the device making the read noise the limiting factor for detector accuracy. The read noise is removed

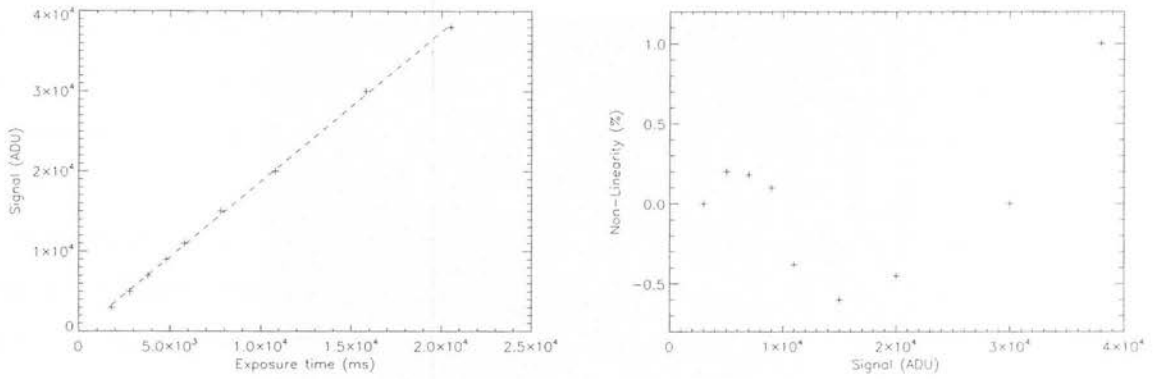

Figure 5.14: Linearity response of device #60. The left hand plot shows signal in ADU versus exposure time in milliseconds with the over drawn dashed line showing the linear relation. The right hand plot shows how the true response of the detector deviates from linear over the commonly utilised signal range. As the signal increase towards saturation the response becomes less and less linear. The non-linearity peak-to-valley percentage is $< 3\%$ for all four WFCAM science detectors from 5% to 80% of the full well capacity.

from the raw images by subtracting a bias image, an exposure with no integration time which contains only the system noise.

Spatial read noise is the inherent noise in the detector measured over a full frame. The read noise for the WFCAM science detectors is $\sim 13e^-$ when using double correlated sampling. To look for structure in the read noise two dark frames of 1 second integration time were divided, removing the effects of dark current and reset anomaly, leaving behind the inherent read noise. Figure 5.15 shows an image the residual read noise in the test cryostat. As can be seen there is structure visible. The banding seen is in line with the detector's amplifiers on each quadrant and is at the 10% level. Optimisation can be carried out to eliminate or minimise banding with the complete instrument on the telescope. However, during commissioning of WFCAM an unstable low frequency banding at the level of $\sim 40e^-$ peak to peak was seen. This is attributed to bias instability in the detectors themselves which would require re-design of the array PCBs to remove (Hirst et al. 2006).

5.4.5 Persistence

'Persistence' is an excess dark current which may be seen on frames taken immediately after the detector has been exposed to a strong incident signal. Subsequent exposures

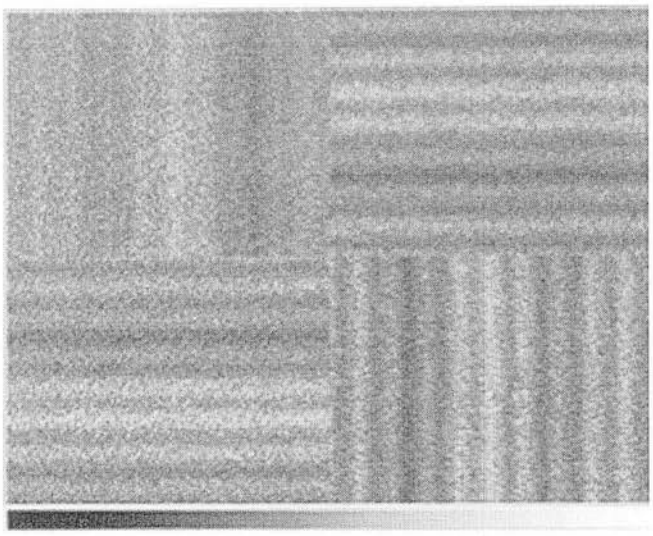

Figure 5.15: Image of the inherent read noise, obtained by dividing two dark frames of 1 second integration time removing the effects of dark current and reset anomaly. The visible banding is a the 10% level and is in line with each quadrant's amplifiers. Though optimisation of the system on the telescope was carried out during commissioning to reduce banding there is a low frequency banding at the level of $\sim 40e^-$ peak-to-peak attributed to bias instability in the devices.

with the lamp switched off exhibit residual excess dark current on the pixels which were heavily illuminated. Any process which releases electrons into the conduction band can contribute to latency, not just genuine astronomical sources, such as cosmic rays. It is important to quantify this effect for reduction purposes and to verify that the effect won't hamper observations of crowded fields. If persistence is not accounted for in post-reduction ghost artefacts could be left on images which may be mistaken for real astronomical objects. Persistence is a significant problem with the Hawaii-II PACE devices due to a lattice mismatch between the HgCdTe active layer and the sapphire substrate inherent in the design of the device.

Test Setup & Analysis

An isolated spot was projected from the precision XY stage onto one channel of one quadrant of a detector. A simple instrument control script took 10 consecutive CDS frames with 5 second integration times and stored them into sequential extension of a multi-extension fits file. The exposure was started with the detector illuminated, and

at a given time through the exposure, roughly after 2–3 frames, the spot was switched off. This process offered a precise method for taking images at accurate time intervals, important for determining the length of time that latency is visible. It was not possible to automate switching the lamp so this had to be done somewhat less accurately by hand.

For analysis purposes each of the multi-extension fits files were separated into 10 individual frames corresponding to each 5 second time step, a dark frame of equal integration time was subtracted from each frame. Following the procedure documented by Daou and Skinner (1997), using standard IRAF commands the mean signal value of an area of the detector centred on the position of the incident spot was measured, a box of 32 pixels. The decay of the excess dark current as time lapsed was recorded for each of the four science arrays. As a cut-off visible latency was deemed to be where the mean signal level of the spot region is higher than the upper noise level of each given detector.

Results

Persistence is an issue on all four science arrays, though some to a greater extent than others. At the time of laboratory testing in the small cryostat detectors #60, #63 & #76 were available for testing.

Caution needs to be taken when interrupting the persistence results presented here. Due to the crude way the light source was switched off there is no way to guarantee that a small amount of radiation did not fall on to the first 'persistence' image if the source was switched off too close to the exposure being readout. Light leakage of this nature would heighten the level of the persistence by adding a small number of photons to the genuine latency.

Detector #76 demonstrated the worst level of persistence, with a latent artefact clearly visible 10 seconds after the incident light source was removed. Fig.5.16 shows a series of exposures taken with device #76 with the incident light projected onto quadrant 1. The first image (top left) is the spot at full strength, top right is the image taken 5 seconds after the lamp has been switched off. The artefact here is $\sim 30\%$ the intensity of the incident spot. Five seconds later the artefact has dropped to 0.2% the spot

intensity (bottom left) but it is still quite clear, even 15 seconds after the light source is switched off the latency can be seen (bottom right) though the level is now just above the read noise. Figs.5.17 & 5.18 show a similar series of images for devices #63 & #60 respectively. In all measurements the first latency ghost was $\sim 30 - 40\%$ the strength of the incident spot.

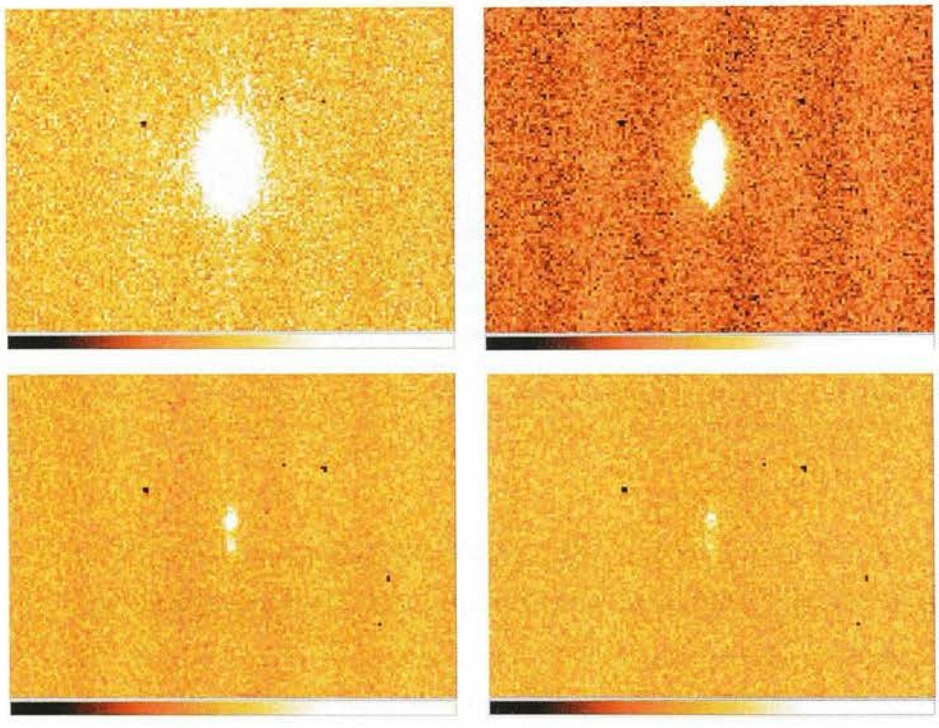

Figure 5.16: Series images showing the decay of a persistent image on device #76. The first (top left) shows the full strength incident signal projected on to quadrant 1 of the array. The top right image is an exposure taken 5 seconds after the radiation source is switched off, the latent artefact has signal strength 30% the intensity of the incident spot. As time passes the level of the ghost drops to 0.2% (bottom left) and eventually into the read noise after 15 seconds (bottom right). Detector #76 was found to be the device worse affected by persistence in the testing cryostat.

Even though the accuracy of the testing in the laboratory was not sufficient to categorically state latency values it, importantly, highlighted persistence as an issue with the

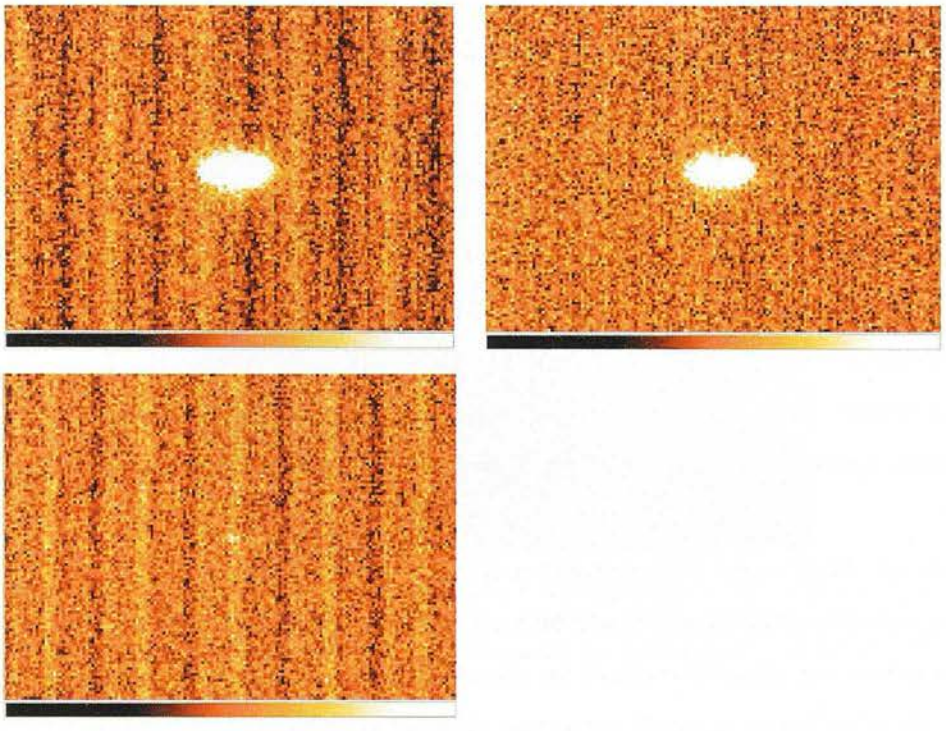

Figure 5.17: As Fig.5.16 for device #63.

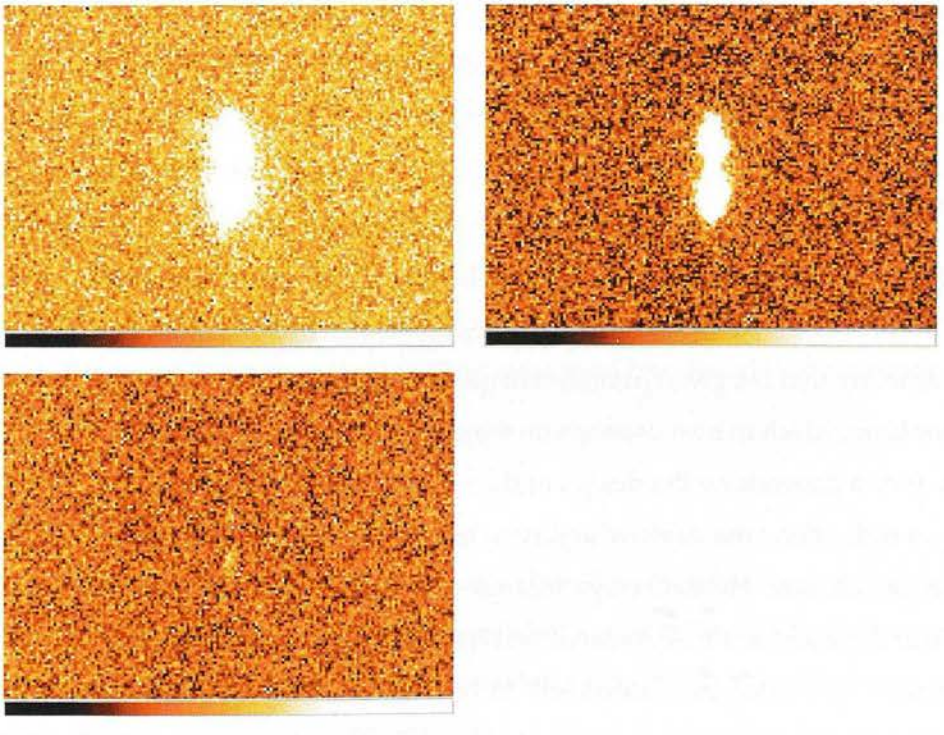

Figure 5.18: As Fig.5.16 for device #60.

WFCAM Hawaii-II devices to be followed up during commissioning. The follow up investigations were completed by JAC and CASU during on-sky commissioning and science verification.

They confirmed the expected persistence and found that bright incident stars left a latent ghost 7−8 magnitudes fainter, visible up to ~ 25 seconds as the incident signal. Any star or astronomical object fainter than 9^{th} magnitude was found not to generate a persistent image. They also found the level of persistence decreased with increasing wavelength such that a latent ghost was stronger in the z′ and Y filters than the K filter for an incident star of the same brightness (Evans 2006). Unfortunately the latency artefacts mimic astronomical sources so are difficult to remove in an automated reduction pipeline.

Fig.5.19 shows an object frame with persistent artefacts from a 9 point-jitter sequence of an open cluster taken immediately beforehand Irwin (2006). CASU concluded that even with a complicated method for identifying and characterising persistence through the pipeline an accurate correction was not possible as it is a non-repeatable, variable effect. For most survey images the effect of the persistence is reduced by stacking the images so it was recommended to rather than attempt to correct for the persistence the entries which might cause persistent ghosts are flagged in the catalogues - a similar procedure adopted by the 2MASS team (Evans 2006).

5.4.6 Quantum Efficiency

The Quantum Efficiency (QE) of a device is the probability that a photon which arrives at the detector surface is captured and recorded. This depends on a number of factors including the probability that the given photon will generate an electron-hole pair in the semiconductor layer, which in turn depends on the materials used and the operating temperature. It also depends on the design of the storage diode junction and the readout circuitry, which effects the devices' ability to transfer the generated electron to the charge storage structure. Hybrid arrays are back-side illuminated meaning the photons must travel through the a base material and the sapphire layer before reaching the sensitive area where they are most likely to be detected. Any reflection or

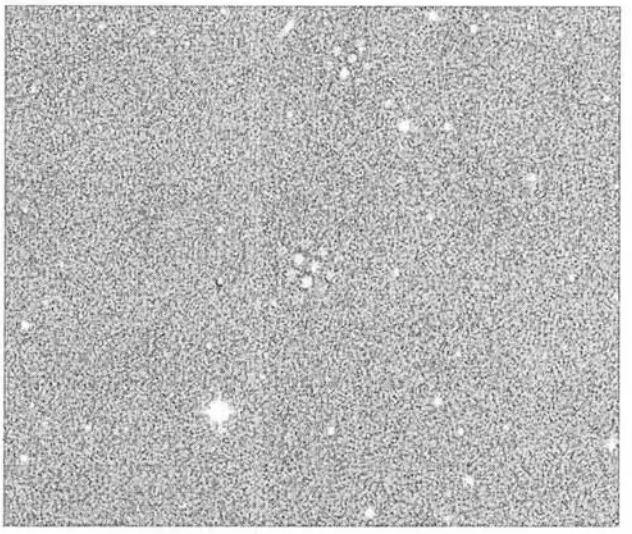

Figure 5.19: An image demonstrating the effect of persistence on a WFCAM science frame. The latent artefacts are from a 9-point jitter sequence on an open cluster taken immediately beforehand. The ghosts mimic genuine astronomical signal making it very difficult to correct for an automated way (Irwin 2006).

transmission losses in the substrate or the detector material also lead to a loss in efficiency. QE is also temperature dependant, at lower temperatures absolute QE tends to reduce. Bezawada et al. (2004) found a reduction of $\sim 5\%$ in QE over J,H, & K for the VISTA HgCdTe detectors when changing operating temperature from 77K – 65K.

An ideal detector would have a QE of 100%, the lower the QE the less astronomical information successfully recorded hence manufacturers always strive for high QE results across the operating wavelength range. The QE measurements were completed by Rockwell Scientific Ltd and the values supplied at the time of detector delivery. Table 5.2 summaries the measured QE over the main broadband filters for each of the four science arrays.

5.4.7 Well Capacity & Gain

The 'full well capacity' (or 'well depth') of a given detector is the maximum number of photons each pixel can store during one read-out cycle of the detector. The 'dynamic range' of the device extends from the lowest signal level that a quantitative measurement can be made to the maximum signal at which the detectors response is linear.

IR Detector	J band	H band	K band
#41	67.8%	76.9%	75.8%
#60	70.9%	89.0%	86.3%
#63	90.6%	87.5%	85.8%
#76	83.4%	89.9%	85.5%

Table 5.2: The quantum efficiency as measured by Rockwell Scientific Ltd for each of the four WFCAM science devices over the broadband filters J, H & K.

The dynamic range of the device is set by the well capacity and the read noise of the system. For mid to long wavelength infrared the well capacity becomes significant. The high background flux means it can become difficult to read out the device quickly enough to prevent pixel saturation.

The system gain is the amount of amplification of the signal voltage from the detectors by the readout electronics. The final output for the system is in 'analogue to digital units' (ADU) and to know the conversion between pixel detection in electrons to ADU you need to know the gain of the whole system, detector and controller, and it must be measured for each system in turn due to differences in the electronic components.

The measurements for the WFCAM detectors' well capacity and gain was executed by Derek Ives of the UK ATC and are offered here for completeness. To obtain the well capacity a series of flat field images with a range of exposure times from 150ms – 4000ms were used to determine the point at which the output became strongly non-linear, with a reset voltage of 0.95V. The full well capacity depends on the rest voltage. (Ichikawa et al. 2004) found the well capacity for a Hawaii-II device destined for MOIRCS on Subaru varies from 10 x $10^5 e^-$ to 1.8 x $10^5 e^-$ for reset voltage range of 0.5 - 1.0V, in agreement with measurements made by D. Ives. The full well capacities and gain values for the WFCAM science devices in electrons and ADU are given in Table 5.3.

5.4.8 Interpixel Capacitance

After WFCAM was commissioned in late 2004 an error in the method of calculation of the conversion gain for infrared detectors was uncovered by G. Finger and colleagues

IR detector	Full Well (e^-)	Full Well (ADU)	Gain (e^-/ADU) *
# 41	156,000	27,900	5.6 ± 0.2
# 60	185,000	40,000	4.6 ± 0.2
# 63	181,000	40,000	4.5 ± 0.2
# 76	186,000	40,000	4.7 ± 0.2

Table 5.3: Measured full well capacity, in electrons and ADU, and system gain for each of the four WFCAM science arrays (Hirst 2006). * not taking into account inter-pixel capacitance, see §5.4.8.

at the European Southern Observatory. This is important as the accuracy of the calculation of conversion gain C_0/e^-, measured in units of electrons per Volt, affects all other detector parameters including read noise, dark current, full well capacity and quantum efficiency. Measurements of the QE of a Hawaii-2RG HgCdTe device by Finger et al. (2005) gave impossible quantum efficiencies exceeding 100%, even after narrowing down the errors of all the factors influencing the efficiency they were unable to obtain a K band QE below 105%. The only remaining major uncertainty was in the calculation of the conversion gain, which appears to be too large. The capacitance, C_0, is usually determined by the 'shot noise method' assuming photon shot noise is the limiting factor on the detector performance. Poisson statistics govern photons so the variance of the collected number of photons is equal to the mean number of photons (Finger et al. 2006). Hence, C_0, can be calculated from the slope of a plot of 'noise squared versus mean' signal according to:

$$C_0 = e^- \frac{\langle V \rangle}{\langle V^2 \rangle} \tag{5.8}$$

However, this equation only holds true if the signals of neighbouring pixels are uncoupled. As C_0 is inversely proportional to the variance of the detector signal, $\langle V^2 \rangle$, the measured variance should be larger to get a reasonable but smaller capacitance. The over estimated capacitance measured with the shot noise method could be explained by coupling capacitance between neighbouring pixels, meaning the signal of the pixel recording the incident photon is spread to the adjacent pixels reducing the apparent photon shot noise. The mean signal remains unchanged but the variations about the mean are 'smoothed' by the capactive coupling to neighbouring pixels (Finger et al.

2006). The photon shot noise method actually gives the sum of C_0 and all the coupling capacitors in series. Finger et al. (2005) detail a 2D autocorrelation method for determining the level of inter-pixel capacitance and thus the correction factor needed to be applied to calculated gain.

Post-commissioning significant inter-pixel capacitance was identified in the WFCAM Hawaii-II devices, the gain as quoted above in §5.4.7 is over estimated by approximately 20%. This also means Rockwell Scientific Ltd over-estimated the QE for the Hawaii-II detectors (Hirst et al. 2006).

At the end of the engineering on-sky commissioning period the full working potential of WFCAM began to be realised through a series of promotional images for press releases. Figs.5.20 & 5.21 show two beautiful images taken of the Orion Nebula. Fig.5.20 is a full WFCAM tile of a region in the Orion constellation taken in the K band. The Trapezium cluster can be seen heating up the surrounding interstellar dust and gas causing it to glow brightly in the infrared. The full tile image covers 1,200 times more area than UKIRT's previous IR camera, UFTI. The second image, Fig.5.21, is a three colour image (H_2, K, J) of the southern half of the Orion nebula.

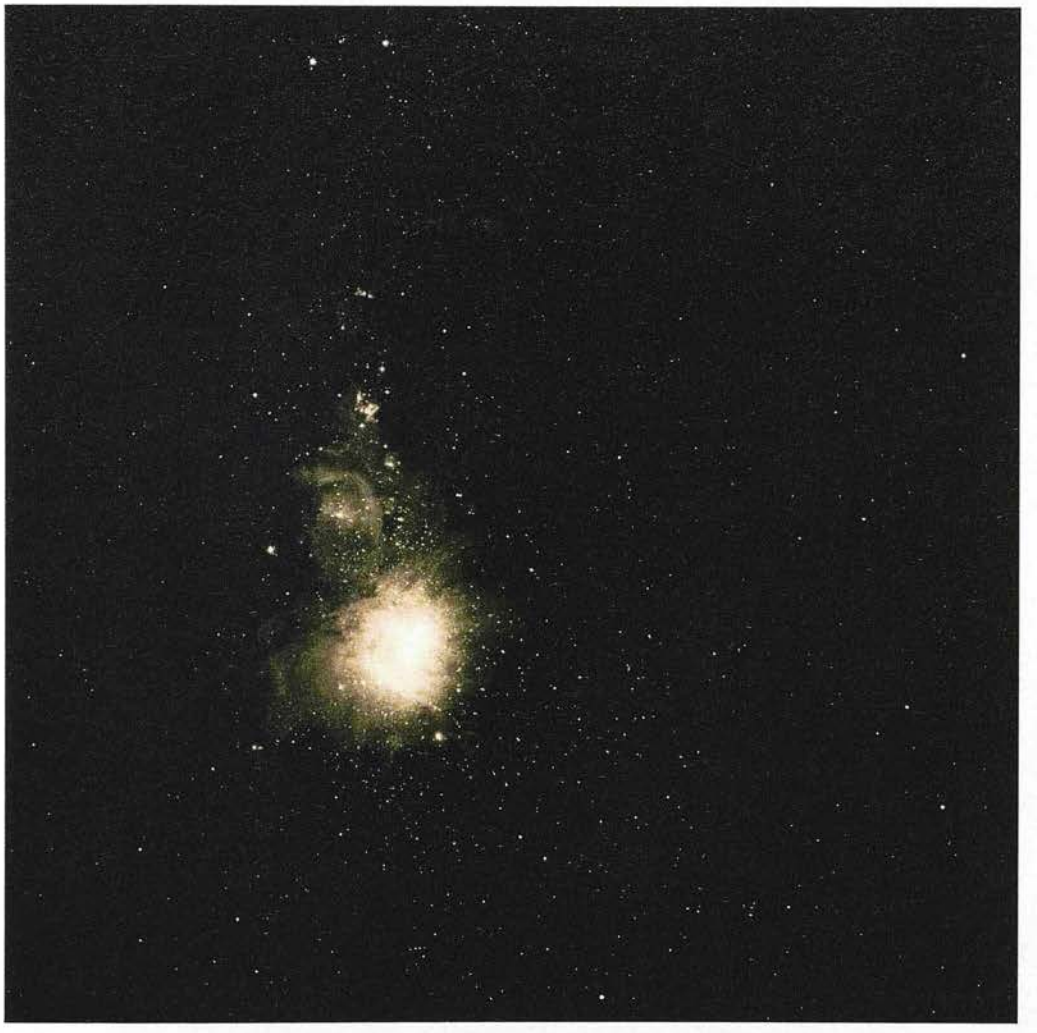

Figure 5.20: A K band image of the section of the Orion nebula surrounding the Trapezium cluster using the full WFCAM 'tile' taken at the end of the initial engineering commissioning.

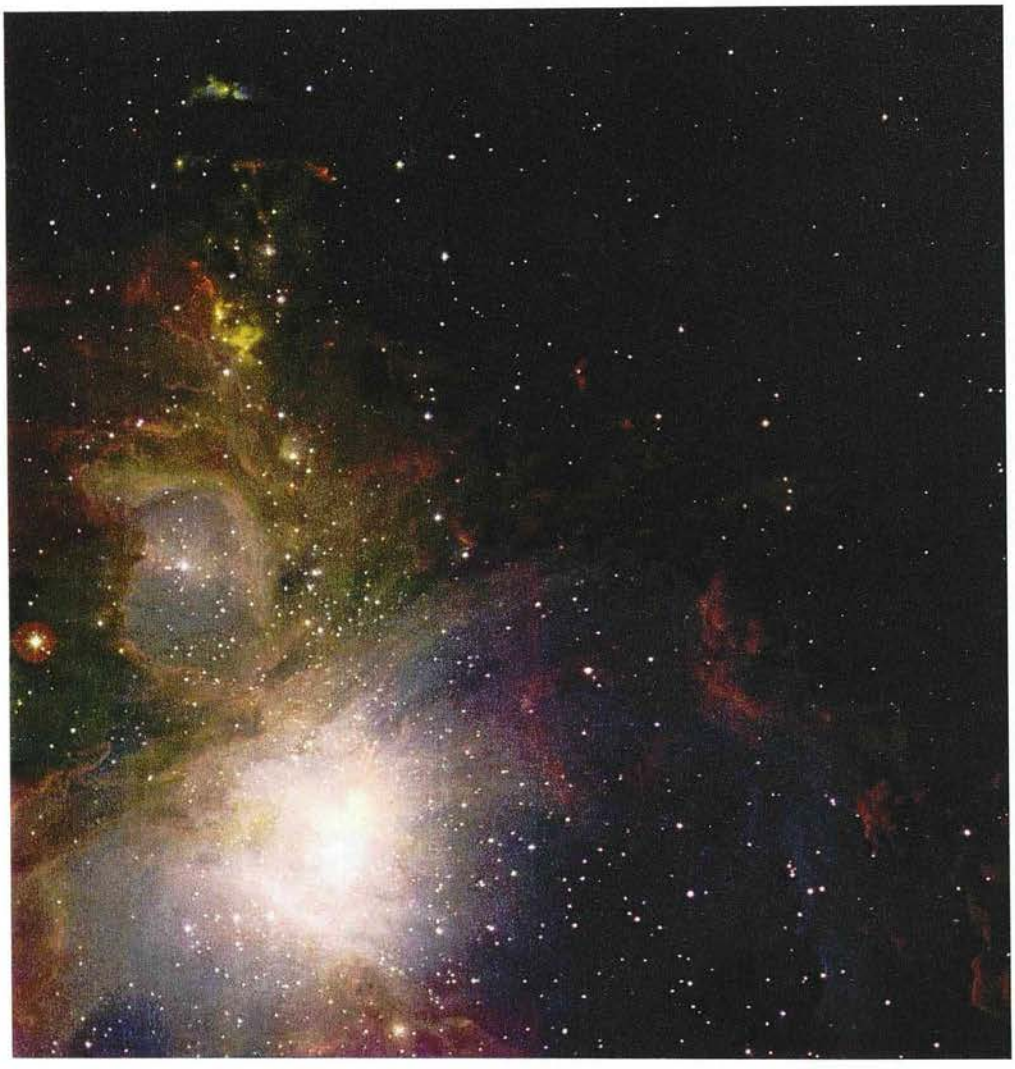

Figure 5.21: A three band colour image of the southern half of the Orion nebula taken with the H_2, K and J filters.

Appendix A

Spectra

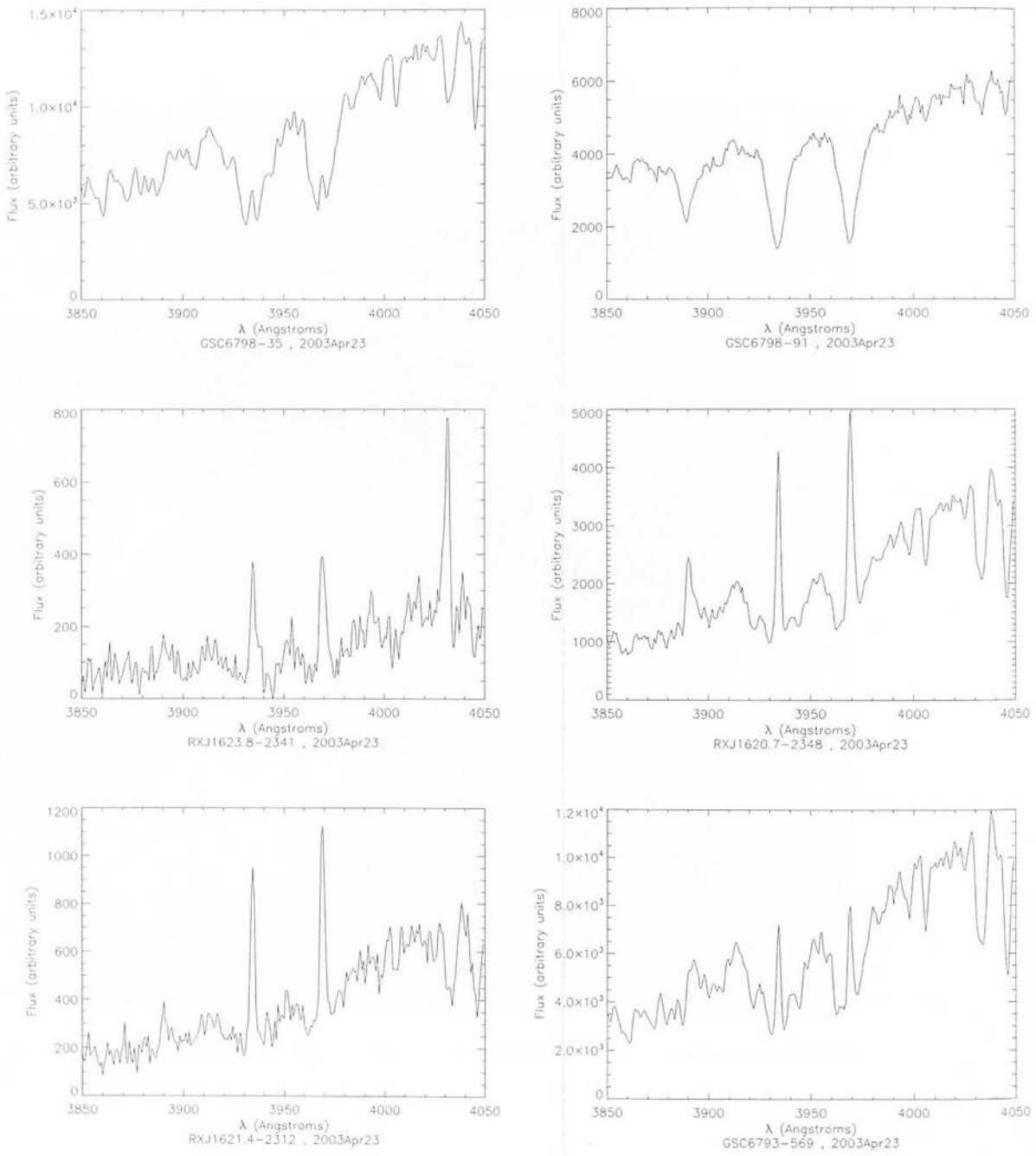
Flux (arbitrary units)
λ (Angstroms)
GSC6798-35 , 2003Apr23
GSC6798-91 , 2003Apr23
RXJ1623.8-2341 , 2003Apr23
RXJ1620.7-2348 , 2003Apr23
RXJ1621.4-2312 , 2003Apr23
GSC6793-569 , 2003Apr23

Figure A.1:

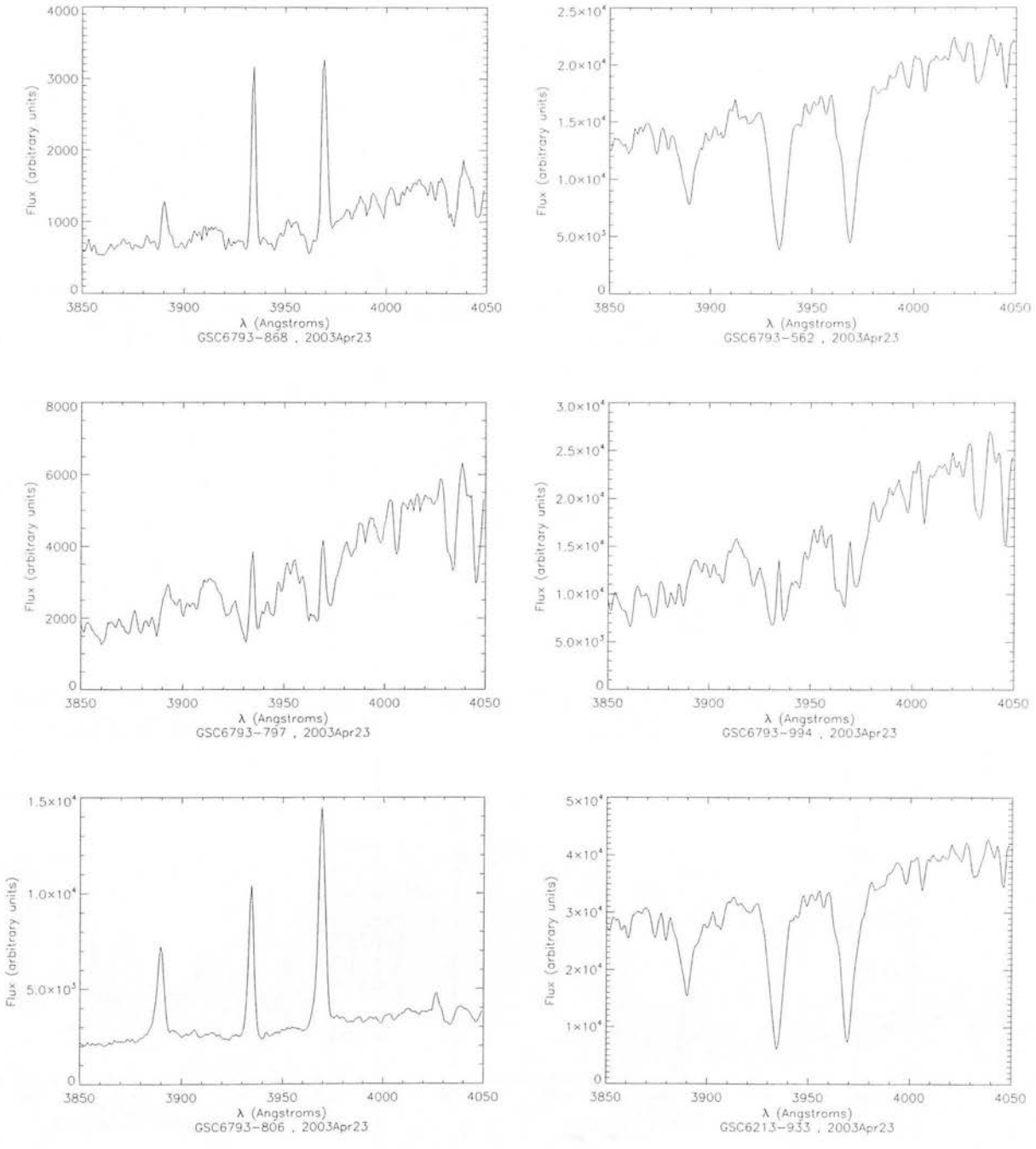
Flux (arbitrary units)
λ (Angstroms)
GSC6793-868 , 2003Apr23
GSC6793-562 , 2003Apr23
GSC6793-797 , 2003Apr23
GSC6793-994 , 2003Apr23
GSC6793-806 , 2003Apr23
GSC6213-933 , 2003Apr23

Figure A.2:

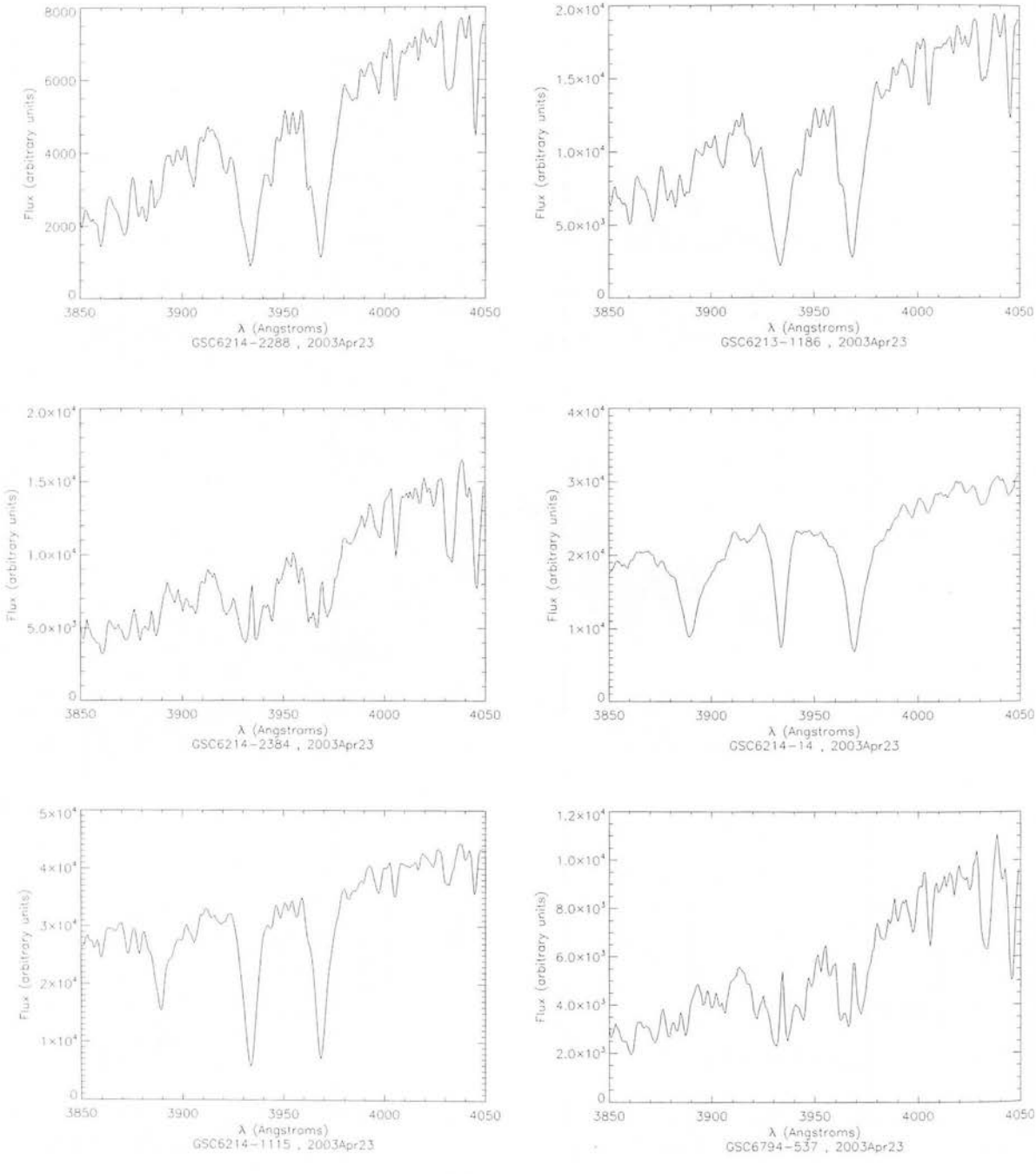
Flux (arbitrary units)
λ (Angstroms)
GSC6214-2288 , 2003Apr23
GSC6213-1186 , 2003Apr23
GSC6214-2384 , 2003Apr23
GSC6214-14 , 2003Apr23
GSC6214-1115 , 2003Apr23
GSC6794-537 , 2003Apr23

Figure A.3:

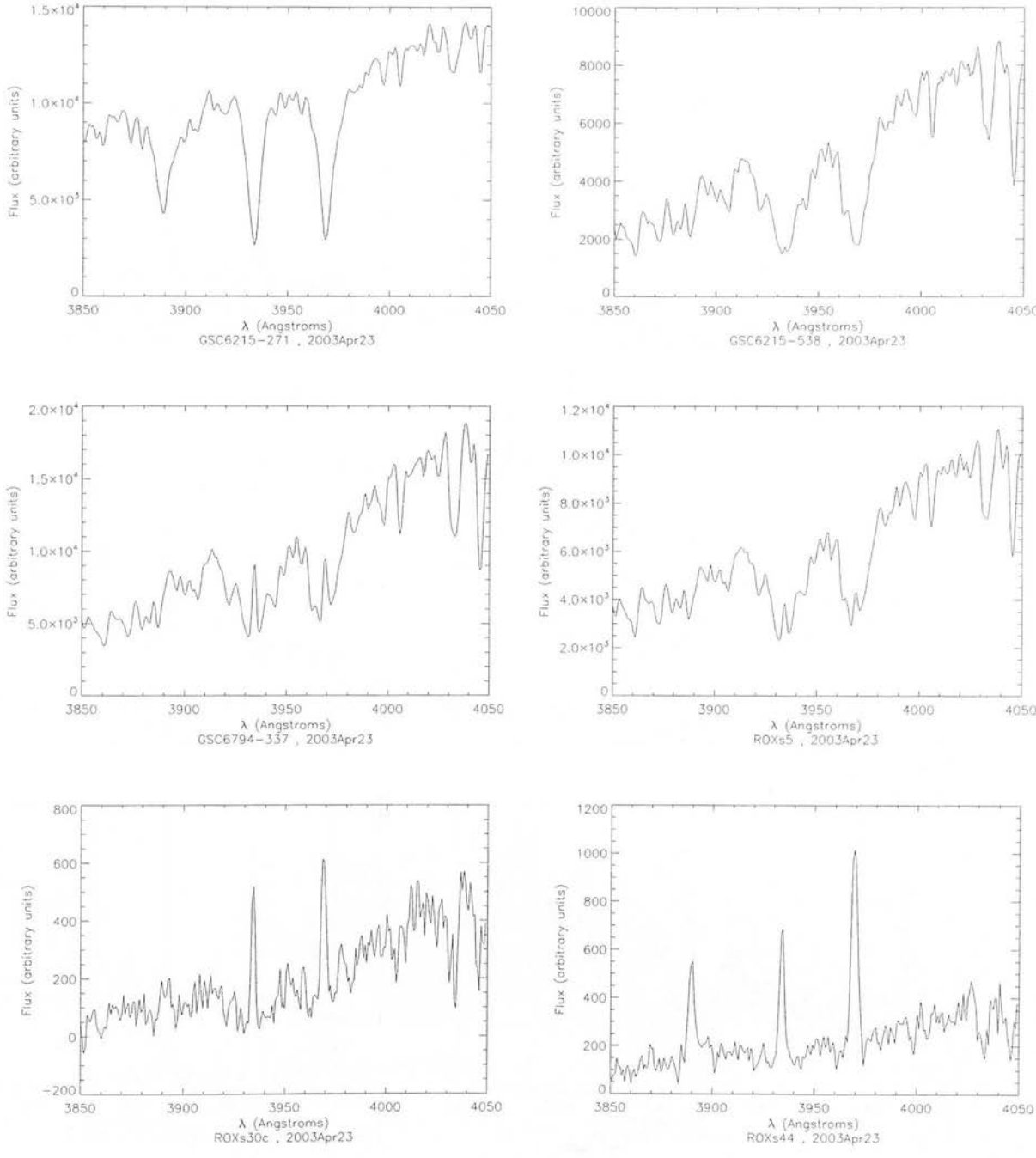
Flux (arbitrary units)
λ (Angstroms)
GSC6215-271 , 2003Apr23
GSC6215-538 , 2003Apr23
GSC6794-337 , 2003Apr23
ROXs5 , 2003Apr23
ROXs30c , 2003Apr23
ROXs44 , 2003Apr23

Figure A.4:

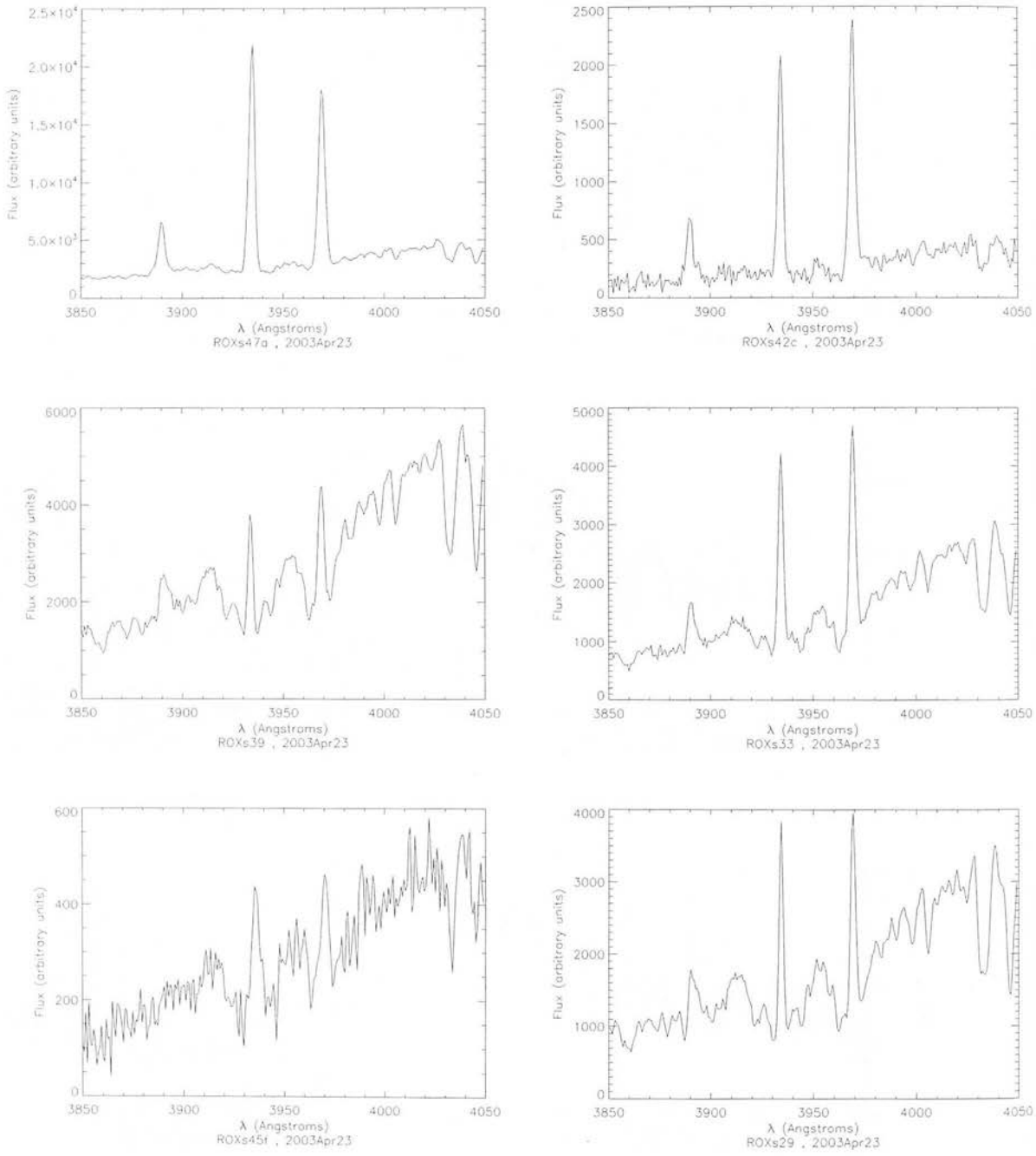
Flux (arbitrary units)
λ (Angstroms)
ROXs47a , 2003Apr23
ROXs42c , 2003Apr23
ROXs39 , 2003Apr23
ROXs33 , 2003Apr23
ROXs45t , 2003Apr23
ROXs29 , 2003Apr23

Figure A.5:

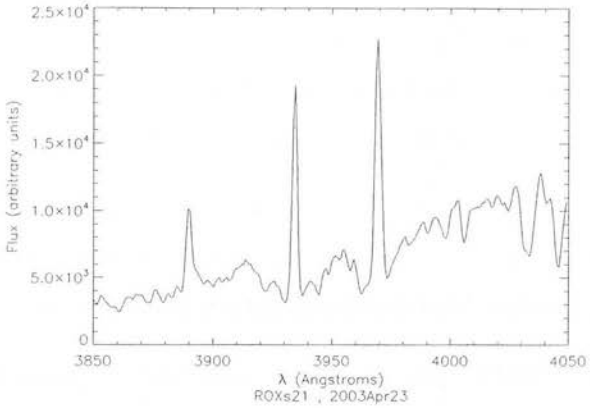
Flux (arbitrary units)
λ (Angstroms)
ROXs21 , 2003Apr23

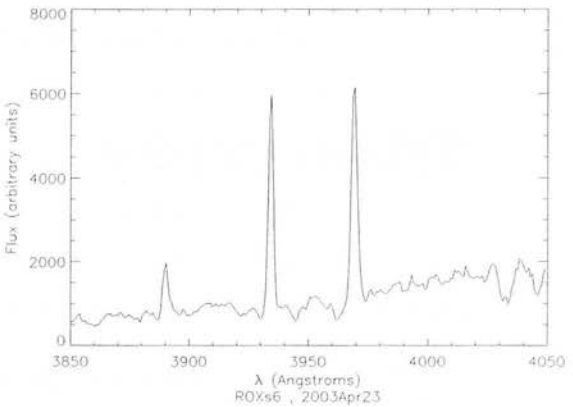
Flux (arbitrary units)
λ (Angstroms)
ROXs6 , 2003Apr23

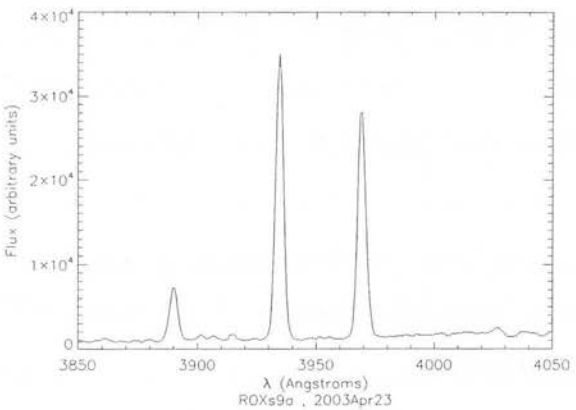
Flux (arbitrary units)
λ (Angstroms)
ROXs9a , 2003Apr23

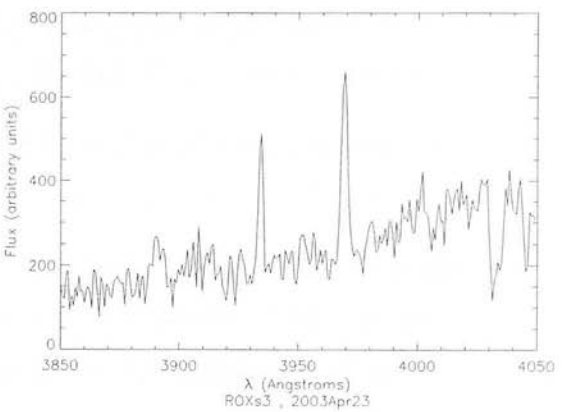
Flux (arbitrary units)
λ (Angstroms)
ROXs3 , 2003Apr23

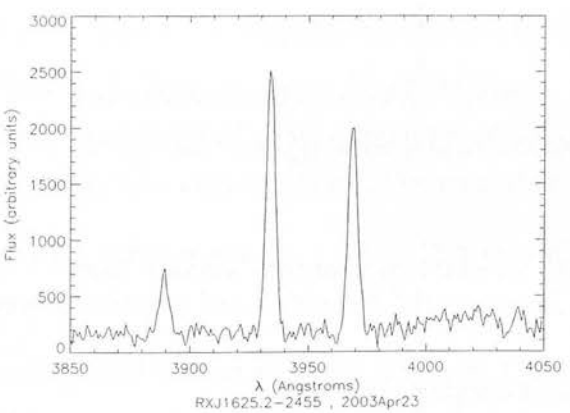
Flux (arbitrary units)
λ (Angstroms)
RXJ1625.2−2455 , 2003Apr23

Figure A.6:

Bibliography

Allen, C. W. (1973), *Astrophysical quantities*, London: University of London, Athlone Press, —c1973, 3rd ed.

Andre, P., Ward-Thompson, D. and Barsony, M. (1993), 'Submillimeter continuum observations of Rho Ophiuchi A - The candidate protostar VLA 1623 and prestellar clumps', *Astrophys. J.* **406**, 122–141.

Appenzeller, I. and Mundt, R. (1989), 'T Tauri stars', *Ann. Rev. Astron. Astrophys.* **1**, 291–334.

Baraffe, I., Chabrier, G., Allard, F. and Hauschildt, P. H. (1998), 'Evolutionary models for solar metallicity low-mass stars: mass-magnitude relationships and color-magnitude diagrams', *Astron. Astrophys.* **337**, 403–412.

Barnes, T. G. and Evans, D. S. (1976), 'Stellar angular diameters and visual surface brightness. I. Late spectral types.', *Mon. Not. R. Astr. Soc.* **174**, 489–502.

Barnes, T. G., Evans, D. S. and Parsons, S. B. (1976), 'Stellar angular diameters and visual surface brightness. II. Early and intermediate spectral types.', *Mon. Not. R. Astr. Soc.* **174**, 503–512.

Basri, G., Martin, E. L. and Bertout, C. (1991), 'The lithium resonance line in T Tauri stars', *Astron. Astrophys.* **252**, 625–638.

Beckett, M. G. (1995), 'High Resolution Infrared Imaging', *Ph.D. Thesis* .

Beckwith, S. V. W., Sargent, A. I., Chini, R. S. and Guesten, R. (1990), 'A survey for circumstellar disks around young stellar objects', *Astron. J.* **99**, 924–945.

Berdyugina, S. (2005), 'Starspots: A Key to the Stellar Dynamo', *Living Reviews in Solar Physics* pp. 5–62.

Berdyugina, S. V. and Solanki, S. K. (2002), 'The molecular Zeeman effect and diagnostics of solar and stellar magnetic fields. I. Theoretical spectral patterns in the Zeeman regime', *Astron. Astrophys.* **385**, 701–715.

Bernard, J. P., Boulanger, F. and Puget, J. L. (1993), 'Modeling of Infrared Emission of Interstellar Clouds - Part Two - Self-Consistent Models of Individual Nearby Clouds', *Astron. Astrophys.* **277**, 609–+.

Bertout, C., Robichon, N. and Arenou, F. (1999), 'Revisiting Hipparcos data for pre-main sequence stars', *Astron. Astrophys.* **352**, 574–586.

Bessell, M. S. and Brett, J. M. (1988), 'JHKLM photometry - Standard systems, passbands, and intrinsic colors', *Publs. Astr. Soc. Pacif.* **100**, 1134–1151.

Bezawada, N., Ives, D. and Woodhouse, G. (2004), Characterization of VISTA IR detectors, *in* J. D. Garnett and J. W. Beletic, eds, 'Optical and Infrared Detectors for Astronomy. Edited by James D. Garnett and James W. Beletic. Proceedings of the SPIE, Volume 5499, pp. 23-34 (2004).', pp. 23–34.

Blaauw, A. (1964), 'The O Associations in the Solar Neighborhood', *Ann. Rev. Astron. Astrophys.* **2**, 213–+.

Böker, T., Bacinski, J., Bergeron, L., Calzetti, D., Jones, M., Gilmore, D., Holfeltz, S., Monroe, B., Nota, A., Sosey, M., Schneider, G., O'Neil, E., Hubbard, P., Ferro, A., Barg, I. and Stobie, E. (2001), 'Properties of PACE-I HgCdTe Detectors in Space: The NICMOS Warm-Up Monitoring Program', *Publs. Astr. Soc. Pacif.* **113**, 859–871.

Bouvier, J. and Appenzeller, I. (1992), 'A magnitude-limited spectroscopic and photometric survey of Rho Ophiuchus X-ray sources', *Astr. Astrophys. Suppl.* **92**, 481–516.

Bouvier, J. and Bertout, C. (1989), 'Spots on T Tauri stars', *Astron. Astrophys.* **211**, 99–114.

Bouvier, J., Bertout, C., Benz, W. and Mayor, M. (1986), 'Rotation in T Tauri stars. I - Observations and immediate analysis', *Astron. Astrophys.* **165**, 110–119.

Bouvier, J., Covino, E., Kovo, O., Martin, E. L., Matthews, J. M., Terranegra, L. and Beck, S. C. (1995), 'COYOTES II: SPOT properties and the origin of photometric period variations in T Tauri stars.', *Astron. Astrophys.* **299**, 89–+.

Brandt, P. N., Schmidt, W. and Steinegger, M. (1990), 'On the umbra-penumbra area ratio of sunspots', *Solar Physics* **129**, 191–194.

Bruls, J. H. M. J., Solanki, S. K. and Schuessler, M. (1998), 'Doppler imaging: the polar SPOT controversy', *Astron. Astrophys.* **336**, 231–241.

Cabelli, C. A., Cooper, D. E., Haas, A. K., Kozlowski, L. J., Bostrup, G. L., Chen, A. C., Blackwell, J. D., Montroy, J. T., Vural, K., Kleinhans, W. E., Hodapp, K.-W. and Hall, D. N. (2000), Latest results on HgCdTe 2048x2048 and silicon focal plane arrays, *in* E. L. Dereniak and R. E. Sampson, eds, 'Proc. SPIE Vol. 4028, p. 331-342, Infrared Detectors and Focal Plane Arrays VI, Eustace L. Dereniak; Robert E. Sampson; Eds.', pp. 331–342.

Cardelli, J. A., Clayton, G. C. and Mathis, J. S. (1989), 'The relationship between infrared, optical, and ultraviolet extinction', *Astrophys. J.* **345**, 245–256.

Carter, B. D., Ashley, M. C. B., Bembrick, C. S., Brooks, P. W., Mitchell, P. and Storey, J. W. V. (1995), Astronomy with the Automated Patrol Telescope, *in* J. Chapman, R. Cannon, S. Harrison and B. Hidayat, eds, 'ASP Conf. Ser. 84: IAU Colloq. 148: The Future Utilisation of Schmidt Telescopes', pp. 44–+.

Casali, M., Adamson, A., Alves de Oliveira, C., Almaini, O., Burch, K., Chuter, T., Eliot, J., Folger, M., Hambly, N., Hastie, M., Henry, D., Hirst, P., Irwin, M., Ives, D., Lawrence, A., Laidlaw, K., Lee, D., Lewis, J., Lunney, D., Maclay, S., Montgomery, D., Pickup, A., Read, M., Rees, N., Robson, I., Sekiguchi, K., Vick, A., Warren, S. and Woodward, B. (2006), 'The UKIRT Wide Field Camera', Astron. Astrophys. In Prep.

Casali, M. M. (2003), Strong Magnetic Fields in T Tauri Stars and Their Observational Consequences, *in* J. M. De Buizer and N. S. van der Bliek, eds, 'ASP Conf. Ser. 287: Galactic Star Formation Across the Stellar Mass Spectrum', pp. 292–297.

Casanova, S., Montmerle, T., Feigelson, E. D. and Andre, P. (1995), 'ROSAT X-ray sources embedded in the rho Ophiuchi cloud core', *Astrophys. J.* **439**, 752–770.

Catalano, S. (1979), 'Photoelectric calibration of the H and K lines and nearby continuum of late type stars', *Astron. Astrophys.* **80**, 317–324.

Chandler, C. J., Richer, J. S. and Visser, A. E. (2001), Star Formation in Lynds Dark Clouds, *in* 'Bulletin of the American Astronomical Society', Vol. 33 of *Bulletin of the American Astronomical Society*, pp. 1306–+.

Chapman, G. A., Cookson, A. M. and Dobias, J. J. (1997), 'Solar Variability and the Relation of Facular to Sunspot Areas during Solar Cycle 22', *Astrophys. J.* **482**, 541–545.

Chelli, A., Cruz-Gonzalez, I., Zinnecker, H., Carrasco, L. and Perrier, C. (1988), 'Infrared companions to T Tauri stars', *Astron. Astrophys.* **207**, 46–54.

Chen, H., Myers, P. C., Ladd, E. F. and Wood, D. O. S. (1995), 'Bolometric temperature and young stars in the Taurus and Ophiuchus complexes', *Astrophys. J.* **445**, 377–392.

Coelho, P., Barbuy, B., Meléndez, J., Schiavon, R. P. and Castilho, B. V. (2005), 'A library of high resolution synthetic stellar spectra from 300 nm to 1.8 μm with solar and α-enhanced composition', *Astron. Astrophys.* **443**, 735–746.

Cohen, M. (1981), 'Are we beginning to understand T Tauri stars', *Sky and Telescope* **62**, 300–303.

Collier-Cameron, A. and Unruh, Y. C. (1994), 'Doppler Images of Ab-Doradus in 1992JAN', *Mon. Not. R. Astr. Soc.* **269**, 814–+.

D'Antona, F., Oliva, E. and Zeppieri, A. (1999), 'The density of methane brown dwarfs: observational and theoretical constraints', *Astron. Astrophys.* **352**, 567–573.

Daou, D. and Skinner, C. (1997), Persistence in NICMOS: Results from On-Orbit data, *in* 'The 1997 HST Calibration Workshop with a new generation of instruments /edited by Stefano Casertano, Robert Jedrzejewski, Charles D. Keyes, and Mark Stevens. Baltimore, MD : Space Telescope Science Institute (1997) QB 500.268 C35 1997, p. 263.'.

de Bruijne, J. H. J., Hoogerwerf, R., Brown, A. G. A., Aguilar, L. A. and de Zeeuw, P. T. (1997), Improved Methods for Identifying Moving Groups, *in* 'ESA SP-402: Hipparcos - Venice '97', pp. 575–578.

de Jager, C. and Nieuwenhuijzen, H. (1987), 'A new determination of the statistical relations between stellar spectral and luminosity classes and stellar effective temperature and luminosity', *Astron. Astrophys.* **177**, 217–227.

Delgado, A. J., Miranda, L. F. and Alfaro, E. J. (1999), 'Spectroscopy of Pre-Main-Sequence Candidates of Spectral Type AF in the Young Galactic Cluster IC 4996', *Astron. J.* **118**, 1759–1765.

Diaz-Cordoves, J., Claret, A. and Gimenez, A. (1995), 'Linear and non-linear limb-darkening coefficients for LTE model atmospheres.', *Astr. Astrophys. Suppl.* **110**, 329–+.

D'Silva, S. and Howard, R. F. (1993), 'Limits on the magnetic field strength at the base of the solar convection zone', *Solar Physics* **148**, 1–9.

Evans, D. (2006), *CASU Report on WFCAM Persistence.*

Feigelson, E. D. and Montmerle, T. (1985), 'An extremely variable radio star in the rho Ophiuchi cloud', *Astrophys. J. Letters* **289**, L19–L23.

Fernandez-Figueroa, M. J., Montes, D., de Castro, E. and Cornide, M. (1994), 'CA II H and K and H alpha emissions in chromospherically active binary systems (RS Canum Venaticorum and BY Draconis)', *Astrophys. J. Suppl.* **90**, 433–465.

Finger, G., Beletic, J. W., Dorn, R., Meyer, M., Mehrgan, L., Moorwood, A. F. M. and Stegmeier, J. (2005), 'Conversion Gain and Interpixel Capacitance of Cmos Hybrid Focal Plane Arrays', *Experimental Astronomy* **19**, 135–147.

Finger, G., Biereichel, P., Mehrgan, H., Meyer, M., Moorwood, A. F., Nicolini, G. and Stegmeier, J. (1998), Infrared detector development programs for the VLT instruments at the European Southern Observatory, *in* 'Proc. SPIE Vol. 3354, p. 87-98, Infrared Astronomical Instrumentation, Albert M. Fowler; Ed.', pp. 87–98.

Finger, G., Dorn, R. J., Meyer, M., Mehrgan, L., Stegmeier, J. and Moorwood, A. F. M. (2004), Performance of large-format 2Kx2K MBE grown HgCdTe Hawaii-2RG arrays for low-flux applications, *in* J. D. Garnett and J. W. Beletic, eds, 'Optical and Infrared Detectors for Astronomy. Edited by James D. Garnett and James W. Beletic. Proceedings of the SPIE, Volume 5499, pp. 47-58 (2004).', pp. 47–58.

Finger, G., Dorn, R., Meyer, M., Mehrgan, L., Moorwood, A. F. M. and Stegmeier, J. (2006), Interpixel capacitance in large format CMOS hybrid arrays, *in* 'High Energy, Optical, and Infrared Detectors for Astronomy II. Edited by Dorn, David A.; Holland, Andrew D.. Proceedings of the SPIE, Volume 6276, pp. 62760F (2006).'.

Finger, G., Mehrgan, H., Meyer, M., Moorwood, A. F., Nicolini, G. and Stegmeier, J. (2000), Performance of large-format HgCdTe and InSb arrays for low-background applications, *in* M. Iye and A. F. Moorwood, eds, 'Proc. SPIE Vol. 4008, p. 1280-1297, Optical and IR Telescope Instrumentation and Detectors, Masanori Iye; Alan F. Moorwood; Eds.', pp. 1280–1297.

Fowler, A. M. and Gatley, I. (1990), 'Demonstration of an algorithm for read-noise reduction in infrared arrays', *Astrophys. J. Letters* **353**, L33+.

Frasca, A., Biazzo, K., Catalano, S., Marilli, E., Messina, S. and Rodonò, M. (2005), 'Measuring starspot temperature from line-depth ratios. II. Simultaneous modeling of light and temperature curves', *Astron. Astrophys.* **432**, 647–655.

Fukui, Y., Iwata, T., Mizuno, A., Bally, J. and Lane, A. P. (1993), Molecular outflows, *in* E. H. Levy and J. I. Lunine, eds, 'Protostars and Planets III', pp. 603–639.

Garnett, J. D. and Forrest, W. J. (1993), Multiply sampled read-limited and background-limited noise performance, *in* A. M. Fowler, ed., 'Proc. SPIE Vol. 1946, p. 395-404, Infrared Detectors and Instrumentation, Albert M. Fowler; Ed.', pp. 395–404.

Glass, I. (1999), *Handbook of Infrared Astronomy*, Cambridge University Press ©1999.

Górski, K. M., Hivon, E., Banday, A. J., Wandelt, B. D. and Hansen, F. K. (2005*a*), *HEALPix IDL Facilities Overview, Version* 2.

Górski, K. M., Hivon, E., Banday, A. J., Wandelt, B. D. and Hansen, F. K. (2005*b*), *The HEALPix Primer, Version 2.*

Górski, K. M., Hivon, E., Banday, A. J., Wandelt, B. D., Hansen, F. K., Reinecke, M. and Bartelmann, M. (2005), 'HEALPix: A Framework for High-Resolution Discretization and Fast Analysis of Data Distributed on the Sphere', *Astrophys. J.* **622**, 759–771.

Granzer, T., Schüssler, M., Caligari, P. and Strassmeier, K. G. (2000), 'Distribution of starspots on cool stars. II. Pre-main-sequence and ZAMS stars between 0.4 $M_{\odot}$ and 1.7$M_{\odot}$', *Astron. Astrophys.* **355**, 1087–1097.

Gras-Velázquez, À. and Ray, T. P. (2005), 'Weak-line T Tauri stars: circumstellar disks and companions. I. Spectral energy distributions and infrared excesses', *Astron. Astrophys.* **443**, 541–556.

Grevesse, N. and Sauval, A. J. (1998), 'Standard Solar Composition', *Space Science Reviews* **85**, 161–174.

Grossmann-Doerth, U. and Schmidt, W. (1981), 'The brightness distribution in sunspot penumbrae', *Astron. Astrophys.* **95**, 366–372.

Hall, D. S. (1991), Learning about stellar dynamos from long-term photometry of starspots, *in* I. Tuominen, D. Moss and G. Rüdiger, eds, 'LNP Vol. 380: IAU Colloq. 130: The Sun and Cool Stars. Activity, Magnetism, Dynamos', pp. 353–+.

Hartigan, P., Edwards, S. and Ghandour, L. (1995), Accretion and Outflow from Young Stars, *in* M. Pena and S. Kurtz, eds, 'Revista Mexicana de Astronomia y Astrofisica Conference Series', pp. 93–+.

Hartmann, L. and Stauffer, J. R. (1989), 'Additional measurements of pre-main-sequence stellar rotation', *Astron. J.* **97**, 873–880.

Hass, A. (2002), *Users Guide for the Hawaii - 2048x2049 Pixel Focal Plane Array.*

Hatzes, A. P. (1995), 'Doppler Imaging of the Cool SPOT Distribution on the Weak T Tauri Star V410 Tauri', *Astrophys. J.* **451**, 784–+.

Henry, D. and Lee, D. (2002), *WFCAM Optical System Design Description.*

Herbig, G. H. (1962), 'The properties and problems of T Tauri stars and related objects.', *Advances in Astronomy and Astrophysics* **1**, 47–103.

Herbig, G. H. (1987), 'The T Tauri stars.', *Journal of the American Association of Variable Star Observers (JAAVSO)* **16**, 1–3.

Herbst, W. (1989), 'Spots on the weak T Tauri star V410 Tau - The sun at one million years', *Astron. J.* **98**, 2268–2274.

Herbst, W., Herbst, D. K., Grossman, E. J. and Weinstein, D. (1994), 'Catalogue of UBVRI photometry of T Tauri stars and analysis of the causes of their variability', *Astron. J.* **108**, 1906–1923.

Hidas, M. G. (2005), 'A Search for Transiting Extrasolar Planets with the Automated Patrol Telescope', *Ph.D. Thesis* .

Hidas, M. G., Ashley, M. C. B., Webb, J. K., Irwin, M., Phillips, A., Toyozumi, H., Derekas, A., Christiansen, J. L., Nutto, C. and Crothers, S. (2005), 'The University of New South Wales Extrasolar Planet Search: methods and first results from a field centred on NGC 6633', *Mon. Not. R. Astr. Soc.* **360**, 703–717.

Hillenbrand, L. A. (1997), 'On the Stellar Population and Star-Forming History of the Orion Nebula Cluster', *Astron. J.* **113**, 1733–1768.

Hirst, P. (2006), *WFCAM Users Guide.*

Hirst, P., Casali, M., Adamson, A., Ives, D. and Kerr, T. (2006), The UKIRT wide-field camera (WFCAM): commissioning and performance on the telescope, *in* 'Ground-based and Airborne Instrumentation for Astronomy. Edited by McLean, Ian S.; Iye, Masanori. Proceedings of the SPIE, Volume 6269, pp. (2006).'.

Horrobin, M. J. and Casali, M. M. (1998), Detection of low temperature regions on T Tauri stars, *in* J. Yun and L. Liseau, eds, 'ASP Conf. Ser. 132: Star Formation with the Infrared Space Observatory', pp. 366–+.

Ichikawa, T., Katsumo, Y., Suzuki, R., Tokoku, C. and Nishimura, T. (2004), Performance of HAWAII-2 FPA for SUBARU Multi-Object Near-Infrared Camera and

Spectrograph, *in* P. Amico, J. W. Beletic and J. E. Belectic, eds, 'Scientific Detectors for Astronomy, The Beginning of a New Era', pp. 529–533.

Irwin, M. (2006), *CASU Analysis of SV Data for WFCAM*.

Irwin, M. and Lewis, J. (2001), 'INT WFS pipeline processing', *New Astronomy Review* **45**, 105–110.

James, D. J., Melo, C., Santos, N. C. and Bouvier, J. (2006), 'Fundamental properties of pre-main sequence stars in young, southern star forming regions: metallicities', *Astron. Astrophys.* **446**, 971–983.

Johns, C. M. and Basri, G. (1995), 'Hamilton Echelle Spectra of Young Stars. II. Time Series Analysis of H(alpha) Variations', *Astron. J.* **109**, 2800–+.

Johns-Krull, C. M. and Hatzes, A. P. (1997), 'The Classical T Tauri Star SZ 68: Doppler Imaging and Evidence for Magnetospheric Accretion', *Astrophys. J.* **487**, 896–+.

Johnson, H. L. (1966), 'Astronomical Measurements in the Infrared', *Ann. Rev. Astron. Astrophys.* **4**, 193–+.

Joncour, I., Bertout, C. and Bouvier, J. (1994), 'Doppler imaging of the T Tauri star HDE 283572', *Astron. Astrophys.* **291**, L19–L22.

Joncour, I., Bertout, C. and Menard, F. (1994), 'Doppler imaging of the T Tauri star V410 Tau', *Astron. Astrophys.* **285**, L25.

Joy, A. H. (1945), 'T Tauri Variable Stars.', *Astrophys. J.* **102**, 168–+.

Knude, J. and Hog, E. (1998), 'Interstellar reddening from the HIPPARCOS and TYCHO catalogues. I. Distances to nearby molecular clouds and star forming regions', *Astron. Astrophys.* **338**, 897–904.

Kuerster, M., Schmitt, J. H. M. M. and Cutispoto, G. (1994), 'Doppler imaging with a CLEAN – like approach. 2: A photospheric image of AB Doradus (=HD 36705)', *Astron. Astrophys.* **289**, 899–921.

Kulesa, C. A., Hungerford, A. L., Walker, C. K., Zhang, X. and Lane, A. P. (2005), 'Large-Scale CO and [C I] Emission in the ρ Ophiuchi Molecular Cloud', *Astrophys. J.* **625**, 194–209.

Kürster, M., Hatzes, A. P., Pallavicini, R. and Randich, S. (1992), A Comparison of Star SPOT Distributions for Various Active Stars Based on Doppler Images, *in* M. S. Giampapa and J. A. Bookbinder, eds, 'ASP Conf. Ser. 26: Cool Stars, Stellar Systems, and the Sun', p. 249.

Lada, C. J. and Wilking, B. A. (1984), 'The nature of the embedded population in the Rho Ophiuchi dark cloud - Mid-infrared observations', *Astrophys. J.* **287**, 610–621.

Lang, K. R. (2006), *Sun, Earth and Sky*, ISBN 978-0-387-30456-4. Berlin: Springer, 2006.

Lawerence, A., Warren, S. J., Almaini, O., Edge, A. C., Hambly, N. C., Jameson, R. F., Lucas, P., Casali, M., Adamsom, A., Dye, S., Emerson, J. P., Foucaud, S., Hewett, P., Hirst, P., Hodgkin, S. T., Irwin, M. J., Lodie, N., McMahon, R. G., Simpson, C., Smail, I., Mortlock, D. and Folger, M. (2006), 'The UKIRT Infrared Deep Sky Survey (UKIDSS)', *ArXiv Astrophysics e-prints* .

Liang, M., Seppala, L., Sweeney, D. and LSST Project Team (2005), The LSST Optical System, *in* 'Bulletin of the American Astronomical Society', p. 1205.

Linsky, J. L., McClintock, W., Robertson, R. M. and Worden, S. P. (1979), 'Stellar model chromospheres. X - High-resolution, absolute flux profiles of the CA II H and K lines in stars of spectral types F0-M2', *Astrophys. J. Suppl.* **41**, 47–74.

Liseau, R., White, G. J., Larsson, B., Sidher, S., Olofsson, G., Kaas, A., Nordh, L., Caux, E., Lorenzetti, D., Molinari, S., Nisini, B. and Sibille, F. (1999), 'Looking at the bright side of the rho Ophiuchi dark cloud. Far infrared spectrophotometric observations of the rho Oph cloud with the ISO', *Astron. Astrophys.* **344**, 342–354.

Lisse, C., Suchkov, A. A. and Schultz, A. (2001), Tracing Recent Star Formation in and around the molecular ρ Oph with F stars from the 2MASS and uvby Surveys, *in* 'Bulletin of the American Astronomical Society', pp. 1308–+.

Love, P. J., Ando, K. J., Bornfreund, R. E., Corrales, E., Mills, R. E., Cripe, J. R., Lum, N. A., Rosbeck, J. P. and Smith, M. S. (2002), Large-format infrared arrays for future space and ground-based astronomy applications, *in* M. Strojnik and B. F. Andresen, eds, 'Proc. SPIE Vol. 4486, p. 373-384, Infrared Spaceborne Remote Sensing IX, Marija Strojnik; Bjorn F. Andresen; Eds.', pp. 373–384.

Mackay, C. D. (1999), *The Reset Anomaly in HAWAII-1, 1024 x 1024 Arrays*.

Mackay, C. D., Beckett, M. G., McMahon, R. G., Parry, I. R., Piche, F., Ennico, K. A., Kenworthy, M. A., Ellis, R. S. and Aragon-Salamanca, A. (1998), Infrared imaging and spectroscopy with HAWAII and PICNIC arrays, *in* A. M. Fowler, ed., 'Proc. SPIE Vol. 3354, p. 14-23, Infrared Astronomical Instrumentation, Albert M. Fowler; Ed.', pp. 14–23.

Magazzu, A., Rebolo, R. and Pavlenko, I. V. (1992), 'Lithium abundances in classical and weak T Tauri stars', *Astrophys. J.* **392**, 159–171.

Martin, E. L. (1997), 'Quantitative spectroscopic criteria for the classification of pre-main sequence low-mass stars.', *Astron. Astrophys.* **321**, 492–496.

Martin, E. L. and Kun, M. (1996), 'Spectroscopy of possible Hα emission stars in regions of high galactic latitude molecular clouds.', *Astr. Astrophys. Suppl.* **116**, 467–471.

Martin, E. L., Montmerle, T., Gregorio-Hetem, J. and Casanova, S. (1998), 'Spectroscopic classification of X-ray selected stars in the rho Ophiuchi star-forming region and vicinity', *Mon. Not. R. Astr. Soc.* **300**, 733–746.

Mathieu, R. D., Walter, F. M. and Myers, P. C. (1989), 'The discovery of six pre-main-sequence spectroscopic binaries', *Astron. J.* **98**, 987–1001.

McCabe, C., Ghez, A. M., Prato, L., Duchêne, G., Fisher, R. S. and Telesco, C. (2006), 'Investigation Disk Evolution: A High Spatial Resolution Mid-Infrared Survey of T Tauri Stars', *Astrophys. J.* **636**, 932–951.

McLean, I. S., ed. (1997), *Electronic imaging in astronomy. Detectors and instrumentation*.

Meyer, M. R., Calvet, N. and Hillenbrand, L. A. (1997), 'Intrinsic Near-Infrred Excesses of T Tauri Stars: Understanding the Classical T Tauri Star Locus', *Astron. J.* **114**, 288–300.

Montes, D., de Castro, E., Fernandez-Figueroa, M. J. and Cornide, M. (1995), 'Application of the spectral subtraction technique to the CA II H & K and Hϵ lines in a sample of chromospherically active binaries.', *Astr. Astrophys. Suppl.* **114**, 287.

Montes, D., Fernandez-Figueroa, M. J., de Castro, E. and Cornide, M. (1995), 'Excess Hα emission in chromospherically active binaries.', *Astron. Astrophys.* **294**, 165–176.

Montmerle, T. (1996), X-rays from young stellar objects: from T Tauri stars to protostars, *in* R. Pallavicini and A. K. Dupree, eds, 'ASP Conf. Ser. 109: Cool Stars, Stellar Systems, and the Sun', pp. 405–+.

Montmerle, T., Koch-Miramond, L., Falgarone, E. and Grindlay, J. E. (1983), 'Einstein observations of the Rho Ophiuchi dark cloud - an X-ray Christmas tree', *Astrophys. J.* **269**, 182–201.

Morel, T., Micela, G., Favata, F. and Katz, D. (2004), 'The photospheric abundances of active binaries. III. Abundance peculiarities at high activity levels', *Astron. Astrophys.* **426**, 1007–1020.

Neuhaeuser, R., Wolk, S. J., Torres, G., Preibisch, T., Stout-Batalha, N. M., Hatzes, A. P., Frink, S., Wichmann, R., Covino, E., Alcala, J. M., Brandner, W., Walter, F. M., Sterzik, M. F. and Koehler, R. (1998), 'Optical and X-ray monitoring, Doppler imaging, and space motion of the young star Par 1724 in Orion', *Astron. Astrophys.* **334**, 873–894.

O'Neal, D., Neff, J. E., Saar, S. H. and Cuntz, M. (2004), 'Further Results of TiO-Band Observations of Starspots', *Astron. J.* **128**, 1802–1811.

Padgett, D. L., Cieza, L., Stapelfeldt, K. R., Evans, II, N. J., Koerner, D., Sargent, A., Fukagawa, M., van Dishoeck, E. F., Augereau, J.-C., Allen, L., Blake, G., Brooke, T., Chapman, N., Harvey, P., Porras, A., Lai, S.-P., Mundy, L., Myers, P. C., Spiesman, W. and Wahhaj, Z. (2006), 'The SPITZER c2d Survey of Weak-Line T Tauri Stars. I. Initial Results', *Astrophys. J.* **645**, 1283–1296.

Parker, Q. A. and Watson, F. (2000), 6dF: A new spectroscopic survey facility for the U.K. Schmidt Telescope, *in* 'IAU Commission on Instruments', pp. 5–+.

Pasquini, L., Pallavicini, R. and Pakull, M. (1988), 'CA II absolute line profiles of southern late-type stars', *Astron. Astrophys.* **191**, 253–266.

Petrov, P. P. (2003), 'T Tauri Stars', *Astrophysics* **46**, 506–529.

Preibisch, T., Guenther, E., Zinnecker, H., Sterzik, M., Frink, S. and Roeser, S. (1998), 'A lithium-survey for pre-main sequence stars in the Upper Scorpius OB association', *Astron. Astrophys.* **333**, 619–628.

Ramseyer, T. F., Hatzes, A. P. and Jablonski, F. (1995), 'Doppler Imaging of V471 Tau', *Astron. J.* **110**, 1364–+.

Rice, J. B. (2002), 'Doppler imaging of stellar surfaces - techniques and issues', *Astronomische Nachrichten* **323**, 220–235.

Rice, J. B. and Strassmeier, K. G. (1996), 'Doppler imaging of stellar surface structure. II. The weak-lined T Tauri star V410 Tauri.', *Astron. Astrophys.* **316**, 164–172.

Romano, G. (1975), 'Observations of T Tauri stars and related objects in Taurus dark cloud', *Memorie della Societa Astronomica Italiana* **46**, 81–95.

Santos, N. C., Israelian, G. and Mayor, M. (2004), 'Spectroscopic [Fe/H] for 98 extra-solar planet-host stars. Exploring the probability of planet formation', *Astron. Astrophys.* **415**, 1153–1166.

Sartori, M. J., Lépine, J. R. D. and Dias, W. S. (2003), 'Formation scenarios for the young stellar associations between galactic longitudes l = 280degr - 360degr', *Astron. Astrophys.* **404**, 913–926.

Schrijver, C. J., Cote, J., Zwaan, C. and Saar, S. H. (1989), 'Relations between the photospheric magnetic field and the emission from the outer atmospheres of cool stars. I - The solar CA II K line core emission', *Astrophys. J.* **337**, 964–976.

Schrijver, C. J. and Zwaan, C. (2000), *Solar and Stellar Magnetic Activity*, Solar and stellar magnetic activity / Carolus J. Schrijver, Cornelius Zwaan. New York : Cambridge University Press, 2000. (Cambridge astrophysics series ; 34).

Schuessler, M., Caligari, P., Ferriz-Mas, A., Solanki, S. K. and Stix, M. (1996), 'Distribution of starspots on cool stars. I. Young and main sequence stars of $1M_{\odot}$.', *Astron. Astrophys.* **314**, 503–512.

Schuessler, M. and Solanki, S. K. (1992), 'Why rapid rotators have polar spots', *Astron. Astrophys.* **264**, L13–L16.

Schüssler, M. (2002), 'The formation of sunspots and starspots', *Astronomische Nachrichten* **323**, 377–382.

Schussler, M., Caligari, P., Ferriz-Mas, A. and Moreno-Insertis, F. (1994), 'Instability and eruption of magnetic flux tubes in the solar convection zone', *Astron. Astrophys.* **281**, L69–L72.

Shu, F. H. (1977), 'Self-similar collapse of isothermal spheres and star formation', *Astrophys. J.* **214**, 488–497.

Siegel, R. and Howell, J. R. (1981), *Thermal radiation heat transfer*, Series in Thermal and Fluids Engineering, New York: McGraw-Hill, 1981, 2nd ed.

Siess, L., Dufour, E. and Forestini, M. (2000), 'An internet server for pre-main sequence tracks of low- and intermediate-mass stars', *Astron. Astrophys.* **358**, 593–599.

Simon, M., Howell, R. R., Longmore, A. J., Wilking, B. A., Peterson, D. M. and Chen, W.-P. (1987), 'Milliarcsecond resolution infrared observations of young stars in Taurus and Ophiuchus', *Astrophys. J.* **320**, 344–355.

Skinner, C. J., Bergeron, L. E. and Daou, D. (1997), Characteristics of the NICMOS detectors, *in* 'The 1997 HST Calibration Workshop with a New Generation of Instruments, p. 171'.

Skrutskie, M. F., Cutri, R. M., Stiening, R., Weinberg, M. D., Schneider, S., Carpenter, J. M., Beichman, C., Capps, R., Chester, T., Elias, J., Huchra, J., Liebert, J., Lonsdale, C., Monet, D. G., Price, S., Seitzer, P., Jarrett, T., Kirkpatrick, J. D., Gizis, J. E.,

Howard, E., Evans, T., Fowler, J., Fullmer, L., Hurt, R., Light, R., Kopan, E. L., Marsh, K. A., McCallon, H. L., Tam, R., Van Dyk, S. and Wheelock, S. (2006), 'The Two Micron All Sky Survey (2MASS)', *Astron. J.* **131**, 1163–1183.

Sterzik, M. F., Alcala, J. M., Neuhaeuser, R. and Schmitt, J. H. M. M. (1995), 'The spatial distribution of X-ray selected T-Tauri stars. I. Orion.', *Astron. Astrophys.* **297**, 418–+.

Strassmeier, K. G., Welty, A. D. and Rice, J. B. (1994), 'A Doppler image of the weak T Tauri star V410 Tau', *Astron. Astrophys.* **285**, L17–L20.

Unruh, Y. C. and Collier Cameron, A. (1997), 'Does chromospheric emission mimic polar starspots in Doppler images?', *Mon. Not. R. Astr. Soc.* **290**, L37–L42.

Unruh, Y. C., Collier Cameron, A. and Cutispoto, G. (1995), 'The Evolution of Surface Structures on Ab-Doradus', *Mon. Not. R. Astr. Soc.* **277**, 1145–+.

Valenti, J. A. and Johns-Krull, C. M. (2004), 'Observations of Magnetic Fields on T Tauri Stars', *Astrophysics and Space Science* **292**, 619–629.

Varshni, Y. P. (1967), 'Temperature dependence of the energy gap in semiconductors', *Physica* **34**, 149–154.

Vaughan, A. H., Preston, G. W. and Wilson, O. C. (1978), 'Flux measurements of CA II H and K emission', *Publs. Astr. Soc. Pacif.* **90**, 267–274.

Vrba, F. J., Herbst, W. and Booth, J. F. (1988), 'SPOT evolution on the T Tauri star V 410 Tau', *Astron. J.* **96**, 1032–1039.

Walter, F. M., Vrba, F. J., Mathieu, R. D., Brown, A. and Myers, P. C. (1994), 'X-ray sources in regions of star formation. 5: The low mass stars of the Upper Scorpius association', *Astron. J.* **107**, 692–719.

Warren, S. J., Hambly, N. C., Dye, S., Almaini, O., Cross, N. J. G., Edge, A. C., Foucaud, S., Hewett, P. C., Hodgkin, S. T., Irwin, M. J., Jameson, R. F., Lawrence, A., Lucas, P. W., Adamson, A. J., Bandyopadhyay, R. M., Bryant, J., Collins, R. S., Davis, C. J., Dunlop, J. S., Emerson, J. P., Evans, D. W., Gonzales-Solares, E. A., Hirst, P., Jarvis, M. J., Kendall, T. R., Kerr, T. H., Leggett, S. K., Lewis, J. R., Mann, R. G., McLure, R. J.,

McMahon, R. G., Mortlock, D. J., Rawlings, M. G., Read, M. A., Riello, M., Simpson, C., Smith, D. J. B., Sutorius, E. T. W., Targett, T. A. and Varricatt, W. P. (2006), 'The United Kingdom Infrared Telescope Infrared Deep Sky Survey First Data Release', *Mon. Not. R. Astr. Soc.* pp. 1426–+.

Wilking, B. A., Lada, C. J. and Young, E. T. (1989), 'IRAS observations of the Rho Ophiuchi infrared cluster - Spectral energy distributions and luminosity function', *Astrophys. J.* **340**, 823–852.

Willstrop, R. V. (1965), 'Absolute measures of stellar radiation, II', *Mem. R. Astr. Soc.* **69**, 83–+.

Wilson, O. C. (1968), 'Flux Measurements at the Centers of Stellar H- and K-Lines', *Astrophys. J.* **153**, 221–+.

Wolk, S. J. (1996), 'Watching the Stars go 'Round and 'Round', *Ph.D. Thesis* .

Young, I. T., Gerbrands, J. J. and Van Vliet, L. J. (1998), *Fundamentals of Image Processing*, The Netherlands: Delf University of Technology, —c1998, Version 2.2.

Young, J. S. (1999), 'Infrared Imaging with COAST', *Ph.D. Thesis* .